Functional and Correlative Analysis of Common Endometrial Cancer Driver Mutations

Matthew William Brown

Somerville College

University of Oxford

This thesis is submitted for the degree of

Doctor of Philosophy in Clinical Medicine

Michaelmas Term 2022

Functional and Correlative Analysis of Common Endometrial Cancer Driver Mutations

Matthew Brown

Somerville College, University of Oxford, Michaelmas Term 2022

Abstract

Endometrial cancer is a growing concern with increasing incidence and mortality countering the downward trend observed in many other cancers. Despite recent advances in understanding, much remains unknown about endometrial cancer pathogenesis and the molecular mechanisms that drive its initiation and growth. This has led to worse outcomes for patients due to a lack of effective prediction of disease course and of effective targeted therapeutics, particularly when surgery is not possible or curative. One of the largest advancements in our understanding of endometrial cancer has come from increased mutational profiling of human tumours. These studies have highlighted many genes exhibiting high rates of mutation as drivers of endometrial cancer, with one such gene being *FBXW7*.

In this work, I used genetically engineered mouse models to investigate the role of the $Fbxw7^{R482Q}$ mutation as a driver of endometrial cancer, both independently and in combination with other frequent endometrial cancer drivers (*Pten* loss of function and *Trp53* mutation). When expressed alone, heterozygous $Fbxw7^{R482Q}$ mutation does not induce any uterine pathology in a Pgr^{Cre}-driven murine model system. However, when combined with either *Pten* loss ($Pten^{\Delta/\Delta}$) or $Trp53^{R172H/\Delta}$, it significantly accelerated cancer development leading to significantly reduced overall survival.

Examination of the potential mechanism leading to accelerated carcinogenesis in $Pten^{\Delta/\Delta}$ $Fbxw7^{R482Q/+}$ mice highlighted potential dysregulation of Wnt and Hippo pathway transcription factors. Further molecular analysis found an interaction between FBXW7 with LEF1 and TCF7L2. In the case of TCF7L2, interaction could be almost completely disrupted by introduction of common mutations (R465C, R479Q, and R505C) to the WD40 domain of FBXW7. Together, highlighting these Wnt transcription factors as novel FBXW7 substrates.

In conclusion, $Fbxw7^{R482Q}$ mutation does not initiate carcinogenesis alone, however, it does promote more aggressive cancer development when combined with other cancer driver mutations. Future work should focus on further characterisation of the mechanisms behind co-operation of *Fbxw7* mutation with other cancer driver genes and the potential role of *FBXW7* mutation as a pre-malignant alteration that may provide a foundation for future malignant transformation.

Acknowledgements

Firstly, I would to thank my supervisor, David Church, for providing me with support and the opportunity to undertake a DPhil. Thank you for your guidance, feedback and encouragement throughout the process of this DPhil.

Thank you to the members of the Church group, past and present, for all the help and support I received throughout my time in the lab. Specifically, I would like to thank Kasia for your help with all things computational, for the many parties organised, and hours spent talking science, ranting and everything in between. Charlotte for being a massive help in the lab and making it a more enjoyable place to work. Mark for organising a plethora of lab outings. Emily for helping me to get my bearings in the lab and teaching me a variety of new techniques. Eleni for the valuable guidance and advice given.

I would like to thank members of staff at the Wellcome Centre for Human Genetics. Everyone that aided and facilitated my research during my time in the centre: the lab support members, glass wash members, staff at the Oxford Genomics Centre, and the IT team. In particular, thank you to all the technicians and staff of the FGF Unit for their hard work and diligence in the care of my mice. Additionally, to James and Ed, of the Cellular Imaging Core, for making cellular imaging accessible and all the training, help and guidance with the various imaging work performed during my time in the centre.

Thank you to my Mum, Dad and Kate for all the love and support throughout the years, I certainly would not be where I am today with you. Thank you to Lewis, Andy, Ash, Stephen, Matt, and Joe for the many years of pints, laughs and good times.

Thank you to Nadia. Your love and support throughout this DPhil has completely

transformed the experience, it would have been significantly more difficult if not for you. Your work ethic and determination pushed me to try to do better every day and made me a better person and scientist. From amazing meals (and Aperols) shared to long chats about everything to constant advice about protocols and lab issues, you never failed to lift my spirits and brighten my days; you made completion of this work possible. For all that and more, thank you.

Lastly, thank you to anybody that helped me throughout my DPhil that I have not mentioned above, I promise the exclusion is not intentional.

Preface

This thesis is a collection of research carried out by the author in the Cancer Genomics and Immunology Laboratory at the Wellcome Centre for Human Genetics, Nuffield Department of Medicine, University of Oxford, between October 2017 and July 2022, under the supervision of Professor David Church. The research described herein is original, though the work of others is cited with appropriate references within the text. No part of this research has previously been submitted for a degree at this or any other university.

Some of the work described in this thesis has been submitted for publication:

- **Brown, M.**, Leon-Castillo, A., Kedzierska, K., Moore, C., Belnoue-Davis, H.L., Flach, S., Lydon, J.P., DeMayo, F.J., Lewis, A., Bosse, T., Tomlinson, I., Church, D.N. Functional analysis of endometrial cancer drivers reveals cooperativity and identifies LEF1 and TCF7L2 as FBXW7 substrates. *Under Review*.

I have additionally contributed to the following publications that are not covered in this thesis:

- Barr, C., Wan, Y.L., Quille, N., **Brown, M.**, Kedzierska, K., Church, D.N., Edmondson, R., Crosbie, E. The prognostic value of serum CA125 and HE4 in endometrial cancers stratified by molecular subgroup: a prospective cohort study. *Under Review*.

- Temko, D., Van Gool, I.C., Rayner, E., Glaire, M., Makino, S., **Brown, M.**, Chegwidden, L., Palles, C., Depreeuw, J., Beggs, A., Stathopoulou, C., Mason, J., Baker, A.-M., Williams, M., Cerundolo, V., Rei, M., Taylor, J.C., Schuh, A., Ahmed, A.,

Amant, F., Lambrechts, D., Smit, V.T., Bosse, T., Graham, T.A., Church, D.N. and Tomlinson, I. Somatic POLE exonuclease domain mutations are early events in sporadic endometrial and colorectal carcinogenesis, determining driver mutational landscape, clonal neoantigen burden and immune response. *The Journal of Pathology* **245**, 283-296 (Mar. 2018)

- Glaire, M.A., **Brown, M.**, Church, D.N., Tomlinson, I. Cancer predisposition syndromes: lessons for truly precision medicine. *The Journal of Pathology* **241**, 226-235 (Nov. 2016)

Contents

Abbreviations

AA amino acids.

AH atypical hyperplasia.

Akt AKT serine/threonine kinase.

Amhr2 anti-Mullerian hormone type 2 receptor.

AP-1 activator protein-1.

Apc Adenomatous polyposis coli.

Arid1a AT-rich interaction domain 1A.

ASPA Animals (Scientific Procedures) Act.

Atg12 autophagy related 12.

Atg5 autophagy related 5.

Atm ATM serine/threonine kinase.

Atr ATR serine/threonine kinase.

BAC bacterial artificial chromosome.

Bax BCL2 associated X, apoptosis regulator.

Bbc3 BCL2 binding component 3.

Bcl2l11 BCL2 like 11.

BDT BigDye Terminator.

Blm BLM RecQ like helicase.

Bmf BCL2 modifying factor.

BMI body mass index.

bp base pairs.

Brca1 BRCA1 DNA repair associated.

Brca2 BRCA2 DNA repair associated.

CAG CMV early enhancer/chicken beta actin.

CAH complex atypical hyperplasia.

Ccn1 cellular communication network factor 1.

Ccn2 cellular communication network factor 2.

Ccn4 cellular communication network factor 4.

Ccne1 cyclin E1.

Ccne2 cyclin E2.

Cd274 CD274 molecule.

Cd3e CD3 epsilon subunit of T-cell receptor complex.

Cdk2 cyclin dependent kinase 2.

Cdkn1a cyclin dependent kinase inhibitor 1A.

Cdkn1b cyclin dependent kinase inhibitor 1B.

Cdkn2a cyclin dependent kinase inhibitor 2A.

cDNA complementary DNA.

CDS coding sequence.

Cebpd CCAAT/enhancer-binding protein δ.

Chek1 checkpoint kinase 1.

Chek2 checkpoint kinase 2.

Ck1 casein kinase 1.

CN copy-number.

CNA copy-number alteration.

CPD Cdc4 phosphodegron.

Cre Cre recombinase.

Ctnnb1 catenin β 1.

Cul1 cullin 1.

Ddb2 damage specific DNA binding protein 2.

DEG differentially expressed gene.

DMEM Dulbecco's modified Eagle medium.

DNA deoxyribose nucleic acid.

DTT dithiothreitol.

Dvl dishevelled.

EC endometrial cancer.

EDTA ethylenediaminetetraacetic acid.

Egfr epidermal growth factor recptor.

Eif2b eukaryotic initiation factor 2B.

Eif4ebp1 eukaryotic translation initiation factor 4E binding protein 1.

EIN endometrioid intraepithelial neoplasia.

EMT epithelial to mesenchymal transition.

Erbb2 erb-b2 receptor tyrosine kinase 2.

Fas Fas cell surface death receptor.

Faslg FAS ligand.

FBS foetal bovine serum.

Fbxw7 F-box and WD repeat domain containing 7.

FFPE formalin fixed paraffin embedded.

Foxa2 forkhead box A2.

Foxo forkhead box O.

Fzd frizzled.

G6PC glucose 6-phophatases.

Gadd45a growth arrest and DNA damage inducible alpha.

GDP guanosine diphosphate.

GEMM genetically engineered mouse model.

Glut glucose transporter.

Gs glycogen synthase.

GSEA gene set enrichment analysis.

Gsk3 glycogen synthase kinase 3.

GTP guanosine triphosphate.

H&E haematoxylin and eosin.

Hdac6 histone deacetylase 6.

Hes5 hes family bHLH transcription factor 5.

Hif1a hypoxia inducible factor 1 subunit alpha.

Hk2 hexokinase 2.

HotSHOT Hot Sodium Hydroxide and Tris.

Hsf1 heat shock transcription factor 1.

Hsp90aa1 heat shock protein 90 alpha family class A member 1.

Igf1 insulin like growth factor 1.

Igfbp1 insulin like growth factor binding protein 1.

Igfbp2 insulin like growth factor binding protein 2.

IHC immunohistochemistry.

Inppl1 inositol polyphosphate phosphatase like 1.

JNK Jun N-terminal kinase.

Jun Jun proto-oncogene, AP-1 transcription factor subunit.

KCl potassium chloride.

Ki67 marker of proliferation Ki-67.

Klf5 KLF transcription factor 5.

Kras KRAS proto-oncogene, GTPase.

Krt5 keratin 5.

Krt8 keratin 8.

Lats1 large tumor suppressor kinase 1.

LB Luria-Bertani.

LCM laser capture microdissection.

Lef1 lymphoid enhancer binding factor 1.

LOH loss of heterozygosity.

LRP low density lipoprotein receptor-related protein.

LS Lynch syndrome.

Ltf lactoferrin.

LVSI lympho-vascular space invasion.

Map4k mitogen-activated protein kinase kinase kinase kinases.

Max MYC associated factor X.

Mb megabase.

Mcl1 MCL1 apoptosis regulator, BCL2 family member.

Mdm2 MDM2 proto-oncogene.

MEM minimum essential medium.

$MgCl_2$ magnesium chloride.

Mlh1 mutL homolog 1.

Mmp13 matrix metallopeptidase 13.

MMRd mismatch repair deficiency.

MMRd mismatch repair deficient.

Mob1 MOB kinase activator 1.

Msh2 mutS homolog 2.

Msh6 mutS homolog 6.

MSI microsatellite instability.

Mst1 mammalian STE kinase 1.

Mtor mechanistic target of rapamycin kinase.

mTORC1 MTOR complex 1.

mTORC2 MTOR complex 2.

Mutyh mutY DNA glycosylase.

Myc MYC proto-oncogene, bHLH transcription factor.

NaCl sodium chloride.

NHEJ non-homologous end joining.

NICD notch intracellular domain.

NMR nuclear magnetic resonance.

Notch1 notch receptor 1.

NSCLC non-small cell lung cancer.

NSMP no specific molecular pathology.

OCT Optimal Cutting Temperature.

Parp1 poly(ADP-ribose) polymerase 1.

PBS phosphate buffered saline.

PCAWG Pan-Cancer Analysis of Whole Genomes.

Pck phosphoenolpyruvate carboxykinase.

PCR polymerase chain reaction.

Pdcd1 programmed cell death 1.

Pdpk1 3-phosphatidylinositide dependent protein kinase 1.

Pgr progesterone receptor.

Phlpp PH domain and leucine rich repeat protein phosphatase.

PI3K phosphatidylinositide 3-kinase.

Pik3ca phosphatidylinositol-4,5-bisphosphate 3-kinase catalytic subunit alpha.

Pik3cb phosphatidylinositol-4,5-bisphosphate 3-kinase catalytic subunit beta.

Pik3cd phosphatidylinositol-4,5-bisphosphate 3-kinase catalytic subunit delta.

Pik3cg phosphatidylinositol-4,5-bisphosphate 3-kinase catalytic subunit gamma.

Pik3r1 phosphatidylinositide-3-kinase regulatory subunit 1.

Pik3r2 phosphatidylinositide-3-kinase regulatory subunit 2.

Pik3r5 phosphatidylinositide-3-kinase regulatory subunit 5.

Pin1 peptidylprolyl cis/trans isomerase, NIMA-interacting 1.

Plk1 polo-like kinase 1.

Pmaip1 phorbol-12-myristate-13-acetate-induced protein 1.

Pms2 PMS1 homolog 2.

Pold1 DNA polymerase δ1, catalytic subunit.

Pole DNA polymerase ε, catalytic subunit.

Polh DNA polymerase eta.

Pp2a protein phosphatase type 2A.

Ppp2r1a protein phosphatase 2 scaffold subunit alpha.

ProMisE Proactive Molecular Risk classification tool for Endometrial cancers.

PtdIns phosphatidylinositol.

Pten phosphatase and tensin homolog.

PTM post-translational modification.

Rb1 RB transcriptional corepressor 1.

Rbx1 RING-box 1.

RE restriction enzyme.

Rheb Ras homolog, mTORC1 binding.

RIPA radio immunoprecipitation assay.

RMA robust multi-array average.

Rpa replication protein A.

Rps6kb1 ribosomal protein S6 kinase B1.

RT-qPCR real-time quantitative PCR.

rtTA reverse tetracycline transactivator.

S.O.C. super optimal broth with catabolite repression.

Sav1 salvador homolog 1.

SCF Skp, Cullin, F-box.

SDM site-directed mutagenesis.

SEIC serous endometrial intraepithelial carcinoma.

Shbg sex-hormone binding globulin.

Skp1 S-phase kinase-associated protein 1.

SLN sentinel lymph node.

Snai1 snail family transcriptional repressor 1.

Sprr2f small proline rich protein 2F.

Srebf1 sterol regulatory element binding transcription factor 1.

T-ALL T lymphoblastic leukaemia.

Tbc1d4 TBC1 domain family member 4.

Tbc1d7 TBC1 domain family member 7.

TBE Tris-borate-EDTA.

TBS tris-buffered saline.

Tcf7 transcription factor 7.

Tcf7l1 transcription factor 7 like 1.

Tcf7l2 transcription factor 7 like 2.

TCGA The Cancer Genome Atlas.

TE Tris-EDTA.

Tead TEA domain transcription factor.

Tfeb transcription factor EB.

Tgif1 TGFB induced factor homeobox 1.

Tnfrsf10b TNF receptor superfamily member 10b.

TP53 tumour protein 53.

Trp53 transformation related protein 53.

Tsc1 TSC complex subunit 1.

Tsc2 TSC complex subunit 2.

UCEC uterine corpus endometrial carcinoma.

UCS uterine carcinosarcoma.

UK United Kingdom.

Ulk1 unc-51 like autophagy activating kinase 1.

UPS ubiquitin proteasome system.

US United States.

WCHG Wellcome Centre for Human Genetics.

WHO World Health Organisation.

Wwtr1 WW domain containing transcription regulator 1.

Xrcc4 X-ray repair cross complementing 4.

Yap1 Yes1 associated transcriptional regulator.

Ywhaz tyrosine 3-monooxygenase/tryptophan 5-monooxygenase activation protein zeta.

Zeb2 zinc finger E-box binding homeobox 2.

List of Tables

List of Figures

Chapter 1

Introduction

Cancer, a disease of uncontrolled cell growth and invasion, is caused by the corruption of normal cellular processes by progressive genetic and epigenetic alterations [1]. While specific alterations vary between different types of cancer (and even within cancers from the same site of origin), collectively they function to provide characteristics that are fundamental to the disease, often termed the hallmarks of cancer [2–4]. Over twenty years ago, six hallmarks were proposed: (i) sustained proliferative signalling, (ii) evasion of growth suppressors, (iii) resistance to cell death, (iv) induction of angiogenesis, (v) acquisition of replicative immortality and (vi) achieving the ability to invade and metastasise to spread beyond the organ of origin and colonise other areas of the body [2]. Through subsequent decades of work, further key cancer characteristics have been identified including immune evasion and increased cellular plasticity [3, 4]. Understanding the mechanisms by which these hallmarks are attained is a pivotal area of cancer research, and one that is vital in tackling the cancer epidemic affecting populations worldwide.

Cancer is currently one of the largest global health issues facing humanity. In 2020, the estimated worldwide cancer incidence and mortality reached 19.3 million new cases and almost 10 million cancer deaths [5]. Worryingly, incidence and mortality remains on an upward trend and cancer now ranks in the top two leading causes of death in more than half of the countries in the world; comparable incidence and mortality data from 2012 indicated there were 14.1 million new cancer cases and 8.2 million cancer deaths

[5, 6]. These trends are due in large part to increasingly aged populations and general population growth. In fact, examination of age-standardised mortality rates between 1990 and 2019, reveal a 15% decrease in mortality due to improvements in treatment and screening/early detection programs [7].

While improvements in survival are to be lauded, the overall health burden of cancer is a less-discussed matter and one that is borne not just by those that ultimately succumb to the disease. Even those that respond favourably to treatment and enter remission can suffer life changing consequences and significantly decreased quality of life due to the negative effects of surgery, radiotherapy, chemotherapy or other necessary treatments [8, 9]. Therefore, even as improvements are made in the length of life of those diagnosed with cancer, there is still significant space for refinement of treatment regimes through improved risk stratification and targeted therapeutics, to better preserve quality of life.

1.1 The uterus and menstrual cycle

The uterus forms a central part of the female reproductive system as the location of embryonic implantation and host organ for fetal growth. Structurally, the human uterus can be subdivided in to four parts: the fundus, corpus, isthmus, and cervix (Figure 1.1A) [10]. At the cellular level the corpus, isthmus and fundus are comprised of three main layers: the innermost layer, the endometrium, composed of the simple, columnar, surface epithelial lining (glandular and luminal epithelium) and the underlying stroma (which includes cell types such as fibroblasts, myofibroblasts, mesenchymal stromal cells, endothelial cells, and immune cells) [11]. The central layer is formed of smooth muscle cells termed the myometrium, and the outermost layer, the perimetrium, consisting of a single layer of mesothelial cells which define the boundary of the organ (Figure 1.1B).

Throughout a woman's reproductive life, the uterus exhibits a remarkable level of plasticity and regeneration. It will undergo approximately 450 menstrual cycles and unless nulligravida (never pregnant), the dramatic remodelling required to support gestation [12]. During the menstrual cycle changes in the histological structure of the

endometrium are driven by the ovarian hormones oestrogen and progesterone (Figure 1.1C) [13]. The cycle begins with menstruation, when the upper layers of the endometrium are sloughed off due to restricted blood flow from declined oestrogen and progesterone levels [14]. In the proliferative phase, gradually increasing oestrogen levels drive thickening of the endometrium due to expansion of both the glandular epithelium and stroma [15]. Post-ovulation, the secretory phase begins, during which rising and then sustained progesterone levels drive glandular secretion of mucus and glycogen in preparation for potential implantation of a fertilised embryo [15]. In the absence of implantation, declining progesterone and oestrogen levels lead to vasoconstriction and the endometrium begins to shrink [15].

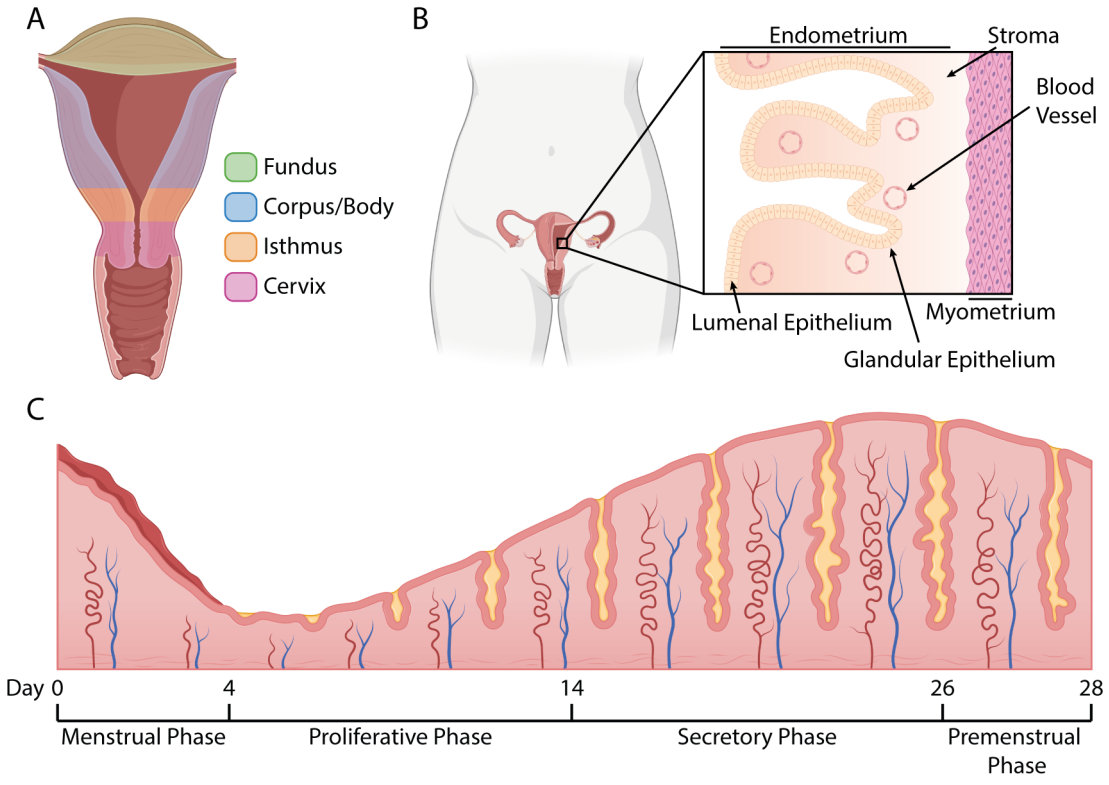

Figure 1.1: Schematic depicting **A.** The regions of the human uterus, **B.** The longitudinal histological structure of normal uterus and **C.** the histological changes in the endometrium during the menstrual cycle. Figure panels were created using assets from BioRender and adapted from [10] - **A**, and [16] - **B**.

1.2 Uterine cancer

Normal uterine function is characterised by repeated cycles of endometrial tissue shedding, repair, and regeneration [17]. It is therefore unsurprising that corruption of the mechanisms that tightly control this process can lead to cancer. Cancer can commonly affect the uterine corpus, although cancer can arise in the both the fundus and isthmus and together these are collectively called uterine cancers [18]. There are two broad categories of uterine cancer: endometrial cancer (EC) (also referred to as uterine corpus endometrial carcinoma (UCEC)) and uterine sarcomas. Uterine sarcoma can arise from endometrial stroma cells (endometrial stromal sarcomas) or from the smooth muscle cells of the myometrium (leiomyosarcomas) [19]. ECs are a subset of uterine cancers that arise from the epithelial lining of the uterus. They are the most common type of cancer arising in the uterine corpus, accounting for more than 90% of cancers [20].

1.2.1 Epidemiology - incidence and mortality

EC is currently the sixth most common cancer in women worldwide with an estimated 417,000 new cases and 97,000 deaths in 2020 [5]. Incidence rates across the world vary by up to 10-fold, with higher rates seen in western regions such as Northern America and Europe and the lowest rates in Africa and South Central Asia [5]. Mortality rates exhibit less variation, but higher rates are seen in Eastern Europe, the Caribbean and North America [5]. In the United Kingdom (UK), EC is the fourth most common female cancer, comprising 5% of all new female cancer diagnoses (9,703 per year) and is the eighth most common cause of female cancer death, comprising 3% of total female cancer deaths (2,453 per year) [21, 22].

In keeping with upwards trend seen in incidence rates of many other cancer types in the UK, incidence of EC has been also rising. Over the last decade the age-standardised incidence rate, in the UK, has increased by 12% [21]. Importantly, EC has opposed the current declining mortality trend exhibited by most cancer types [22]. Over the last decade the age-standardised mortality rate has increased by 24% in the UK and a similar trend has been observed in the United States (US), with a 1.3% annual increase between

2012-2016 [22, 23].

Projections to 2035 suggest there will be a 6.8% decrease in the age-standardised incidence rates for EC [24]. However, there is predicted to be a 24% increase in the total number of cases due to the increasingly elderly population [24]. Additionally, age-standardised EC mortality is predicted to increase by 18.7%, with an estimated 76.8% increase in total EC deaths [24]. This means that by 2035, there will be an estimated 3830 deaths per year from EC, which would make it the sixth most common cause of female cancer death [24].

1.2.2 Aetiology - risk factors

Increasing age is a major risk factor for EC, with over 50% of diagnosed cases occurring in women over the age of 65 [21]. Aside from age, the primary risk factor for EC is high oestrogen exposure, particularly in the absence of progesterones, for example, early menarche and late menopause are noted risk factors [25–31]. When age of menarche and menopause are considered together as lifetime number of menstrual cycles, a stronger association with risk of EC is seen where longer menstrual lifetime indicates a higher risk [25–30]. Therefore, nulliparity and infertility increase risk of EC while increasing parity decreases risk [29, 32]. Pregnancy has a positive influence on EC risk as it reduces lifetime number of menstrual cycles and is associated with a hormonal shift away from oestrogen and towards progesterone [33].

Other causes of unopposed oestrogen include various pathologies that drive endogenous oestrogen production, for example, oestrogen-producing tumours (granulosa cell tumours), or progesterone deficiency caused by anovulatory cycles and the lack of corpus luteum formation characteristic of polycystic ovary syndrome [34, 35]. Additionally, use of exogenous oestrogen which often forms part of hormone replacement therapy is associated with a higher risk of developing EC [31]. However, this risk can be mostly or wholly mitigated by the addition of continuous or cyclical progesterone to counter oestrogen [36, 37]. Furthermore, the oestrogen mimetic, tamoxifen, is also linked with a 2-fold increased EC risk during prolonged use [38]. Conversely, to tamoxifen usage, oral contraceptive use is linked with a decreased risk of EC [39].

High body mass index (BMI) and obesity are also strongly linked with EC. In women, elevated BMI has the strongest association with incidence of and mortality from EC than any other cancer type [40, 41]. Risk of incidence shows a dose-dependent response with relative risk increasing from 1.5 for overweight women (BMI 25-29.9) to 7.1 in women with class 3 obesity (BMI $\geq$40) [42]. In Calle *et al.*'s study of mortality risk in the US, women in the highest BMI category ($\geq$40) had a relative risk of EC mortality 6.25-fold higher than those in the normal BMI range (18.5-24.9) [40].

Mechanistically, the link between obesity and EC is incompletely understood, but several hypotheses have been proposed. The endogenous sex hormone hypothesis posits that excess adipose tissue drives synthesis of oestrogen, and increases its bioavailability through reduction of sex-hormone binding globulin (SHBG) concentration in the blood [43]. The insulin-insulin like growth factor 1 (IGF1) hypothesis postulates that obesity-induced hyperinsulinaemia reduces expression of insulin like growth factor binding protein 1 (IGFBP1) and IGFBP2. This increases the bioavailability of IGF1, driving cell proliferation and angiogenesis, and protecting against apoptosis [44]. The final hypothesis involves adipokines and systemic inflammation, in which adipocyte-derived adipokines are expressed at higher levels. Adipokines are associated with modulation of the inflammatory response and cellular proliferation pathways [44]. Independent of BMI, both type 1 and type 2 diabetes have been linked as a risk factor for EC [45, 46], which may add credence to the hypothesis that hyperinsulinaemia and IGF1 play a mechanistic role in endometrial carcinogenesis.

EC risk is heavily influenced by environmental factors, although, numerous studies have identified a hereditary component; the relative risk of a woman with a diagnosed first-degree relative has been reported to be between 1.5-2.8 [47–50]. While close relatives will frequently share similar environmental risk factors, an increased risk remains independently of these [51]. To date, numerous genes with low penetrance and a small effect on endometrial cancer risk have been identified [52–55]. However, there are several genetic syndromes that have high penetrance for EC, such as as Lynch syndrome (LS) and Cowden's syndrome. LS is characterised by germline mutation of genes involved in the mismatch repair pathway: mutL homolog 1 (*MLH1*), mutS ho-

molog 2 (*MSH2*), mutS homolog 6 (*MSH6*), and PMS1 homolog 2 (*PMS2*). Overall, lifetime (to age 75) risk of EC for LS patients is reportedly between 30-60%, with extent of risk dependent on the specific mutation: 42.7% for *MLH1*, 56.7% *MSH2*, 46.2% *MSH6*, and 26.4% *PMS2* [56–58]. Similarly, women with Cowden's syndrome (germline mutation of *PTEN*) have an increased lifetime risk of EC between 19-28% [59, 60]. Further rare germline mutations that confer risk of endometrial cancer include those in mutY DNA glycosylase (*MUTYH*), DNA polymerase ε, catalytic subunit (*POLE*) and DNA polymerase $\delta 1$, catalytic subunit (*POLD1*), and BRCA1 DNA repair associated (*BRCA1*)/*BRCA2* [61–65].

1.2.3 Classification

Classification of cancer is key for predicting patient prognosis and informing clinical decision-making. EC is a complex and heterogeneous disease and throughout years of ongoing research, several methods for classification have been developed, implemented and iterated over.

1.2.3.1 Pathogenetic

An initial classification model for EC was proposed by Bokhman in 1983 [66]. This dualistic classification method proposed two distinct pathogenetic mechanisms driving EC which further inform their distinct characteristics and prognosis. Type I cancers, which comprise 60-70% of ECs, are derived from an environment with evidence of endometrial hyperplasia due to a background of unopposed oestrogen stimulation, a characteristic more common in patients exhibiting obesity, diabetes and other metabolic diseases [31]. Type II cancers, accounting for around 30-40% of ECs, arise in the background of atrophic endometrium and are oestrogen independent. This class of disease is generally diagnosed in post-menopausal women [66].

When dichotomised according to these characteristics, two differing disease courses are apparent. Type I ECs are more indolent, frequently presenting after a longer duration of symptoms, but with a well differentiated tumour that displays sensitivity to progesterones, low frequency of myometrial/lymphatic invasion, and is associated with a

favourable prognosis (85.6% 5-year survival) [66]. Type II cancers generally have a more rapid onset of symptoms with patients frequently presenting with poorly differentiated tumours and evidence of myometrial/lymphatic invasion. The prognosis for these patients is poor (58.8% 5-year survival) [66].

1.2.3.2 Histomorphological

The primary method of classifying EC is based on their characteristic appearance under the microscope (histology and grade) and the extent of localisation or invasion to surrounding tissues (FIGO stage, lympho-vascular space invasion (LVSI) and myometrial invasion) with guidelines provided by the World Health Organisation (WHO) [67, 68]. This methodology has been the gold standard for classification of patients to inform clinical management throughout the last decades.

Endometrial Cancers Classification of histological features of EC divides patients in to two groups: those with endometrioid or non-endometrioid histology. Endometrioid carcinomas are the more common with around 80% patients diagnosed. This group most closely correlates with the type I cancer described by Bokhman and share similar clinical features (Table 1.1) [69, 70]. However, as many as 15-30% of endometrioid carcinomas present as high grade (grade 3) and have characteristics overlapping that of type II cancers such as higher risk of locoregional relapse and death related to endometrial cancer [69, 71–75]. The overall characteristics of these cancers are intermediate of type I and type II cancers [69, 72–75]. The non-endometrioid category is composed of three main histologies: serous carcinomas ($\sim$10% of all EC), clear cell carcinomas ($\sim$5% of all EC) and carcinosarcomas ($\sim$5% of all EC). These histologies correlate more closely with type II cancers and are characterised by high grade and poor prognosis, with 5-year survival estimated at 30-38%, 50-55%, and 30% for serous, clear cell, and carcinosarcoma, respectively [69, 70, 76].

For a long time carcinosarcomas, a subgroup of tumours that have a mixed epithelial and mesenchymal component, were considered more closely related to uterine sarcomas than endometrial carcinomas due to the uncertainty around their origins. Several

Table 1.1: Epidemiological and molecular correlations observed between the histomorphological and Bokhman classification methods

Characteristic	Type I	Type II
Histology	Endometrioid	Serous; Clear Cell; Carcinosarcoma
Tumour Grade	I-II	III
Uterine Background	Hyperplasia	Atrophy
Risk Factors	High BMI/Obesity	None Specific
Menopausal Status [83]	Pre- (18.3%) or Post- (75.6%)	Post- (85.8%)
Median Age at Diagnosis [83]	60 years	68 years
Common Genetic Alterations	*PTEN*, *KRAS*, *CTNNB1* mutation; MSI	*TP53* mutation; Aneuploidy
5-year Survival Rate [84]	82.4%	40.9%

hypotheses were proposed, including: (a) collision theory, where two independent, simultaneous tumours grow in to each other, (b) composition theory in which the stromal component is not truly neoplastic and is instead reactive to the epithelial component, (c) combination theory which suggests both components have a single cell of origin, (d) conversion theory in which the sarcomatous component is derived from the carcinoma component [77]. It is now accepted that these cancers are of monoclonal origin, with sarcoma derived from metaplastic carcinoma [77–82]. This is based on the overlapping mutations present in the epithelial and sarcomatous component [78–82].

Precursor Lesions Endometrioid carcinomas, as their overlap with type I classification would suggest, grow from a hyperplastic precursor lesion. However, hyperplasia in the endometrium can take on different forms, which were initially classified based on two main characteristics according to the WHO [67, 68]. Firstly, the extent of hyperplasia, designated as either simple or complex. Simple hyperplasia is indicated by increased volume of both gland and stroma beyond the expansion typically seen during normal uterine cycling. Complex hyperplasia shows a more pronounced increase in the glandular volume without concomitant stromal volume increase. This typically leads to glandular crowding and exclusion of inter-glandular stroma. The second characteristic feature was the presence or absence of abnormalities in nuclear appearance, nuclear

atypia [85]. The combination of these features produced four potential categories for hyperplasia:

- Simple hyperplasia without atypia
- Complex hyperplasia without atypia
- Simple atypical hyperplasia
- Complex atypical hyperplasia

However, diagnostic challenges were evident with this system, particularly in the differentiation of the more severe atypical hyperplasias and low-grade adenocarcinomas and the clinical relevance of complex hyperplasia without atypia and simple atypical hyperplasia [86, 87]. In 2014, a new classification method for endometrial hyperplasia was proposed, a simplified system that centred on the presence of nuclear atypia which has been shown to be a stronger indicator of risk of developing EC [88]. The new system defines two diagnoses: hyperplasia without atypia (benign endometrial hyperplasia), which has a relative risk of progression to invasive carcinoma of 1.01-1.03 and atypical hyperplasia (AH)/endometrioid intraepithelial neoplasia (EIN), which has a relative risk of progression between 14-45 [88].

Precursor lesions for type II, non-endometrioid cancers are less well characterised. However, serous endometrial intraepithelial carcinoma (SEIC) is a recognised precursor to endometrial serous carcinoma and some clear cell carcinomas. These lesions exhibit cells with similar appearance to serous carcinoma, but confined to the epithelial surface without apparent invasion.

1.2.3.3 Molecular

With advances in molecular biology and sequencing, studies began to examine the molecular correlates of the tumour types defined above. Type I/endometrioid carcinomas are typified by mutations of the phosphatidylinositide 3-kinase (PI3K)-pathway (in particular *PTEN*), KRAS proto-oncogene, GTPase (*KRAS*), catenin β 1 (*CTNNB1*), and epigenetic silencing of *MLH1*. In contrast, type II and non-endometrioid carcinomas

carry tumour protein 53 (*TP53*) mutations, erb-b2 receptor tyrosine kinase 2 (*ERBB2*) amplification and chromosomal instability. Interestingly, high grade endometrioid carcinomas also exhibit correlates similar to non-endometrioid carcinomas, such as *TP53* mutations [89].

The first steps towards a classification system based on molecular information alone came in 2013, with the seminal work performed by The Cancer Genome Atlas (TCGA) consortium [90]. Through combined analysis of mutational, RNA-expression, copy-number alterations (CNAs), and methylation data they were able to distinguish four distinct subtypes of EC (Figure 1.2A):

- *POLE*-mutated - A group of tumours that exhibit an ultramutated phenotype with between 50-500 $\times 10^{-6}$ mutations per megabase (Mb) as the result of exonuclease domain mutations of *POLE*.
- MSI - Tumours that have microsatellite instability (MSI) (also termed mismatch repair deficient (MMRd)), mostly due to *MLH1* promoter methylation. These tumours exhibit a hypermutated phenotype (5-50 $\times 10^{-6}$ mutations per Mb) with numerous small insertion/deletion mutations.
- CN-high - Tumours characterised by a low mutation rate, but extensive CNAs.
- CN-low - Tumours that have a low mutation rate and few CNAs.

The POLE, MSI, and CN-low subtypes are mostly composed of tumours with endometrioid histology and exhibit frequent *PTEN* mutation (Figure 1.2B) [90]. Tumour grade differs between the subtypes with POLE tending to have a higher grade, CN low generally being low grade and heterogeneous grade in the MSI subtype. The CN-high subtype are almost exclusively composed of high grade serous or mixed histology tumours, with prevalent *TP53* mutations [90]. These subtype groupings correlated well with progression-free survival with the POLE subtype having a favourable prognosis, MSI and CN-low an intermediate prognosis and CN-high a poor prognosis (Figure 1.2C). This study clarified some prognostic issues with previous methods, such as the heterogeneity in prognosis of high grade endometrioid tumours. These tumours

were found to map to all four subtypes, but mainly to POLE, MSI, and CN-high with prognosis in line with the molecular subtype as opposed to the tumour grade [90].

Carcinosarcomas and clear cell carcinomas were excluded from the initial TCGA endometrial analysis, but were later examined as separate groups [91, 92]. Analysis of carcinosarcomas highlighted the likely mono-cellular origin for this cancer, but also their similarity to epithelial histology cancers. All previously identified molecular subtypes were apparent in this group (analysis of 56 carcinosarcomas) with one having a *POLE* mutation, two exhibiting MSI, a small minority characteristic of endometrioid subtypes with fewer CN alterations. However, the majority of these samples resembled the CN-high, serous-like subtype identified previously (Figure 1.2E) [91]. Gotoh *et al.*'s examination of carcinosarcomas also recapitulated the four TCGA endometrial subtypes and examined their prediction of progression-free survival (Figure 1.2D) [93]. Subtype survival in uterine carcinosarcoma (UCS) broadly mirrored that of the prior TCGA endometrial analysis, with the POLE subtype having favourable prognosis, MSI having intermediate prognosis and CN-high having poor prognosis [93]. However, the prognosis for the CN-low subtype in this study appears worse than previously reported. This may have been due to characteristic differences behaviour of CN-low carcinosarcomas or potentially due to the increased proportions of CN-high samples and a tendency towards overfitting of the non-POLE or MSI samples in to two groups based on CNAs. Similar analysis of clear cell carcinomas also found representation of all four of the TCGA molecular subtypes, with *TP53* found to be the most commonly altered gene, and the majority of samples resembled the CN-high, serous-like subtype [92].

1.2.3.4 Classification of disease risk

As previously discussed, histomorphological assessment has been a mainstay in the diagnosis and risk management of EC. FIGO stage, grade, histology, and LVSI are all factors used to segregate disease risk in to four categories (Table 1.2). One of the issues of this method of classification is the noted inter-operator variability, particularly from biopsy samples and for high-grade samples [74, 94]. Further to this, while the understanding gained from the TCGA study was invaluable, it did not have immediate

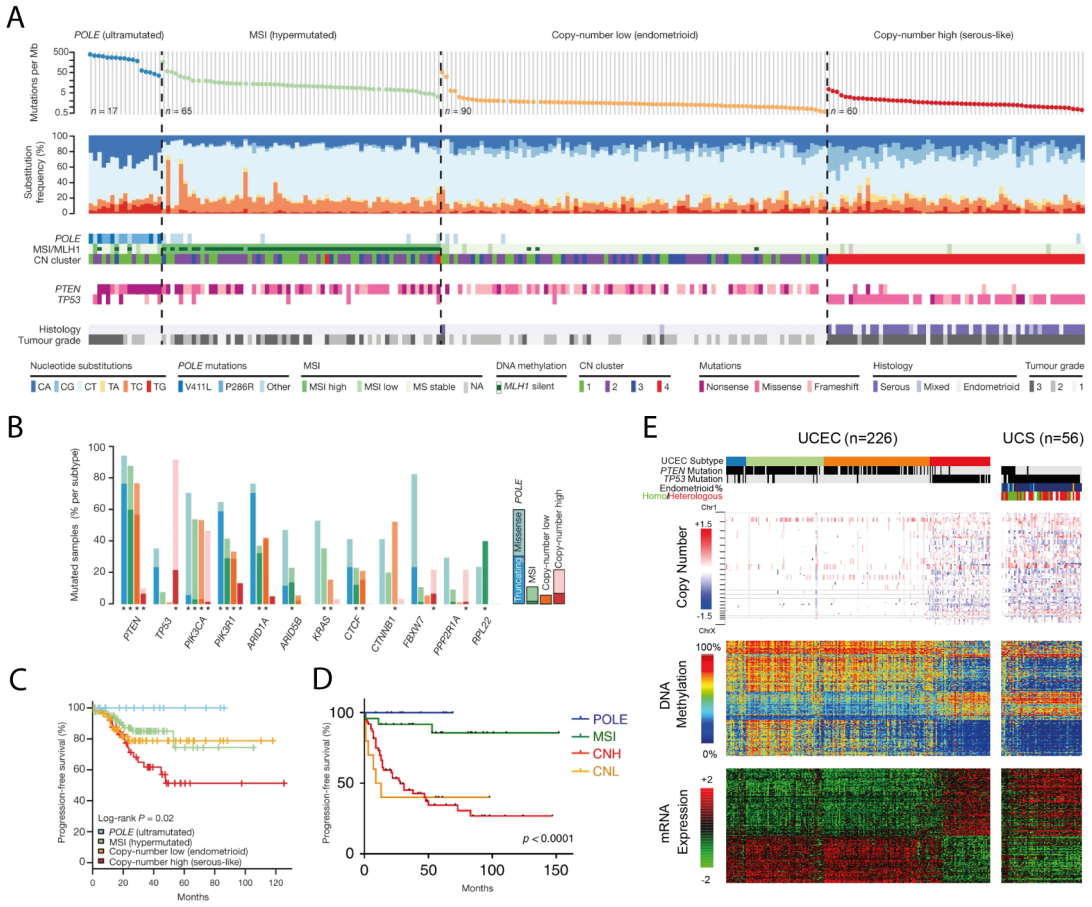

Figure 1.2: Molecular classification of endometrial cancer by TCGA consortium. **A.** Highlights the classification of cancer analysed as part of the TCGA UCEC cohort. Reproduced from [90]. **B.** Indicates the frequency of individual gene mutations across the four subtypes of UCEC cancers. Reproduced from [90]. **C.** Shows the progression-free survival of the four subtypes of UCEC cancers. Reproduced from [90]. **D.** Represents the progression-free survival of gynaecological carcinosarcomas as classified using the four endometrial subtypes, the data represented is a mixed cohort of uterine (n=92) and ovarian (n=17) carcinosarcomas. Reproduced from [93] **E.** Shows the patterns in the data used to define the endometrial subtypes and highlights the similarity between the CN-high subtype and the uterine carcinosarcomas. Reproduced from [91]

impact on clinical management of patients. The sample requirements for generation of multi-omic data (relatively large amounts of fresh-frozen tissue) are generally not available prior to surgical intervention and the associated costs were prohibitive for clinical use. This led to the publication of two clinically-relevant, simplified methods for distinguishing the subtypes using routine techniques [95, 96]. The Proactive Molecular Risk classification tool for Endometrial cancers (ProMisE) study proposed the use of MMRd protein immunohistochemistry (IHC) as the first step to define the MSI group, then *POLE* mutation status to define the POLE group, and finally TP53 IHC was used as

a surrogate of CN-high status to define p53 abn (TP53 abnormal) or p53 wt (otherwise referred to as no specific molecular pathology (NSMP)) [96]. This regime of tests has subsequently been examined on biopsy samples and surgical resection samples with positive implications for risk stratification [97, 98]. Both studies noted that the best prognostic value was obtained by integrating clincopathologic and molecular information [96, 99]. As such these molecular classifiers have been added to complement the existing clinicopathological risk classification methods (Table 1.2).

1.2.4 Clinical management

For the vast majority of patients with EC, surgical resection is the primary form of treatment, with staging also performed during surgery to assess the potential risk of recurrence and aid further decisions on adjuvant therapy. Standard surgery is total hysterectomy with bilateral salpingo-oophrectomy [100]. Additional omentectomy is recommended for patients with serous or carcinosarcoma histology [100]. The preferred surgical method uses minimally invasive techniques, such as laproscopy, as opposed to laprotomy due to shorter recovery times and fewer complications [101, 102].

The extent of lymphadenectomy during surgery is controversial and occurs to a variable extent worldwide. For complete staging, removal of the pelvic and para-aortic lymph nodes is recommended [103, 104]. However, this procedure is associated with reduced of quality of life, due to lymphedema, lymphocele, and neuralgia [105, 106]. Furthermore, several studies have shown no survival and risk of recurrence benefits from lymphadenectomy, particularly for early-stage disease [104, 107]. In contrast, pelvic and para-aortic lymphadenectomy is associated with better overall and progression-free survival in patients with high-risk histologies [108]. An alternative to lymphadenectomy, sentinel lymph node (SLN) evaluation, has been examined and was found sufficiently sensitive to detect nodal metastasis without high false negative rates and superior in terms of lymphatic complications [109–111]. As a result of these findings, the current ESMO-ESGO-ESTRO recommendations call for SLN evaluation to be considered for low- or intermediate-risk endometrioid cancers. It can be omitted if there is no evidence of myometrial invasion, but lymphadenectomy is not recommended for these

Table 1.2: The 2020 endometrial cancer risk categorisation guidelines recommended by ESGO/ESTRO/ESP, table reproduced from [100].

Risk Group	Histomorphological Assessment	Molecular Classification
Low	• Stage IA endometrioid + low-grade + LVSI negative or focal	• Stage I-II *POLE* mutant endometrial carcinoma, no residual disease • Stage IA MMRd/NSMP endometrioid carcinoma + low-grade + LVSI negative or focal
Intermediate	• Stage IB endometrioid + low-grade + LVSI negative or focal • Stage IA endometrioid + high-grade + LVSI negative or focal • Stage IA non-endometrioid (serous, clear cell, carcinosarcoma) without myometrial invasion	• Stage IB MMRd/NSMP endometrioid carcinoma + low-grade + LVSI negative or focal • Stage IA MMRd/NSMP endometrioid carcinoma + high-grade + LVSI negative or focal • Stage IA p53abn and/or non-endometrioid (serous, clear cell, carcinosarcoma) without myometrial invasion
High-Intermediate	• Stage I endometrioid + substantial LVSI regardless of grade and depth of invasion • Stage IB endometrioid high-grade regardless of LVSI Status • Stage II	• Stage I MMRd/NSMP endometrioid carcinoma + substantial LVSI regardless of grade and depth of invasion • Stage IB MMRd/NSMP endometrioid carcinoma high-grade regardless of LVSI status • Stage II MMRd/NSMP endometrioid carcinoma
High	• Stage III-IVA with no residual disease • Stage I-IVA non-endometrioid (serous, clear cell, carcinosarcoma) with myometrial invasion, and with no residual disease	• Stage III-IVA MMRd/NSMP endometrioid carcinoma with no residual disease • Stage I-IVA p53abn endometrial carcinoma with myometrial invasion, with no residual disease • Stage I-IVA MMRd/NSMP serous or carcinosarcoma with myometrial invasion, with no residual disease

groups. Lymphadenectomy (or at minimum SLN evaluation) is recommended in patients with intermediate-high- or high-risk disease or that exhibit myometrial invasion greater than 50%, as well as those with non-endometrioid histologies [16].

As full staging to determine disease risk occurs at the point of surgery, this determination mainly influences the use or extent of adjuvant chemo- or radiotherapy. For patients with low-risk disease, no adjuvant treatment is currently recommended. Radiotherapy is recommended for patients with intermediate-risk and intermediate-high risk disease, in the form of vaginal brachytherapy to reduce risk of local recurrence. However, for intermediate-high risk patients with substantial LVSI, whole pelvis external beam therapy can be considered to reduce risk of locoregional recurrence [100]. High-risk patients should receive combined treatment with whole pelvis external beam therapy and chemotherapy (cisplatin followed by carboplatin-paclitaxel), which has been found to have a survival benefit in the recent PORTEC-3 trial [112].

Patients that are diagnosed with metastatic or recurrent disease should only receive surgery if complete resection is possible without significant morbidity [100]. Otherwise, the only available treatment is systemic chemotherapy, usually in the form of combined carboplatin-paclitaxel [113]. However, hormonal therapy with progestins or tamoxifen has show reasonable response rates at 21.6% in an unselected population [114]. This rate is driven by oestrogen and progesterone receptor positive tumours, which have a 26.5% and 35.5% response rate respectively [114].

With the increase in molecular understanding of EC there have been increasing clinical trials looking to target specific genetic alterations. The ERBB2 inhibitor, trastuzumab, has shown positive effects on progression-free survival in small trials targetting the frequent occurrence of *ERBB2* amplification or overexpression, particularly in carcinosarcoma and serous carcinomas [115, 116]. Immunotherapy, such as PD1/PDL1 (otherwise known as programmed cell death 1 (PDCD1) and CD274 molecule (CD274), respectively) checkpoint inhibitors have been suggested as a potential targeted therapy for high mutation burden tumours, such as the mismatch repair deficiency (MMRd) and *POLE* subtypes. It is hypothesised that the mutation burden is likely to generate neoepitopes that will contribute to an effective immune response. The recent KEYNOTE-

158 trial examined efficacy of pembrolizumab and found a 57.1% overall response rate for endometrial cancer with 25.7 median progression-free survival [117]. As a result pembrolizumab has been approved by the FDA as a single agent therapeutic for advanced endometrial cancers with MMRd. Due to the frequent occurrence of *PTEN* and phosphatidylinositol-4,5-bisphosphate 3-kinase catalytic subunit alpha (*PIK3CA*) mutations, therapeutic benefit from everolimus, an inhibitor of downstream mechanistic target of rapamycin kinase (MTOR), has been hypothesised and is currently being investigated [118]. Similarly, the frequent mutation of AT-rich interaction domain 1A (*ARID1A*) and its role in homologous recombination have driven examination of poly(ADP-ribose) polymerase 1 (PARP1) inhibitors [119].

Due to the high incidence and relatively favourable survival, uterine cancer is currently the second most prevalent cancer in women in the US, with around 891,560 women alive after a diagnosis [120]. In the UK that number was 70,200 people in 2010, ranking as the third most prevalent cancer in females [121]. Many of those that survive will face numerous adverse effects such as infertility (in pre-menopausal patients), lymphoedema, neurotoxicity, urinary and bowel issues [105, 106]. This highlights the need for continuing efforts to better understand how molecular alterations affect prognosis and which molecular alterations could be successfully targeted therapeutically. Together these aspects would allow for more personalised treatment regimes to avoid overtreatment of patients, thereby maximising both survival and quality of life.

1.2.5 Modelling Endometrial Cancer in Mice

Over the last decades there has been significant improvement in the understanding of the molecular biology of uterus and EC facilitated, in part, by the use of *in vivo* models. The earliest models of EC in mice and rats were derived using strains that spontaneously developed EC with a high frequency, which highlighted *Kras* mutation as a driver of EC. Alternatively, EC could be induced chemically using reagents such as N-ethyl-N-nitrosourea or 1,2-dimethylhydrazine, which were found to potently induce EC in transformation related protein 53 (*Trp53*) deficient mice [122–124].

The methods utilised by the above studies were useful for highlighting genes with

importance to EC development but do not allow investigation of the contribution of a specific gene to carcinogenesis. Therefore, methods to selectively introduce mutations or gene deletions in to the murine uterus were developed, predominantly utilising the Cre recombinase (Cre)-Lox recombination system [125]. The first example of this was using Cre expressed from the progesterone receptor (*Pgr*) gene locus (Pgr^{Cre}), which was used to initiate deletion of *Pten* from the entire uterus (epithelial, stromal and myometrial cells) as well as other reproductive tissues (breast, ovary, and cervix) [126]. Deletion of *Pten* from all cells of the uterus led to rapid onset of EC [126].

However, simultaneous gene mutation in both the epithelium and stroma is not a common feature of EC, therefore, methods for more specific targetting to a single cell compartment were developed. *Cre* expression from the anti-Mullerian hormone type 2 receptor (*Amhr2*) gene locus ($Amhr2^{Cre}$) was used for selectively deleting *Pten* from the endometrial stromal and myometrial cells and from the lactoferrin (Ltf) gene locus (Ltf^{Cre}) for *Pten* deletion from the endometrial epithelium [127, 128]. Interestingly, these studies highlighted the significance of retaining *Pten* expression in one of the two cell compartments as neither model developed EC, with only hyperplasia observed following epithelial deletion [127, 128].

Further insights specifically in to the development and maintenance of the uterus have been provided by recent lineage tracing experiments that have sought to identify the cell populations responsible for the growth and regeneration of the different uterine compartments [129–131]. It was originally hypothesised that the endometrial epithelium could be repopulated through the process of mesenchymal to epithelial transition, these studies have shown that during normal homeostasis this process does not occur [130, 132]. The work of Seishima *et al.* highlighted a population of indispensable Lgr5-positive cells responsible for development of uterine glands postnatally, with gland formation significantly reduced following selective ablation of these cells [131]. In adult mice, Syed *et al.* identified a population of Axin2-positive cells located at the basal tips of the endometrial glands that are responsible for regeneration of the ciliated and non-ciliated lineages of the glandular and luminal epithelium [130]. When cultured *in vitro* these cells readily formed functional endometrial organoids and their ablation

in vivo significantly reduced the regenerative potential of the endometrial epithelium [130]. Additionally, these cells were found to be responsible for clonal expansion and formation of hyperplastic or cancerous lesions following repeated stimulation with tamoxifen or specific introduction of cancer-associated mutations in *Pik3ca* and *Ctnnb1* [130]. A previously hypothesised characteristic of the then unidentified endometrial epithelial stem cell was high WNT activity, which was noted by a study examining differences in the gene expression profiles of pre- and post-menopausal women [133]. Interestingly both stems cells populations identified by these studies share the similarity of high WNT activity, highlighting the importance of this pathway for maintenance of endometrial homeostasis and regeneration [130, 131].

Despite these advances in modelling and targetting of genetic alterations to specific endometrial compartments, there still remain fundamental differences in the basic biology of the mouse and human endometrium. Primarily in the fact that mice lack a menstrual phase of the reproductive cycle. To aid the study of menstruation, it was discovered that the process could be induced by hormonal manipulation in ovariectomised mice [134, 135]. Furthermore, the recent discovery and characterisation of the spiny mouse, a mouse exhibiting natural human-like menstruation has been highlighted as a potential model, although the unique physiology and challenging husbandry has proved an issue for widespread uptake [136, 137]. As repopulation of the endometrium following menstruation is akin to a form of wounding repair, a similar process can be replicated in mice through de-nuding of the epithelial layer of the uterus [130]. The subsequent re-epithelialisation would simulate the process of epithelial regrowth following menstruation [130].

The exact implication of the lack of menstruation on the development of EC is not fully apparent. However, it is apparent that this difference has implications for other uterine pathologies, such as endometriosis, which is not spontaneously observed in mice and requires models of induced menstruation to occur [137]. Additionally, several studies have noted significant inflammatory and immune response differences in settings of oestrus and menstruation [134–136, 138]. Due to the importance of immune cell interaction with nascent cancer cells it could be hypothesised that a differential of

this nature could impact carcinogenesis but a thorough investigation of this has yet to be performed.

1.3 PTEN and the PI3K pathway

The PI3K-pathway is a key signal transduction mechanism that connects growth factor activation with changes to cellular function. The namesake of the pathway, PI3K, describes a family of proteins with kinase activity. The family can be subdivided in to three major classes (I, II, and III) that can phosphorylate phosphatidylinositol (PtdIns) to different extents [139]. All classes can generate PtdIns-3-P, class I and II can produce PtdIns-3,4-P and only class I can generate PtdIns-3,4,5-P [139]. Class I proteins have been the most widely studied group and have the strongest links with cancer. The class Ia subfamily comprises heterodimeric complexes formed of a catalytic subunit: p110α (*PIK3CA*), p110β (phosphatidylinositol-4,5-bisphosphate 3-kinase catalytic subunit beta (*PIK3CB*)), or p110δ (*PIK3CD*) with a regulatory subunit: p85α (phosphatidylinositide-3-kinase regulatory subunit 1 (*PIK3R1*)) or p85β (*PIK3R2*), whereas class Ib is formed of p110γ (*PIK3CG*) and p101 (*PIK3R5*) [140].

Activation of PI3K occurs during its recruitment to the plasma membrane through prior activation and phosphorylation of receptor tyrosine kinases, cytokine receptors or G protein-coupled receptors (Figure 1.3) [140]. Once active, it phosphorylates PtdIns-4,5-P forming PtdIns-3,4,5-P [140]. Accumulation of PtdIns-3,4,5-P in the plasma membrane act as docking sites for various proteins such as AKT serine/threonine kinase (AKT) and its regulator PDK1 (encoded by 3-phosphatidylinositide dependent protein kinase 1 (*PDPK1*)). Subsequent phosphorylation at Thr308 activates AKT kinase activity; additional phosphorylation by MTOR complex 2 (mTORC2) can occur at Ser473 to further enhance AKT activity [140, 141].

Activity of the pathway is opposed by the negative regulator, PTEN, a lipid and protein phosphatase that hydrolyses the phosphate from the 3' hydroxyl position of PtdIns-3,4,5-P to generate PtdIns-4,5-P, thereby inhibiting the accumulation of AKT and its activators at the plasma membrane [142]. Additionally, active AKT is dephosphorylated by

protein phosphatase type 2A (PP2A), which preferentially removes the required Thr308 phosphate group to inactivate AKT [143]. Dephosphorylation of the Ser473 site is performed by PH domain and leucine rich repeat protein phosphatase (PHLPP). This event exerts weaker control of AKT activity as phosphorylation of Ser473 greatly enhances AKT activity, but is not required for activation [144].

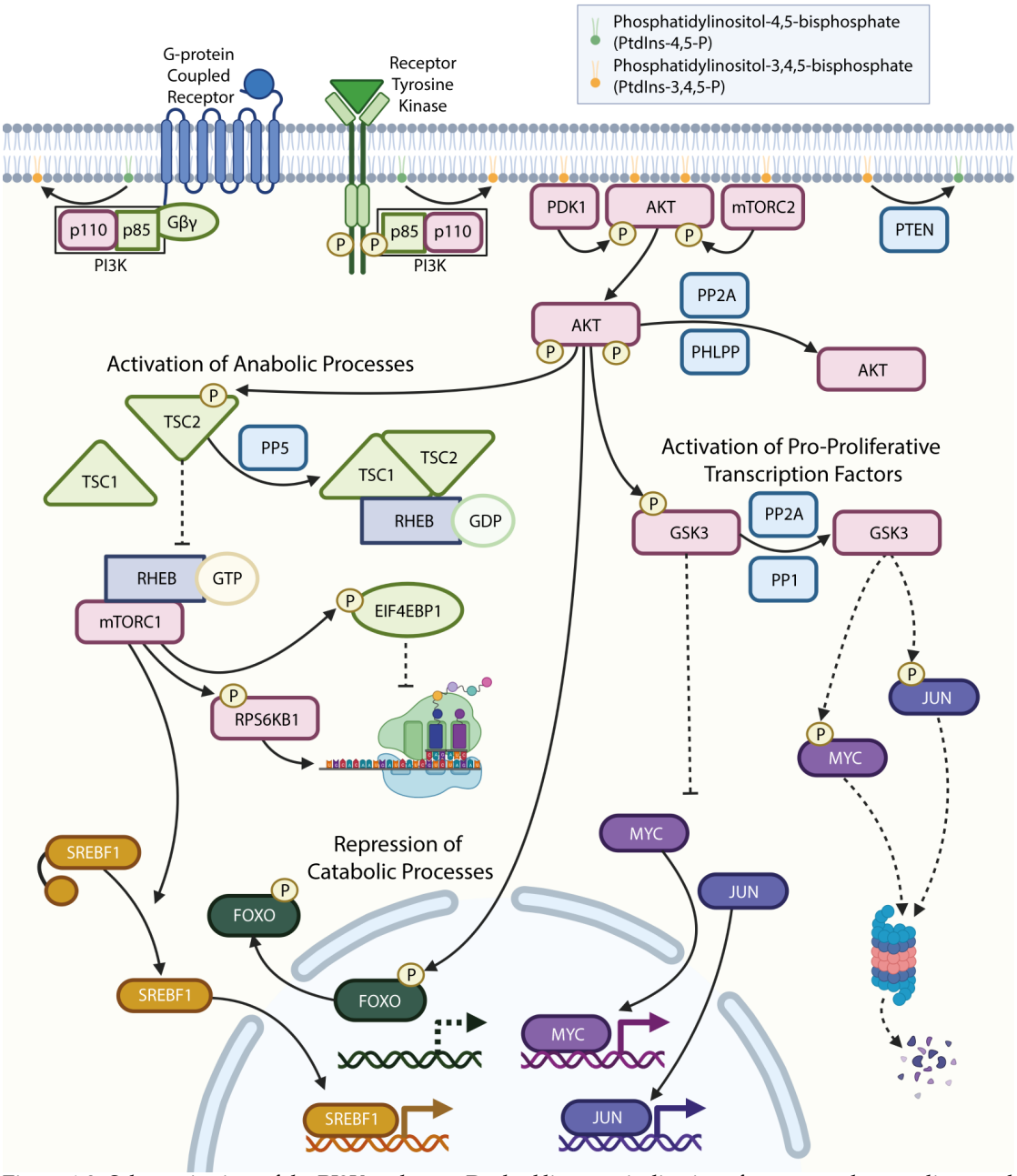

Figure 1.3: Schematic view of the PI3K pathway. Dashed lines are indicative of processes that are disrupted by pathway activation. Figure was created using assets from BioRender.

1.3.1 Function in physiological homeostasis

Under normal physiological conditions the PI3K-AKT pathway functions to amalgamate information from the cellular environment and to relay it to downstream effectors that can modulate cellular functionality accordingly. There are three well characterised downstream effectors following activation of AKT: glycogen synthase kinase 3 (GSK3), forkhead box O (FOXO), and MTOR. Inhibition of the two GSK3 isoforms (-α and -β) occurs directly by AKT catalysed phosphorylation at positions Ser21 and Ser9, respectively [145]. In its active state GSK3 phosphorylates numerous targets, including glycogen synthase (GS), Jun proto-oncogene, AP-1 transcription factor subunit (JUN), MYC proto-oncogene, bHLH transcription factor (MYC), hypoxia inducible factor 1 subunit alpha (HIF1A), eukaryotic initiation factor 2B (EIF2B), and CTNNB1, generally leading to their inactivation or degradation [145, 146]. Therefore, reduced GSK3 activity promotes activity of proteins and transcription factors that drive growth and survival.

FOXO transcription factors (FOXO1, 3, 4, and 6) are generally active under low nutrient conditions and function to drive expression of gluconeogenesis enzymes (glucose 6-phophatases (G6PC), phosphoenolpyruvate carboxykinase (PCK)), autophagy related genes (autophagy related 5 (ATG5) and autophagy related 12 (Atg12)), negative regulators of the cell cycle (cyclin dependent kinase inhibitor 1A (CDKN1A), cyclin dependent kinase inhibitor 1B (CDKN1B)) and pro-apoptotic factors (FAS ligand (FASLG), BCL2 like 11 (BCL2L11), BCL2 modifying factor (BMF)) [147, 148]. When AKT is activated, phosphorylation of FOXO proteins occurs at three conserved sites, allowing binding of 14-3-3 family proteins [145]. These proteins shuttle FOXO out of the nucleus occluding its deoxyribose nucleic acid (DNA) binding potential and transcriptional activity, thereby alleviating the catabolic processes it promotes [145].

Activation of MTOR complex 1 (MTORC1) plays a vital role in initiation of an anabolic, growth promoting cell state. AKT indirectly promotes activation of MTOR by removing the negative regulation of its activator Ras homolog, mTORC1 binding (RHEB). Activation of RHEB requires association with guanosine triphosphate (GTP). However, under normal conditions this is hydrolysed to guanosine diphosphate (GDP) by a com-

plex containing TSC complex subunit 1 (TSC1), TSC complex subunit 2 (TSC2) and TBC1 domain family member 7 (TBC1D7), in which TSC2 is a GTPase-activating protein [149]. When the PI3K-AKT pathway is active, AKT phosphorylates TSC2, suppressing its ability to form the TSC1/TSC2 complex and allowing accumulation of RHEB-GTP, subsequently activating mTORC1 [149]. Once active mTORC1 promotes protein synthesis (by phosphorylation of ribosomal protein S6 kinase B1 (RPS6KB1) and eukaryotic translation initiation factor 4E binding protein 1 (EIF4EBP1)), nucleic acid synthesis (through promotion of RNA-polymerase activity) and lipid synthesis (through sterol regulatory element binding transcription factor 1 (SREBF1)) [149]. Simultaneously, catabolic processes such as autophagy and lysosome synthesis are inhibited by phosphorylation of factors such as unc-51 like autophagy activating kinase 1 (ULK1) and transcription factor EB (TFEB) [149].

AKT itself has been shown to phosphorylate numerous targets directly involved with glucose metabolism such as TBC1 domain family member 4 (TBC1D4). This relieves the negative regulation of glucose transporter (GLUT) trafficking to the plasma membrane, thereby increasing glucose uptake in muscle cells [140]. Hexokinase 2 (HK2) is also activated by AKT, leading to phosphorylation of glucose to glucose-6-phosphate, a form that cannot be transported out of the cell [140].

1.3.2 Dysregulation in cancer

The PI3K pathway forms a central avenue for neoplastic development and is one of the most frequently dysregulated pathways in cancer [150]. Links to cancer were evident in early work linking the activation of the pathway with various known oncogenes. However, the transformative potential of the PI3K pathway itself was initially demonstrated by observations that avian sarcoma virus 16 encoded an oncogene homologous to the catalytic subunit of PI3K and that the virus and exogenously expressed PIK3CA showed transformative potential in chicken cells [151].

Subsequent studies of human cancer have identified multiple members of the pathway, including *PIK3CA* (14% of patients), *PTEN* (7%), and *PIK3R1* (3%), as some of the most commonly mutated genes across all cancers, ranking 2nd, 3rd, and 15th, respec-

tively [150, 152]. Aside from mutations of specific members of the pathway, frequent mutation of upstream factors including growth factor receptors such epidermal growth factor recptor (*EGFR*) and *ERBB2* also result in activation of the pathway [145]. Mutations in the PI3K-pathway are common in endometrial cancer, specifically, and as previously mentioned, mutation of *PTEN* typifies endometrioid carcinomas. A more thorough discussion of PI3K-pathway mutations and their importance to endometrial cancer can be found in Section 4.1.1.

1.3.3 Therapeutic targeting

Due to their pervasive pathway activation in cancer, PI3K and AKT have been targeted for therapeutic inhibition, albeit without significant success to date. The major limiting factors are toxicity, due to the vital nature of the pathway in non-cancerous tissues, and resistance, due to compensatory upregulation of activating receptors or alternative activation of downstream effectors [153]. Pan-PI3K inhibitors, targeting all catalytic p110 subunits of class I kinases, and dual PI3K-MTOR inhibitors have demonstrated significant anti-proliferative effects on cancer cells however due to the broad nature of their activity, toxicity has abrogated their use at concentrations that would be therapeutically beneficial [141]. Issues of toxicity may be bypassed through use of isoform specific PI3K inhibitors. In particular, tumours harbouring *PIK3CA* mutations are often sensitive to inhibition of p110α alone and these agents frequently exhibit improved safety profiles over pan-PI3K inhibitors [154]. However, in tumours with *PTEN* mutations the choice of isoform to target is less clear and studies so far have shown mutational context and tissue specific differences in ideal targets, complicating the choice of agent to use [141]. Additionally, tumour cells have been found to be resistant to single isoform agents, but retain sensitivity to pan-PI3K agents, suggesting resistance due to isoform compensation could be an issue for these inhibitors [155].

Three types of AKT inhibitors have been examined, ATP-competitive, catalytic, and allosteric. ATP-competitive inhibitors, designed to block the ATP binding pocket have shown good effectiveness, but have been limited by toxicity due their ability to bind to all members of the AGC kinase family (of which AKT is a member) [145]. Catalytic

inhibitors, which bind to active AKT and stop downstream phosphorylation, and allosteric inhibitors, which bind to the inactive form of AKT and prevent its activation, also show anti-cancer activity, with allosteric inhibitors seemingly more effective in promoting cell death [145]. However, in clinical trials both classes of inhibitors have shown limited efficacy, potentially due to heterogeneity of response caused by lack of patients stratification [145].

1.4 *TP53* and the p53 pathway

The protein p53, encoded by the *TP53* gene, has been referred to as the "guardian of the genome" due to its vital role in response to DNA damage and protection of the cell from acquisition, and effects, of oncogenic mutations [156]. Whilst recognised now as one of the most important tumour suppressor genes, when originally identified as an endogenous protein interacting with the SV40 large T-antigen, it was believed to be an oncogene due to the subsequent discovery of its high expression in a variety of cancer cells and cells infected with tumour viruses [157–161]. This belief was compounded by the isolation of *TP53* coding sequences from cancer cells, which could induce cancerous transformation when expressed in normal cells [162–164]. Finally, 10 years after its discovery, the isolation of a *TP53* coding sequence, which did not induce transformation, highlighted the mutant nature of previously isolated coding sequences and subsequent studies solidified p53 as a tumour suppressor [165].

The p53 protein has several important domains including two N-terminal transactivation domains, a proline-rich region, a central, highly conserved DNA-binding core domain, an oligomerisation domain and finally at the C-terminus an unstructured basic domain [166, 167]. The transactivation domains allow interaction with numerous cofactors and are vital for transcriptional activation of target genes [168]. The proline-rich region has importance for the stability of p53, with its deletion linked with nuclear export and increased ubiquitination [169]. Furthermore, loss of this region inhibits p53 from inducing apoptosis, but does not affect its ability to arrest the cell cycle [170, 171]. The central DNA-binding core domain allows binding to a p53 recognition element in the

promoter or enhancer regions of its transcriptional targets in order to modulate their expression [169]. The oligomerisation domain towards the C-terminus allows p53 to tetramerise as a dimer of dimers and is vital for effective DNA binding [172, 173]. The unstructured basic domain at the C-terminus has a negative regulatory role, inhibiting DNA binding ability. Post-translational modifications (PTMs), such as acetylation, phosphorylation, methylation and ubiquitination of this site are required to relieve this inhibition [169].

1.4.1 Function in physiological homeostasis

Under normal cellular conditions expression of p53 is maintained at low levels through persistent degradation mediated by MDM2 proto-oncogene (MDM2), an E3 ubiquitin ligase, which also binds tightly to the transactivation domains to sterically hinder co-factor binding to further inactivate p53 (Figure 1.4) [161]. This degradation is alleviated in response to cellular stresses such as, but not limited to, DNA damage, replicative stress (often induced by oncogenes or activation of oncogenic pathways), and nutrient stress (ribonucleotide depletion and hypoxia) [167]. Negative regulation of MDM2 is performed by $p14^{ARF}$, encoded by the cyclin dependent kinase inhibitor 2A (*CDKN2A*) gene locus as an alternative reading frame to $p16^{INK4A}$ [174]. Expression of $p14^{ARF}$ occurs as a result of cell stress and through the transcriptional activity of many common oncogenes (such as MYC). When active it is capable of binding to MDM2, blocking its ability to interact with and degrade p53 [175, 176].

An alternative method for p53 activation, seen in response to DNA damage, heavily relies on PTMs. DNA damage induced kinases ATM serine/threonine kinase (ATM), ATR serine/threonine kinase (ATR), their downstream effectors checkpoint kinase 1 (CHEK1) and CHEK2, and other kinases phosphorylate numerous residues in the N-terminal transactivation domain (Ser6, 9, 15, 20, 33, 37, 46 and Thr18 and 81) and the C-terminal basic domain impairing the ability of MDM2 to bind to p53 [177]. Additionally, ATM is also responsible for directly phosphorylating MDM2; the loss of interaction with p53 and subsequent phosphorylation allow for ubiquitin-mediated degradation of MDM2 removing the constraints on p53 [177, 178]. After PTM and accumulation of p53,

it is able to tetramerise and bind to p53 responsive elements to initiate transcriptional changes and downstream functional effects. There are many downstream effects of p53 activation, but the most well studied are its control over cell cycle arrest and apoptosis.

The ultimate decision between which of these two pathways is actioned is not fully understood [179]. It has been suggested that pro-apoptotic targets have a weaker p53 responsive element and therefore require more accumulation of p53 to be transcriptionally activated [179, 180]. This gives rise to a model whereby increasing p53 levels initiate cell cycle arrest and if sufficient DNA repair or correction of the stress is not achieved then continued accumulation will trigger apoptosis. Lending credence to this hypothesis is the observation that cell cycle arrest genes are upregulated much earlier than those associated with apoptosis [181]. However, several studies have found that pro-apoptotic genes do exhibit high affinity p53 responsive elements [182]. Oscillation in the intensity of p53 signalling may instead be a defining characteristic of response with short interval pulses being linked to cell cycle arrest and sustained signalling with apoptosis [181].

Furthermore, PTMs predominantly in the C- and N-terminal domains have a functional role in defining the nature of the p53 response. Ser46 phosphorylation is more heavily linked to induction of apoptosis [183]. Acetylation of K320 in response to DNA damage favours cell cycle arrest over apoptosis, whereas acetylation of K120 pushes the balance towards apoptosis [178]. Not all PTMs are activating, dephosphorylation of inhibiting Ser376 is triggered during DNA damage to activate p53 [184].

Another likely modifier is the presence of p53 cofactors that can influence the exact nature of the transcription program initiated by p53, factors such as p63 and p73 may be required for binding to apoptotic promoters [185]. There may also be cell-type or -context specific effects based on factors such as chromatin organisation and promoter accessibility which influences the balance of gene transcription [167]. It is unlikely that any singular factor is solely responsible for the decision on cell fate and instead a decision by committee is more likely to determine which pathway is ultimately chosen.

Cell cycle arrest is predominantly mediated through transcriptional upregulation of *CDKN1A*, encoding $p21^{WAF1}$, which is capable of inhibiting cyclin dependent kinase

complexes resulting in G1/S or G2/M phase arrest [169]. Other cell cycle arrest factors include 14-3-3δ, encoded by tyrosine 3-monooxygenase/tryptophan 5-monooxygenase activation protein zeta (*YWHAZ*), and growth arrest and DNA damage inducible alpha (GADD45A), both of which initiate G2/M growth arrest [186, 187]. In response to DNA damage p53 can also promote transcription of genes that function in DNA repair, including damage specific DNA binding protein 2 (*DDB2*), DNA polymerase eta (*POLH*), replication protein A (*RPA*), and BLM RecQ like helicase (*BLM*) [167, 169]. If repair of DNA damage is not sufficient or the cellular stress is too severe then p53 is capable of priming the cell for induction of apoptosis by the extrinsic pathway through upregulation of apoptotic receptors Fas cell surface death receptor (FAS) and TNF receptor superfamily member 10b (TNFRSF10B), also known as death receptor 5 [169]. It also induces expression of numerous intrinsic pro-apoptotic factors including BCL2 binding component 3 (*BBC3*) also known as *PUMA*, BCL2 associated X, apoptosis regulator (*BAX*) and phorbol-12-myristate-13-acetate-induced protein 1 (*PMAIP1*) also known as *NOXA* [167, 169]

1.4.2 Dysregulation in cancer

Coinciding with its vital role in protecting the integrity of the genome, mutation or loss of *TP53* is a common feature of cancer and represents the most frequently mutated gene across all cancer types, found in 36% of cancers [150]. The majority of *TP53* mutations are missense mutations (∼73%) as opposed to the frequent frameshift or nonsense mutations seen in other tumour suppressors [188, 189]. The DNA-binding domain residues are the most commonly affected region accounting for up to 85-95% of all *TP53* mutations [169, 188]. These mutations generally affect residues directly required for DNA-binding (Arg248, Arg273), or residues that induce a local (Arg249, Gly245) or global (Arg175, Arg282) conformation change [189]. Missense mutations are commonly observed alongside a secondary loss of heterozygosity (LOH) event impacting the integrity of the remaining wild-type *TP53* copy [189]. In colorectal cancer up to 86% of *TP53*-mutant tumours exhibit deletion of the second copy and LOH is observed in 74% and 80% of all *TP53* mutant breast cancers and sarcomas, respectively [190, 191]. Addi-

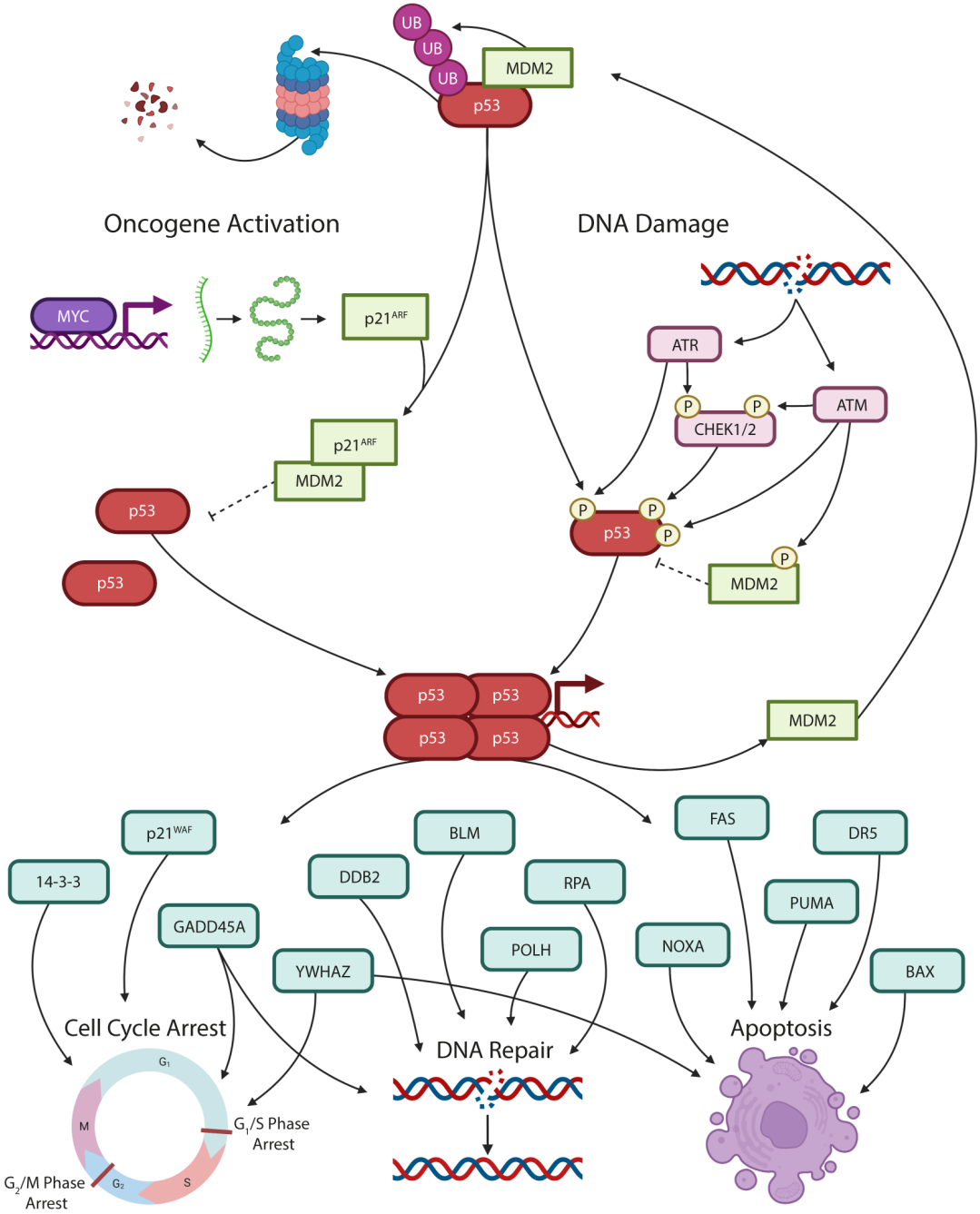

Figure 1.4: Schematic view of the p53 pathway and the downstream functions. Figure was created using assets from BioRender.

tionally, mutations of *TP53* occur frequently in EC, discussed in more depth in Section 5.1.1 [90].

The consequences of *TP53* mutation have proved difficult to fully determine, although 92% of cancers exhibiting increased copy number alterations also exhibit *TP53*

mutation [192]. It appears that different missense mutations and the surrounding cellular context may result in unique cancer phenotypes [167]. However, it is likely that many of these mutations, in particular those in the DNA-binding domain, will exhibit some extent of loss of function, impeding the ability of p53 to bind to DNA [193]. In this context, mutant p53 appears to function in a dominant negative manner due to the requirement for tetramerisation for functionality. Incorporation of mutant p53 has been shown to inactivate complexes containing wild-type p53, causing reduced expression of genes associated with cell cycle arrest [194]. Although, it has also been demonstrated that up to three mutant monomers may be required to inactivate a tetramer [195].

Further to the loss of tumour suppressive function it has been hypothesised that some mutations alter the nature of p53 causing defection from tumour suppressor to oncogene, often termed gain-of-function mutations. These gain-of-function effects were initially proposed based on the increased tumorigenic effect of missense mutation versus *TP53*-loss in model systems and the heterogeneity of tumour onset in patients with Li-Fraumeni syndrome, a cancer syndrome caused by germline *TP53* mutation [167, 196, 197]. The most common phenotypes that have been linked with gain-of-function effects include increased invasion and metastasis, chemoresistance through reduced apoptosis, angiogenesis and changes to chromatin regulation [196, 198–200].

1.4.3 Therapeutic targeting

The vital role that p53 plays in opposing tumorigenic pathways coupled with the potent anti-cancer effect exhibited by restoration of wild-type p53 in model systems has made the p53 pathway a desirable therapeutic target [201–205]. In non-*TP53* mutant cancer, activation of p53 can be achieved by pharmaceutical disruption of the negative regulator MDM2, leading to development of Nutlins, which block the p53 binding pocket [206]. Clinical trials with new generation Nutlin analogues have shown mixed results, with several phase I studies investigating RG7112 highlighting significant toxicity resulting in neutropenia and thrombocytopenia [167, 207, 208]. This method of targeting p53 would not be suitable for patients with mutant p53. However, it has been suggested that combination of Nutlins with cytotoxic treatments may have a beneficial effect by

inducing state of cell cycle arrest in cells containing wild-type p53, which could improve tolerance of the cytotoxic therapeutic and allowing use of higher doses [167].

Targeting mutant p53 is a more daunting prospect, nonetheless, it has been demonstrated that small molecules can induce conformational changes in mutant p53 and revert function to that of wild-type p53 [167, 169]. These types of agents are likely to be more effective against mutations that induce a conformational change in p53 as opposed to those that alter direct DNA-binding residues, as such, compounds reverting Ser249, Trp220, and Arg175 have been reported [209–211]. A recent phase Ib/II clinical trial of APR-246 in combination with azacitidine in myelodysplastic syndromes has shown promising results with the inhibitor being well tolerated and inducing a high rate of response with complete remission in 44% of patients [212]. An alternative method to target mutant p53 is through promoting its degradation. Mutant p53 is believed to be stabilised by interaction with Hsp90 (encoded by heat shock protein 90 alpha family class A member 1 (*HSP90AA1*)), whose expression is promoted by histone deacetylase 6 (HDAC6). Thus inhibitors of both Hsp90 and HDAC6 can result in increased degradation of mutant p53 [169].

1.5 FBXW7 and the ubiquitin proteasome system

Tight regulation and rapid turnover of proteins is vital to the ability of a cell to maintain homeostasis and respond to changes in environment, as demonstrated in the p53 pathway. In the eukaryotic cell, the ubiquitin proteasome system (UPS) is predominantly responsible for identification, targeting, and turnover of proteins. The process of target identification and flagging for proteolysis is referred to as ubiquitination and is a cascading pathway involving three types of enzymes: E1 (ubiquitin-activating), E2 (ubiquitin-conjugating) and E3 (ubiquitin-ligases). This cascade culminates in the addition of the small protein, ubiquitin, to the side chain of a lysine residue in the target (Figure 1.5A). Following addition of the first ubiquitin monomer, further chained ubiquitination events are required to trigger proteasomal degradation. Ubiquitin itself contains several lysines to which additional ubiquitin monomers can be added (K6, K11, K27,

K29, K33, K48, and K63), to form varied linear or branched chains; linear, K48-poly-ubiquitin ($\geq$4 ubiquitin residues) most efficiently promotes proteasomal degradation [213]. Tagging of a protein in this manner forms a motif that can be recognised by the 26S proteasome, a multi-catalytic protease complex, thereby triggering its degradation.

Inhibition of the proteasome has shown that anywhere between 75-95% of protein degradation occurs via the UPS [214, 215]. Protein degradation on this scale without homeostatic disruption indicates a high level of specificity, which occurs through the limited repertoire of target interactions that are possible for each E3 ligase coupled with the sheer number of E3 ligases encoded in the human genome (estimated to be between 600-700). These E3 ligases fall in to three major families (Figure 1.5) [216]:

- RING E3s - These ligases stimulate the direct transfer of ubiquitin from the E2 enzyme to the target protein. This is the largest family with $\sim$600 members, which are characterised by a RING or U-box domain that interacts with the E2 enzyme. They also feature the most in-family variation as these ligases can function as monomers, homodimers, heterodimers, or larger multi-subunit complexes, such as Cullin-RING-ligases and the anaphase promoting complex.

- HECT E3s - A family with $\sim$30 members, which contain a C-terminal HECT domain consisting of two lobes connected by a flexible hinge. The more N-terminal lobe binds the E2 enzyme and the C-terminal lobe contains a catalytic cysteine residue that initially accepts ubiquitin from the E2 enzyme before transferring it to the target protein which interacts with the domain(s) that are N-terminal of HECT domain.

- RBR E3s - Otherwise known as RING-betweenRING-RING E3 ligases have the fewest members, $\sim$12. They contain a RING domain that interacts with the E2 enzyme, equivalent to that of RING E3s. However, they contain another RING-like domain (Rcat domain) that contains a catalytic cysteine residue that accepts ubiquitin before transferring to the target protein.

Skp, Cullin, F-box (SCF) ubiquitin ligase complexes are a subtype of Cullin-RING ligases. They are multi-subunit ligase complexes formed of a RING box containing pro-

tein, a cullin scaffold protein, an adapter protein to conjugate the cullin subunit to the final component, the F-box substrate binding protein. There are multiple members of each subunit family but a classical example, and the focus of this work, SCF^{FBXW7} contains RING-box 1 (RBX1), cullin 1 (CUL1), S-phase kinase-associated protein 1 (SKP1), and FBXW7 (Figure 1.5B).

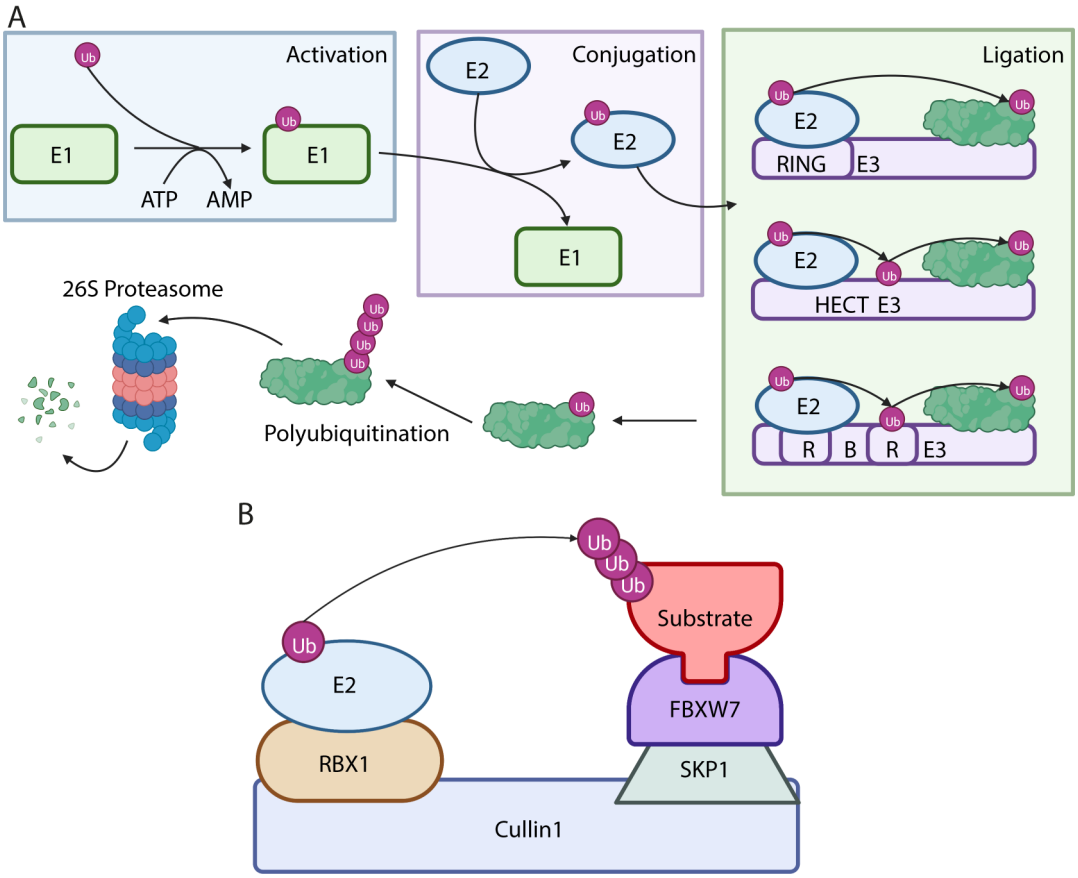

Figure 1.5: **A.** Schematic representation of the ubiquitin proteasome system and the broad differences in E3 ligase families. **B.** Schematic representation of the SCF^{FBXW7} complex binding to and ubiquitinating a target substrate. Figure panels were created using BioRender assets and were adapted from [216].

1.5.1 FBXW7 discovery and characterisation

1.5.1.1 Discovery

Cdc4p was initially discovered by Hartwell *et al.* through a genetic screen of regulators of the cell cycle in *Saccharomyces cerevisiae*, where it was observed to function as a regulator of initiation of DNA replication [217, 218]. Its role in ubiquitination and protein

degradation was first indicated by Schwob *et al.* who reported that it was likely involved in the inactivation of Sic1p, an S-phase CDK inhibitor [219]. This was followed by several studies that simultaneously identified phosphorylation of Sic1p as a vital step required for its degradation and that Cdc4p functioned as the F-box protein of a SCF ubiquitin ligase complex containing Skp1p, Cdc53p and Cdc4p [220–223].

Alongside the work performed in yeast, the gene *sel-10* was characterised in *Caenorhabditis elegans* [224]. Shortly after, SEL-10 was found to be a member of the Cdc4 family of F-box proteins that negatively regulated LIN-12 and murine Notch4 [225]. The human orthlogue, *FBXW7*, was identified simultaneously by groups working on Cdc4p, SEL-10 and Ago (orthologue in *Drosophila melanogaster*), predominantly due to its homology with SEL-10 and Ago [226–230]. In addition, through these studies it was shown that FBXW7 was capable of ubiquitinating notch receptor 1 (NOTCH1) and cyclin E1 (CCNE1) and that prior phosphorylation of the targets was vital for interaction [226–230].

1.5.1.2 Gene and protein structure

FBXW7 is found on the reverse strand of chromosome 4q31.3. The genomic locus spans ~215,000 base pairs (bp) and consists of 13 coding exons, which produce three mRNA isoforms (termed -α, -β, and -γ) generated by alternative splicing [231]. All isoforms share the same 10 exons that form the C-terminal portion of the protein, but each contains a unique exon encoding the N-terminus of the protein [231]. Expression of the three isoforms varies depending on the tissue, *FBXW7*-α is ubiquitously expressed, whereas -β and -γ are predominantly expressed in brain and testis, and heart and skeletal muscle, respectively [232]. However, subsequent work has identified expression of *FBXW7*-β and -γ in a colon cancer and an osteosarcoma cell line, foreskin fibroblasts and umbilical cord blood cells, albeit at significantly lower levels than *FBXW7*-α [233].

Each of the isoforms is associated with their own promoter, allowing for differential regulation of their expression. However, all three isoforms share some mutual regulation and are all downregulated upon entry to the cell cycle, with downregulation of FBXW7-γ being most pronounced [234]. The three isoforms are differentially regulated

in response to cellular stress *FBXW7*-β is upregulated in a p53-dependent manner in response to genotoxic stress, but no change in -α was observed [232, 234–236]. Other factors controlling the expression of FBXW7 have focussed mainly on those that lead to decreased *FBXW7* expression, which include CCAAT/enhancer-binding protein δ (CEBPD), hes family bHLH transcription factor 5 (HES5), and numerous miRNAs (miR-27a, -32, -92a, -92b-3p, -223) [237–243].

The protein structure of FBXW7 contains several domains that are shared by all isoforms and are vital for its function. The primary motifs, for which the protein is named, are the 8 WD40 repeats located at the C-terminal end of the protein and the neighbouring F-box domain, which interacts with SKP1 allowing formation of the SCF^{FBXW7} E3 complex [231]. A third protein interaction domain is the dimerisation domain, N-terminal of the F-box, that allows homo-dimerisation of FBXW7 monomers [231]. Only the N-terminal end of the protein differs between the isoforms and although no recognised domains are present in this region, it functions to direct the subcellular localisation of each isoform [231]. FBXW7-α is the largest isoform at 707amino acids (AA) and is expressed in the nucleus, the -β isoform at 627AA is retained in the cytoplasm and the -γ isoform, 589AA is located at the nucleolus (Figure 1.6B) [244].

The WD40 motifs have a β-sheet secondary structure and the 8 repeated motifs together form a toroidal-barrel, β-propeller domain that is the substrate recognition site (Figure 1.6A). The interaction with its targets occur in a phosphorylation dependent manner through recognition of a conserved Cdc4 phosphodegron (CPD) sequence. The CPD sequence was initially identified as "I/L I/L/P pT P", although interaction with pS at the "0" position is possible, pT is favoured [245]. This was later updated to incorporate the importance of a having a negatively charged residue at the "+4" position, either through a secondary phosphorylated S/T or a negatively charged E residue, giving the current consensus CPD: "I/L I/L/P (pT/pS) P X X (pS/pT/E)", where X is any amino acid [231, 246]. However, based on published targets of FBXW7 there is clearly more variation than is captured by this sequence alone (Figure 1.6C). X-ray crystallography studies of FBXW7's substrate binding domain in complex with several of its targets have identified that the "0" position of the CPD resides close to the centre of the

toroidal, β-propeller structure and interacts with the amino acids at the tips of several WD40 propeller "blades" (Figure 1.6D) [247–249].

The importance of dimerisation to the functionality of FBXW7 has yet to be fully elucidated, but coupled with the variation seen in published CPDs has given rise to a hypothesis of variable strengths of CPDs. Welcker and Clurman's study identifying the dimerisation domain also highlighted that ubiquitination of substrates with strong CPDs, closely matching the consensus with phosphorylation at position "0" and "+4", is not dependent on dimerisation, such as CCNE1 and MYC [250]. Furthermore, Welcker *et al.*'s follow-up study mutating the "+4" position serine (S) of the CCNE1-CPD1 to an glutamic acid (E), forming a weaker CPD, abrogated interaction with FBXW7 monomers, but coupled with a second weak CPD allowed interaction with FBXW7 dimers (Figure 1.6C) [251]. However, FBXW7 monomers may be capable of interacting with suboptimal CPDs as evidenced by Csizmok *et al.*'s study showing the interaction of dimerisation deficient FBXW7 with JUN-CPD2, although, whether this interaction would be sufficient to allow ubiquitination was not elucidated (Figure 1.6C) [252]. It is clear that dimerisation has an important role in the functionality of FBXW7, adding an extra layer of regulation to the process of substrate recognition.

In addition to the role in substrate recognition dimerisation also functions in regulation of FBXW7 stability, as it promotes trans-autoubiquitination and loss of the dimerisation domain has been shown to stabilise protein monomers [251]. Furthermore, modulation of FBXW7 stability by other factors has been observed in several studies. Peptidylprolyl cis/trans isomerase, NIMA-interacting 1 (PIN1) is a protein capable of isomerising the peptide bond between a phosphorylated serine/threonine and proline. Its overexpression has been linked to destabilisation of FBXW7 through disruption of dimerisation and promotion of autoubiquitination [253]. However, dimerisation is, reportedly, important for autoubiquitination and other reports did not observe changes to FBXW7 expression with PIN1 overexpression [251, 254]. PIN1 may play a larger role in regulation of FBXW7 function, as its recognised binding site matches the consensus CPD (pS/pT-P). This allows PIN1 to bind to the CPDs of FBXW7 targets, where it is can isomerise the peptide bond hindering the ability of FBXW7 to bind and ubiquitinate its

targets [252].

1.5.2 Targets of FBXW7

Many of the targets of FBXW7 are recognised oncogenes that play pivotal roles in cell proliferation, survival, homeostasis and differentiation. Summarised below are some the most studied and highly recognised targets of FBXW7.

1.5.2.1 Cell cycle and apoptosis

Much of the work that led to the identification of *FBXW7* was based on its role in regulation of the cell cycle and more specifically CCNE1, although close relative cyclin E2 (CCNE2) has also been identified as a target of FBXW7 [255]. Cyclin E acts as a positive progression factor in the cell cycle, promoting the transition from G1 to S-phase. Promotion of this transition occurs through complex formation with cyclin dependent kinase 2 (CDK2) thus activating the kinase activity and triggering phosphorylation of numerous targets including CDKN1A, CDKN1B, and ultimately RB transcriptional corepressor 1 (RB1) [256]. Overexpression of cyclin E has been identified in numerous types of cancer, gene amplification was observed in $\sim$8% of patients in a recent pan-cancer study [257]. The method by which overexpression drives carcinogenesis is not increased proliferation as might be expected instead increased expression of CCNE1 has been linked with genomic instability [257, 258].

Another FBXW7 target that plays a vital role in cell proliferation and homeostasis is MTOR, which forms a vital component of the mTORC1 and mTORC2 complexes [259, 260]. mTORC1 receives information from growth factor receptors and regarding nutrient and energy supplies and is deterministic of cell growth through promotion of protein, lipid, and nucleotide synthesis and inhibition of catabolic processes, such as autophagy and the proteasome [261, 262]. In contrast, mTORC2 is more directly responsible for cell proliferation through phosphorylation of kinases in the PKA/PKC/PKG family and AKT [261]. Activation of the MTOR pathway is a common feature of human cancers through upstream activation of growth factor signalling pathways, amplification, or mutation.

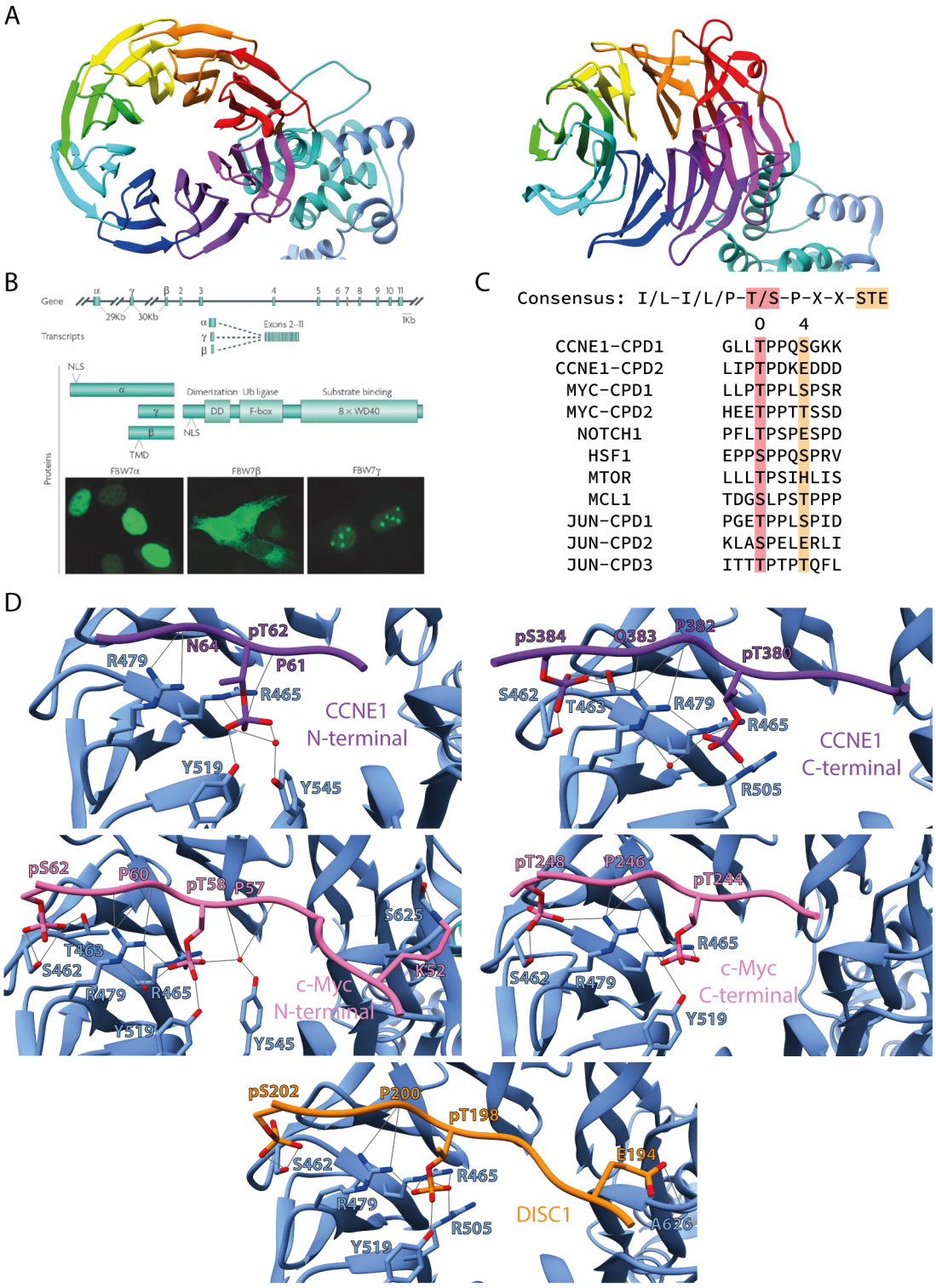

Figure 1.6: Structural and functional characteristics of FBXW7. **A.** Ribbon diagram representations of the crystal structure of FBXW7. **B.** Schematic of FBXW7 protein domains and isoform localisation. Reproduced from [231]. **C.** Representation of the CPD sequences published for select FBXW7 targets. The "0" position is highlighted in red and the "+4" position in orange. **D.** Ribbon diagram representations of the WD40 domain of FBXW7 in complex with the CPD sequences of CCNE1, MYC, and DISC1. Predicted hydrogen bonding is indicated by the grey lines between atoms. Crystal structures were published in [247–249].

MCL1 apoptosis regulator, BCL2 family member (MCL1) is an anti-apoptotic regulator of mitochondrial outer membrane permeabilisation and cyctochrome c release [263]. FBXW7 has been reported to target MCL1 for degradation and loss of this capability has been linked to overexpression of MCL1 [264]. Furthermore, this overexpression can influence cell fate by preventing induction of apoptosis.

1.5.2.2 Transcription factors

One of the major functional classes of FBXW7 targets are the transcription factors and co-factors from various pathways. One of the earliest identified as a substrate of FBXW7 was NOTCH1 [230], a transmembrane receptor of the Notch signalling pathway. Upon ligand binding, proteolytic cleavage of the internal domain of the receptor occurs (forming notch intracellular domain (NICD)) which translocates to the nucleus and interacts with a DNA binding complex, modulating expression of a variety of genes [265]. Notch signalling is an important component of developmental patterning and cell fate determination [265]. As the primary Notch pathway ligands are also expressed on the cell surface, this signalling pathway forms an important method of localised cell communication to determine neighbouring cell fate decisions [265]. The role of Notch signalling in cancer is quite varied with different patterns of alterations observed. The first observation of Notch in cancer was through chromosomal translocations in T lymphoblastic leukaemia (T-ALL), resulting in truncated protein expression capable of undergoing ligand-independent proteolysis [266, 267]. Secondly, are mutations affecting the PEST domain, responsible for negative regulation of protein function, therefore leading to increased protein activity, which has been observed in up to 56% of T-ALL samples [268].

Another well characterised oncogenic transcription factor regulated by FBXW7 is MYC [269, 270]. MYC is a basic-helix-loop-helix-leucine zipper transcription factor that functions as an obligate heterodimer with its binding partner MYC associated factor X (MAX) [271]. It is considered a master regulator of gene expression, controlling an estimated 15% of all genes, including cell cycle regulators and other metabolic pathways [272]. Due to its central role in cellular homeostasis, dysregulation of MYC has been shown to have links to cancer and estimates suggest that up to 70% of all cancers exhibit

dysregulation or overexpression of MYC [273].

FBXW7 is a negative regulator of the Jun N-terminal kinase (JNK) signalling pathway through ubiquitination and degradation of JUN [274, 275]. JUN is a subunit of the activator protein-1 (AP-1) transcription factor complex, which responds to growth factor signalling and stress stimuli to modulate cell pathways including cell proliferation, survival, and tissue morphogenesis [276]. Overexpression or amplification of JUN has been found in several cancer types, particularly highly aggressive sarcomas [277–279].

In addition to previous links with cellular homeostasis, FBXW7 has been linked to the cellular stress response through its regulation of heat shock transcription factor 1 (HSF1) [280]. During times of cellular stress, particularly those that induce denaturing conditions, unfolding of HSF1 allows homo-trimerisation and nuclear translocation. Once in the nucleus, this complex function as a transcriptional regulator inducing genes related to protein folding, such as chaperones and pro-survival factors [281]. In particular overexpression HSF1 has been linked with a metastatic phenotype in cancer [280–282].

1.5.2.3 DNA damage and repair

FBXW7 has been previously linked with genomic instability due to its regulation of CCNE1 [283]. However, recent studies have suggested its role in DNA damage and repair may multifaceted and more direct than previously appreciated. The role of TP53 in upregulation of *FBXW7* expression has been discussed previously, but recent publications have highlighted the role of FBXW7 in ubiquitination and turnover of TP53 in response to its phosphorylation by ATM, forming a negative feedback loop to attenuate the TP53 response [284–286]. In a more direct role, FBXW7 has been shown to be recruited to sites of double strand breaks through its recognition of poly(ADP-ribose) and once recruited is responsible for non-degradative poly-ubiquitination of X-ray repair cross complementing 4 (XRCC4) to facilitate non-homologous end joining [287, 288].

1.5.3 Dysregulation in cancer

Given the pool of substrates and their known links to cancer, it is perhaps unsurprising that *FBXW7* also exhibits dysregulation in cancer. However, whether loss of regulatory control of the above targets is a relevant feature of cancer with altered *FBXW7* activity has yet to be established in many cases. The first indication of a role for FBXW7 in cancer came from Koepp *et al.*'s study originally identifying the human orthlogue of Cdc4. They posited that FBXW7 may function as a tumour suppressor due to its role in regulation of CCNE1 and observations that RNA expression was decreased in breast cancer cell lines [226]. This was followed by Moberg *et al.* and Strohmaier *et al.*, who noted the frequency of *CCNE1* amplification in cancer and examined human cancer cell lines for mutations of *FBXW7*, which they found in T-ALL, ovarian and breast cancer cell lines [227, 228].

Since then *FBXW7* has been solidified as a *bona fide* tumour suppressor and studies characterising the genetic landscape of human cancers have repeatedly highlighted the frequency of alterations in *FBXW7* [257, 289, 290]. Mutation rates in pan-cancer cohorts have been reported between 3-6% and is among a small group of genes found to be significantly mutated in multiple cancer types [150, 257, 289, 290]. However, the mutation rate varies greatly between cancer types with the highest rates seen in endometrial carcinosarcoma (39%), T-ALL (24%), endometrial carcinoma (18%; discussed in further detail in Section 3.1.2), colorectal adenocarcinoma (11%), cervical squamous cell carcinoma (11%), stomach adenocarcinoma (10%), bladder urothelial carcinoma (10%), and lung squamous cell carcinoma (6%) [90, 91, 291–296].

1.5.3.1 Propeller tip mutations

Interestingly, *FBXW7* does not commonly exhibit the two-hit mutation profile of typical tumour suppressors, which tend to exhibit multiple protein inactivating mutations (gene deletion and truncating mutations), instead, it exhibits frequent mono-allelic missense alterations [297]. Missense mutations make up 66-74% of *FBXW7* mutations in cancer [257, 289, 290]. These mutations are found throughout the length of the gene,

however there is an increased frequency of mutations in the WD40 repeats that define the substrate binding domain. Of the mutations in the TCGA pan-cancer cohort 83% of all missense mutations occur within the WD40 repeats [298]. In particular, three arginine hotspots (R465, R479 and R505) account for 44% of all *FBXW7* missense mutations [298]. These arginine residues sit at the centre of the binding pocket that is formed from the WD40 repeats and have a potentially vital role in hydrogen bonding with the CPD of its substrates (Figure 1.6D). Therefore, mutation of these residues is highly likely to impact efficiency or capability of substrate binding.

The increased frequency of missense mutations as opposed to truncating mutations or other inactivating mutations has led to suggestions that these missense mutations may not solely imbue a loss of function and that instead they may function in a dominant negative fashion. This has been observed experimentally with accumulation of CCNE1 occurring after titration of mutant FBXW7 in to cells expressing wild-type FBXW7 [289]. However, a solely dominant negative mechanism does not account for the mutation profile observed, as if complete inactivation of wild-type FBXW7 was favoured it may be expected that higher rates of truncating mutations and LOH would be observed. An alternative hypothesis suggests that there may be a selective advantage in retaining some level of protein functionality, a "just right" level of disruption that provides a selective advantage and drives malignancy where total or even mono-allelic loss would not [299]. This may include the specific abrogation of a particular substrate or group of substrates that favour neoplastic transformation, without disrupting other factors that may trigger an oncogenic stress response.

1.5.3.2 Loss of expression

Deletion of *FBXW7*, particularly through loss of the 4q chromosome arm, has been reported with modest frequency in several cancer types: colorectal (23%), oesophageal (30-40%), and gastric cancer (∼30%) [300–303]. In most cases loss of one allele was reported and those that performed sequencing analysis of the remaining *FBXW7* gene found a lack of missense mutation. Furthermore, copy number loss was associated with increased MYC expression. The frequent retention of one functional copy of *FBXW7* in

cancer further suggests that it may function as a haploinsufficient tumour suppressor. Analysis of copy number changes in model systems has shown increased tumour incidence after homozygous and heterozygous deletion confirming *FBXW7* does function as a haploinsufficient tumour suppressor [236].

In addition to gene deletion, loss of protein function can be induced by mutations that lead to truncation or early termination of the protein sequence, such as nonsense and frameshift mutations. These types of mutations can lead to differential extent of protein inactivation, but if occurring early in the gene sequence could cause total loss of the substrate binding domain. Examination of the spectrum of truncating mutations in pan-cancer TCGA data indicates that they account for 30% of all *FBXW7* mutations [298]. The impact of truncating mutations has not been thoroughly investigated, and many studies have utilised deletion of the WD40 domain as a surrogate of protein truncation. However, the most frequently recurrent truncating mutations, Arg658 and Ser668, account for 17.5% of all truncating mutations and occur within the final WD40 repeat of the binding domain. Whether these mutations represent a substrate binding-null version or have more similarity to WD40 point mutations of *FBXW7* warrants further study.

A potentially underappreciated mechanism for dysregulation of *FBXW7* is through reduced expression, independent of gene mutation. Iwatsuki *et al.* reported that low expression of *FBXW7* was associated with more invasive tumours [300]. Furthermore, several additional studies that have found correlation between low expression of *FBXW7* and poor prognosis in colorectal, pancreatic, gastric, breast and lung cancer [300, 304–307]. Reduced expression has also been linked with drug resistance in cancer cells suggested to be through a HSF1- and MCL1-dependent mechanism [306, 307]. The mechanistic means by which *FBXW7* expression is suppressed vary, although as previously mentioned increased expression of a variety of miRNAs have been linked with decreased *FBXW7* expression. Promoter hypermethylation has been shown to reduce expression, in particular *FBXW7*-β appears to most significantly affected by promoter methylation [308]. Finally, several factors have been implicated in regulation of FBXW7 stability and overexpression or activation of these factors have been linked with reduced

FBXW7 expression at the protein level.

1.6 Motivation for this study

There is clear evidence that *FBXW7* is a mutational cancer driver and has been identified as frequently mutated in numerous cancer types. EC, and in particular carcinosarcoma, has some of the highest rates of *FBXW7* mutation and yet very little is known about its function and contribution towards endometrial carcinogenesis. Several studies to date have examined the role of *FBXW7* deletion from endometrial cells, covered in more detail in Section 3.1. However, this is not an analogous model of the types of alterations that are commonly seen in human cancers and are particularly present in EC. The aim of this study, therefore, is to examine the effect and potential contribution of heterozygous *FBXW7* missense mutation towards endometrial carcinogenesis. To investigate this process, characterisation of genetically engineered mouse models (GEMMs) was performed, utilising tissue specific expression of Cre to restrict introduction of a knock-in hotspot R479Q mutation in to the *Fbxw7* gene of mouse uterine cells. Due to the frequency of *PTEN* and *TP53* mutations in EC, *Fbxw7* mutation was examined alone and in combination with mutation of both of these key genes.

Chapter 2

Materials and methods

2.1 Mice

All procedures were performed in compliance with the Animals (Scientific Procedures) Act (ASPA), 1986, under the Project Licences: PB802BC1E and PDF0B94C3 and my Personal Licence: I8E73D7F0.

2.1.1 Mutations and background strains

The following alleles were used for the work described in this thesis:

- *Pgr*^{cre} (Pgr$^{tm2(cre)Lyd}$ [309]; MGI ID: 3576366) in which the coding sequence (CDS) for Cre recombinase has been inserted in to exon 1 of the *Pgr*. This allows tissue specific recombination of floxed alleles only in the female reproductive tissues.

- *Fbxw7*$^{fl(R482Q)}$ (Fbxw7^{tm1Itom} [310]; MGI ID: 5007620) consists of a loxp flanked copy of the final three exons of the wild-type *Fbxw7* CDS with an intact stop codon. This precedes a second copy of the final three exons in which a G to A substitution has been induced by site-directed mutagenesis (SDM). After recombination the wild-type exons are removed and expression of the mutation results in the substitution of the arginine residue at position 482 with a glutamine residue.

- *Pten*^{fl} (Pten^{tm2Mak} [311]; MGI ID: 2182005) consists of loxp sites flanking exons 4 and 5 of *Pten*. These two exons encode the majority of the dual specificity phos-

phatase catalytic domain. When recombined, the two exons are deleted, removing the phosphatase activity, ultimately causing a loss of Pten protein expression.

- *Trp53*^{fl} (Trp53^{tm1Brn} [312]; MGI ID: 1931011) consists of loxp sites flanking exons 2 to 10 of *Trp53*. When recombined the exons are deleted thus causing a loss of Trp53 expression.

- *Trp53*$^{LSL\text{-}R172H}$ (Trp53^{tm2Tyj} [196]; MGI ID: 3039263) consists of insertion of a loxp flanked stop cassette in to intron 1 of *Trp53* and site directed mutation of exon 5 to induce the R172H mutation. Before recombination this allele would constitute of a truncation of Trp53 (essentially a knock-out) but after recombination the premature stop is removed and full length Trp53 with the mutation is expressed.

All alleles were bred on to a C57BL/6J background for at least 5 generations before commencement of experimental breeding.

2.1.2 Animal husbandry

All animals were housed in the Functional Genetics Facility in the Wellcome Centre for Human Genetics (WCHG), University of Oxford. Mice were housed in individually ventilated cages (with no more than six mice per cage) with continuous access to a normal diet and water. A standard 12-hour light/dark cycle was maintained within the facility. Day to day care of the animals: food and water changes, health monitoring, cage cleaning, and weaning was performed by the animal technicians within the facility. Additional health monitoring, initiation of breeding, and ear clipping were performed by myself.

2.1.3 Murine breeding

Breeding was performed by mixing of a male and female or a male and two females, all over the age of 6 weeks (sexual maturity) and of the desired genotypes.

2.1.4 Ear clipping

Ear clipping of the mice was performed for the purpose of identification and genotyping. Tissue samples were collected from animals post-weaning (around 3 weeks of age) through use of an ear punch (AgnTho's AB). Ear clips were transferred to an Eppendorf tube and DNA extracted as described in Section 2.2.1. Mouse identification was possible through the combination of number and location of ear punches.

2.1.5 Genotyping and confirmation of allelic recombination

For all genotyping polymerase chain reactions (PCRs), DNA from mouse ear clips extracted as described in Section 2.2.1, was used. For confirming recombination, DNA from fresh frozen uterus extracted as described in Section 2.2.2, was used. Two general PCR master mixes requiring either BIOTAQ DNA polymerase (Meridian Bioscience) or the Qiagen Multiplex PCR kit (Qiagen) were used, as shown in Tables 2.1 and 2.2 respectively. Size separation of PCR products for genotype determination was performed as described in Section 2.3.1.

Table 2.1: Generic PCR master mix using BIOTAQ DNA polymerase and two primers.

Reagent	**Volume (uL)**	**Final Concentration**
Water	18.5	-
10x NH_4 Reaction Buffer	2.5	1x
$MgCl_2$ (50 mM)	0.75	1.5 mM
dNTPs (2.5 mM)	1	100 µM
Forward Primer (10 µM)	0.5	200 nM
Reverse Primer (10 µM)	0.5	200 nM
BIOTAQ DNA Polymerase	0.25	-

*For reactions requiring three primers, 0.5 µL of the additional primer (10 µM) was added and the amount of water used was reduced to 18 µL.

2.1.5.1 Pgr^{Cre} PCR conditions

Genotyping for Pgr^{Cre} allele was performed by adding 1 µL of DNA to 14 µL of the master mix described in Table 2.2, with the stated modifications as three primers are re-

Table 2.2: Generic PCR master mix using the Qiagen Multiplex PCR kit and two primers.

Reagent	Volume (uL)	Final Concentration
Water	2.9	-
Forward Primer (10 µM)	0.3	200 nM
Reverse Primer (10 µM)	0.3	200 nM
2x QIAGEN Multiplex PCR Master Mix	7.5	1x
5x Q-Solution	3	1x

*For reactions requiring three primers, 0.3 µL of the additional primer (10 µM) was added and the amount of water used was reduced to 2.6 µL.

quired. The reactions were thermocycled using the conditions described in Table 2.3.

Primer Sequences:

- PRCre 1 - TATACCGATCTCCCTGGACG
- PRCre 2 - ATGTTTAGCTGGCCCAAATG
- PRCre WT - CCCAAAGAGACACCAGGAAG

Table 2.3: Thermocycling conditions for Pgr^{Cre} and $Trp53^{fl}$ genotyping.

Cycles	Temperature (°C)	Time
1	95	15 minutes
40	95	60 seconds
	58	90 seconds
	72	60 seconds
1	72	10 minutes

The Pgr^{Cre} allele produces a band at 590 bp and the wild-type allele produces a band at 285 bp.

2.1.5.2 *Fbxw7*$^{fl(R482Q)}$ PCR conditions

Genotyping PCR. Genotyping of the $Fbxw7^{fl(R482Q)}$ allele was performed by adding 1 µL of DNA to 24 µL of the master mix described in Table 2.1 before thermocycling

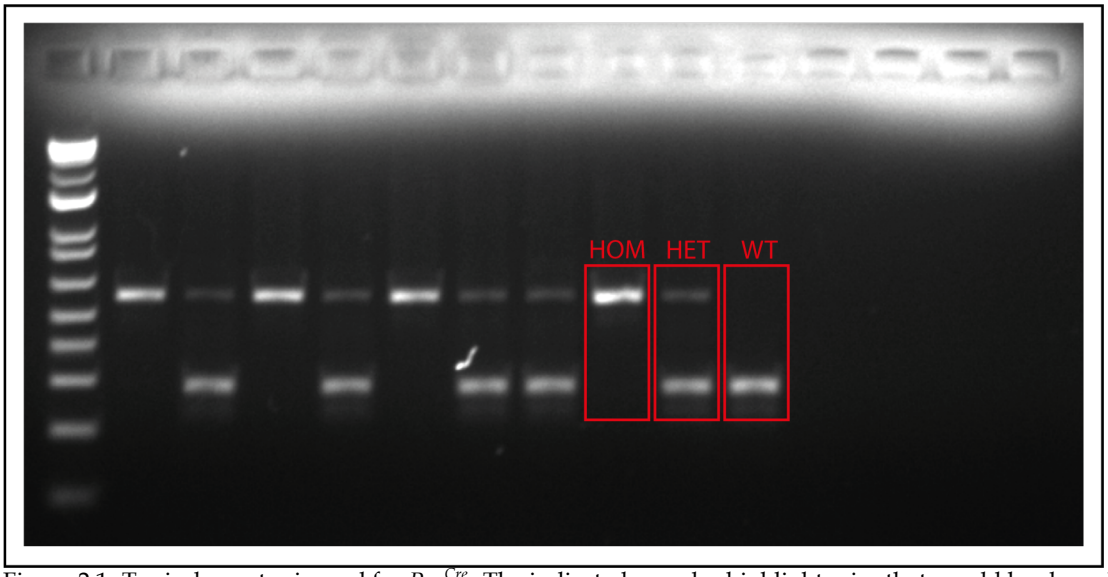

Figure 2.1: Typical genotyping gel for Pgr^{Cre}. The indicated samples highlight mice that would be classed as homozygous (HOM), heterozygous (HET) or wild-type (WT) for the allele.

using the conditions described in Table 2.4.

Primer Sequences:

- Cdc4-1: TTCCTCACTTCCCATTCCAG
- Cdc4-3: TCTCTGGATCCCACACCTTC

Table 2.4: Thermocycling conditions for $Fbxw7^{fl(R482Q)}$ genotyping and for confirmation of recombination of the $Fbxw7^{fl(R482Q)}$, $Pten^{fl}$, and $Trp53^{fl}$ alleles.

Cycles	Temperature (°C)	Time
1	95	5 minutes
35	95	60 seconds
	55	60 seconds
	72	60 seconds
1	72	5 minutes

The $Fbxw7^{fl(R482Q)}$ allele generates a band at 477 bp and the wild-type allele at 322 bp.

Recombination PCR. For confirming recombination, 1 µL (20 ng) of DNA was added to 24 µL of the master mix described in Table 2.1 before thermocycling using the conditions described in Table 2.4.

Primer Sequences:

- Cdc4-1: TTCCTCACTTCCCATTCCAG
- Cdc4-6: GATTGGCCAGTACTGAACCT

Successful recombination is indicated by the presence of a band at 294 bp.

2.1.5.3 *Pten*^{fl} PCR conditions

Genotyping PCR. Genotyping of *Pten*^{fl} was performed by adding 1 µL of DNA to 24 µL of the master mix in Table 2.1, before thermocycling using the conditions described in Table 2.5.

Primer Sequences:

- Pten-fl-1: CTCCTCTACTCCATTCTTCCC
- Pten-fl-2: ACTCCCACCAATGAACAAAC

Table 2.5: Thermocycling conditions for *Pten*^{fl} genotyping.

Cycles	Temperature (°C)	Time
1	95	2.5 minutes
35	95	60 seconds
	58	60 seconds
	72	60 seconds
1	72	10 minutes

The *Pten*^{fl} allele produces a band at 335 bp and the wild-type allele at 228 bp.

Recombination PCR. Recombination was confirmed by addition of 1 µL (20 ng) of DNA to 24 µL of master mix from Table 2.1, followed by thermocycling using the conditions described in Table 2.4.

Primer Sequences:

- Pten-Δ4-5-Fw: GTCACCAGGATGCTTCTGAC

- Pten-Δ4-5-Rv: ACTATTGAACAGAATCAACCC

Successful recombination is indicated by a band at 859 bp.

2.1.5.4 *Trp53^{fl}* PCR conditions

Genotyping PCRs. Genotyping of *Trp53^{fl}* was performed by adding 1 µL of DNA to 14 µL of the master mix described in Table 2.2, followed by thermocycling using the conditions described in Table 2.3.

Primer Sequences:

- p53-int1-Fwd: CACAAAAACAGGTTAAACCCA
- p53-int1-Rev: AGCACATAGGAGGCAGAGAC

The *Trp53^{fl}* allele produces a band at 584 bp and the wild-type allele a band at 431 bp.

Recombination PCR. Recombination was confirmed by addition of 1 µL (20 ng) of DNA to 24 µL of the master mix from Table 2.1, before thermocycling using the conditions described in Table 2.4.

Primer Sequences:

- 10RM23': ACAGAAAAGGGGAGGGATGAAGTGA
- 1FM5': GTGCCCTCCGTCCTTTTTCGCAATC

Successful recombination is indicated by a band at 467 bp.

2.1.5.5 *Trp53^{R172H}* PCR conditions

For genotyping of the *Trp53^{R172H}* allele, 1 µL of DNA was added to 24 µL of the master mix specified in Table 2.1, followed by thermocycling using the conditions described in Table 2.6.

Primer Sequences:

- Trp53 R172H WT ALT: AGGTGTGGCTTCTGGCTTC
- Trp53 R172H Mut Alt: CCATGGCTTGAGTAAGTCTGCA

- Trp53 R172H Univ Alt: GAAACTTTTCACAAGAACCAGATCA

Table 2.6: Thermocycling conditions for *Trp53*^{R172H} genotyping.

Cycles	Temperature (°C)	Time
1	94	2 minutes
10 (Touchdown)	95	15 seconds
	64 to 59	15 seconds
	72	45 seconds
30	95	15 seconds
	59	15 seconds
	72	45 seconds
1	72	5 minutes

The *Trp53*^{R172H} allele generates a band at 170 bp and the wild-type allele at 370 bp.

2.1.5.6 Sanger sequencing for mutation expression

To confirm transcription of the *Fbxw7*^{R482Q} and *Trp53*^{R172H} mutations, Sanger sequencing of RNA was performed. RNA was extracted by the method described in Section 2.2.3 and was reverse transcribed to complementary DNA (cDNA) as described in Section 2.4.1. To amplify the region of interest prior to performing the sequencing reaction, 20 ng of cDNA was added to the master mix in Table 2.7 and was thermocycled using the conditions in Table 2.8. The primers used for amplification were as follows:

- R482Q-cDNAseq-F: TTGTGGCAACCGCATAGTTA
- R482Q-cDNAseq-R: ACCCTCCTGCCATCATACTG

This primer pair target exons 7 to 9 of the *Fbxw7* CDS to generate an amplicon of 375bp.

- R172H-cDNAseq-F: GTTATGTGCACGTACTCTCC
- R172H-cDNAseq-R: GTTCCCACTGGAGTCTTC

These primers target exons 4 to 6 of *Trp53* and generate an amplicon of 426bp.

Table 2.7: Components of the master mix used for amplification of *Fbxw7* and *Trp53* CDS.

Reagent	Volume (uL)	Final Concentration
Water	14.75	-
5x Q5 Reaction Buffer	5	1x
10 mM dNTPs	0.5	200 nM
10 µM Primer 1	1.25	500 nM
10 µM Primer 2	1.25	500 nM
Q5 Polymerase	0.25	-

Table 2.8: Thermocycling conditions for amplification of *Fbxw7* and *Trp53* CDS.

Cycles	Temperature (°C)	Time
1	98	30 seconds
35	98	10 seconds
	65/63*	20 seconds
	72	20 seconds
1	72	2 minutes

*65 °C and 63 °C are the annealing temperatures used for $Fbxw7^{R482Q}$ and $Trp53^{R172H}$ respectively.

The amplicons were cleaned using the DNA Clean & Concentrator kit (#D4013, Zymo Research) as per the manufacturer's protocol (with all centrifugation steps performed at 10 000 × g). In brief, DNA binding buffer was added to the PCR sample at a 5:1 ratio (125 µL of buffer for a 25 µL reaction) and vortexed to mix. The mixture was added to a Zymo-Spin column and centrifuged for 30 seconds. 200 µL of DNA Wash Buffer was then added to the column before centrifuging for 30 seconds. This wash step was performed twice. The amplicon was eluted by addition of 11 µL of ultrapure water and incubation for 5 minutes at room temperature before centrifuging for 30 seconds.

The Sanger sequencing reaction was performed using the BigDye Terminator (BDT) v3.1 Sequencing Kit (#4337455, Applied Biosystems) with a modified protocol. To prepare the reaction, 15 ng of the purified amplicon was added to the master mix outlined in Table 2.9. For each sample, two reactions were made, one using the forward primer and one using the reverse primer from the primer pairs used for the prior amplification. After mixing, the reactions were thermocycled using the conditions in Table 2.10.

Table 2.9: Sanger sequencing master mix using the BDT kit.

Reagent	Volume (uL)	Final Concentration
Water	11	-
Primer (3.2 µM)	2	320 nM
BDT Sequencing Buffer	3	-
BDT Ready Reaction Mix	2	-

Only one primer (either forward or reverse) is added to the master mix, a separate master mix is prepared if sequencing in both directions is required.

Table 2.10: Thermocycling conditions for dye terminator reaction using the BDT kit.

Cycles	Temperature (°C)	Time
1	96	2 minutes
35	96	10 seconds
	52	15 seconds
	60	3 minutes
1	72	1 minute

An annealing temperature of 52 °C was used regardless of the primer's annealing temperature.

Following the sequencing reactions, the samples were purified to remove any unincorporated dye terminators using the DyeEx 2.0 Spin Kit (#63204, Qiagen), following the manufacturer's protocol. In brief, DyeEx spin columns were vortexed and inverted several times to resuspend the resin. The lid of the spin column was loosened but not removed and the sealing tag on the bottom of the column was removed before placing the column in the provided collection tube. The tubes were centrifuged at 750 × g for 3 minutes. The lids were fully removed, and the columns transferred to a 1.5 mL tube. The full 20 µL sequencing reaction was then added to the resin bed and the columns were centrifuged again at 750 × g for 3 minutes and the eluent was retained.

After BDT clean-up, the samples were dehydrated by heating at 70 °C for 30 minutes. The dehydrated samples were sent to Source BioScience for capillary electrophoresis and DNA sequencing. The sequencing traces returned by Source BioScience were aligned to the mRNA sequence of the relevant gene using SnapGene software (Insightful Science).

2.1.6 Animal sacrifice and tissue collection

Sacrifice of the mice was performed at predefined time points or due to the onset of ill-health. Daily visual health monitoring for grimacing, hunching, lack of activity, loss of grooming or other signs of poor health. Additional, semi-weekly abdominal palpation for uterine enlargement allowed timely detection of phenotype development requiring sacrifice. Mice were culled by cervical dislocation and immediately dissected for collection of tissues.

Once collected, tissues were processed by one of several methods depending on the intended downstream application. (i) Fresh freezing of tissue was performed by partitioning of the organ in to several similar sized pieces and transfer to a labelled 2 mL cryovial. The cryovial was then submerged in a dewar containing liquid nitrogen before transfer for storage at −80 °C. (ii) For Optimal Cutting Temperature (OCT) compound embedding, the tissue was cut in to smaller pieces. These pieces were then added to a cyromold filled with OCT (#361603E, Avantor) and oriented using forceps to get the most biologically relevant face towards the bottom. After which the cyromold was placed on dry ice and allowed to freeze before transferring to −80 °C for storage. (iii) Fixation in formalin for later paraffin embedding. Tissues were immersed in a 10% neutral buffered formalin solution (#HT501128, Sigma-Aldrich) for 24 hours. Uterine horns were rolled in a piece of tissue paper prior to immersion in order to prevent folding or curling. The tissue was then transferred to 70% ethanol for storage until processing as described in Section 2.5.1.

2.2 Nucleic acid extractions

2.2.1 DNA extraction from mouse ear clips

DNA from mouse ear clips was extracted using the Hot Sodium Hydroxide and Tris (HotSHOT) method [313]. In brief, 50 µL of alkaline lysis reagent (25 mM NaOH with 0.2 mM EDTA) was added to the samples and heated at 95 °C for 30 minutes. The samples were briefly centrifuged to collect the liquid and 50 µL of the neutralising reagent

(40 mM Tris-HCl) was added before vortexing.

2.2.2 DNA extraction from fresh frozen tissue

For extraction of DNA alone from fresh frozen tissue, the DNeasy Blood and Tissue Kit (#69504, Qiagen) was used according to the manufacturer's guidance. In brief, a frozen tissue piece (up to a maximum of 25 mg) was added to 180 µL of Buffer ATL and was homogenised using a micropestle for 30-60 seconds. 20 µL of proteinase K was then added, and the samples were briefly vortexed before incubation overnight at 56 °C until all tissue was completely digested.

The following day, the samples were briefly vortexed before 200 µL of Buffer AL was added, followed by 200 µL of 100% ethanol, with thorough vortexing between each addition. The mixture was then added to a DNeasy Mini spin column and centrifuged for 1 minute at 6000 × g. The flow-through was discarded and 500 µL of Buffer AW1 was added followed by centrifugation for 1 minute at 6000 × g. The spin columns were transferred to a new 2 mL collection tube and 500 µL of Buffer AW2 was added followed by centrifugation at 20 000 × g for 3 minutes. The spin columns were then transferred to a 1.5 mL collection tube and 200 µL of Buffer AE was added. The buffer was incubated on the column for 5 minutes at room temperature before elution by centrifuging at 6000 × g for 1 minute. To ensure high concentration, the eluent was added back on to the column for a second elution in the same manner as the first. DNA samples were stored at 4 °C for short term and −20 °C for long term.

2.2.3 RNA extraction from fresh frozen tissue

RNA Extraction from fresh frozen tissue was performed using the RNeasy Mini Kit (#74104, Qiagen) according to the manufacturer's protocol with all centrifugation steps performed for 30 seconds at 8000 × g unless otherwise stated. In brief, a frozen piece of tissue (between 20-30 mg) was added to a 1.5 mL tube containing 600 µL of Buffer RLT (with 0.01% (v/v) β-mercaptoethanol (#M6250, Sigma)) and was disrupted using a micropestle for 30-60 seconds. The full volume of the sample was then added to a QIAshredder column (#79656, Qiagen) and was centrifuged for 2 minutes at 20 000 × g

to homogenise the sample. The lysate was centrifuged for 3 minutes at 20 000 × g and the supernatant was carefully removed and retained. One volume (600 µL) of 70% ethanol was added to the lysate and mixed by pipetting.

700 µL of the sample was transferred to an RNeasy mini spin column before centrifuging. The flow through was discarded and 700 µL of Buffer RW1 was added to the column which was again centrifuged. The flow through was discarded and 500 µL of Buffer RPE was added, and gently washed around the inside of the column by holding horizontally and turning slowly. The column was then centrifuged and flow through discarded before addition of another 500 µL of buffer RPE and centrifugation for 2 minutes at 8000 × g. After this the column was transferred to a new 2 mL collection tube and the samples were centrifuged for 1 minute at 20 000 × g to fully dry the membrane.

To elute the RNA, 50 µL of RNAse free water was added to the membrane of the column and incubated at room temperature for 5 minutes before centrifugation for 1 minute at 8000 × g. The elution step was then repeated by re-addition of the eluent to the column, incubation and centrifugation.

2.2.4 DNA and RNA extraction from fresh frozen tissue

For scarce tissue samples, I utilised the AllPrep DNA/RNA mini kit (#80204, Qiagen) to obtain DNA and RNA from a single piece of tissue. All centrifugation steps were performed at 8000 × g for 30 seconds unless otherwise stated. In brief, a frozen piece of tissue weighing between 20-30 mg was added to a 1.5 mL tube containing 600 µL of Buffer RLT Plus (with 0.01% (v/v) β-mercaptoethanol) and was immediately disupted by micropestle for 30-60 seconds. The samples were homogenised by transfer to a QIAshredder column and centrifugation at 20 000 × g for 2 minutes. Then centrifuged again for 3 minutes at 20 000 × g and the supernatant transferred to an AllPrep DNA spin column. After centrifugation, the flow-through was retained and the column placed in a new collection tube at 4 °C until required.

To the flow-through from the previous step an equal volume of freshly prepared 70% ethanol was added and mixed thoroughly by pipetting. 700 µL of this solution was added to an AllPrep RNeasy spin column and centrifuged. The flow-through was

discarded and 700 µL of Buffer RW1 was added to the column before centrifugation. The flow-through was discarded and the column was washed by adding 500 µL of Buffer RPE, orienting horizontally and slowly turning several times to allow the buffer to wash the entirety of the inside of the column. The tubes were centrifuged and the was step repeated before centrifuging for 2 minutes at 8000 × g. The spin column was placed in a new collection tube and centrifuged at full speed for 1 minute to dry. The column was transferred to a collection tube and RNA eluted by addition of 30 µL of RNase free water and incubation at room temperature for 5 minutes, followed by centrifugation at 8000 × g for 1 minute. The elution step was repeated by adding the eluent back on to the column, incubating and centrifuging as in the previous step.

The DNA columns were removed from 4 °C and 500 µL of Buffer AW1 was added before centrifugation. The flow-through was discarded and 500 µL of Buffer AW2 was added to the column before centrifugation at full speed for 1 minute. The column was then transferred to a collection tube and DNA was eluted by adding 100 µL of Buffer EB to the centre of the column before incubating at room temperature for 5 minutes then centrifugation at 8000 × g for 1 minute. The elution step was repeated by adding the eluent back on to the column and repeating the incubation and centrifugation steps.

2.2.5 Nucleic acid quantification and quality assessment

Quantification of nucleic acids was performed by either Nanodrop or Qubit depending on the downstream methods required. For samples used in general laboratory molecular biology methods, nucleic acids were quantified using the Nanodrop One Spectrophotometer (Thermo Scientific). The Qubit RNA High Sensitivity assay kit (#Q32852, Invitrogen) was used for quantification of RNA samples sent for microarray analysis due to its improved accuracy. In brief, Qubit RNA HS Reagent was diluted 1:200 with Qubit RNA HS Buffer to creating a working solution, 199 µL of this working solution was added to each sample tube and 190 µL to two tubes for the standards. For samples, 1 µL was added to the working solution and 10 µL for each of the included standards. The tubes were vortexed for 5-10 seconds and left at room temperature for 5 minutes. The fluorescence of the samples and standards were measured using the Qubit 3 Fluo-

rometer (#Q33216, Invitrogen).

To examine RNA quality for samples that were submitted for sequencing the RIN was determined using High Sensitivity RNA ScreenTapes (#5067-5579, Agilent). High Sensitivity RNA Sample Buffer (1 µL; #5067-5580, Agilent) was added to 2 µL of the RNA sample and vortexed for 1 minute at 2000 rpm on the IKA vortexer (IKA). The samples were briefly centrifuged before incubating at 72 °C for 3 minutes followed by 2 minutes on ice. The samples were centrifuged again and loaded in to a TapeStation 4200 instrument (Agilent) along with a High Sensitivity RNA ScreenTape for processing and determination of the sample RIN. Only samples with a RIN $\geq$7 were used for microarray analysis.

2.3 DNA analysis

2.3.1 Agarose gel electrophoresis

PCR products were separated and visualised by gel electrophoresis and UV transillumination. Gels were cast from 0.8-2% (w/v) agarose (Thistle Scientific) in Tris-borate-EDTA (TBE) buffer (89 mM Tris, 89 mM boric acid, 2 mM EDTA; Merck) supplemented with 0.2 µg/mL ethidium bromide (Sigma) and were loaded in to the mini-sub cell GT horizontal electrophoresis system (Bio-Rad) and submerged in TBE buffer.

Samples were diluted with 5x Orange G loading buffer (0.25% (w/v) Orange G, 40% (w/v) sucrose, in 2.5x TBE buffer) before loading in to the agarose gel. For accurate sizing, the samples were loaded alongside a 1 Kb Plus DNA ladder (#10787018, Invitrogen), which was similarly diluted with 5x Orange G loading buffer. Gel electrophoresis was performed for 30-60 minutes at 120 V before visualisation using the ChemiDoc MP system (Bio-Rad).

2.4 RNA analysis

2.4.1 Reverse transcription of RNA to cDNA

For conversion of RNA to cDNA, the high capacity cDNA reverse transcription kit (#4368814, Applied Biosystems) was used as per the manufacturer's guidance. In brief, up to 1500 ng of RNA (10 µL at 150 ng/µL or 10 µL at the extracted concentration, if less than 150 ng/µL) was added to 10 µL of the master mix described in Table 2.11 and was thermocycled using the conditions in Table 2.12.

Table 2.11: Master mix for cDNA synthesis reactions.

Reagent	**Volume (**uL**)**	**Final Concentration (in** 20 µL **volume)**
10x RT Buffer	2	1x
100 mM dNTP Mix	0.8	4 mM
10x Random Primer	2	1x
Multiscribe Reverse Transcriptase	1	-
RNase Inhibitor	1	-
Nuclease-free Water	3.2	-

Table 2.12: Thermocycling conditions for high capacity cDNA reverse transcription kit.

Cycles	**Temperature (°C)**	**Time**
1	25	10 minutes
1	37	120 minutes
1	85	5 minutes

Based on the assumption that cDNA conversion was 100% efficient, the cDNA concentration was calculated as $\frac{Input\ RNA\ (ng)}{20\,\mu L}$ and all samples were diluted to 10 ng/µL.

2.4.2 Real-time quantitative PCR

For real-time quantitative PCR (RT-qPCR), TaqMan assays (Thermo Scientific) were used, a list of which can be found in Appendix A.1. To prepare the reactions, 8 µL of

master mix, Table 2.13, were added to a MircoAmp Fast Optical 96-well plate (#4346906, Applied Biosystems). 2 µL of cDNA (at 10 ng/µL) were loaded in duplicate and pipetted to mix. After loading all samples, the plate was sealed with a MicroAmp Optical Adhesive Film (#4311971, Applied Biosystems) and the plate was briefly centrifuged to collect samples to the bottom of the wells. The plate was loaded in to a QuantStudio 6 Flex Real-Time PCR System (Applied Biosystems) and thermocycled as described in Table 2.14. Calculation of relative expression was performed as outlined by Hellemans *et al.* [314]

Table 2.13: Master mix for RT-qPCR using TaqMan assays.

Reagent	**Volume (**uL**)**	**Final Concentration (in** 20 µL **volume)**
Nuclease-free water	2.5	-
2x TaqMan Fast Universal PCR Master Mix	5	1x
20x TaqMan Probe Mix	0.5	1x

Table 2.14: Thermocycling conditions for high capacity cDNA reverse transcription kit.

Cycles	**Temperature (**°C**)**	**Time**
1	95	20 seconds
40	95	1 second
	60*	20 seconds

*Data collection was performed at this point of the cycling program.

2.4.3 RNA microarray

RNA microarray was performed by the Oxford Genomics Centre. Quantified and quality checked samples (as described in Section 2.2.5) were submitted for analysis using the Clariom S Assay HT microarray (Affymetrix). Data was obtained in the form of sample level, probe set intensities values, which were robust multi-array average (RMA) normalised using the "oligo" package for R. Probe sets were annotated to their representative gene using the annotation file provided by the manufacturer and differential

gene expression was performed using the R package "limma".

2.5 Histology and pathological analysis

2.5.1 Tissue processing and embedding

Formalin fixed tissues, prepared as described in Section 2.1.6(iii) were prepared for processing by partitioning in to appropriately sized pieces, placed in a histology cassette (uterine tissue was cut cross-sectionally in to ~10-15 mm), and processed in a HistoMaster 2052 (Bavimed) using the following protocol: 70% ethanol for 45 minutes, 90% ethanol for 45 minutes, 100% ethanol for 30 minutes, 100% ethanol for 45 minutes, 100% ethanol for 45 minutes, Histo-Clear for 30 minutes, Histo-Clear for 30 minutes, Histo-Clear for 30 minutes, molten wax (60-65 °C) for 30 minutes, molten wax for 45 minutes, molten wax for 45 minutes. After processing, the tissue was then embedded in paraffin wax using the EG1150H Paraffin Embedding Station (Leica).

2.5.2 Tissue sectioning

2.5.2.1 Microtome sectioning of FFPE tissue

Formalin fixed paraffin embedded (FFPE) tissue blocks were sectioned using a RM2255 microtome (Leica). Tissue was cut at either 4 µm or 10 µm depending on the downstream use. Sections were floated on nuclease-free water, captured with Superfrost Plus microscope slides (#631-0108, VWR) and dried at 37 °C.

2.5.2.2 Cryostat sectioning of OCT embedded tissue

OCT embedded, fresh frozen tissue sections were cut using the CM1950 cryostat (Leica) with the chamber and chuck temperature was set to −16 °C. Sections were cut at either 4 µm or 10 µm, transferred to polysine adhesion slides and briefly placed tissue side up on to the cryostat stage to allow the tissue to freeze. The slides were loosely wrapped with aluminium foil and placed on dry ice until ready to proceed.

2.5.3 Haematoxylin and Eosin staining

2.5.3.1 FFPE tissue sections

FFPE sections (4 µm thickness) cut as described in Section 2.5.2.1 were baked for 1 hour at 55 °C. Baked tissue sections were deparaffinised in xylene (Fisher) for 5 minutes then hydrated through a decreasing ethanol series of 100% ethanol, 90% ethanol, and 70% ethanol for 5 minutes each before immersion in distilled water for 2 minutes.

Haematoxylin staining was performed by immersing the tissue sections in freshly filtered Harris haematoxylin solution for 30 seconds followed by washing with running tap water until clear. The haematoxylin stain was regressed by briefly dipping (1-2 seconds) the tissue sections into acid alcohol (50 mM HCl in 70% ethanol) before washing with running tap water for 5 minutes. Counter-staining with eosin was performed by immersing the slides in Eosin solution for 3 minutes, before briefly dipping in tap water to remove the excess.

The tissue sections were dehydrated through an increasing ethanol series of 70% ethanol, 90% ethanol, and 100% ethanol for 1 minute at each stage before clearing by immersion in xylene for 1 minute. The sections were cover slipped using DPX mountant, which was allowed to dry for 24 hours, prior to scanning of the tissue sections using the Aperio CS2 slide scanner at 20x or 40x magnification.

2.5.3.2 OCT tissue sections

Tissue sections (4 µm thickness), prepared as described in Section 2.5.2.2, were placed at room temperature and allowed to thaw briefly (~30 seconds). The slides were then placed in ice-cold 80% methanol for 5 minutes, before washing with phosphate buffered saline (PBS) twice. Followed by immersion (on a see-saw rocker) in 95% ethanol for 3 minutes, 75% ethanol for 3 minutes, then deionised water for 3 minutes. Slides were removed from the rocker and immersed in Harris haematoxylin solution for 30 seconds followed by washing under running tap water until excess solution was removed and water ran clear. Slides were dipped 4 times in 95% ethanol, followed by 10 times in eosin solution, 10 times in 95% ethanol, 10 times in 95% ethanol, 10 times in 100% ethanol, 10

times in 100% ethanol, 10 times in 100% ethanol before immersion in xylene. The slides were cover slipped using pertex and allowed to dry for 24 hours before scanning using the Aperio CS2 slide scanner at 20x or 40x magnification.

2.5.4 Pathological classification

Pathological classification of uteri from the mouse models was performed from haematoxylin and eosin (H&E) slides (from FFPE or OCT embedded tissue) by two gynaecological pathologists that were blinded to the mouse genotypes: Dr Tjalling Bosse (Leiden University Medical Centre) and Dr Alicia Leon-Castillo (Leiden University Medical Centre). Either physical slides or digitised slide scans were provided to allow pathological classification. Annotation of regions of hyperplasia in $Trp53^{R172H/\Delta}$ $Fbxw7^{+/+}$ and $Trp53^{R172H/\Delta}$ $Fbxw7^{R482Q/+}$ mice was performed by Dr Lai Mun Wang (Changi General Hospital) from digitised H&E stained OCT embedded tissue slides.

2.6 Molecular cloning

All plasmids used in this thesis and their sources can be found in Appendix A, along with the antibiotic selection conditions used for bacterial plates and liquid cultures.

2.6.1 Gateway cloning

The majority of plasmids used in this thesis were obtained as entry clones ready for the LR recombination reaction. However, the transcription factor 7 like 2 (*TCF7L2*) CDS was only available in a non-gateway plasmid and required both the BP and LR reactions.

2.6.1.1 LR reaction

The LR reaction was performed to recombine the CDS present in an entry vector into a destination vector to generate the desired expression plasmid. This was performed by mixing of 1 µL of donor vector (100 ng/µL), 1 µL of destination vector (150 ng), 6 µL of Tris-EDTA (TE) buffer (10 mM Tris-HCl, 1 mM EDTA, pH 8.0), and 2 µL LR Clonase II enzyme mix (#11791020, Invitrogen). The mix was incubated at 25 °C for 1 hour,

followed by addition of 1 µL of proteinase K, brief vortexing to mix and incubation at 37 °C for 10 minutes. The mix was then transformed in bacteria as described in Section 2.6.1.3.

2.6.1.2 Combined BP and LR reaction

For the *TCF7L2* plasmid, an initial amplification reaction was performed to add the attB1 and attB2 flanking sequences required for BP recombination. Additionally, in this amplification step the reverse primer was altered to introduce a stop codon at the end of the CDS as the obtained plasmid did not include the stop codon. Q5 high fidelity DNA polymerase (#M0491, New England BioLabs) was used to amplify the sequence due to its low error rates. Plasmid DNA (1 µL at 10 ng/µL) was added to 49 µL of the mastermix in Table 2.15 and thermocycled using the conditions in Table 2.16. The entirety of the PCR product was run on a 1% agarose gel, as described in Section 2.3.1 and the amplified product was extracted as described in Section 2.6.3.

Primer sequences:

- TCF7L2-BP-Fwd: GGGGACAAGTTTGTACAAAAAAGCAGGCATGCCGC
- TCF7L2-BP-Rev: GGGGACCACTTTGTACAAGAAAGCTGGGTTCATTCTAAAGACTTG

After extraction of the attB1/attB2 flanked CDS, 1 µL (100 ng/µL) was added to 1.3 µL of pDONR221 donor vector (150 ng/µL; #12536017, Invitrogen), 10.7 µL of TE buffer (pH 8.0), and 3 µL of BP Clonase II enzyme mix (#11789020, Invitrogen). This mix was vortexed briefly and incubated at 25 °C for 4 hours then 5 µL of the mix was removed and retained separately. Destination vector (2 µL at 150 ng/µL) and 3 µL of LR Clonase II enzyme mix were added to the remaining 10 µL volume before brief vortexing and incubation at 25 °C for 4 hours. Proteinase K (2 µL) was added to the 15 µL volume and 0.5 µL to the retained 5 µL volume and both were incubated at 37 °C for 10 minutes. After incubation, the two reactions were separately transformed in to bacteria as described in Section 2.6.1.3. The volume removed before addition of the destination vector provides an entry clone of the *TCF7L2* CDS compatible with gateway cloning,

Table 2.15: Components of the master mix used for amplification of the *TCF7L2* CDS

Reagent	**Volume (uL)**	**Final Concentration**
Water	32.5	-
5x Q5 Reaction Buffer	10	1x
10 mM dNTPs	1	200 nM
10 µM Primer 1	2.5	500 nM
10 µM Primer 2	2.5	500 nM
Q5 Polymerase	0.5	-

Table 2.16: Thermocycling conditions for *TCF7L2* CDS amplification.

Cycles	**Temperature (°C)**	**Time**
1	98	30 seconds
30	98	10 seconds
	72	20 seconds
	72	1 minute
1	72	2 minutes

and the volume after will provide the *TCF7L2* CDS recombined into the destination vector.

2.6.1.3 Bacterial transformation of gateway expression plasmids

LR reactions were transformed in to OneShot OmniMax Chemically Competent *Escherichia coli* cells (#C854003, Invitrogen), as these cells are sensitive to CcdB which is present in the destination vector, but is replaced during successful recombination. A 50 µL aliquot of cells was thawed on ice and 1 µL of the LR reaction added before flicking gently to mix. The cells were incubated on ice for 30 minutes before heat-shocking at 42 °C for 30 seconds in a water bath and immediately placing back on ice for 2 minutes. Warmed (37 °C) super optimal broth with catabolite repression (S.O.C.) medium (250 µL) was added to the cells which were then incubated at 37 °C with shaking at 225 rpm for 1 hour. Two volumes of cells (20 µL and 100 µL) were then plated separately on to appropriate antibiotic selective agar plates and placed upside down at 37 °C

overnight.

2.6.2 Restriction enzyme digestion

Restriction enzyme (RE) digestion was performed to confirm successful recombination from gateway cloning, using single or dual REs. Plasmid (10 µL at 50 ng/µL) was added to 7 µL of ultrapure water, 1 µL of the required RE, 2 µL of the recommended buffer (5x CutSmart, 5x NEBuffer 1.1, 5x NEBuffer 2.1 or NEBuffer 3.1). If a dual RE digestion was required, then 1 µL of the secondary RE was added and only 6 µL of ultrapure water added. The reactions were gently mixed and incubated at the recommended temperature for 1-4 hours and the products of digestion were run on a 0.8% agarose gel as described in Section 2.3.1.

2.6.3 Extraction of DNA from agarose gel

DNA was extracted from agarose gels using the Zymoclean Gel DNA Recovery Kit (#D4007, Zymo Research) following the manufacturer's protocol. All centrifugation steps were performed at 10 000 × g unless otherwise stated. In brief, agarose gels were visualised using a UV transilluminator and the desired bands excised using a scalpel before placing a pre-weighed 1.5 mL tube. The tubes were then re-weighed to calculate the mass of gel (in mg) that was excised and 3x the mass of agarose dissolving buffer was added (i.e. if 200 mg of agarose gel was excised then 600 µL of buffer was added). The samples were then incubated at 55 °C for 10 minutes with frequent vortexing. If, after 10 minutes, the gel was not completely dissolved then the samples were incubated for an additional 5 minutes. Once fully dissolved the solution was transferred to a Zymo-Spin Column and centrifuged for 1 minute. The flow-through was discarded and 200 µL of DNA wash buffer added to the column before centrifuging for 30 seconds. The flow-through was discarded and the wash step repeated. After this 10 µL of DNA elution buffer was added to the column and incubated at room temperature for 5 minutes before centrifuging for 1 minute to elute the DNA.

2.6.4 Site-directed mutagenesis

SDM was performed to introduce the R465C, R479Q, and R505C mutations (termed WD40 variant) and to delete the F-box domain (termed ΔFbox variant) from the *FBXW7* coding sequence. Additionally, it was used to introduce T155A and T159A mutations in to the coding sequence of lymphoid enhancer binding factor 1 (*LEF1*) (termed CPD variant) and to delete the first ~60 amino acids from its coding sequence (termed ΔN variant). SDM was performed using the QuikChange Lightning kit (#210518, Agilent) according to the manufacturer's protocol, with primers that were designed using the manufacturer's online design tool.

In brief, the amount of each primer required for the reaction is 125 ng. Thus to calculate the volume of primer to add the following equation was used: $\frac{ng\ of\ primer\ required}{330 \times bp\ length\ of\ primer} \times 1000 = pmol\ of\ primer\ required$, this is then divided by the primer concentration to determine the volume to add. A reaction mix was made as outlined in Table 2.17 and thermocycled as described in Table 2.18. After the mutagenic PCR, 2 µL of *DpnI* was added, pipetted to mix and centrifuged briefly before incubating at 37 °C for 20 minutes. Incubation with *DpnI* acts to digest the methylated plasmid added to the PCR and retained the unmethylated, mutagenesised plasmid generated by the PCR. The reaction was then transformed in to XL10-Gold Ultracompetent *E. coli* cells (#200315, Agilent), as described in Section 2.6.5.

2.6.5 XL10-gold bacterial transformation

For propagation of gateway entry plasmids, transformation in to XL10-Gold bacterial cells was used. A 45 µL aliquot of cells was thawed on ice, 2 µL of β-mercaptoethanol added and mixed by gently flicking before incubating on ice for 2 minutes. Plasmid (25 ng) or 2 µL of a ligation or SDM reaction was added to the cells, flicked gently to mix and incubated on ice for 30 minutes. The cells were then heat-shocked by immersion in a 42 °C water bath for 30 seconds, followed by incubation on ice for 2 minutes. Pre-warmed (37 °C) S.O.C. medium (500 µL) was added to the cells which were incubated at 37 °C with shaking at 225 rpm for 1 hour. Two volumes of cells (20 µL and 200 µL) were

Table 2.17: Master mix used for SDM using the QuikChange Lightning Kit.

Reagent	**Volume (**uL**)**	**Final Concentration**
10x Reaction Buffer	5	1x
Plasmid (5 ng/µL)	5	25 ng
10 µM Primer 1	1.3*	260 nM
10 µM Primer 2	1.3*	260 nM
dNTP Mix	1	-
QuikSolution Reagent	1.5	-
Ultrapure Water	33.9	-
QuikChange Enzyme	1	-

*This reaction mix is based on primers that were 29 bp, the volume and final concentration of primer required will vary and adding or removing a volume of ultrapure water may be required.

Table 2.18: Thermocycling conditions for SDM using the QuikChange Lightning Kit.

Cycles	**Temperature (°C)**	**Time**
1	95	2 minutes
18	95	20 seconds
	60	20 seconds
	68	2.5 minutes *
1	68	5 minutes

*Extension time is calculated as 30 seconds per kb of plasmid length

separately plated on to the relevant antibiotic selective plates before incubation upside down at 37 °C overnight.

2.6.6 Mini-prep plasmid extraction

To extract plasmid for all purposes except for transfection, the QIAprep Spin Miniprep Kit (#27106, Qiagen) was used according to the manufacturer's protocol. All centrifugation steps were performed at 17 900 × g unless otherwise stated. In brief, 2.5 mL of Miller's Luria-Bertani (LB) broth, with the required selective antibiotic, was added to a 15 mL round bottom tube. Individual colonies from overnight plates were then picked using a pipette tip and added to the tube. Cultures were grown overnight (12-16 hours) at 37 °C and 225 rpm shaking.

The bacteria were pelleted by centrifugation at 5000 × g for 3 minutes at room temperature. The supernatant was discarded and the pellet fully resuspended in 250 µL of Buffer P1 (with RNase A added). The cells were lysed by addition of 250 µL of Buffer P2 and gently mixed by inverting the tube 6 times. The lysis reaction was terminated by addition of 350 µL of Buffer N3 and gentle mixing by inverting 6 times. Any precipitate was pelleted by centrifugation at 17 900 × g for 10 minutes, after which 800 µL of the supernatant was transferred to a QIAprep 2.0 Spin Column and centrifuged for 1 minute. The flow-through was discarded, and the column washed with 500 µL of Buffer PB and centrifuged for 1 minute. The flow-through was discarded, and the column washed with 750 µL of Buffer PE and centrifuged for 1 minute, before discarding the flow-through and drying the membrane by centrifugation at the maximum speed for 1 minute. The column was transferred to a 1.5 mL collection tube and the plasmid DNA was eluted with 50 µL of Buffer EB (10 mM Tris-HCl, pH 8.5), incubation at room temperature for 5 minutes and centrifugation for 1 minute.

2.6.7 Confirmation of site-directed mutagenesis by Sanger sequencing

To confirm the correct incorporation of mutations by SDM and to ensure no other mutations were introduced, Sanger sequencing of the plasmid CDS was performed. The protocol used is described in Section 2.1.5.6, with the exception of the amplification

step. Instead, 250 ng of plasmid DNA (2 µL at 125 ng/µL) was added to the master mix described in Table 2.9, the remaining steps were performed as previously described.

2.6.8 Maxi-prep plasmid extraction

To generate plasmid for transfection of cells, the Plasmid Plus Maxi Kit (#12963, Qiagen) was used according to the manufacturer's protocol. In brief, 2.5 mL of Miller's LB media with selective antibiotic was added to a 14 mL round bottom tube and inoculated with a bacterial stab before incubation at 37 °C with 225 rpm shaking for 6-8 hours. This culture (100-1000 µL) was used to seed to a 500 mL conical flask containing 130 mL of Miller's LB media with selective antibiotic and incubated at 37 °C with 225 rpm shaking for 12-16 hours.

The bacterial culture was transferred to a 250 mL centrifuge tube and the pelleted by centrifugation at 5000 × g for 15 minutes at 4 °C. The supernatant was discarded and pellet was resuspended with 8 mL of Buffer P1. The bacteria were lysed by addition of 8 mL of Buffer P2 with gentle inversion and incubation at room temperature for 3 minutes. The lysis was stopped by addition of 8 mL of Buffer S3 and gentle mixing by inversion. The lysate was transferred to a 50 mL centrifuge tube and incubated at room temperature for 10 minutes, after which it was centrifuged at 4500 × g for 5 minutes. Any precipitate floating on the surface of the supernatant was carefully discarded. The supernatant transferred to a QIAfilter cartridge and filtered in to a new 50 mL centrifuge tube. Buffer BB (5 mL) was then added and mixed by inversion. The lysate was transferred to a Plasmid Plus spin column with tube extender, placed on a vacuum manifold and a vacuum was applied to pull the lysate through the column. The spin column was removed from the vacuum manifold and placed in a collection tube, 700 µL of Buffer ETR was added to the column before centrifugation at 10 000 × g for 1 minute. The flow-through was discarded and 700 µL of Buffer PE was added before centrifuging at 10 000 × g for 1 minute. The flow-through was discarded and centrifugation was repeated to fully dry the membrane. The spin column was transferred at a 2 mL tube and the plasmid DNA was eluted by addition of 400 µL of Buffer EB, incubation at room temperature for 5 minutes and centrifugation at 10 000 × g for 1 minute.

2.7 Cell culture

2.7.1 Maintenance of cells

All cell culture work was performed in a class II biosafety cabinet using aseptic techniques with cells maintained in at 37 °C and 5% CO_2 in a humidified cell culture incubator. The work in this thesis required the use of two cell lines: HEK293T and NOU-1. HEK293T was maintained in Dulbecco's modified Eagle medium (DMEM) with 10% (v/v) foetal bovine serum (FBS) and 1% (v/v) penicillin-streptomycin. NOU-1 was maintained in minimum essential medium (MEM) with 15% (v/v) FBS and 1% (v/v) penicillin/streptomycin.

To bring cells in to culture, a frozen aliquot of cells was thawed at 37 °C in a water bath, then cells were added to 9 mL of culture medium and centrifuged at 500 × g for 5 minutes. The supernatant was aspirated and the pellet resuspended in fresh culture medium before transferring to an appropriately sized flask (either a T25 or T75). Cells were passaged when at ∼70-80% confluence, at which point the cells were washed with sterile PBS before addition of 0.05% (w/v) trypsin-EDTA solution (Gibco) followed by incubation at 37 °C for 5 minutes. Cells were resuspended with cell culture medium and centrifuged at 500 × g for 5 minutes. The supernatant was aspirated and cells resuspended in fresh culture medium and $\frac{1}{10}$th of the volume was transferred to a new flask containing culture medium. For long term storage of cells in liquid nitrogen, an appropriate number of cells (>1,000,000) were pelleted, resuspended in freezing medium (90% FBS and 10% DMSO) and transferred to a 2 mL cyrovial. Cells were slowly frozen in a CoolCell freezing container (#432001, Corning) at −80 °C for 24 hours, after which they were stored in a vapour phase liquid nitrogen storage tank.

2.7.2 Cell counting

Cell counting was performed using a Countess II automated cell counter (ThermoFisher Scientific). Cells were diluted using a 1:1 volumetric ratio of cells to 0.4% trypan blue solution before loading 15-20 µL in to a Countess chamber slide. The slide was inserted in to the Countess II and estimation of the cell viability and cell number performed by

the counter.

2.7.3 Transient transfection for protein expression

HEK-293T and NOU-1 cells were used for transient plasmid transfection to generate lysates for co-immunoprecipitation, and the protocol followed was identical for both. Cells were seeded (5,000,000) in a 10 cm dish and incubated for 24 hours at normal conditions. The cells (∼70% confluent) were washed once with sterile PBS before addition of low serum medium (5% FBS and no penicillin-streptomycin). In a 1.5 mL tube, 10 µg of plasmid (or 5 µg each for dual transfections) was diluted in 500 µL of Opti-MEM I reduced serum medium (#31985062, Gibco) and gently mix by flicking. 30 µL of Fugene HD (#E2311, Promega) was then added to the tube and gently mixed by flicking, followed by incubation at room temperature for 20 minutes. The plasmid solution was then added drop-wise to the 10 cm cell plate and incubated for 24 hours under normal conditions.

After incubation, the cells were washed once with sterile PBS before addition of 500 µL of 0.05% trypsin-EDTA solution for 5 minutes to detach the cells. The cells were resuspended in 14 mL of normal culture medium which was separated in to two 10 cm plate. These plates were incubated for 24 hours under normal conditions and which the cells were ready for lysis as described in Section 2.8.2.

2.8 Protein analysis

2.8.1 Protein extraction from fresh frozen tissue

To extract protein from fresh frozen tissues, a frozen tissue piece was added to a pre-chilled and weighted 1.5 mL tube, which was subsequently re-weighed to determine the mass of the tissue. Chilled radio immunoprecipitation assay (RIPA) buffer (50 mM Tris-HCl pH 8, 150 mM sodium chloride (NaCl), 1% (v/v) IGEPAL CA-630 (Sigma), 1% (v/v) sodium deoxycholate, 0.1% (v/v) sodium dodecyl sulfate, 1x cOmplete EDTA-free protease inhibitor (Roche), 1x phosphatase inhibitor cocktail 2 (Sigma), 1x phosphatase inhibitor cocktail 3 (Sigma)) was added at a 1:10 ratio (tissue mg: buffer µL).

The tissue was immediately disrupted using a micropestle for 30-60 seconds followed by gentle vortexing. The samples were incubated on ice for 30 minutes with regular agitation before centrifugation at 4 °C for 20 minutes at the maximum possible speed. The supernatant was split into several aliquots and was quantified as described in Section 2.8.3 then stored at −80 °C.

2.8.2 Protein extraction from cell lines for immunoprecipitation

Protein extraction for immunoprecipitation was performed as described in [315]. For each condition, two 10 cm dishes of cells that had been transiently transfected, as described in Section 2.7.3, were washed once with ice-cold PBS. The plates were rested at a 45° angle for 1 minute to allow excess PBS to collect before aspiration. Room temperature Benzonase lysis buffer (500 µL; 20 mM Tris-HCl pH 7.5, 40 mM potassium chloride (KCl), 2 mM magnesium chloride ($MgCl_2$), 10% (v/v) glycerol, 0.5% (v/v) IGEPAL CA-630, 1x cOmplete EDTA-free protease inhibitor, 0.5x phosphatase inhibitor cocktail 2, 0.5x phosphatase inhibitor cocktail 3, 50 U/mL Benzonase) was added to the first dish before the cells were scraped and homogenised by pipetting. The lysate was then transferred to the second dish and the cells were again scraped and mixed by pipetting before being transferred to a pre-chilled 1.5 mL Eppendorf on ice. The samples were incubated on ice for 10 minutes with frequent agitation.

Following incubation the salt concentration was adjusted to 450 mM by addition of 5 M KCl and thorough mixing by pipetting. The samples were placed on a tube rotator for 30 minutes at 4 °C before clarification of the lysate by centrifugation at 13 000 × g and 4 °C for 10 minutes. After centrifugation the supernatant was transferred to a new tube before quantification as described in Section 2.8.3. The lysate was then aliquoted into volumes containing 2 mg of protein before snap freezing in liquid nitrogen and long term storage at −80 °C.

2.8.3 Protein quantification

Protein samples were quantified using the CB-X assay (#786-12X, G-Biosciences), a modified Bradford's assay. The assay has two protocols depending on the lysis buffer that is

used. For samples with lower detergent concentrations, such as the samples extracted with Benzonase lysis buffer, 5 µL of the protein sample was diluted 1:10 with water (to a total of 50 µL) and mixed briefly by vortexing. CB-X assay dye (1 mL) was added to the diluted samples before vortexing to mix and incubating at room temperature for 5 minutes. The protein/dye mix was pipetted in triplicate (200 µL per well) in to a clear bottom 96-well plate and absorbance at 595 nm was measured using a microplate reader. Protein concentration was calculated through generation of a standard curve using known protein concentrations.

For samples with higher concentrations of detergents, such as samples using RIPA lysis buffer, an initial sample clean-up step was performed. The samples were diluted with water, as above, and the protein was precipitated by addition of 1 mL pre-chilled (−20 °C) CB-X reagent before vortexing to mix. The precipitate was pelleted by centrifugation at 16 000 × g for 5 minutes, the supernatant was carefully removed and discarded. The pellet was dissolved by addition of 50 µL each of CB-X solubilization buffers I and II followed by incubation at room temperature for 10 minutes with periodic vortexing. 1 mL of CB-X assay dye was then added to the samples, and they were processed as per the previously described protocol.

2.8.4 Co-immunoprecipitation

2.8.4.1 Preparation of anti-FLAG tag conjugated magnetic beads

To prepare the magnetic beads required for co-immunoprecipitation, 3.33 µg of anti-FLAG tag antibody (F3165; Sigma) was conjugated per 50 µL of Protein G Dynabeads (#10004D, Invitrogen) according to the manufacturer's protocol. In addition to the anti-FLAG tag beads, isotype control beads were also prepared, using mouse IgG_1 isotype control antibody (MAB002; R&D Systems) and the same antibody to bead ratio previously stated.

In brief, 50 µL per sample of beads were transferred to an appropriately sized tube and were placed on a DynaMag-2 magnet (ThermoFisher Scientific) for 1-2 minutes, until the supernatant had fully cleared. The supernatant was then discarded and twice the

initial bead volume of PBS was added, and the bead pelleted resuspended by pipetting. 3.33 µg of antibody per 50 µL of Protein G Dynabeads was then added and incubated at room temperature on a tube rotator for 1 hour. After incubation, the bead and antibody slurry was placed back on to the magnetic rack for 1-2 minutes until the supernatant had cleared. The supernatant was discarded, and the beads were resuspended in their initial volume of PBS with 0.02% (v/v) Tween-20. Prepared beads were kept at 4 °C and were used within 1 week of preparation.

2.8.4.2 Co-immunoprecipitation

The protocol used for co-immunoprecipitation was adapted from the method described in [315]. To a volume containing 2 mg of protein, generated as described in Section 2.8.2, twice the volume of "no-salt equilibration buffer" (20 mM Tris-HCl pH 7.5, 10% (v/v) glycerol, 0.5 mM dithiothreitol (DTT), 0.5 mM ethylenediaminetetraacetic acid (EDTA), 1x cOmplete EDTA-free protease inhibitor, 0.5x phosphatase inhibitor cocktail 2, 0.5x phosphatase inhibitor cocktail 3) was added to reduce the salt concentration. This was followed by pipetting to mix and equilibration on ice for 15 minutes.

During the equilibration period, the required volume (50 µL per sample) of mouse IgG_1 isotype control conjugated beads, prepared as described in Section 2.8.4.1, were placed on a magnetic rack for 1-2 minutes until the supernatant had cleared. The supernatant was discarded, and the beads were resuspended in 500 µL of "IP wash buffer" (20 mM Tris-HCl pH 7.5, 100 mM KCl, 10% (v/v) glycerol, 0.5 mM DTT, 1x cOmplete EDTA-free protease inhibitor, 0.5x phosphatase inhibitor cocktail 2, 0.5x phosphatase inhibitor cocktail 3) before placing back on the magnetic rack and discarding the supernatant. This wash step was repeated two more times. After the discarding the supernatant from the final wash, the beads were resuspended in their original volume of IP wash buffer and 50 µL aliquots were added to individual 1.5 mL tubes before placing on the magnetic rack and discarding the supernatant.

After the samples had equilibrated and the magnetic beads aliquoted, the samples were used to resuspend the magnetic beads which were then incubated at 4 °C on a tube rotator for 2 hours. During this time anti-FLAG tag conjugated beads were washed

and aliquoted as previously described. After incubation, the samples were placed on a magnetic rack until the supernatant had cleared, then the supernatant was transferred to tubes of anti-FLAG tag beads which were resuspended by pipetting. The samples were again incubated at 4 °C on a tube rotator for 2 hours.

After the second incubation, the samples were placed back on a magnetic rack until the supernatant had cleared. The supernatant was discarded and 100 µL of IP wash buffer was used to resuspend the beads before placing back on the magnetic rack. The supernatant was discarded and the beads again resuspended in 100 µL of IP wash buffer. The samples were transferred at a new 1.5 mL Eppendorf and placed back on the magnetic rack to pellet the beads. The wash step was repeated a further two times and after removal of the final wash supernatant the beads were resuspended in 30 µL LDS elution buffer (50 mM glycine pH 2.8, 1x NuPAGE LDS Sample Buffer, 1x NuPAGE Sample Reducing Agent) before heating at 70 °C for 10 minutes. The samples were placed on the magnetic rack for 2 minutes and the supernatant was retained and used directly for loading polyacrylamide gels for size separation.

2.8.5 Polyacrylamide gel electrophoresis and western blotting

Gel electrophoresis and protein transfer were performed using Bolt Mini system (Invitrogen), as per the manufacturer's protocol. In brief, protein samples were prepared using 20-40 µg of protein diluted to a final volume of 10 µL with 2.5 µL 4x Bolt LDS Sample Buffer, 1 µL 10x Bolt Sample Reducing Buffer and ultrapure water (to 10 µL total volume). If the protein volume required for the desired protein amount was >6.5 µL then a final volume of 20 µL was used and the Bolt LDS Sample Buffer and Sample Reducing Buffer volumes were doubled. After dilution, the samples were heated at 70 °C for 10 minutes before cooling on ice and briefly centrifuging.

A 4-12 % Bolt Bis-Tris Mini protein gel was placed in the gel tank, which was then filled with 1x Bolt MOPS SDS running buffer. Bolt Antioxidant (500 µL) was added to the buffer in the lower chamber. The samples were loaded into the gel, along with a pre-stained protein ladder (#P7719, New England BioLabs) and electrophoresis was performed at 200 V for 30-35 minutes.

Following size separation, the gel was removed from its plastic cassette and washed with ultrapure water. The PVDF membrane (#IPFL00010, Merck Millipore) was soaked in 100% methanol for 1 minute before soaking in transfer buffer until required (1x Bolt Transfer Buffer with 10% (v/v) methanol and 0.001% (v/v) Bolt antioxidant). Two blotting sponges and two pieces of blotting paper were also soaked in transfer buffer. The transfer stack was then assembled, using a Mini blot module (Invitrogen), as follows starting from the cathode: blotting sponge, blotting paper, protein gel, PVDF membrane, blotting paper, blotting sponge. The module was filled with transfer buffer and loaded in to the gel tank with deionised water surrounding the module and the transfer was performed at 20 V for 1 hour.

After the transfer, the membranes were allowed to fully dry for 1 hour before reactivation with 100% methanol for 1 minute. Following a brief wash with tris-buffered saline (TBS), the membranes were blocked for 1 hour at room temperature with 5% (w/v) skimmed milk in TBS. Primary antibodies were prepared in 5% (w/v) skimmed milk in TBS with 0.2% (v/v) Tween-20 and were incubated with the membrane overnight at 4 °C. After primary incubation, the membrane was washed three times for 10 minutes with TBS containing 0.1% (w/v) Tween-20, then incubated with the secondary antibody prepared in 5% (w/v) skimmed milk in TBS with 0.2% (v/v) Tween-20 and 0.01% SDS for 2 hours. Then their membrane was washed three times for 10 minutes with TBS containing 0.1% (w/v) Tween-20 . Followed by a single wash with TBS before imaging using an Odyssey CLx near-infrared fluorescence scanner (LI-COR). A list of primary and secondary antibodies used can be found in Appendix A.3.

2.8.6 Immunohistochemistry

IHC was performed using two methods, for single target identification chromogenic IHC was used and for multiplexed detection of targets fluorescent IHC was used.

2.8.6.1 Chromogenic

Tissue sections (4 µm), prepared as described in Section 2.5.2.1, were baked for 1 hour at 55 °C. Then deparaffinised by two sequential incubations in xylene for 10 minutes

each, followed by rehydration through an ethanol series: 2 minutes in 100% ethanol, 2 minutes in 90% ethanol, 2 minutes in 70% ethanol, and finally two incubations of 5 minutes in ultrapure water. Antigen retrieval was performed by boiling slides in antigen retrieval buffer (10 mM sodium citrate, pH 6) for 5 minutes at the maximum possible temperature using a pressure cooker. The cooker was cooled for 20 minutes before the slides were removed and washed once with ultrapure water for 5 minutes. To inactivate any potential endogenous peroxidase activity, a peroxidase quench step was performed by incubating the slides in 3% H_2O_2 for 10 minutes, followed by two 5 minute washes in ultrapure water and a final 5-minute wash in TBS.

A border was drawn on the slide around the extent of the tissue using an ImmEdge hydrophobic pen, to allow smaller volumes of blocking and antibody buffers to be used. Blocking was then performed by addition of blocking buffer (5% (v/v) normal goat serum (#S-1000, Vector Laboratories) in TBS with 0.1% Tween-20). The slides were incubated with blocking buffer for 1 hour at room temperature in a humidified slide tray. The blocking buffer was then removed and the primary antibody (diluted in 5% normal goat serum in TBS with 0.1% Tween-20) added for 1 hour at room temperature or overnight at 4 °C. After the primary incubation, the slides were washed three times for 5 minutes each in TBS with 0.1% Tween-20. SignalStain Boost IHC Reagent (Cell Signaling Technology) matched to the species of the primary antibody was used in place of a secondary antibody, and was added to the slides and incubated at room temperature for 30 minutes in a humidified box. The slides were washed three times for 5 minutes with TBS with 0.1% Tween-20, before addition of ImmPACT DAB substrate (#SK-4105, Vector Laboratories), the length of incubation with DAB was dependent on the antibody used. Ideal timings were determined by developing a slide under the microscope to allow visualisation of the reaction progress, the same incubation length was then used for subsequent slides. After treatment with DAB the slides were washed with deionised water for 5 minutes before counter staining in Harris haematoxylin solution for 5 minutes, running water to remove excess solution, a quick dip in acid alcohol, 5 minutes in deionised water and dehydration through an ethanol series (1 minute in 70%, 1 minute in 90%, 1 minute in 100% and 1 minute in xylene). Cover slips were mounted using DPX

and allowed to dry for 24 hours before scanning using the Aperio CS2 slide scanner at 20x or 40x magnification. All antibodies used for this protocol are listed in Appendix (A.3)

2.8.6.2 Fluorescent

The protocol for fluorescent IHC is identical to the chromogenic protocol. However, the peroxidase quench step was not performed, and the samples were not outlined using the ImmEdge pen due to autofluorescence. Incubation of primary antibodies were performed simultaneously, overnight at 4 °C. Instead of the SignalStain reagent, AlexaFluor conjugated secondary antibodies were used (listed in Appendix A.3) and incubation was performed for 45 minutes. After the wash steps directly following secondary incubation, the slides were cover slipped using VECTASHIELD vibrance antifade mounting medium with DAPI (#H-1800, Vector Laboratories) and left at 4 °C overnight to harden. The slides were imaged at 20x magnification using the Olympus SpinSR SoRA spinning disk confocal microscope.

2.9 Computational analysis

2.9.1 Survival analysis

Mouse survival analysis was performed using the R packages ”survminer” and ”survival”.

2.9.2 Differential gene expression analysis

Differential gene expression analysis for the mouse microarray data was performed as described in Section 2.4.3. For TCGA, the gene-level expression counts were obtained from the R package ”recount3”, MC3 mutation data was obtained using the ”maftools” package, and differential expression was determined using ”DEseq2”.

2.9.3 Gene set enrichment analysis

Gene set enrichment analysis (GSEA) was performed by ranking the genes based on signal-to-noise ratio ($\frac{\mu_A - \mu_B}{\sigma_A + \sigma_B}$; microarray data) or $-log_{10}(p\,value) \times (sign\,of\ fold\,change)$ (RNAseq data). GSEA was performed using the R package "clusterprofiler" with the gene sets defined by MSigDB.

2.9.4 Fluorescent-IHC quantification

Quantification of protein-expressing cells was performed using QuPath. Identification of cells was performed based on their expression of DAPI and protein positivity based on their fluorescent intensity in the respective channels.

2.9.5 Statistics

Any statistical tests performed are indicated in the text. Reporting of P value significance in figures is as follows: * - P value $\leq$ 0.05, ** - P value $\leq$ 0.01, *** - P value $\leq$ 0.001, **** - P value $\leq$ 0.0001.

Chapter 3

Functional characterisation of *Fbxw7*$^{R482Q/+}$ mutation in the mouse uterus

3.1 Introduction

3.1.1 *FBXW7* has a variable role in cellular homeostasis and exhibits context-specificity in regulation of targets

FBXW7 is commonly mutated in cancer, and particularly in endometrial cancer. However, to date, only one study has explored the functional role of *Fbxw7* deletion in the context of the uterus, with no studies examining missense mutation [316]. Work performed in other cancer types has highlighted an array of dysregulated pathways consequent to *FBXW7* mutation, which lead to acquisition of different cancer-specific, cellular characteristics [231]. Indicating that its role and major targets may vary in different cell types, and thus suggesting a level of context-specificity in its potential contribution to carcinogenesis.

One example of this is the link between loss or mutation of *FBXW7* and induction of epithelial to mesenchymal transition (EMT) in several cancer types including colorectal cancer, cholangiocarcinoma, non-small cell lung cancer (NSCLC), renal cell cancer,

and breast cancer [317–322]. The mechanistic induction of this state change across these cancer types is not homogenous. In colorectal cancer, breast cancer, and cholangiocarcinoma it has been linked with loss of regulation of MTOR, with additional dysregulation of zinc finger E-box binding homeobox 2 (ZEB2) and NOTCH1 reported in colorectal cancer and breast cancer, respectively [317–320]. However, in NSCLC dysregulation of snail family transcriptional repressor 1 (SNAI1) has been mechanistically linked to EMT induction [321, 322].

FBXW7 has also been shown to regulate cellular differentiation and is relevant in many tissue types as a regulator of cell stemness [323]. In neuronal cells, loss of *Fbxw7* reduces neurogenesis and increases stem cell populations through accumulation of Jun and Notch1 [324, 325]. Similarly, these substrates are overexpressed after homozygous or heterozygous deletion of FBXW7 in intestinal cells, again leading to accumulation of progenitor cells and reduction of terminally differentiated cell populations [238, 326]. Alternatively, accumulation of Myc and Notch1 has been linked with loss of Fbxw7 in haematopoietic stem cells, leading to depletion of this population due to activation of the cell cycle and increased p53-dependent apoptosis [327, 328].

3.1.2 Clinicopathological correlation with *FBXW7* mutation

The observation that EMT genes are upregulated in response to loss of *Fbxw7* suggests that *FBXW7*-mutant cancers may exhibit a more invasive phenotype. Corresponding clinical features, such as lymph node and vascular invasion or metastasis, exhibit heterogeneity in their correlation with FBXW7 dysregulation. Several studies have reported that mutation or reduced expression of *FBXW7* significantly correlates with muscle, lymph node or vessel invasion in melanoma, oesophageal, pancreatic, and gastric cancer [306, 329–331]. Reduced *FBXW7* expression correlates with extent of differentiation in gastric cancer [331]. Similar correlation with invasive characteristics is observed in colorectal cancers that exhibit low FBXW7 expression [300, 332]. Interestingly, analysis of patients exhibiting *FBXW7* missense mutation failed to show the same correlation [333, 334]. However, a recent meta-analysis of studies examining a combined dataset of mutation and reduced expression of FBXW7 did find a significant link with lymph

node metastasis, but not with extent of cell differentiation [335].

The correlation between mutations of *FBXW7* and survival is more consistent across studies, with reduced expression linked to poor prognosis or worse 5-year overall or disease-free survival in multiple cancer types [300, 306, 329–332]. Interestingly, although missense mutation was not found to correlate with invasiveness, it strongly correlated with poor overall survival in colorectal cancer [334]. Further to this, a relationship between *FBXW7* dysregulation and therapeutic resistance has been established in gastric cancer (apparent resistance to paclitaxel and platinum therapies) and pancreatic cancer (gemcitabine) [306, 331].

Examination of clinical features correlating with *FBXW7* mutation in EC have generated mixed results. Some studies found no connection with any measured clinical features, while others found significant correlation with lymph node involvement, albeit, with the caveat that they may be confounded by the tendency to separate certain cancer types, such as, carcinosarcomas from the analysis [95, 336, 337]. Additionally, a recent study found that *FBXW7* mutation was significantly associated with late stage EC, with vascular invasion and lymph node metastasis, but did not observe correlation with reduced overall survival [338].

3.1.3 Previous functional analysis of *FBXW7* in model systems

Numerous studies have been performed to examine the functional impact of FBXW7 using both *in vitro* and *in vivo* models. Much of the early work, described in Section 1.5.1.1, was performed using yeast and non-mammalian models. However, studies performed in mammalian *in vivo* models (predominantly GEMMs) have greatly improved the understanding of the functional role of Fbxw7 in both normal development, homeostasis and cancer. The first of such studies came simultaneously from Tetzlaff *et al.* and Tsunematsu *et al.* who attempted to generate constitutive homozygous deletion of *Fbxw7*, but found that impaired vascular, haematopoietic and cardiac development led to embryonic lethality, due to loss of Notch1 and Ccne1 regulation [339, 340].

This was followed by targeted homozygous or heterozygous deletion of *Fbxw7* from various cell compartments and organs. Thompson *et al.* and Matsuoka *et al.* simul-

taneously found that homozygous deletion of *Fbxw7* from haematopoietic stem cells severely disrupted the maintenance of a quiescent state by triggering active cycling of the stem cells and, in the Matsuoka *et al.* study, p53-dependent apoptosis [327, 341]. In both studies this was mechanistically linked to accumulation of Myc, with additional accumulation of Notch1 reported by Matsuoka *et al.* [327, 341]. However, accumulation of both Notch1 and Ccne1 were investigated by Thompson *et al.* without evidence of either [341]. Furthermore, in Matsuoka *et al.*'s study combined loss of *Fbxw7* with deletion of *Trp53* resulted in development of T-ALL [327]. Similar studies in liver found induction of a fatty liver phenotype with increased cell proliferation and abnormal differentiation, which caused an increase in cholangiocytes as a result of dysregulation of Notch1 and Srebf1 [342]. In neuronal stem cells, homozygous *Fbxw7* loss was associated with an increased number of progenitor cells instead of depletion [324, 325]. Accumulation of Notch1 and 4 were mechanistically linked to the increased stem cell proliferation and lack of neurogenesis, with stem cell differentiation continuing preferentially astrocytes [324, 325].

In the intestine, studies examining homozygous and heterozygous *Fbxw7* deletion have been performed. The first study performed by Sancho *et al.* noted differential effects on progenitor cell accumulation when comparing homozygous and heterozygous loss (accumulation occurred in homozygous mice) [326]. A decrease of terminally differentiated goblet cells was also apparent with homozygous loss, but not heterozygous loss [326]. When combined with a known driver of colorectal cancer, Adenomatous polyposis coli (*Apc*) deletion, both heterozygous and homozygous loss were found to rapidly induce adenomas with a significantly reduced latency over *Apc* deletion alone [326]. Interestingly, differential molecular perturbation was observed in both models, with accumulation of Notch1 and Jun observed with homozygous deletion and only Notch1 dysregulated with heterozygous deletion [326]. The findings of this study were corroborated by a subsequent study from Babaei-Jadidi *et al.*, in which the same progenitor cell phenotype, cancer inducing phenotype and substrate dysregulation was observed [343]. Interestingly, this study also noted an upregulation of Ctnnb1 in the Apc^{min} $Fbxw7^{-/-}$ mice but not with *Fbxw7* deletion alone [343].

Development of missense mutation based models allowed study of more the biologically relevant effects of Fbxw7 as a potential driver of carcinogenesis. Davis *et al.* reported that germline heterozygous *Fbxw7*^{R482Q} mutation resulted in seemingly normal embryonic development, but subsequent death at or shortly after birth, in contrast to the heterozygous deletion models, previously examined, which were viable and appeared normal up to at least 12 months of age [310]. Mice with *Fbxw7*^{R482Q} mutation exhibited alveolar thickening, frequent cleft palate, and an eyes-open-at-birth phenotype which was found to associated with dysregulation of the Tgf-β pathway, through accumulation of TGFB induced factor homeobox 1 (Tgif1), and of KLF transcription factor 5 (Klf5), but not Notch1 [310].

Further organ specific studies using missense mutation models have been performed in mouse haematopoietic stem cells and intestine. Intriguingly, both studies highlighted differences between their models of missense mutation and models of deletion. King *et al.*, working in haematopoietic stem cells, reported a differential phenotype to that previously exhibited by *Fbxw7* loss, with a lack of disruption to normal stem cell function and a lower degree of Myc stabilisation than exhibited by homozygous loss [344]. However, the levels of stabilisation were much greater than when compared with heterozygous loss of *Fbxw7* [344]. Increased Myc expression was found to correlate with the number of leukaemia-initiating cells observed, suggesting *Fbxw7* mutation could be a driver of T-ALL independently of loss of p53 [344].

Davis *et al.* also reported a stronger phenotype due to *Fbxw7* mutation in the intestine, with heterozygous missense mutation driving more rapid onset of polyposis compared to heterozygous deletion [297]. In contrast to previous intestinal models, the only dysregulated substrates with heterozygous mutation were Tgif1 and Klf5, and not Notch1 or Ccne1 [297]. However, increased levels of Ccne1 were reported with homozygous missense mutation [297].

To date only one study has been performed examining the role of *Fbxw7* mutation in the mouse endometrium. Cuevas *et al.* generated mice with homozygous deletion of *Fbxw7* in the uterine epithelium, driven by bacterial artificial chromosome (BAC)-small proline rich protein 2F (*Sprr2f*)-Cre, which did not induce a strong phenotype or initi-

ate carcinogenesis [316]. However, when *Fbxw7* loss was combined with homozygous loss of *Pten*, a strong cancer phenotype with reduced survival was apparent alongside promotion of an EMT phenotype [316]. Spontaneous disruption of normal p53 activity (predicted to be due to mutation) was observed in tumours, and these mutations together drove development of tumours with a carcinosarcoma histology [316].

Interestingly, *FBXW7* mutation does occur at a higher frequency in carcinosarcoma, which is characterised by both mixed carcinomatous and sarcomatous histologies, with the origins of the sarcomatous portion believed to be through de-differentiation of an epithelial ancestor; a process in which EMT has been hypothesised to play an important role [91, 93, 345]. Whether FBXW7 has a functional role in this process has yet to be fully established, but when considered together with the Cuevas *et al.* study, there is reasonable evidence that FBXW7 could play a role in the acquisition of this biphasic phenotype. However, this was demonstrated using a model of *Fbxw7* loss, therefore, it remains to be seen whether the same pathways would be dysregulated by missense mutation, which are more common in endometrial cancer.

3.1.4 Motivation for studying *Fbxw7*^{R482Q} in endometrial cancer

As has been shown, mutation of *FBXW7* is a frequent event in EC, but there is a paucity of understanding regarding the role that FBXW7 plays in the endometrium. A single, recent study showed *Fbxw7* loss accelerated carcinogenesis caused by *Pten* loss, often following inactivation of p53 [316]. However, total loss of *Fbxw7* is uncommon in EC with missense mutation being more frequently observed. As noted previously, the patterns of dysregulation that occur between *Fbxw7* loss and missense mutation typically differ, and the function and targets of Fbxw7 show context specificity and variation between different cell and tissue types [346]. It is therefore important to examine the role of Fbxw7 and its mutation in the endometrium, to understand the mechanisms of dysregulation that occur following mutation and determine if these could be targeted to improve EC treatment. To address this, I examined the effects of introducing heterozygous *Fbxw7*^{R482Q} mutation into cells of the mouse uterus. The histological and molecular phenotypes of these mice were compared with those of wild-type mice to

determine the effects of the mutation.

3.2 Materials and methods

3.2.1 Examination of *FBXW7* mutation in TCGA data

The TCGA MC3 mutation data was obtained using the R package "maftools" [347, 348]. UCEC and UCS sample subtype and other clinical information, tumour suppressor gene status, and EC drivers were obtained from cBioPortal, COSMIC, and IntOGen, respectively [349–351]. Data was processed and analysed using the R packages "maftools" and "tidyverse".

3.2.2 Classification of patient mutations for survival analysis

To perform survival analysis, patients first were categorised based on their *FBXW7* mutations. This was performed using a hierarchical system based on the assumption that terminating mutations (nonsense and frameshift) would likely have a stronger effect on protein structure and function compared to missense mutation (Figure 3.1). Missense mutations were then non-exclusively categorised as missense and/or recurrent. Recurrent mutations were defined as the mutations in the top 5 most frequently mutated amino acids, G423, R465, R479, R505, and R689, which together account for over 70% of all missense mutations.

3.2.3 Breeding of experimental mice

For introduction of *Fbxw7* mutation in to mouse models, the Fbxw7^{tm1Itom} allele was used (Figure 3.4A). The experimental mice used for this work were generated following the outlined breeding plan, with breeding performed by Dr David Church (Figure 3.4B).

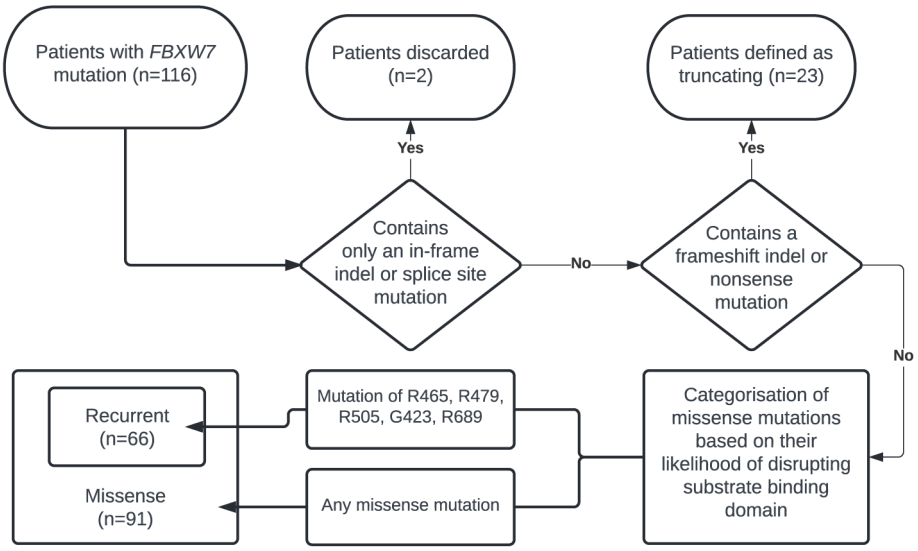

Figure 3.1: Method for classification of the type of *FBXW7* mutation present in cancer from the combined TCGA UCEC and UCS cohorts. Splice site mutations and in-frame indels were discarded unless otherwise indicated.

3.3 Results

3.3.1 Characterisation of *FBXW7* mutational landscape in human endometrial cancer

Examination of the landscape of *FBXW7* mutation in both UCEC (n=531) and UCS (n=57) TCGA cohorts highlights the frequency of mutation in EC, with 18.45% and 38.6% of cases mutated respectively (Figure 3.2A). Comparing frequency of missense and truncating mutation (classified as nonsense and frameshift mutations combined), strongly suggests positive selection for missense mutations over truncating mutations (80.8% vs 17.8%; Figure 3.2B). Additionally, truncating *FBXW7* mutations are most common in the subtypes of EC driven by strong mutational processes. *POLE* mutation generates an increased number of *FBXW7* missense mutations and also generates R/E > * mutations. MMRd induces frameshift insertion/deletions, which often cause premature termination of the CDS. In contrast, the subtypes lacking strong mutational signatures (CN-Low, CN-High, and UCS) have a higher rate of missense mutation, 90%, 87%, and 91.3% respectively (P=0.0019, Fisher Exact test).

To determine if *FBXW7* is enriched for missense mutations, I compared the propor-

tion of missense mutations with that of other tumour suppressor genes. The top 15 most frequently recurrent tumour suppressor genes that had been annotated as a driver of either UCEC or UCS by the IntOGen framework were examined [351]. A noticeable difference in the proportion of missense mutations across these tumour suppressors is apparent, and in this cohort *FBXW7* exhibits the fourth-highest proportion of missense mutations (Figure 3.2D). Furthermore, the *POLE* subtype samples are likely to exhibit a large proportion of passenger mutations, which will greatly inflate the number of both missense and nonsense mutations, due their ultramutated phenotype. If removed from the analysis, *FBXW7* has the second-highest proportion of missense mutations behind only protein phosphatase 2 scaffold subunit alpha (*PPP2R1A*) (Figure 3.2E). Amongst frequently mutated tumour suppressors in EC, *FBXW7* does appear to exhibit a higher than expected frequency of missense mutations which suggests that missense mutation is a stronger driver of carcinogenesis.

Underscoring the importance of hotspot mutations in the substrate binding domain, the top eight most frequently mutated residues are all found within this domain (Figure 3.2C). Conversely to what is observed in other cancer types, R479 is not in the top three mutated residues, instead being 5th overall. However, the two residues ahead, R689 and R658, both exhibit more frequent mutation in the *POLE* subtype which may be over-estimating their importance to carcinogenesis.

Correlation of *FBXW7* mutation with clinicopathological features is not possible with the data available in TCGA due to the unavailability of information regarding invasion, metastasis, and stage, along with heterogeneity between cohorts. However, survival outcomes were available for both UCEC and UCS, which were combined in to a single cohort. Given the possibility of variation in the functional effects of different types of *FBXW7* mutation, the association of missense and truncating mutations with survival were examined separately. *FBXW7* mutation has a limited association with overall survival, comparison of missense mutation versus wild-type (P=0.27, Log-Rank test), truncating mutation versus wild-type (P=1, Log-Rank test), and missense versus truncating (P=0.54, Log-Rank test), indicated no significant differences (Figure 3.3A). When examining disease-specific survival, a slightly stronger association with

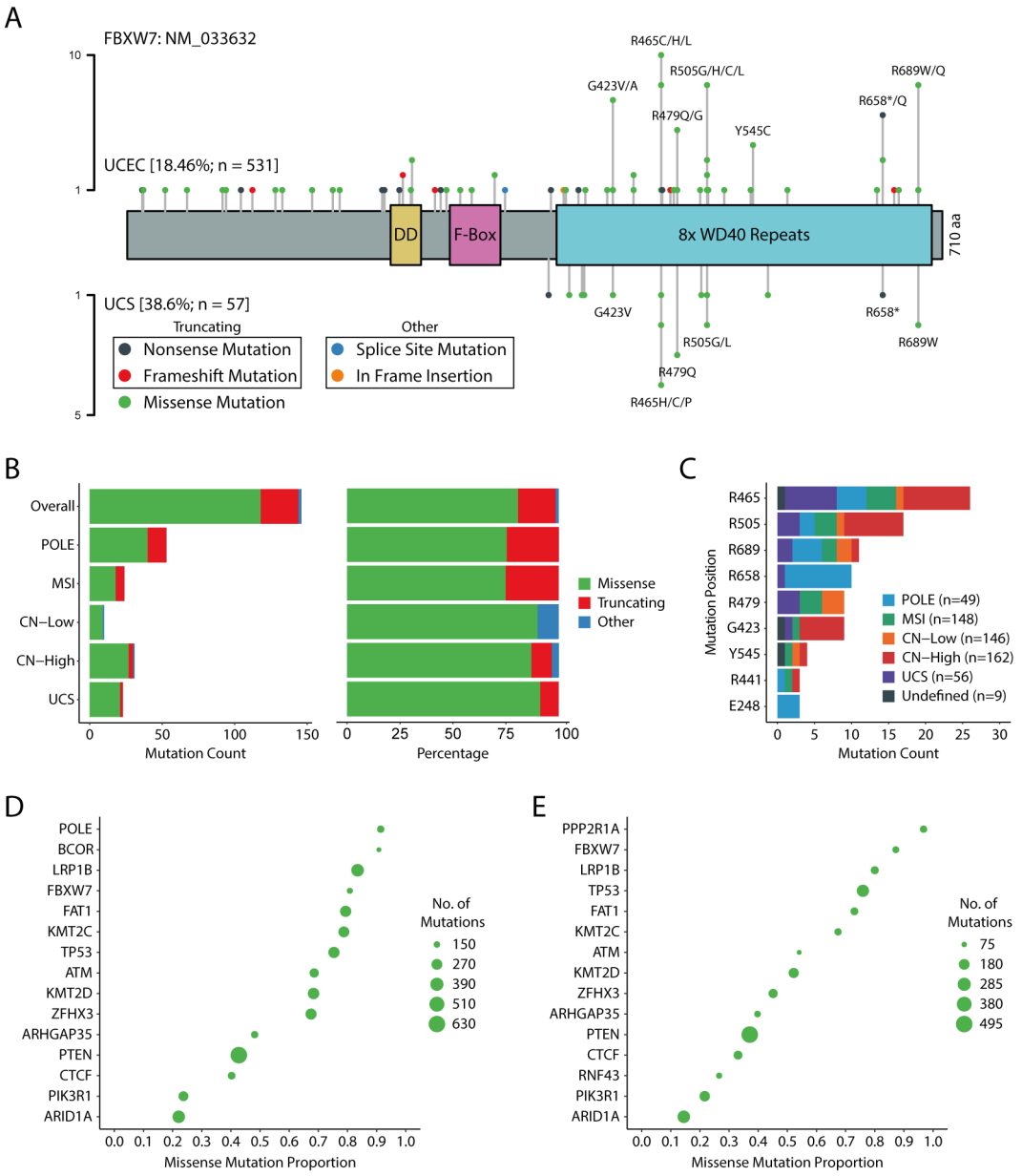

Figure 3.2: Characterisation of *FBXW7* mutations in human endometrial cancers. **A.** Lollipop plot representing the locations and types of *FBXW7* mutations in TCGA UCEC and UCS cohorts. DD refers to the dimerisation domain. **B.** Shows the frequency of each mutation type in endometrial cancer and in each subtype, represented as the total number of mutations in all cancers (left) and as a percentage of the total mutations in that group (right). **C.** Shows the most frequently mutated *FBXW7* amino acids and their frequency in individual subtypes. **D.** Highlights the proportion of missense mutations (from all mutations) of the top 15 most frequently mutated endometrial cancer tumour suppressor genes. **E.** Represents the proportion of missense mutations from the top 15 most frequently mutated endometrial cancer tumour suppressor genes excluding mutations from POLE-ultramutated subtype cancers.

missense mutation can be seen, but this is not statistically significant (P=0.071 vs wild-type, P=0.25 vs truncating group, Log-Rank test; Figure 3.3B). With progression-free survival, a similar trend of slightly worse, but not statistically significant, survival of

patients with missense mutations can be seen (P=0.14 vs wild-type, P=0.12 vs truncating group, Log-Rank test; Figure 3.3C).

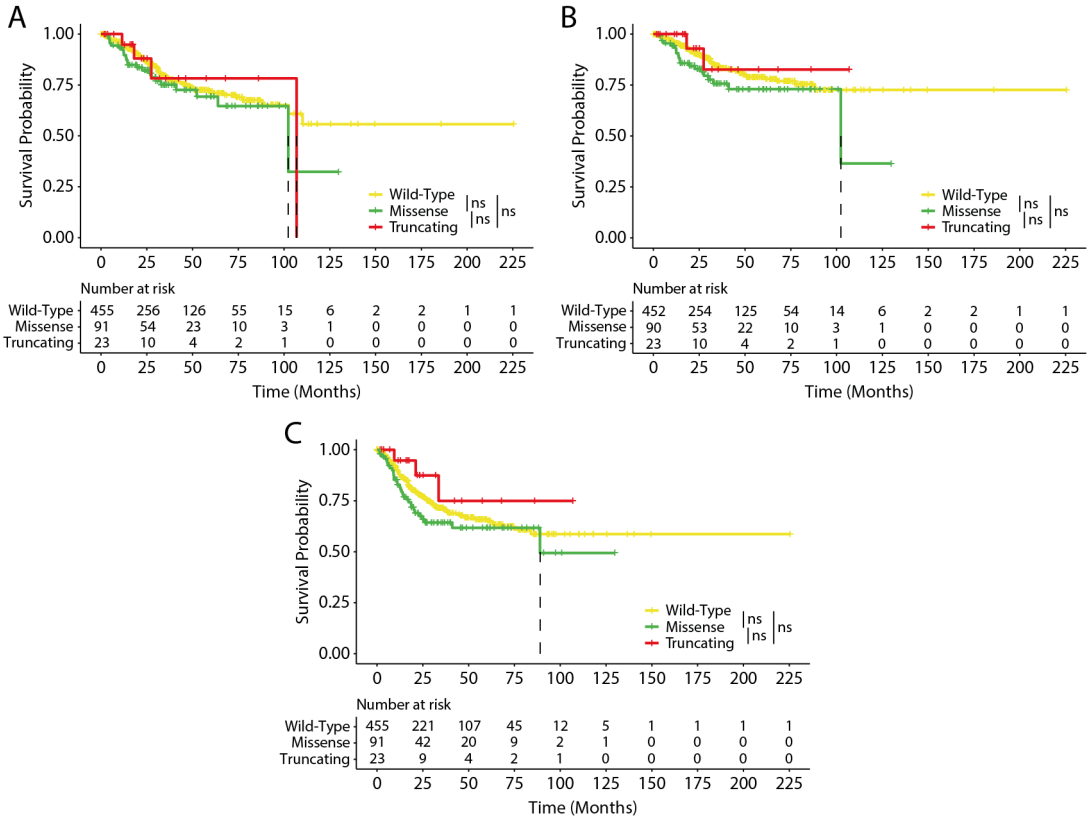

Figure 3.3: Survival analysis of *FBXW7* mutant cancers from the TCGA UCEC and UCS cohorts. **A, B, C.** Show the effect of different classes of *FBXW7* mutation on overall survival - **A**, disease-specific survival - **B**, and progression-free survival - **C**.

3.3.2 Generation of experimental mice and confirmation of allelic recombination and expression of *Fbxw7*^{R482Q} mutation

To investigate the effects of *Fbxw7* missense mutation on uterine carcinogenesis, GEMMs with conditional knock-in mutation of *Fbxw7* directed by Cre expressed from the *Pgr* gene locus (Pgr-Cre) were generated. Once recombined, the *Fbxw7*$^{fl(R482Q)}$ allele drives expression of the *Fbxw7*^{R482Q} mutation in all tissues of the female reproductive system that express *Pgr*. Pgr-Cre driven recombination of loxP sites in these tissues deletes the final three exons of the wild-type *Fbxw7* CDS, which are replaced by a mutagenised copy containing a G to A substitution resulting in expression of *Fbxw7*^{R482Q}, analogous to the human *FBXW7*^{R479Q} mutation. Non-Pgr expressing tissues of will still express

wild-type *Fbxw7* from both alleles. Experimental mice were generated with the following genotypes:

- $Pgr^{cre/+}$ $Fbxw7^{+/+}$ henceforth referred to as $Fbxw7^{+/+}$
- $Pgr^{cre/+}$ $Fbxw7^{fl(R482Q)/+}$ henceforth referred to as $Fbxw7^{R482Q/+}$

Females were culled at 4 and 8 weeks of age for phenotypic analysis and a further cohort was aged until survival endpoint (abdominal distension, bleeding from the vagina, other signs of ill-health or 18 months of age).

Genotypes of the generated mice were determined by PCR of DNA from superficial tissue with amplification targeted over an inserted loxP site. The presence of a wild-type and a mutant allele in the $Fbxw7^{R482Q/+}$ mice and a single band indicating two wild-type alleles in the $Fbxw7^{+/+}$ mice confirmed the correct genotypes (Figure 3.4C). Additionally, successful recombination of the allele was seen from the presence of a band after amplification of uterine DNA using recombination-specific primers, where band formation is only possible after recombination due to the distance between the primers in the unrecombined allele. In order to ensure expression of the $Fbxw7^{R482Q}$ mutation, Sanger sequencing of cDNA generated from uterine tissue was performed. In $Fbxw7^{+/+}$ mice the expression of wild-type *Fbxw7* was observed, whereas, in $Fbxw7^{R482Q/+}$ mice both the wild-type and the mutant allele were expressed (Figure 3.4D).

3.3.3 Overall survival is unaffected by endometrial $Fbxw7^{R482Q/+}$ mutation

To determine if heterozygous $Fbxw7^{R482Q}$ mutation leads to reduced overall survival, mice of both genotypes were aged until phenotypic development or 18 months of age. Comparison of the survival probability of the two groups showed no significant difference (P=0.45, Log-Rank test; Figure 3.5). In both cohorts very few mice displayed any adverse phenotypes and median survival was not reach in either group.

3.3.4 $Fbxw7^{R482Q/+}$ mutation does not alter endometrial histology

To examine the effects of $Fbxw7^{R482Q}$ mutations on uterine histology, FFPE tissue samples, collected at 4 weeks, 8 weeks and survival endpoint, were stained with H&E and

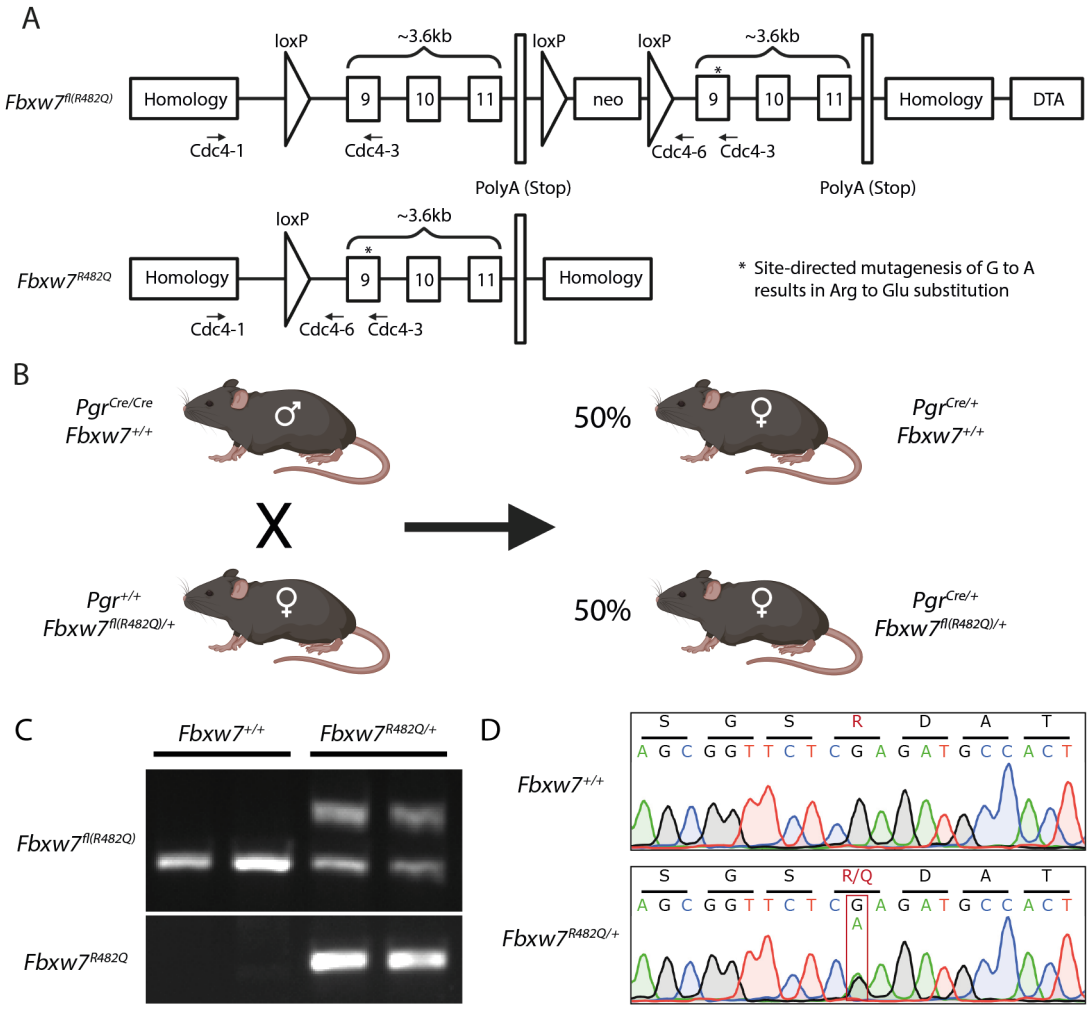

Figure 3.4: Schematic of *Fbxw7*$^{fl(R482Q)}$ allele, breeding program for mice used and confirmation of mouse genotypes and allelic recombination. **A.** Diagrammatic representation of the *Fbxw7* knock-in mutation allele used for generation of experimental mice. Panel is adapted from [310] **B.** Breeding program used to generate experimental mice, the percentage refers to the proportions of the female offspring and disregards the male offspring. **C.** Agarose gels from genotyping PCRs of experimental mice. The top panel represents the presence of the floxed allele (larger band) or wild-type allele (smaller band) and the bottom panel represents successful recombination in the uterus. **D.** Electropherograms representing the sequence of *Fbxw7* in RNA extracted from the uteri of experimental mouse, which highlights the heterozygous expression of the R482Q mutation.

for keratin 8 (Krt8), a cytoskeletal marker of columnar epithelium (Figure 3.6). The staining patterns for both H&E and Krt8 exhibited no apparent difference in intensity or localisation. Examination of H&E-stained sections by expert gynaecological pathologists blinded to genotype (Dr Tjalling Bosse and Dr Alicia Leon-Castillo) revealed no difference in the histology of *Fbxw7*^{R482Q} and wild-type uteri (Figure 3.7). All samples at both 4 weeks (*Fbxw7*$^{+/+}$= 3; *Fbxw7*$^{R482Q/+}$= 3) and 8 weeks (*Fbxw7*$^{+/+}$= 3; *Fbxw7*$^{R482Q/+}$= 3) of age, in both genotypes, were annotated as having normal uterine histology. Fur-

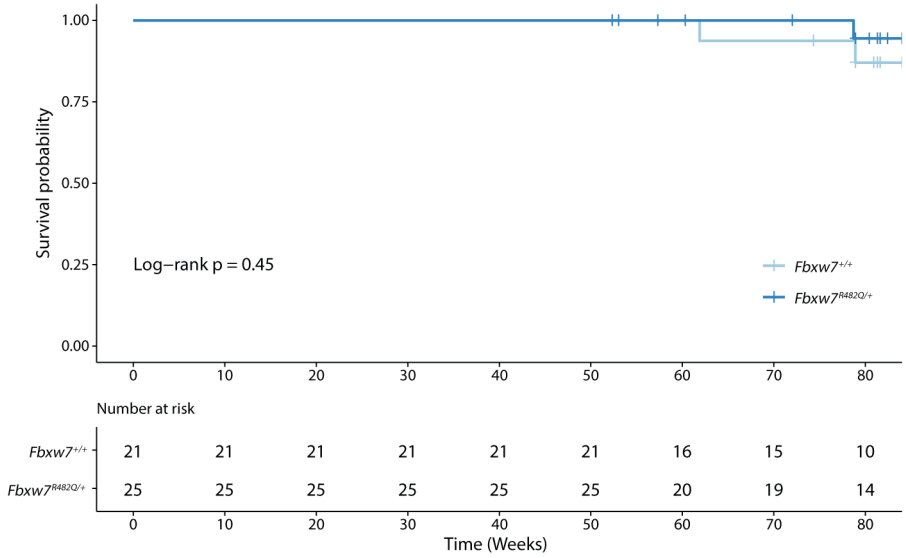

Figure 3.5: Survival analysis of *Fbxw7*$^{+/+}$ and *Fbxw7*$^{R482Q/+}$ mice. Kaplan-Meier estimator analysis of the effects of *Fbxw7*$^{+/+}$ and *Fbxw7*$^{R482Q/+}$ genotypes on overall survival of mice aged until they reached a survival end point.

thermore, the uteri of mice at survival end point also exhibited normal uterine histology (*Fbxw7*$^{+/+}$= 20; *Fbxw7*$^{R482Q/+}$= 24). The only histological features noted were cystically dilated lumen in two of the *Fbxw7*$^{R482Q/+}$ samples and borderline hyperplasia, but within normal range for two *Fbxw7*$^{R482Q/+}$ samples. However, these were not deemed to be evidence of uterine pathology as they were not sufficiently deviant from features found in normal uterine tissue.

3.3.5 Transcriptional changes evident at 4 weeks but not 8 weeks after endometrial *Fbxw7*$^{R482Q/+}$ mutation

As no gross histological changes were observed, I wanted to examine the transcriptional landscape for any effects of *Fbxw7*^{R482Q} mutation. Initially, *Fbxw7* expression was examined to determine if compensatory upregulation may be occurring, alongside *Pten* and *Trp53* as two of the most important tumour suppressors in EC. Expression of these genes was examined by RT-qPCR in cDNA generated from bulk, fresh frozen, uterine tissue taken from mice at 4 weeks and 8 weeks of age. Interestingly, *Fbxw7* expression was significantly increased in uteri of *Fbxw7*$^{R482Q/+}$ mice at 4 weeks of age (median $\log_2$(fold change) 0.910 vs wild-type, P=0.032 Wilcoxon Rank Sum test), as was expression of

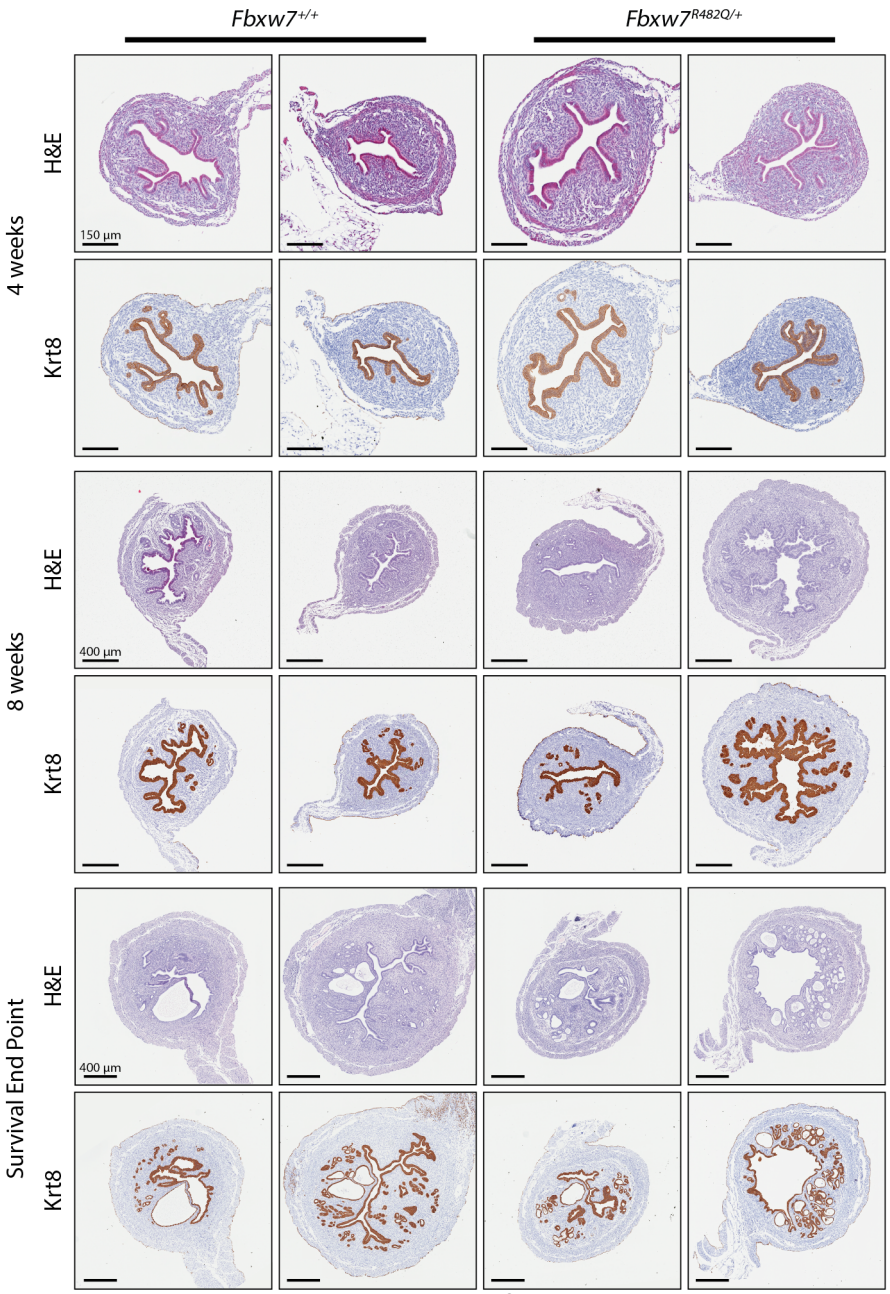

Figure 3.6: Uterine histology of mice expressing *Fbwx7*^{R482Q} mutation. H&E and Krt8 (epithelial marker) staining of FFPE sections from *Fbwx7*$^{+/+}$ and *Fbwx7*$^{R482Q/+}$ mice at 4 weeks (top), 8 weeks (middle), and survival end point (bottom).

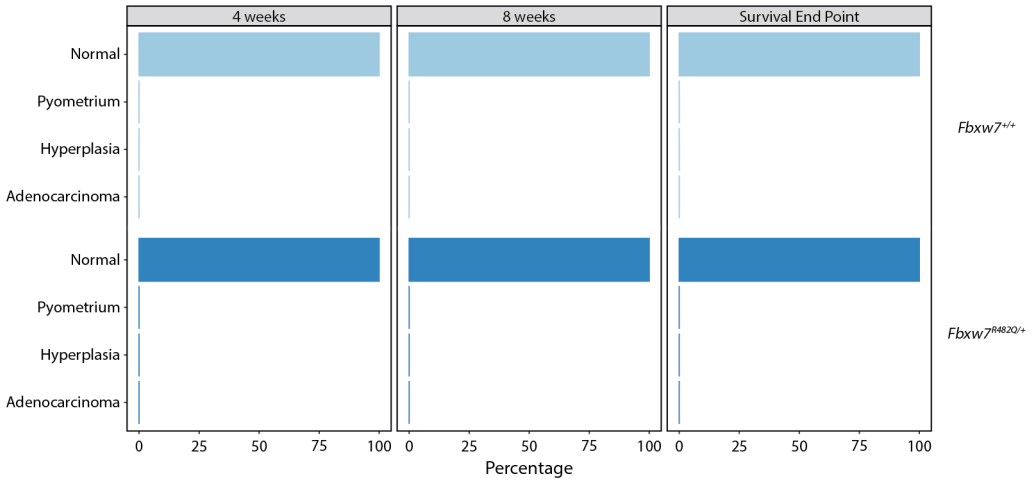

Figure 3.7: Expert pathological review of mice expressing *Fbwx7*^{R482Q} mutation in the uterus. Bar plot of the proportions of diagnosed uterine pathology following expert assessment of H&E-stained, FFPE sections from mice at all time points. Number of mice analysed *Fbxw7*$^{+/+}$: 4w = 3, 8w = 3, survival end point = 20; *Fbxw7*$^{R482Q/+}$: 4w = 3, 8w = 3, survival end point = 24.

Trp53 (median $\log_2$(fold change) 0.552 vs wild-type, P=0.032 Wilcoxon Rank Sum test), whereas, *Pten* expression was not significantly altered (median $\log_2$(fold change) 0.145 vs wild-type, P=0.15 Wilcoxon Rank Sum test; Figure 3.8A). By 8 weeks of age these differences in expression were no longer apparent and the expression of *Fbxw7* and *Trp53* in *Fbxw7*$^{R482Q/+}$ uteri was not significantly different to wild-type (Figure 3.8B).

To examine more broadly any transcriptional changes occurring in these samples, RNA from bulk, fresh frozen tissue taken from mice at 8 weeks and was examined by RNA microarray. In this method, RNA was converted to cDNA and hybridised with an array of immobilised probes representing CDSs of numerous genes, successful hybridisation results in fluorescence signal, which can be determined as a measure of gene expression. Although expression of the genes highlighted were significantly altered in unadjusted analysis, this did not hold after adjusting for multiple testing (Figure 3.8C).

3.3.6 Noted targets of *Fbxw7* do not exhibit dysregulation after mutation

As direct regulation by Fbxw7 occurs at the post-translational level, I wanted to examine protein expression of previously identified targets of Fbxw7, in addition to notable proteins in tumour suppressive/oncogenic pathways in EC. To do this I examined uteri from mice at 8 weeks of age. Examination of the PI3K-pathway found strong Pten stain-

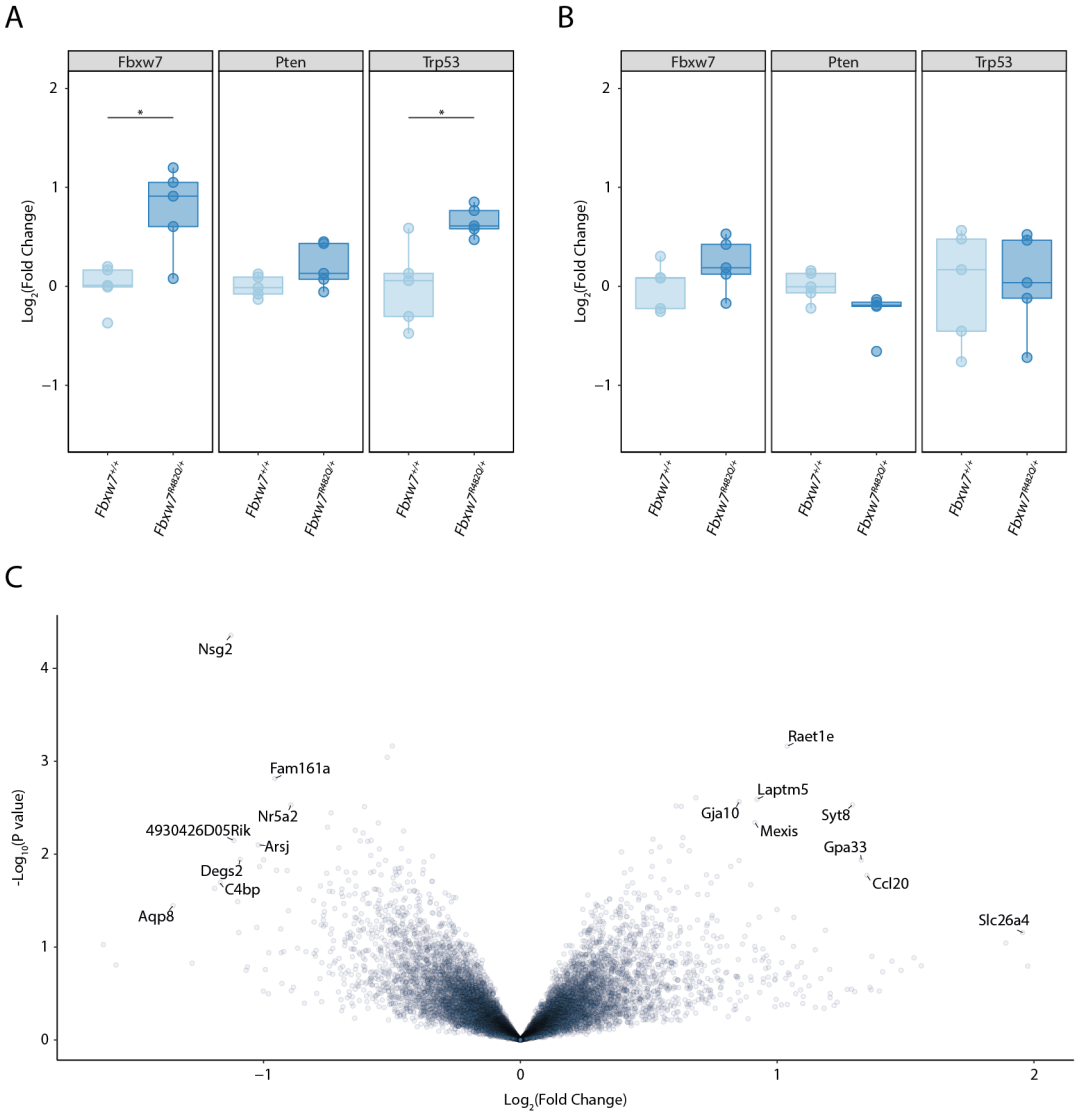

Figure 3.8: Targetted and agnostic examination of transcription changes in the uterus of mice expressing *Fbwx7*^{R482Q} mutation. **A, B.** Examination of *Fbxw7*, *Pten*, and *Trp53* gene expression in the uteri of *Fbwx7*$^{+/+}$ and *Fbwx7*$^{R482Q/+}$ mice at 4 weeks - **A**, and 8 weeks - **B**. Gene expression was determined using RT-qPCR, results are expressed as Log_2(Fold Change) relative to *Fbwx7*$^{+/+}$. **C.** Volcano plot showing the results of differential gene expression analysis performed on RNA microarray expression data generated from bulk RNA extracts from fresh frozen uteri, taken at 8 weeks, of *Fbwx7*$^{+/+}$ and *Fbwx7*$^{R482Q/+}$ mice.

ing and absent or weak p-Akt staining apparent in the epithelium and stroma of mice with no differences between *Fbxw7*$^{+/+}$ and *Fbxw7*$^{R482Q/+}$ genotypes (Figure 3.9A). Expression of p53 was absent from the stroma with only weak cytoplasmic staining present in epithelium, and no differences between the two groups. Ccne1 exhibited weak cytoplasmic staining in epithelial cells and was mostly absent from stromal cells, except for a few samples that had weak staining, however, this again was not different between the two genotypes.

In order to examine potential loss of regulation of known Fbxw7 targets following *Fbxw7*^{R482Q}, western blot analysis of protein extracted from bulk, fresh-frozen uterine tissue collected at 8 weeks was performed to determine the expression of Ccne1, Jun, Myc, and Notch1 (Figure 3.9B). Most proteins investigated exhibited stable expression across both genotypes, with Myc expression found to be the most variable. Nevertheless, this variation did not correlate with mouse genotype. Densitometry analysis of the western blots indicated that there were no significant differences in any of the examined targets (Figure 3.9C).

Interestingly, at survival endpoint, p-Akt staining was apparent in basal glands (closest to the myometrium) in both *Fbxw7*$^{+/+}$ and *Fbxw7*$^{R482Q/+}$ samples (Figure 3.10). However, the staining in *Fbxw7*$^{R482Q/+}$ samples appeared more intense and widespread with most basal glands staining positive for active Akt, whereas in the *Fbxw7*$^{+/+}$ samples positive glands were more sparse and sporadic. Alongside the glandular positivity for p-Akt was increased intensity of Pten staining, which was evident in both genotypes. Notably, the increased staining in these glands appeared heterogeneous with not all cells expressing higher levels of Pten. Luminal epithelium and p-Akt negative glands displayed lower levels of Pten expression, which was mainly constrained to the cytoplasm, analogous to that observed in the 8-week samples. Concomitant with the p-Akt positive glands, nuclear p53 expression was seen, which again appeared to be heterogeneous in the cells of the gland. Similarly to p-Akt expression, this also appeared to be more frequent and with higher intensity in the *Fbxw7*$^{R482Q/+}$ mice, although the staining was not quantified to confirm this. Unfortunately, due to the serial nature of the sections, it was possible to see that cellular expression these targets but not whether they

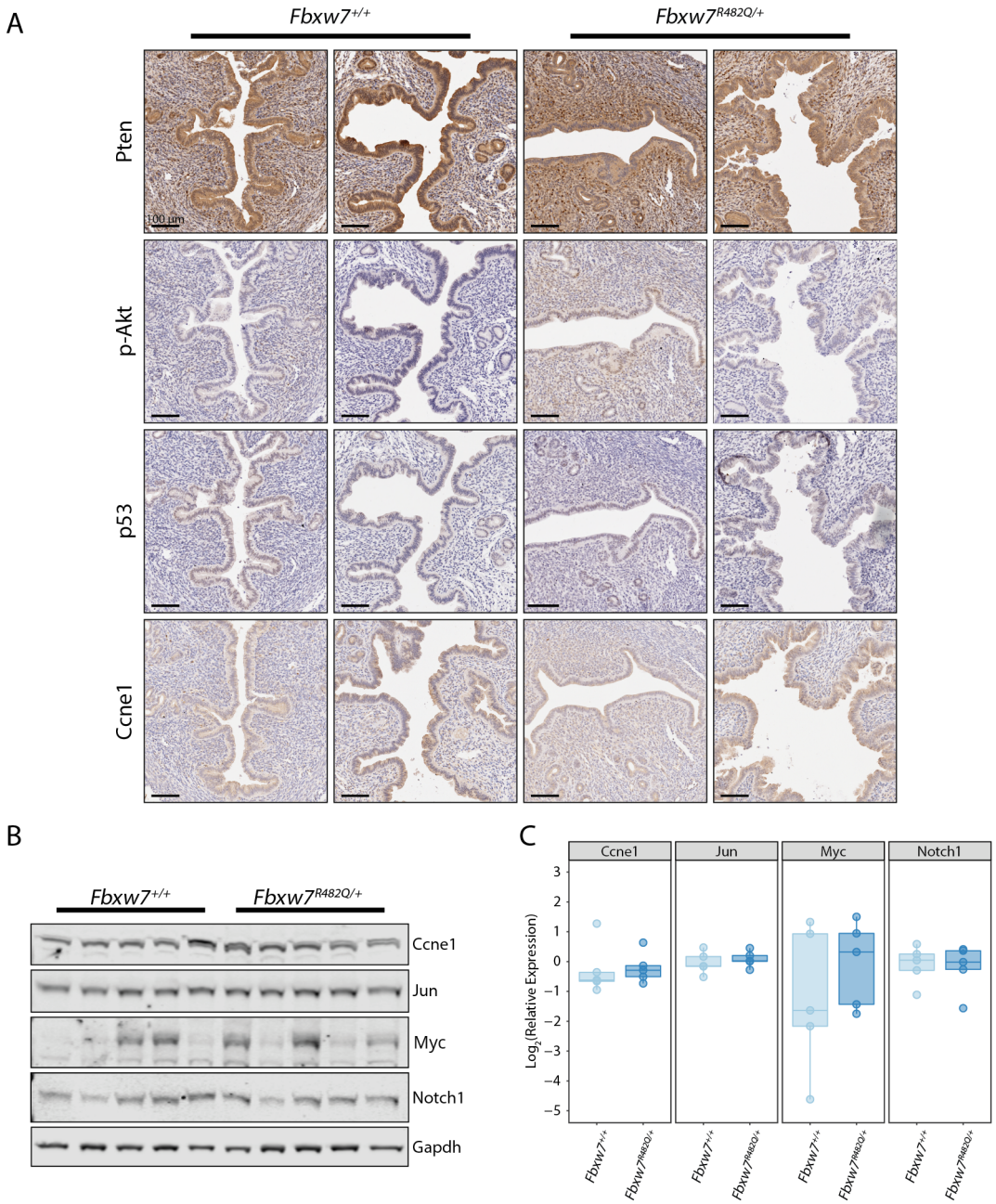

Figure 3.9: Examination of protein changes in the uterus of mice at 8 weeks. **A.** IHC staining for Pten, p-Akt, Trp53, and Ccne1 in FFPE section of the uterus of *Fbxw7*$^{+/+}$ and *Fbxw7*$^{R482Q/+}$ mice at 8 weeks. **B.** Western blotting analysis of Ccne1, Jun, Myc, and Notch1 from protein lysates extracted from fresh frozen uteri, taken at 8 weeks, from *Fbwx7*$^{+/+}$ and *Fbxw7*$^{R482Q/+}$ **C.** Densitometry measure of target expression in the two genotypes. Log_2(Fold Change) is calculated relative to *Fbwx7*$^{+/+}$ mice after normalising for Gapdh expression.

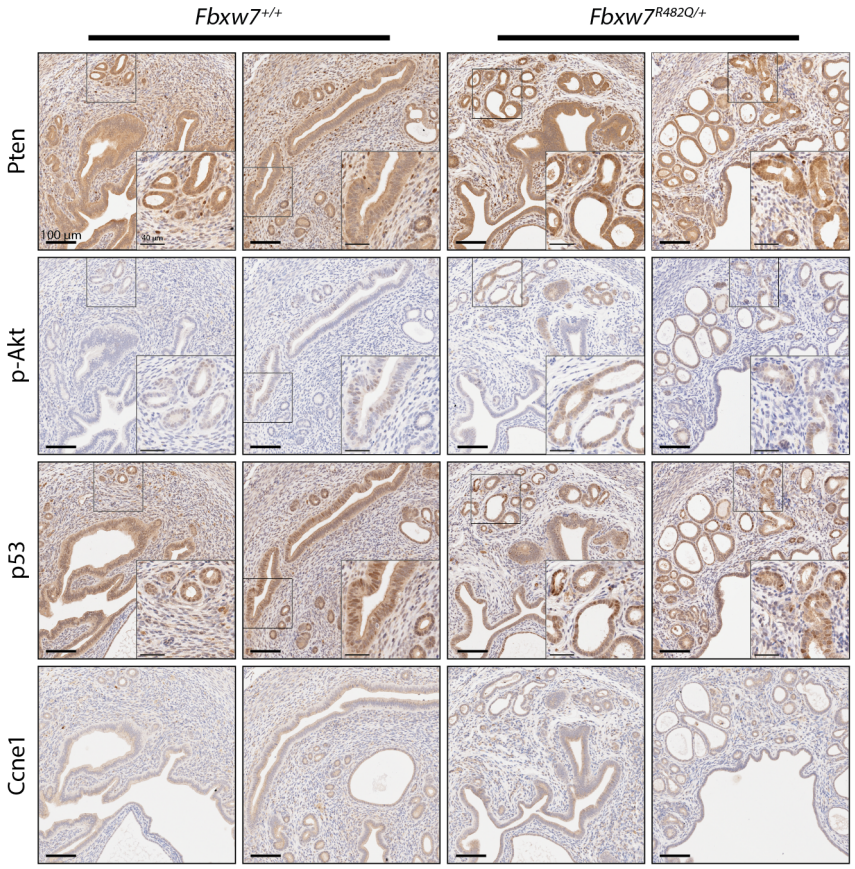

Figure 3.10: Examination of protein changes in the uterus of mice at survival end point. IHC staining for Pten, p-Akt, Trp53, and Ccne1 in FFPE section of the uterus of *Fbxw7*$^{+/+}$ and *Fbxw7*$^{R482Q/+}$ mice collected at survival end point.

were co-expressed in any particular cell. Conversely, Ccne1 did not show evidence of altered expression or localisation in glands showing positivity for p-Akt in either genotype and there was no evidence of altered expression between the genotypes.

3.4 Discussion

FBXW7 mutation is frequent in EC. However, the work shown in this chapter indicates that alone *Fbxw7*^{R482Q} mutation is insufficient to cause carcinogenesis in the mouse uterus. In fact, *Fbxw7*^{R482Q} mutation alone induces little disruption to the normal uterine state, aside from transient increases in expression of *Fbxw7* and *Trp53* at 4 weeks of age, which were subsequently lost at 8 weeks, and some potential differences in expression of p-Akt at survival end point. There were no other major changes to histology or to RNA and protein expression of major Fbxw7 substrates observed following *Fbxw7*^{R482Q}

mutation, and uterine pathology and survival outcome were not altered in *Fbxw7*$^{R482Q/+}$ mice. These findings correlate with the recently published work of Cuevas *et al.*, who modelled *Fbxw7* loss in the uterine epithelium and also concluded that *Fbxw7*$^{-/-}$ was insufficient to drive carcinogenesis [316].

The lack of uterine pathology following *Fbxw7*^{R482Q} mutation correlates with recent publications showing a range of cancer-associated mutations exhibiting positive selection in histologically normal endometrium in humans [352–354]. Furthermore, sequencing of individual endometrial glands highlighted identical mutation spectrums in spatially distinct glands, with mutant allele frequencies often approaching 50%. This suggests that clonal expansion of the mutant cell and colonisation of the regional glandular structures may be occurring [354]. It has therefore been postulated that these cancer-associated mutations may provide a selective advantage, such as enhancing proliferation, that could benefit the fitness of the cell and facilitate colonisation.

FBXW7 have been frequently observed amongst those genes showing positive selection for mutation in normal endometrial tissue and mutations are observed at moderate to high frequency, with 21%-29% of women exhibiting *FBXW7* mutation in at least one gland. Interestingly, the reported mutations tend to exhibit more variety than those found in EC but mutations in the substrate binding domain, including the arginine hotspots, were reported [352–354]. The presence of *FBXW7* mutation in histologically normal tissue supports the observations of this chapter, that alone mutation does not drive cancer development. However, the positive selection of these mutations suggest their effects may not be completely benign, and they may be capable of providing a subtle growth or survival advantage to the cells they occur in, thereby promoting colonisation.

As *FBXW7* plays an important role in regulation of many growth-promoting proteins, it could be hypothesised that cells that acquire mutations in the gene would be provided with a survival or growth benefit. This would potentially prime these cells to colonise areas of the endometrium during the recurring cycles of wounding and healing that occur naturally during the menstrual cycle. This effect may be represented by the potentially increased expression of p-Akt observed in *Fbxw7*$^{R482Q/+}$ mice at survival

endpoint, although quantification would be required to accurately determine if p-Akt expression is increased at this time point. The mice at this time point were around 80-85 weeks of age, at which point they would have entered reproductive senescence, which occurs between 36-52 weeks of age and would no longer be subject to oestrous cycling, meaning those differences in expression could be indicative of proliferative effects of *Fbxw7*^{R482Q} [355].

The over-representation of *FBXW7* mutations in both normal uterine tissue and EC formulate a hypothetical role for *FBXW7* in formation and development of pre-cancerous lesions, potentially by creating a field cancerisation effect by promoting cellular characteristics that allow for clonal expansion across a region of the endometrium. For this to function as a form of field cancerisation, these areas of colonised gland would need to be at greater risk of development in to EC. There is support in the literature for the early involvement of *FBXW7* in endometrial cancer development, which comes from Gerstung *et al.*'s report, performed as part of the Pan-Cancer Analysis of Whole Genomes (PCAWG) collaboration, examining the evolutionary timing of mutations in numerous cancer types [356]. The study highlighted *FBXW7* as an early/clonal mutation in both colorectal adenocarcinoma and endometrial adenocarcinoma [356]. If *FBXW7* mutation was able to co-operate with a secondary, tertiary or other additional hit in the affected gland structure, the mutations together may be able to potentiate development of EC.

3.4.1 Future directions

While it appears that *FBXW7* mutation does not drive carcinogenesis in isolation, there are still remaining questions regarding its role in normal endometrial epithelium and its potential collaborative role in carcinogenesis through co-operation with other cancer mutations. Further characterisation of cells containing *FBXW7* mutation would be vital for determining if it has a functional role in promoting clonal expansion. This could be examined with the use of the GEMMs. Unfortunately, due to the Pgr-Cre used in this work it is not possible to examine the potential for glandular colonisation of *Fbxw7*$^{R482Q/+}$ cells in the uterus, as the mutation is recombined in all cells of the

uterus. However, this could be examined using lineage tracing models in mice, utilising a Tet-On system to control expression of Cre coupled with the reverse tetracycline transactivator (rtTA) inserted to a genetic locus to restrict expression of the Cre to uterine epithelium, as described in [130]. Using this system expression of the *Fbxw7*^{R482Q} mutation and a cell marker (such as EYFP or LacZ) could be induced in a small proportion of uterine epithelial cells by administration of a single, low dose of doxycycline [130]. This system would allow monitoring of the expansion of *Fbxw7*^{R482Q} cells over time and would highlight apparent clonal expansion if occurring.

Additional *in vitro* experiments could be performed to help elucidate the role of *FBXW7* in normal endometrium. Of particular interest would be the examination for differences in response of cells harbouring mutation to the effects of treatment with oestrogen and progesterone, which could highlight pathways that might facilitate clonal expansion. Utilising resources such as a recently published "normal" endometrial epithelial cell line to generate isogenic cell lines containing common *FBXW7* mutations would allow such investigations. Alternatively, this could be investigated using the *Fbxw7*^{R482Q} allele described in this chapter. If combined with an inducible Cre, such as the tamoxifen-inducible CMV early enhancer/chicken beta actin (CAG)-Cre, uterine tissue could be collected from these animals and dissociated for *in vitro* culture with subsequent recombination driven by treatment with tamoxifen, thus allowing isogenic comparison of cellular phenotypes. While these experiments were beyond the scope of this thesis, they would provide a better understanding of the role that FBXW7 plays in the normal function of uterus and how its mutation would alter the characteristics of the cells in which it manifests.

Chapter 4

Functional characterisation of *Fbxw7*$^{R482Q/+}$ in combination with *Pten* loss in the mouse uterus

4.1 Introduction

As shown in the previous chapter, *FBXW7* mutation is common in endometrial cancer, but alone is insufficient to cause cancer in the mouse uterus. However, cancer rarely, if ever, occurs as the result of a single mutation, with multiple mutations typically being required to induce carcinogenesis. Examining how *Fbxw7* mutation interacts with other common EC mutations would advance understanding of the role of *Fbxw7* mutation in carcinogenesis.

4.1.1 Dysregulation of PI3K pathway genes are a common feature of endometrial cancer

As discussed, in Section 1.3, the PI3K pathway is one of the most commonly dysregulated pathways in human cancer and components of this pathway are among the most frequently mutated in EC. Mutation of *PTEN* is found in around 62% of all EC [90, 91]. However, a difference in *PTEN* mutation frequency is reflected in the TCGA-based

molecular classification, which indicates mutation frequencies of 94%, 87%, and 76% in the *POLE*-mutated, MSI, and CN-low subtypes, respectively, whereas, the mutation rate in CN-high and carcinosarcoma subtypes is only 10% and 19%, respectively [90, 91]. Despite this variation, *PTEN* mutation has been identified as a driver in all EC subtypes [90, 93]. Interestingly, studies examining *PTEN* mutation in endometrial hyperplasia have found variable rates between 9-47% of patients [357–359]. The lower frequency of mutation in hyperplasia may indicate that *PTEN* mutation plays an important role in transformation from precursor to cancerous lesion, and a retrospective study did observe that *PTEN* mutation was more common in patients that progressed to cancer than those that did not (60% vs 35%) [359].

Multiple other PI3K pathway components are significantly mutated in EC, including *PIK3CA*, *PIK3R1*, *PPP2R1A*, and inositol polyphosphate phosphatase like 1 (*INPPL1*). *PIK3CA* is the second most commonly mutated PI3K pathway component in EC, found in 53% of cases [90]. Interestingly, *PIK3CA* mutation frequency across EC subtypes is less variable than *PTEN* with 70%, 53%, 53%, 46%, and 35% in *POLE*-mutated, MSI, CN-low, CN-high, and carcinosarcoma, respectively [90, 91]. *PIK3R1* exhibits a mutation pattern similar to *PTEN* with higher frequency in type I cancers (*POLE*-mutant, MSI, CN-low) and is among the top 5 most frequently mutated genes in EC, with an overall mutation rate of 32% [161]. Both *PPP2R1A* and *INPPL1* are more associated with type II cancer (CN-high and carcinosarcoma), and were not found to be significantly mutated in any of the *POLE*-mutant, MSI or CN-low subtypes [90, 91]. *PPP2R1A* is significantly mutated in CN-high cancers (21%) and in carcinosarcoma (28%), whereas, *INPPL1* was found to be significantly mutated only in carcinosarcoma (24%) [90, 91, 93].

4.1.2 PI3K pathway alterations in normal endometrium

Interestingly, alterations of PI3K pathway components are also found frequently in normal human endometrium. Several studies have identified significant enrichment of *PIK3CA*, *PIK3R1*, and *PPP2R1A* mutations in histologically normal endometrium [352, 353, 360]. *PIK3CA* was identified as the most commonly mutated gene, being identified in 41-54% of cases [352, 353]. Both *PIK3R1* and *PPP2R1A* exhibit mutation frequencies

similar to those detected in EC, 34% and 10%, respectively [352].

Notably, these studies reported that *PTEN* mutations are mostly absent from normal endometrial epithelium [352, 353, 360]. Moore *et al.* reported heterozygous mutations in less than 2% of samples and Suda *et al.* reported mutations in 10% of patients evaluated, but did not determine the zygosity of these mutations [352, 353]. Although low rates of mutation were reported in these studies Lac *et al.* also performed immunostaining for *PTEN* and noted clusters of glandular epithelium exhibiting focal loss of PTEN expression [360]. This loss was observed in 27% of cases with simultaneous mutation reported in just one case [360]. Therefore, factors aside from mutation alone could contribute to the loss of PTEN. However, even considering this, the frequency of mutation or expression loss is much lower than *PTEN* mutation in EC, suggesting these changes may be a vital aspect of carcinogenic initiation.

4.1.3 The Wnt pathway

The Wnt pathway plays a vital role in the homeostasis and maintenance of many tissues and cells of the body and is particularly linked to stem cell maintenance and fate decisions (Figure 4.1) [361]. In the inactive state, CTNNB1 is predominantly located at the plasma membrane as a component of adherens junctions or in the cytoplasm. When in the cytoplasm it is primed for ubiquitination by a multicomponent destruction complex consisting of APC, AXIN, casein kinase 1 (CK1)-family kinases, and GSK3, following which it is targeted for degradation by β-TrCP [361]. The pathway is activated by interaction of secreted Wnt ligands in the local extracellular environment, which can bind with transmembrane frizzled (FZD) and low density lipoprotein receptor-related protein (LRP)-family receptors [361]. Ligand-receptor binding allows intracellular recruitment of dishevelled (DVL), which can further recruit key components of the destruction complex to the plasma membrane, abrogating their regulation of CTNNB1 and allowing its accumulation in the nucleus [361]. The main effect of pathway activation is the translocation of CTNNB1 from the cytoplasm to the nucleus, where it can interact with TCF/LEF family members (LEF1, transcription factor 7 (TCF7), transcription factor 7 like 1 (TCF7L1), and TCF7L2) to modify expression of various target genes.

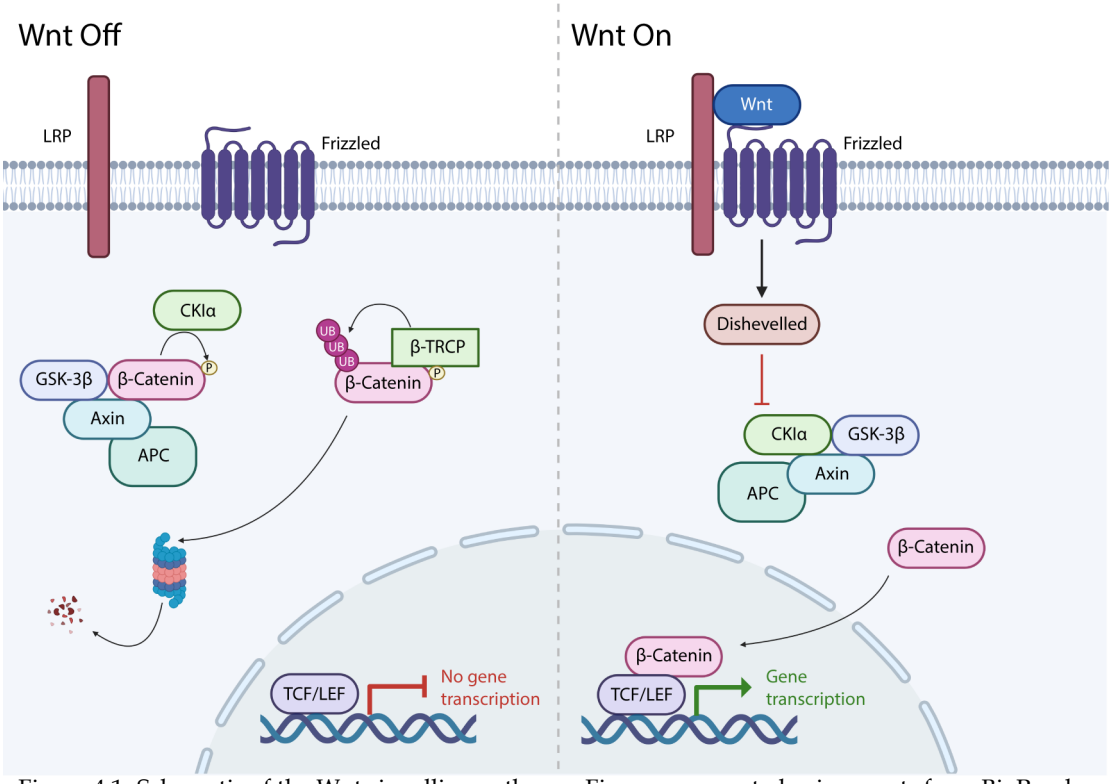

Figure 4.1: Schematic of the Wnt signalling pathway. Figure was created using assets from BioRender

4.1.4 The Hippo pathway

The Hippo pathway is a conserved pathway that dictates the extent of tissue growth, with Yes1 associated transcriptional regulator (YAP1) and WW domain containing transcription regulator 1 (WWTR1) (commonly referred to as TAZ) as the key effectors of the pathway [362]. When not phosphorylated, these factors translocate from the cytoplasm to the nucleus to complex with and activate the TEA domain transcription factor (TEAD)-family transcription factors (Figure 4.2) [362]. Activation of the pathway triggers a kinase cascade involving the phosphorylation of large tumor suppressor kinase 1 (LATS1)/2 by upstream kinases, such as the mammalian STE kinase 1 (MST1)/2-salvador homolog 1 (SAV1) complex or mitogen-activated protein kinase kinase kinase kinases (MAP4K) [362]. This event allows interaction of LATS1/2 with MOB kinase activator 1 (MOB1) and YAP1/WWTR1 driving phosphorylation of the latter. Phosphorylation of YAP1/WWTR1 blocks their translocation to the nucleus either by allowing proteasomal degradation or interaction with cytoplasmic factors, such

as 14-3-3 proteins [362]. The net result of pathway activation is to prevent the transcriptional activity of YAP1 and WWTR1, thereby constraining cell proliferation [362].

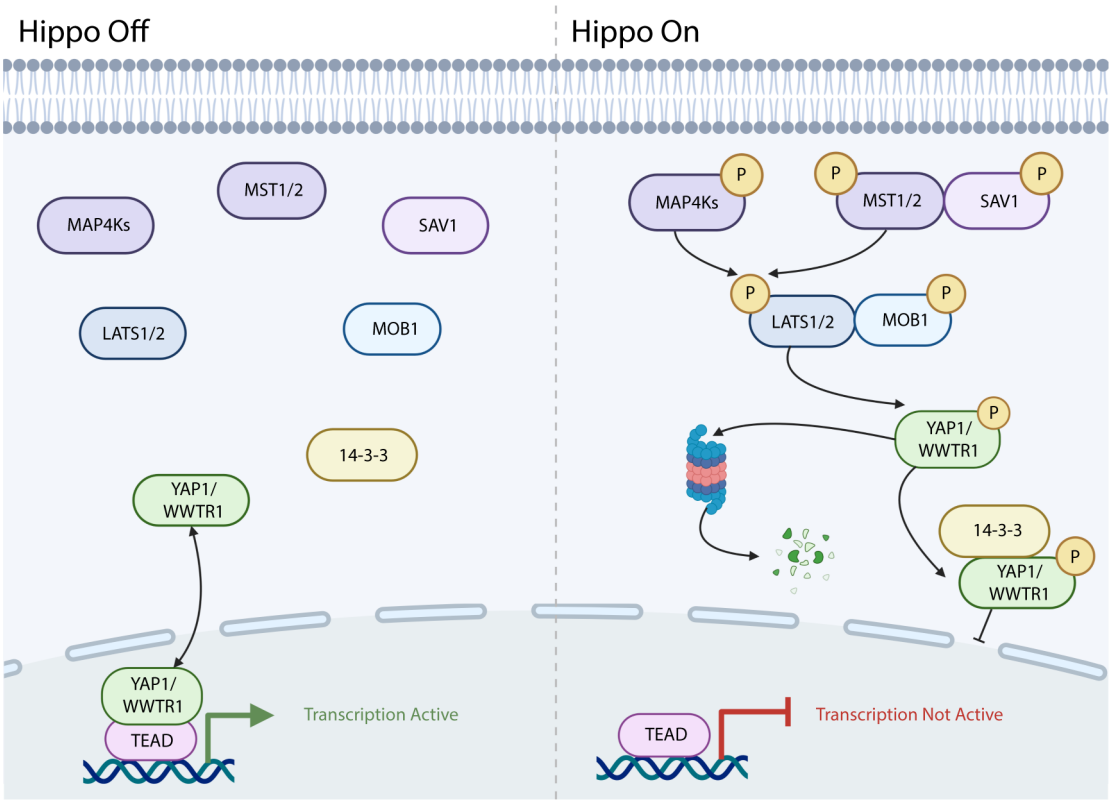

Figure 4.2: Schematic of the Hippo signalling pathway. Figure was created using assets from BioRender

4.1.5 Functional characterisation of PI3K-pathway activation in the endometrium

4.1.5.1 Modelling of *Pten* loss in murine systems

Several studies have examined the effect of *Pten* loss in the various compartments of the murine uterus. The first report of this by Daikoku *et al.* used *Pgr*-Cre to drive homozygous *Pten* deletion in the entire uterus, which resulted in endometrial cancer development at an early age with the uterine epithelium characterised by squamous metaplasia [126]. This study was followed up by targeted deletion of *Pten* from the stroma and myometrium, through use of *Amhr2*-Cre, but with epithelial expression remaining intact. Interestingly, deletion of *Pten* in this manner did not result in formation of endometrial cancer, although infrequent endometrial hyperplasia was observed [127]. Finally, deletion of *Pten* from the endometrial epithelium only was performed, through use of

Ltf-Cre [128]. Surprisingly, these mice rarely developed endometrial cancer, but did exhibit frequent endometrial hyperplasia [128].

4.1.5.2 Modelling of other common PI3K pathway mutations in murine systems

The importance of *Pik3ca* in glandular epithelium has been highlighted by a study examining the deletion of the gene in the uterus, which results in a lack of gland formation [363]. Interestingly, induction of the activating $Pik3ca^{E545K}$ mutation in the endometrial epithelium had no effect on uterine histology [364]. The lack of a phenotype is perhaps surprising considering its mutation frequency in EC, however, this observation does align with frequent *PIK3CA* mutation in histologically normal uterine glands in humans [352–354]. Despite the lack of a phenotype when expressed alone, the combination of activating mutation of *Pik3ca* with homozygous or heterozygous loss of *Pten* was found to promote carcinogenesis [364].

PPP2R1A functions as a regulatory component of PP2A responsible for dephosphorylation of AKT to attenuate PI3K signalling. Despite its high mutation rate, there has not been a comprehensive study of a uterine targeted GEMM with deletion or mutation of *Ppp2r1a*. However, its tumour suppressive potential has been demonstrated in other organs, with expression of the cancer associated mutations, E64D and E64G, in lung increasing susceptibility of the mice to cancer after carcinogen exposure [365]. Additionally, a xenograft model introducing patient-derived *PPP2R1A* mutant cells in to the mouse uterus found that they were more capable of colonisation and growth compared to cells engineered to correct the mutation [366].

4.1.5.3 Combination of *Pten* loss with *Fbxw7* loss

Previous reports have suggested a level of co-operation between FBXW7 and PTEN in tumour suppression and regulation of particular targets, such as MTOR [259]. Furthermore, the combination of heterozygous loss of both *Pten* and *Fbxw7* was found to significantly reduce the latency of cancer formation compared to heterozygous loss of either gene individually [367]. As previously noted, the combined loss of these genes in the endometrium was recently examined by Cuevas *et al.*, who generated mice with homozy-

gous deletion of *Fbxw7* and *Pten* in the mouse endometrium, using BAC-*Sprr2f*-Cre to drive recombination [316]. Combined deletion caused formation of cancer and reduced survival compared to loss of either gene individually [316]. The tumours that formed exhibited a carcinosarcoma histology with strong induction of EMT genes following confirmed spontaneous mutation or inferred mutation from aberrant IHC staining of *Trp53* [316]. It is therefore evident that an interaction between *Fbxw7* deletion and *Pten* deletion does occur and holds relevance for endometrial carcinogenesis. However, whether these findings are comparable to the more common heterozygous *FBXW7* mutation, seen in human cancer, has yet to be determined.

4.1.6 Motivation for studying combined loss of *Pten* and mutation of *Fbxw7*

Heterozygous *FBXW7* mutations commonly occur in normal human endometrial tissue and alone does not drive formation of cancer in the uterus. However, these mutations are also over-represented in cancer, suggesting a functional role in EC. Combinatorial effects of mutations have been widely reported in cancer and based on the frequency of mutation it could be hypothesised that *FBXW7* mutation may co-operate with additional mutations to promote carcinogenesis. PI3K-pathway activation is a hallmark feature of endometrial cancer and *PTEN* is the most frequently mutated member of the pathway. Previous work examining the combined deletion of both *Fbxw7* and *Pten* found a potent and aggressive cancerous phenotype. However, the use of homozygous *Fbxw7* deletion does not align with the nature of *FBXW7* mutation in human cancers and previously discussed findings have confirmed the differential outcomes of *FBXW7* deletion compared to mutation. Therefore, to build on the previous work in this area, there was a need to examine the more biologically relevant heterozygous *Fbxw7* mutation in the context of *Pten* loss in the uterus.

4.2 Materials and methods

4.2.1 Breeding of experimental animals

Mutation of *Fbxw7* with loss of *Pten* was modelled by cross-breeding of the Fbxw7^{tm1Itom} allele, previously described, with the Pten^{tm2Mak} allele (Figure 4.3). Mice were bred to homozygosity for Pten^{tm2Mak} and absence or heterozygosity for Fbxw7^{tm1Itom} with Pgr$^{cre/+}$ to drive recombination in the uterus. Breeding of the mice was performed by Dr David Church.

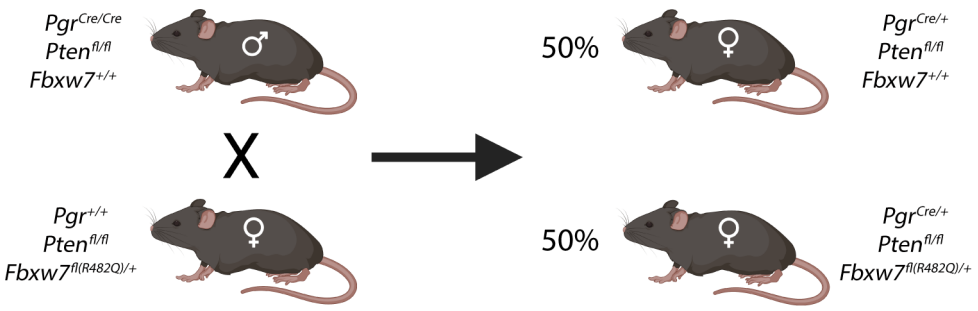

Figure 4.3: Breeding plan for generating *Pten*$^{\Delta/\Delta}$ mice. Percentages represent the proportion of female offspring from the breeding pair.

4.3 Results

4.3.1 Generation of *Pten*$^{\Delta/\Delta}$ mice and confirmation of allelic recombination

To explore the effects of *Fbxw7*^{R482Q} mutation in the context of *Pten* loss of function, the previously examined *Fbxw7* allele was combined with a floxed deletion allele of *Pten* (refer to Section 2.1.1 for more information regarding the alleles used). Mice were bred to homozygosity for the *Pten* allele with or without *Fbxw7*^{R482Q} and *Pgr*^{Cre} was used to target recombination to the uterus and other female reproductive tissues (Figure 4.3). The two genotypes generated were:

- *Pgr*$^{cre/+}$ *Pten*$^{fl/fl}$ *Fbxw7*$^{+/+}$, henceforth referred to as *Pten*$^{\Delta/\Delta}$ *Fbxw7*$^{+/+}$.
- *Pgr*$^{cre/+}$ *Pten*$^{fl/fl}$ *Fbxw7*$^{fl(R482Q)/+}$, henceforth referred to as *Pten*$^{\Delta/\Delta}$ *Fbxw7*$^{R482Q/+}$.

Confirmation of the mouse genotypes and successful recombination of the alleles was performed by PCR amplification (Figure 4.4A).

In addition to confirmation by PCR, successful recombination and reduction of RNA expression was examined using a TaqMan assay spanning the junction of exons 4 and 5, the two exons that are deleted during recombination of the loxP sites. Examination of RNA extracted from fresh frozen uteri at 4 weeks confirmed significant downregulation of *Pten* expression in both $Pten^{\Delta/\Delta}$ $Fbxw7^{+/+}$ (median $\log_2$(fold change) -3.48, P=0.0079 Wilcoxon Rank Sum test) and $Pten^{\Delta/\Delta}$ $Fbxw7^{R482Q/+}$ (median $\log_2$(fold change) -3.43, P=0.0079 Wilcoxon Rank Sum test) uteri when compared to wild-type mice (Figure 4.4B). To ensure that loss of *Pten* expression was maintained, RNA extracted from mouse uteri at 8 weeks was also examined (Figure 4.4C). Similar to the findings at 4 weeks, significant downregulation of *Pten* was observed in both $Pten^{\Delta/\Delta}$ $Fbxw7^{+/+}$ (median $\log_2$(fold change) -4.06, P=0.0025 Wilcoxon Rank Sum test) and $Pten^{\Delta/\Delta}$ $Fbxw7^{R482Q/+}$ (median $\log_2$(fold change) median -2.97, P=0.0025 Wilcoxon Rank Sum test) mice. No significant difference in the expression of *Pten* between $Pten^{\Delta/\Delta}$ $Fbxw7^{+/+}$ and $Pten^{\Delta/\Delta}$ $Fbxw7^{R482Q/+}$ was observed in mice at 4 weeks (median $\log_2$(fold change) 0.05, P=1.0 Wilcoxon Rank Sum test) or 8 weeks (median $\log_2$(fold change) 1.08, P=0.26 Wilcoxon Rank Sum test).

4.3.2 *Fbxw7*$^{R482Q/+}$ significantly reduces survival of mice with uterine *Pten* deletion

To examine the effect of $Pten^{\Delta/\Delta}$ $Fbxw7^{+/+}$ and $Pten^{\Delta/\Delta}$ $Fbxw7^{R482Q/+}$ on overall survival, mice were aged until the onset of ill-health or abdominal distension (survival endpoint). In both $Pten^{\Delta/\Delta}$ $Fbxw7^{+/+}$ and $Pten^{\Delta/\Delta}$ $Fbxw7^{R482Q/+}$ genotypes, mice had to be sacrificed due to development of abdominal distension. In $Pten^{\Delta/\Delta}$ $Fbxw7^{+/+}$ mice this was in line with the time frame reported in prior literature, but for $Pten^{\Delta/\Delta}$ $Fbxw7^{R482Q/+}$ mice was more rapid, requiring earlier sacrifice. Necropsy results found enlargement of both uterine horns in $Pten^{\Delta/\Delta}$ $Fbxw7^{+/+}$ and $Pten^{\Delta/\Delta}$ $Fbxw7^{R482Q/+}$ mice. Kaplan-Meier estimator analysis was performed on this cohort, and it is apparent that survival of mice with $Pten^{\Delta/\Delta}$ was significantly reduced, but the addition of $Fbxw7^{R482Q}$ mutation has a

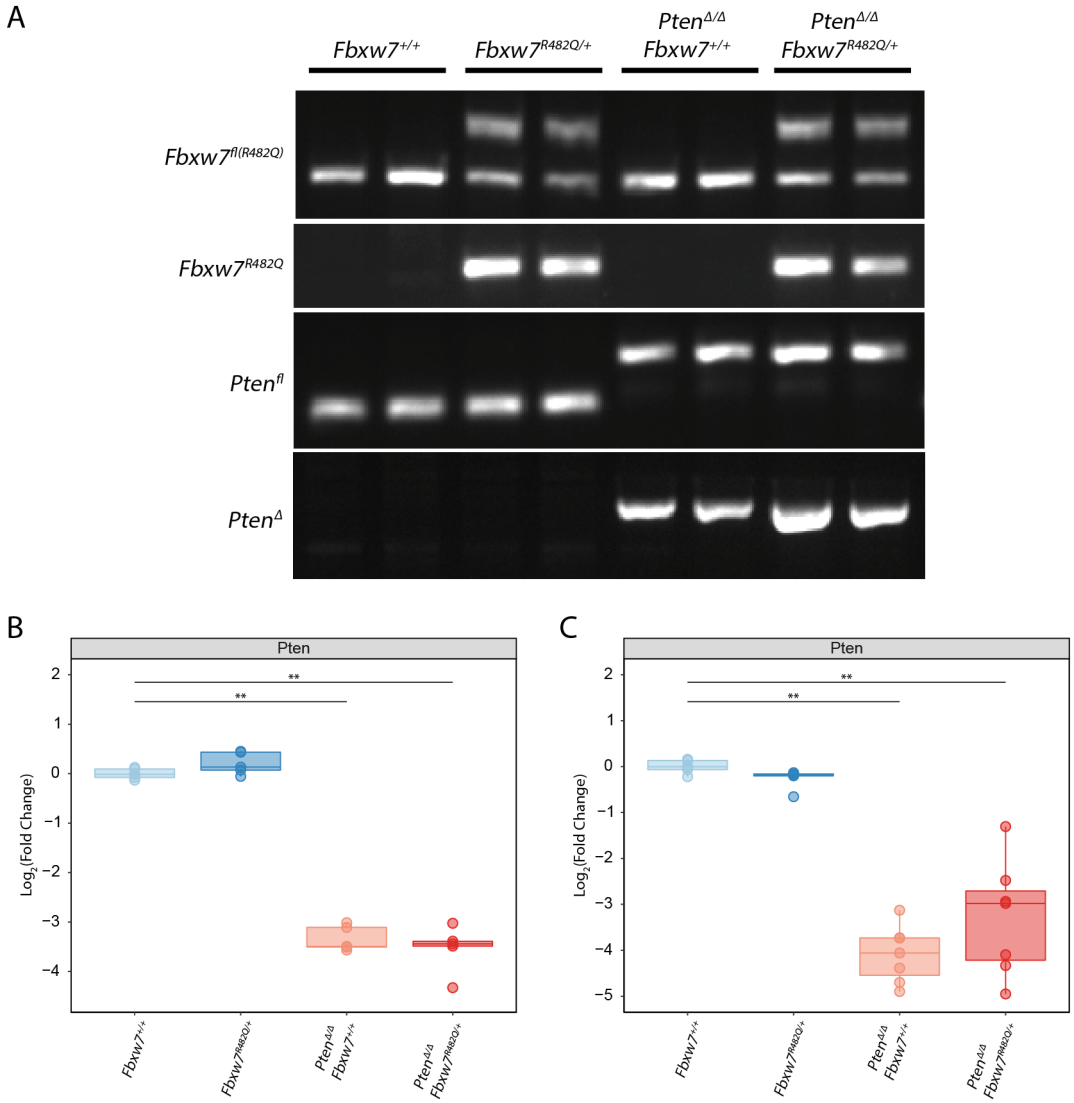

Figure 4.4: Confirmation of allelic recombination and functionality of conditional alleles. **A.** Agarose PCR gel image showing the genotyping of the *Pten*$^{\Delta/\Delta}$ mice alongside the mice from the previous chapter. Presence of the *Pten* floxed allele is apparent from the 335 bp amplicon due to the presence of the loxP sites. Recombination was confirmed by detection of a 859 bp band after amplification with primers spanning the deleted region (which would otherwise be too far apart to generate a band). **B, C.** Gene expression of *Pten*, as determined by RT-qPCR, in the uterus of mice at 4 weeks - **B.** and 8 weeks - **C.**

combinatorial effect on survival of $Pten^{\Delta/\Delta}$ $Fbxw7^{R482Q/+}$ mice, which was significantly reduced when compared to mice expressing $Pten^{\Delta/\Delta}$ alone (median survival 11.9 weeks vs 31.8 weeks, P=0.00014 Log-Rank test) (Figure 4.5).

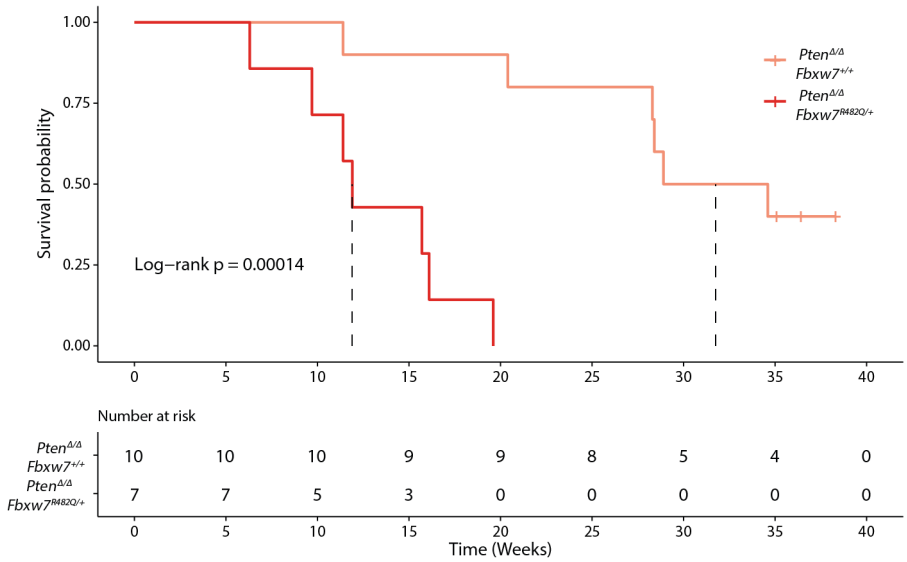

Figure 4.5: Survival analysis of $Pten^{\Delta/\Delta}$ and $Pten^{\Delta/\Delta}$ $Fbxw7^{R482Q/+}$ mice. Kaplan-Meier estimator analysis of the overall survival of $Pten^{\Delta/\Delta}$ and $Pten^{\Delta/\Delta}$ $Fbxw7^{R482Q/+}$ mice.

4.3.3 *Pten*$^{\Delta/\Delta}$ causes endometrial cancer

The previously noted abdominal distension suggested uterine pathology in $Pten^{\Delta/\Delta}$ $Fbxw7^{+/+}$ and $Pten^{\Delta/\Delta}$ $Fbxw7^{R482Q/+}$ uteri. Therefore, to examine the impact of $Pten^{\Delta/\Delta}$ $Fbxw7^{+/+}$ and $Pten^{\Delta/\Delta}$ $Fbxw7^{R482Q/+}$ on uterine histology, FFPE uteri from mice culled at 4 weeks, 8 weeks and survival end point were stained with H&E and by IHC for Krt8. The 8 week and survival end point samples were also stained for forkhead box A2 (Foxa2), a cellular marker of endometrial glands. In addition, FFPE stained sections were reviewed by expert gynaecological pathologists (Dr Tjalling Bosse and Dr Alicia Leon-Castillo) to determine presence of any uterine pathology.

As early as 4 weeks of age a profound difference in the composition of the uterus was apparent, with the uteri of both $Pten^{\Delta/\Delta}$ $Fbxw7^{+/+}$ and $Pten^{\Delta/\Delta}$ $Fbxw7^{R482Q/+}$ mice greatly enlarged compared to that of wild-type mice (Figure 4.6). Expert pathology review highlighted the presence of endometrial adenocarcinoma in 100% of mice, in both genotypes, at this time point (Figure 4.7B). The evidence of adenocarcinoma was most

apparent from Krt8 staining which highlighted the vastly increased epithelial density with glandular crowding and a substantial increase in the ratio of epithelium compared to stroma, typical of endometrial carcinogenesis, in the uteri of mice from both genotypes.

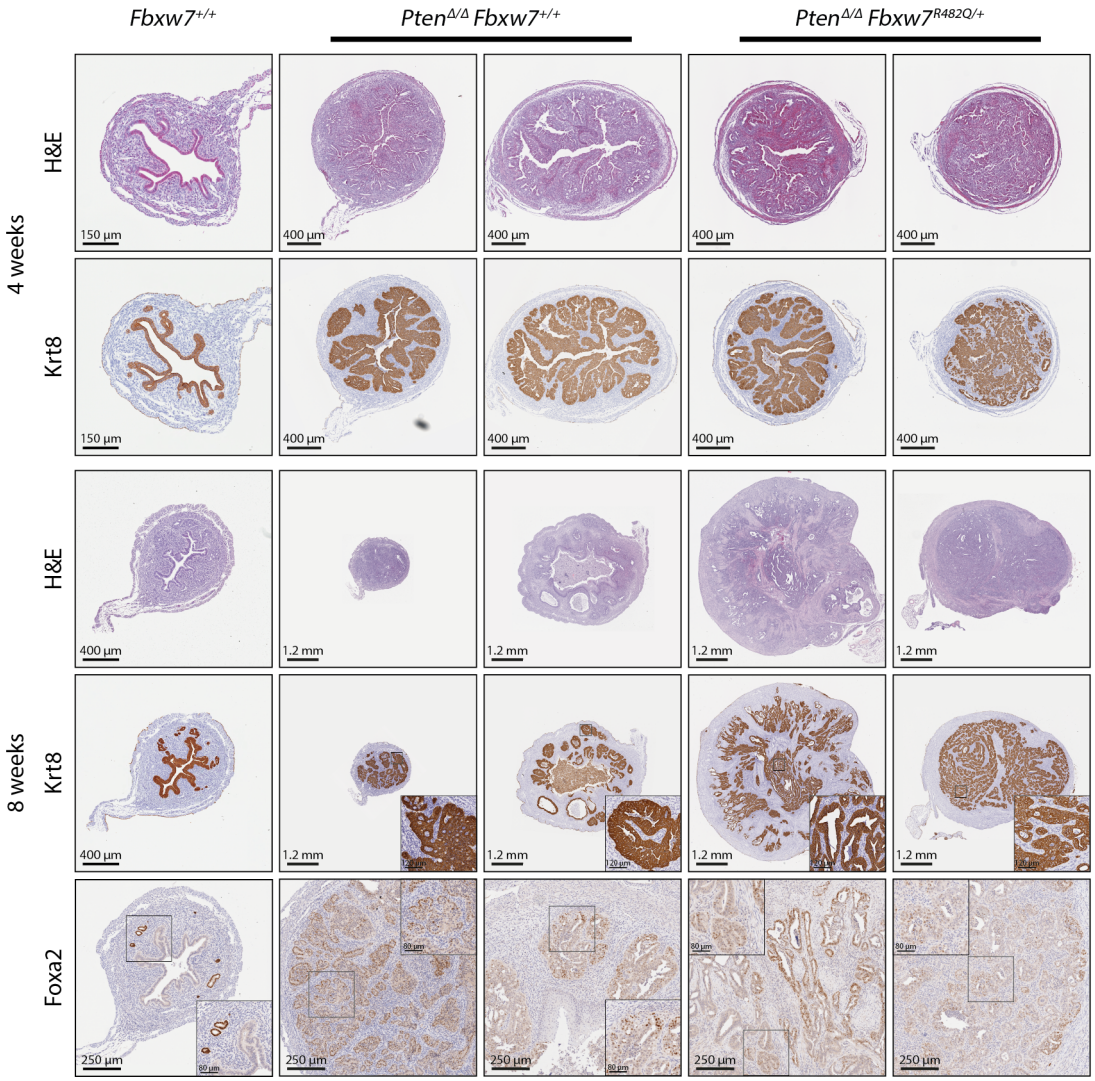

Figure 4.6: Histology changes induced by $Pten^{\Delta/\Delta}$ and combined $Pten^{\Delta/\Delta}$ $Fbxw7^{R482Q/+}$ mutations. H&E staining and Foxa2 (glandular epithelium) or Krt8 (glandular and luminal epithelium) IHC were performed on FFPE tissue from mice at 4 weeks or 8 weeks as indicated.

At 8 weeks of the age, continued enlargement of the uterus was apparent with the size difference compared to wild-type mice being more pronounced than at the 4 week time point (Figure 4.6). Furthermore, expert pathological assessment showed a high proportion of endometrial adenocarcinoma diagnoses in both genotypes. However, at this time point two $Pten^{\Delta/\Delta}$ $Fbxw7^{+/+}$ samples were diagnosed with less severe phe-

notypes of pyometrium and hyperplasia (Figure 4.7B). Krt8 and Foxa2 staining in the *Pten*$^{\Delta/\Delta}$ *Fbxw7*$^{R482Q/+}$ samples showed foci of dense epithelial cells with sporadic and heterogeneous Foxa2 positivity throughout the uterus instead of being concentrated in the epithelium of the stratum basalis, indicating a loss of the clear distinction between luminal and glandular epithelium. A similar pattern of staining was apparent in the majority of *Pten*$^{\Delta/\Delta}$ *Fbxw7*$^{+/+}$ mice, but some still exhibited more obvious luminal epithelium, lacking any nuclear Foxa2 staining (Figure 4.6).

Similar pathological outcomes were seen in the uteri of both *Pten*$^{\Delta/\Delta}$ *Fbxw7*$^{+/+}$ and *Pten*$^{\Delta/\Delta}$ *Fbxw7*$^{R482Q/+}$ mice at survival end point (Figure 4.7B). The majority of mice in both genotypes exhibited endometrial adenocarcinoma with one *Pten*$^{\Delta/\Delta}$ *Fbxw7*$^{R482Q/+}$ and one *Pten*$^{\Delta/\Delta}$ *Fbxw7*$^{+/+}$ mouse displaying pyometrium and one *Pten*$^{\Delta/\Delta}$ *Fbxw7*$^{+/+}$ mouse displaying hyperplasia. Krt8 staining for both genotypes revealed irregular epithelial distribution with no semblance of normal uterine patterning (Figure 4.7A). Interestingly, for *Pten*$^{\Delta/\Delta}$ *Fbxw7*$^{R482Q/+}$ mice Foxa2 exhibited stronger nuclear staining than was observed at 8 weeks, but in *Pten*$^{\Delta/\Delta}$ *Fbxw7*$^{+/+}$ mice it appeared much weaker with less nuclear staining when compared to the 8 week time point, and in particular when compared to the staining in *Pten*$^{\Delta/\Delta}$ *Fbxw7*$^{R482Q/+}$ mice at the same time point. This is potentially surprising as Foxa2 is linked as being a tumour suppressor in cancer and specifically in EC but may indict that the epithelium in these samples retain more of a stem-like phenotype or may be in a non-terminally differentiated state.

4.3.4 Alteration to transcription in *Pten*$^{\Delta/\Delta}$ mice

Due to the changes observed in *Fbxw7*$^{R482Q/+}$ mice, transcriptional changes in *Trp53* and *Fbxw7* were examined. In the RNA extracted from the uteri of mice at 4 weeks of age a trend towards downregulation of *Fbxw7* was observed compared to wild-type mice (Figure 4.8A). This trend reached statistical significance in the *Pten*$^{\Delta/\Delta}$ *Fbxw7*$^{+/+}$ mice (median $\log_2$(fold change) -0.401, P=0.019 Wilcoxon Rank Sum test) but fell short of statistical significance for *Pten*$^{\Delta/\Delta}$ *Fbxw7*$^{R482Q/+}$ mice (median $\log_2$(fold change) -0.260, P=0.095 Wilcoxon Rank Sum test). Interestingly, upregulation of *Fbxw7* expression seen with *Fbxw7*^{R482Q} mutation in the context of wild-type mice was not present when com-

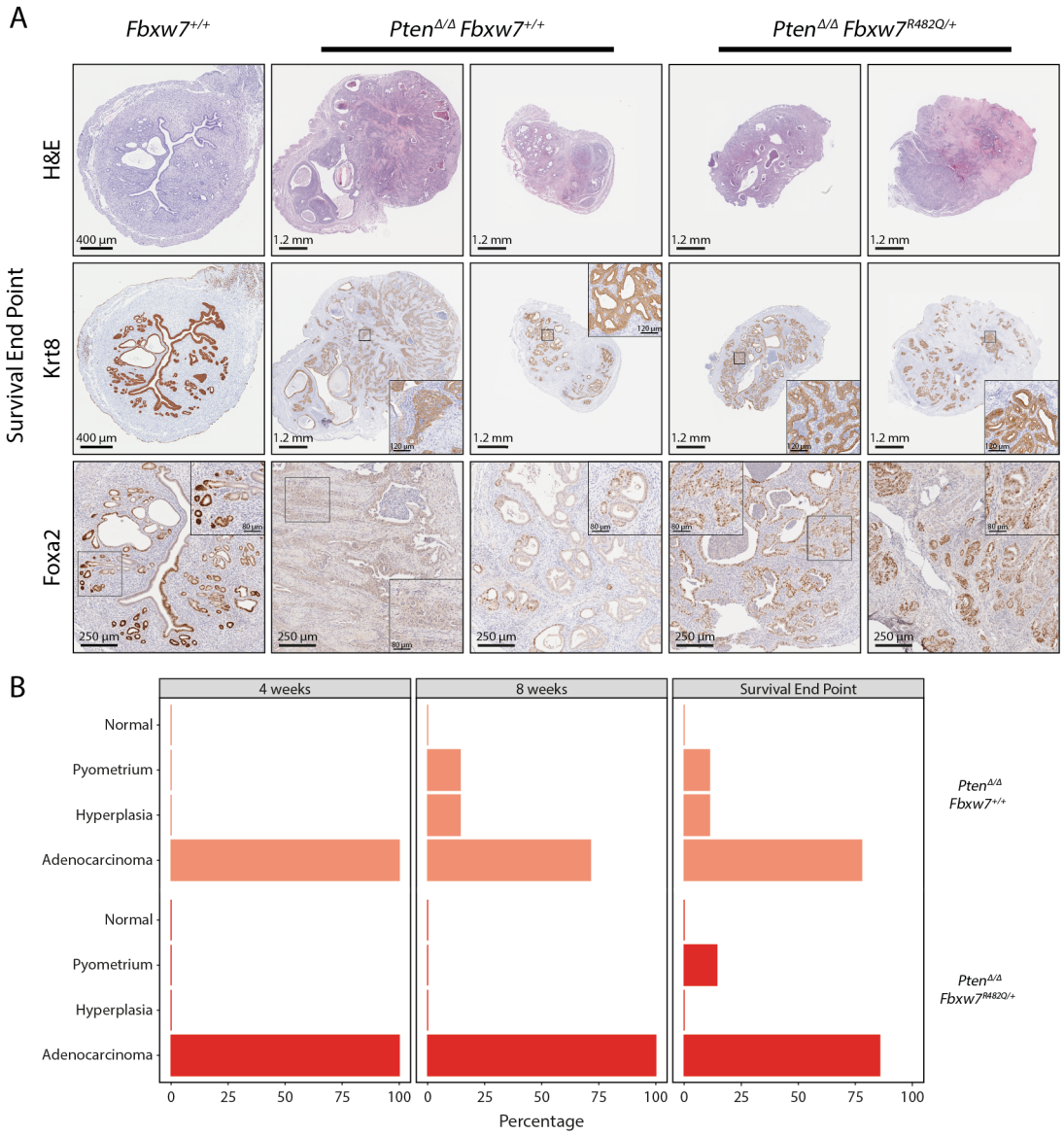

Figure 4.7: Histological appearance of the uterus at survival end point in *Pten*$^{\Delta/\Delta}$ and *Pten*$^{\Delta/\Delta}$ *Fbxw7*$^{R482Q/+}$ mice and expert pathology review of uteri at all timepoints. **A.** Staining with H&E along with Foxa2 (glandular epithelium) and Krt8 (general epithelium) were performed on FFPE tissue sections from the uterus of mice at survival end point. **B.** Shows the proportions of diagnosed uterine pathology in uteri from *Pten*$^{\Delta/\Delta}$ and *Pten*$^{\Delta/\Delta}$ *Fbxw7*$^{R482Q/+}$ mice at all time points. Number of mice analysed *Pten*$^{\Delta/\Delta}$ *Fbxw7*$^{+/+}$: 4w = 3, 8w = 7, survival end point = 9; *Pten*$^{\Delta/\Delta}$ *Fbxw7*$^{R482Q/+}$: 4w = 6, 8w = 7, survival end point = 7.

paring *Pten*$^{\Delta/\Delta}$ *Fbxw7*$^{+/+}$ and *Pten*$^{\Delta/\Delta}$ *Fbxw7*$^{R482Q/+}$ mice, suggesting loss of a feedback loop driving increased *Fbxw7* expression or induction of a factor suppressing *Fbxw7* expression. In both genotypes, the expression of *Trp53* was found to be significantly upregulated compared to expression in the wild type mice (median $\log_2$(fold change) 0.824, P=0.0079 Wilcoxon Rank Sum test for *Pten*$^{\Delta/\Delta}$ *Fbxw7*$^{+/+}$; median $\log_2$(fold change)

0.753, P=0079 Wilcoxon Rank Sum test for $Pten^{\Delta/\Delta}$ $Fbxw7^{R482Q/+}$), suggesting there may be buffering of the negative effects of loss of *Pten* expression.

The same analysis was performed using RNA extracted from mice at 8 weeks of age (Figure 4.8B). The trend in *Fbxw7* expression was equivalent to that seen in mice at 4 weeks of age, with downregulation evident when compared to wild-type mice. Statistically significant downregulation of *Fbxw7* was found in both $Pten^{\Delta/\Delta}$ $Fbxw7^{+/+}$ (median $\log_2$(fold change) -0.504, P=0.0025) and $Pten^{\Delta/\Delta}$ $Fbxw7^{R482Q/+}$ (median $\log_2$(fold change) -0.611, P=0.018) mice. However, the magnitude of the change was more modest, and no difference was observed between $Pten^{\Delta/\Delta}$ $Fbxw7^{+/+}$ and $Pten^{\Delta/\Delta}$ $Fbxw7^{R482Q/+}$ mice. In contrast to expression of *Fbxw7*, the trend in *Trp53* expression did not align with that seen in the 4 week samples, instead a trend towards downregulation was apparent. A decrease in *Trp53* was evident in the $Pten^{\Delta/\Delta}$ $Fbxw7^{R482Q/+}$ samples (median $\log_2$(fold change) -1.08, P=0.018) compared to wild-type, but not in the $Pten^{\Delta/\Delta}$ $Fbxw7^{+/+}$ samples (median -0.610, P=0.15). However, the difference between $Pten^{\Delta/\Delta}$ $Fbxw7^{R482Q/+}$ and $Pten^{\Delta/\Delta}$ $Fbxw7^{+/+}$ samples was not statistically significant (median $\log_2$(fold change) -0.467, P=0.38).

It has been previously demonstrated that *Trp53* mRNA expression does not reliably correlate with p53 expression and activity [368]. Therefore, I examined expression of *Trp53* target genes, *Bbc3*, a p53 induced pro-apoptotic protein and *Cdkn1a*, a negative regulator of cell cycle progression, to gauge the potential activity of p53 in these samples (Figure 4.8C). No significant difference was observed in the expression of *Bbc3* between any of the mouse genotypes, however, significant upregulation of *Cdkn1a* was seen in both $Pten^{\Delta/\Delta}$ $Fbxw7^{+/+}$ (median $\log_2$(fold change) 2.02, P=0.0025) and $Pten^{\Delta/\Delta}$ $Fbxw7^{R482Q/+}$ (median $\log_2$(fold change) 2.00, P=0.0025) mice compared to wild-type mice. Therefore, whilst the expression of *Trp53* is reduced, this may not be impacting the protein expression or activity of p53, alternatively, *Cdkn1a* expression may not be fully representative of p53 activity.

Unfortunately, fresh frozen uterine tissue from wild-type mice at survival end point was not available making it impossible to compare expression of these targets to a wild-type baseline. However, I was able to examine relative expression between the $Pten^{\Delta/\Delta}$

Fbxw7$^{R482Q/+}$ and *Pten*$^{\Delta/\Delta}$ *Fbxw7*$^{+/+}$ mice (Figure 4.8D). Expression of all three markers (including *Pten*) were not significantly different at this time point, in congruence with the previously examined time points. *Bbc3* and *Cdkn1a* were also examined at this time point, with no significant difference observed in either group (Appendix C.1).

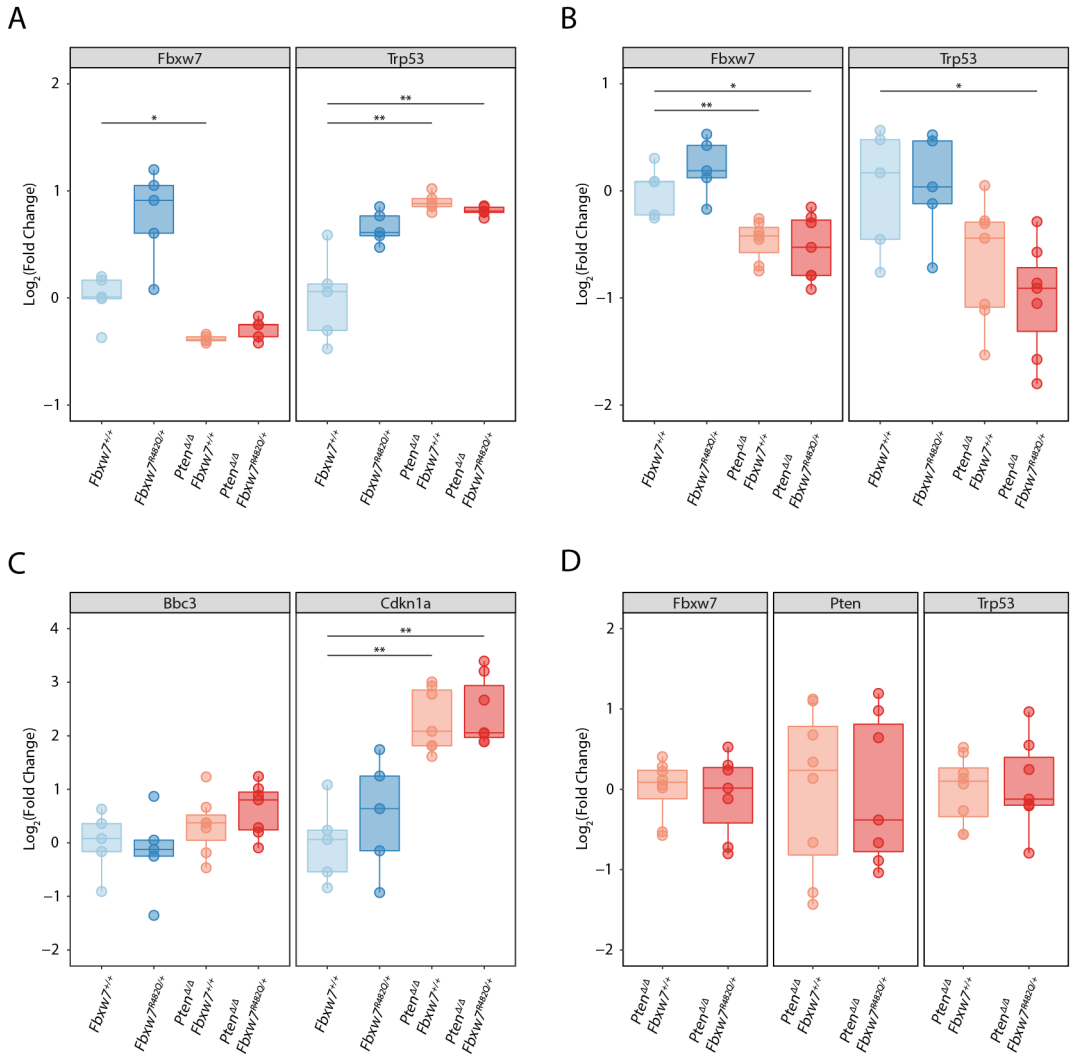

Figure 4.8: Gene expression changes in key genes and p53 target genes. **A, B.** Gene expression, relative to *Fbxw7*$^{+/+}$ mice, as determined by RT-qPCR, for *Fbxw7* and *Trp53* in the uterus of mice at 4 weeks - **A** and 8 weeks - **B**. **C.** Gene expression, relative to *Fbxw7*$^{+/+}$ mice, as determined by RT-qPCR, for two p53 target genes in the mice at 8 weeks. **D.** Gene expression, relative to *Pten*$^{\Delta/\Delta}$ mice, as determined by RT-qPCR, of *Fbxw7*, *Pten*, and *Trp53* at survival end point.

4.3.5 *Fbxw7*^{R482Q} mutation does not drive overexpression of known Fbxw7 targets when combined with *Pten*$^{\Delta/\Delta}$

Histological examination of *Pten*$^{\Delta/\Delta}$ *Fbxw7*$^{+/+}$ and *Pten*$^{\Delta/\Delta}$ *Fbxw7*$^{R482Q/+}$ uteri demonstrated cancer development in both genotypes and the survival analysis indicated the phenotype was significantly more aggressive in *Pten*$^{\Delta/\Delta}$ *Fbxw7*$^{R482Q/+}$ mice. However, RT-qPCR analysis did not show changes in *Pten*, *Fbxw7*, or *Trp53* expression between these genotypes. Therefore, in order to examine for dysregulation of common carcinogenic pathways in EC and known targets of *Fbxw7*, IHC staining of FFPE uterine tissue and western blotting using protein samples extracted from bulk, fresh frozen uterine tissue extracted at 8 weeks, were performed (Figure 4.9). Staining of samples at 8 weeks of age for Pten and p-Akt further confirmed the successful loss of Pten expression (Figure 4.9A). The loss of Pten expression in both the epithelium and stroma was apparent, some Pten-positive cells are present in the tissue, but these appeared to be cells that originate from outside the uterus, such as immune cells. The loss of Pten was accompanied by an increase in the expression of p-Akt, which was confined to epithelial cells, indicating activation of the PI3K-pathway.

Previously, when comparing the *Pten*$^{\Delta/\Delta}$ *Fbxw7*$^{+/+}$ and *Pten*$^{\Delta/\Delta}$ *Fbxw7*$^{R482Q/+}$ samples with wild-type mice, a trend towards reduced expression of *Trp53* was observed, although increased expression of p53 target genes was also observed suggesting increased activity of p53 in these samples. Examination of p53 expression by IHC did suggest there was an increase in both the *Pten*$^{\Delta/\Delta}$ *Fbxw7*$^{+/+}$ and *Pten*$^{\Delta/\Delta}$ *Fbxw7*$^{R482Q/+}$ samples compared to wild-type samples, as well as an increase in nuclear localisation of p53, although no difference was evident between *Pten*$^{\Delta/\Delta}$ *Fbxw7*$^{+/+}$ and *Pten*$^{\Delta/\Delta}$ *Fbxw7*$^{R482Q/+}$. Expression of Ccne1 was examined by IHC (Figure 4.9A) and by western blot (Figure 4.9B), with no significant difference seen between the two genotypes or even evidence of an increase over expression in wild-type animals. Furthermore, expression of Jun, Myc, and Notch1 were examined by western blot (Figure 4.9B,C), with no significant difference found in any of these known targets.

Expression of Pten, p-Akt, p53, and Ccne1 were also examined by IHC in samples at

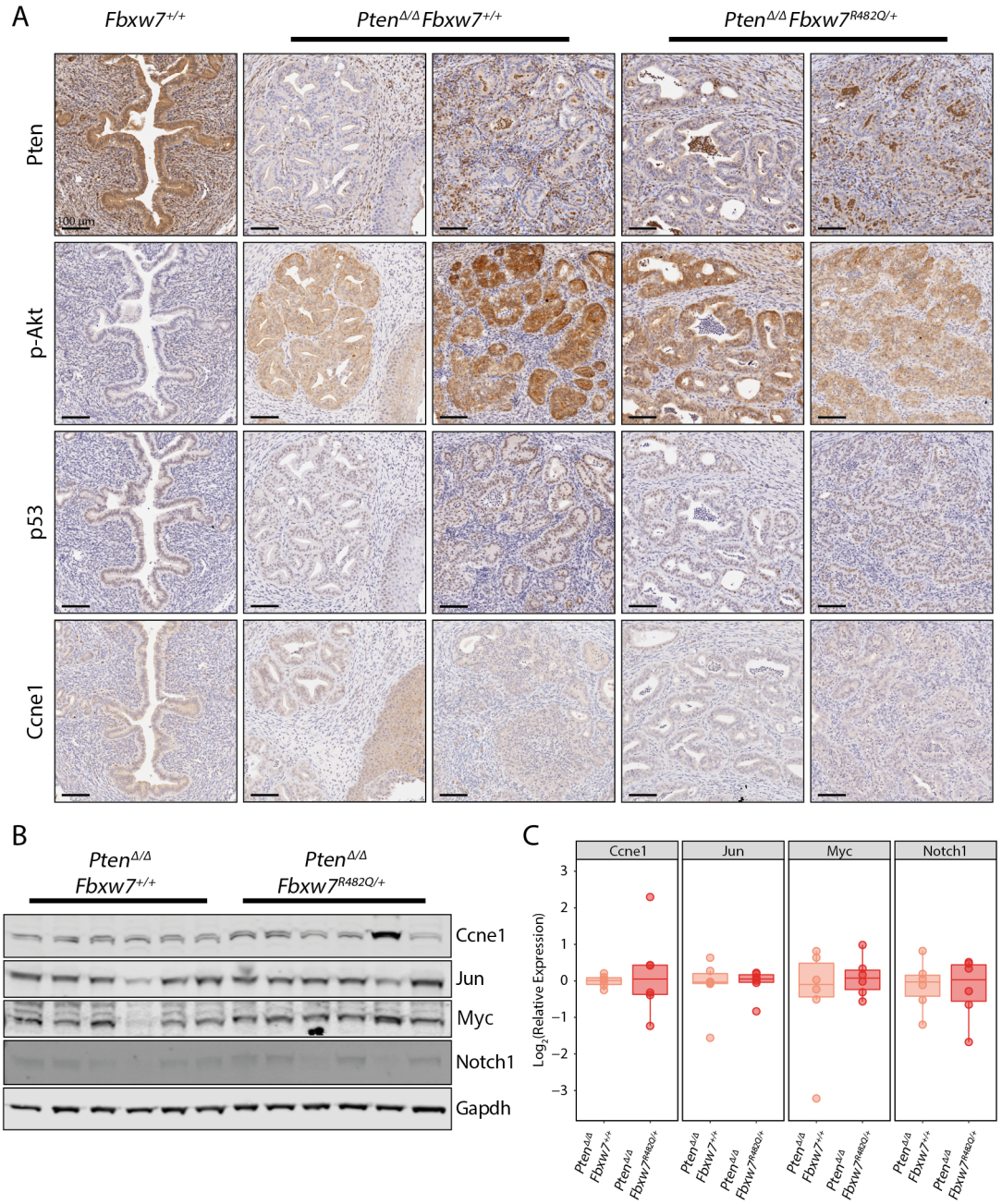

Figure 4.9: Examination of protein expression in $Pten^{\Delta/\Delta}$ and $Pten^{\Delta/\Delta}$ $Fbxw7^{R482Q/+}$ mice at 8 weeks. **A.** IHC staining for Pten, p-Akt, Trp53, and Ccne1 with images from $Fbxw7^{+/+}$ as a reference for normal uterus appearance. **B.** Western blotting analysis for known Fbxw7 targets. **C.** Relative expression of proteins from the western blot, determined by densitometry and normalisation to Gapdh.

survival end point (Figure 4.10). At this time point, the loss of Pten expression was still apparent with the concomitant increase of p-Akt expression, which, as in the 8 week samples, was confined to the epithelium. Compared to wild-type mice, the staining for p53 in both genotypes exhibited stronger nuclear staining potentially indicating increased p53 activity, yet no difference was observed between the two genotypes. As in the 8 week samples, no differences were observed in the staining of Ccne1 either compared to the wild-type samples or between the two genotypes.

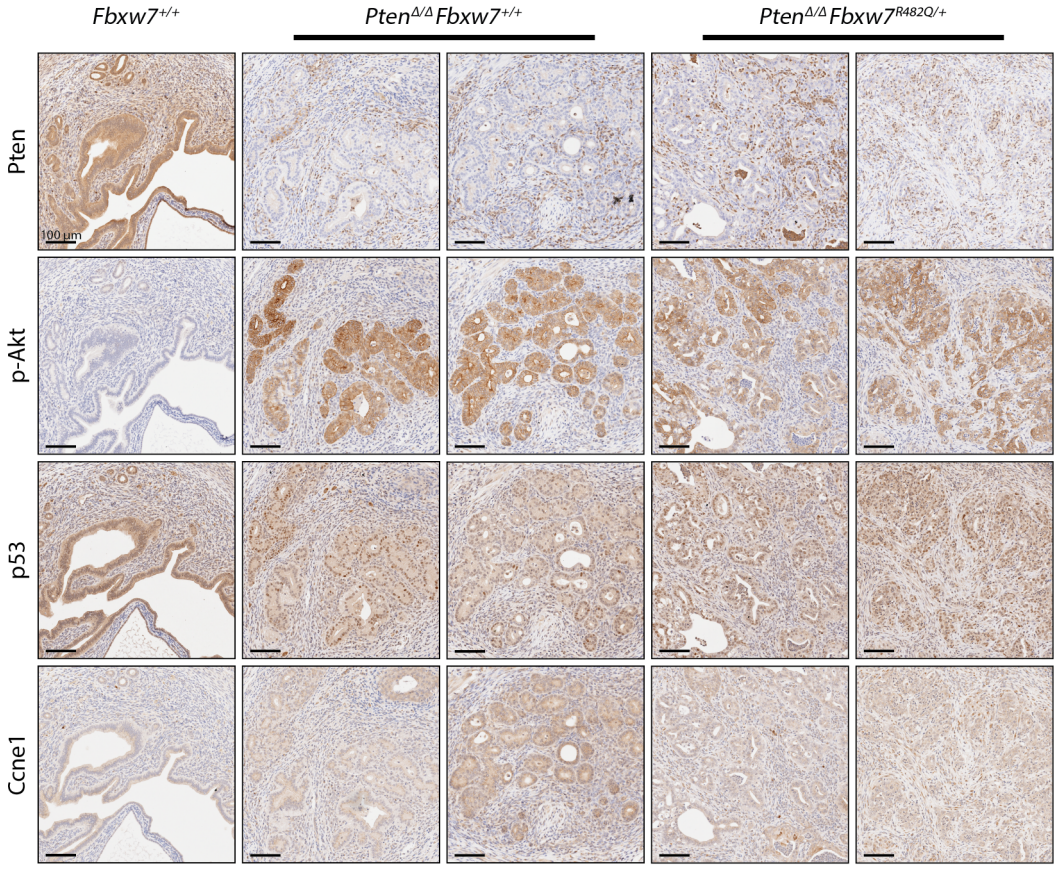

Figure 4.10: Examination of protein expression in $Pten^{\Delta/\Delta}$ and $Pten^{\Delta/\Delta}$ $Fbxw7^{R482Q/+}$ mice at survival end point. IHC staining of FFPE tissue collected from mice at survival end point.

4.3.6 Squamous metaplasia is a frequent feature of $Pten^{\Delta/\Delta}$ mice, but is less prevalent when combined with $Fbxw7^{R482Q}$ mutation

Presence of squamous metaplasia is a previously noted phenotype of *Pgr*-cre driven $Pten^{\Delta/\Delta}$ and was highlighted by pathological review of H&E stained tissue sections from mice at 8 weeks of age [126]. The role and significance of squamous metaplasia in

endometrial cancer is poorly understood, with some studies suggesting it is linked to higher rates of recurrence and others finding no significant difference in prognosis [369, 370]. In order to examine the differential presence and extent of squamous metaplasia in $Pten^{\Delta/\Delta}$ $Fbxw7^{+/+}$ and $Pten^{\Delta/\Delta}$ $Fbxw7^{R482Q/+}$ mice, FFPE uterine tissue sections were co-stained for Krt8, a marker of columnar epithelium, and keratin 5 (Krt5), a marker of squamous epithelium. The amount of squamous epithelium was quantified and calculated as a percentage of the total epithelium (Figure 4.11).

With increasing age, the extent of squamous metaplasia increased for both genotypes, although it appeared to plateau between 8 weeks and survival end point in the $Pten^{\Delta/\Delta}$ $Fbxw7^{+/+}$ mice (Figure 4.11). In both genotypes, squamous metaplasia was present as early as 4 weeks with slightly elevated levels in $Pten^{\Delta/\Delta}$ $Fbxw7^{+/+}$ mice (median 2.46% of all epithelium) compared to $Pten^{\Delta/\Delta}$ $Fbxw7^{R482Q/+}$ (median 0.640% of all epithelium), although not statistically significantly (P=0.40 Wilcoxon Rank Sum test). At 8 weeks of age Krt5 staining was highly prevalent in $Pten^{\Delta/\Delta}$ $Fbxw7^{+/+}$ mice (median 41.8% of all epithelium) and was significantly increased over the levels in $Pten^{\Delta/\Delta}$ $Fbxw7^{R482Q/+}$ mice (median 2.59% of all epithelium; P=0.029 Wilcoxon Rank Sum test). At survival end point, the significant difference in prevalence of squamous metaplasia was lost due plateauing in $Pten^{\Delta/\Delta}$ $Fbxw7^{+/+}$ mice (median 37.7% of all epithelium), but continued increase in $Pten^{\Delta/\Delta}$ $Fbxw7^{R482Q/+}$ mice (median 23.2% of all epithelium; P=0.70 Wilcoxon Rank Sum test).

4.3.7 $Pten^{\Delta/\Delta}$ $Fbxw7^{R482Q/+}$ mouse uteri exhibit gene expression changes that correlate with the transcriptional activity of Lef1

The results above demonstrate profound acceleration of $Pten^{\Delta/\Delta}$ driven tumorigenesis by addition of $Fbxw7^{R482Q/+}$. However, targeted analysis of known Fbxw7 substrates as drivers of this phenotype did not highlight any obvious candidates. I therefore performed an agnostic analysis of the transcriptional changes between $Pten^{\Delta/\Delta}$ $Fbxw7^{+/+}$ and $Pten^{\Delta/\Delta}$ $Fbxw7^{R482Q/+}$ mice. RNA was extracted from bulk, fresh frozen uterine pieces from both genotypes at 8 weeks and was quantified by microarray. The resulting gene expression values were then compared to determine the significantly differentially

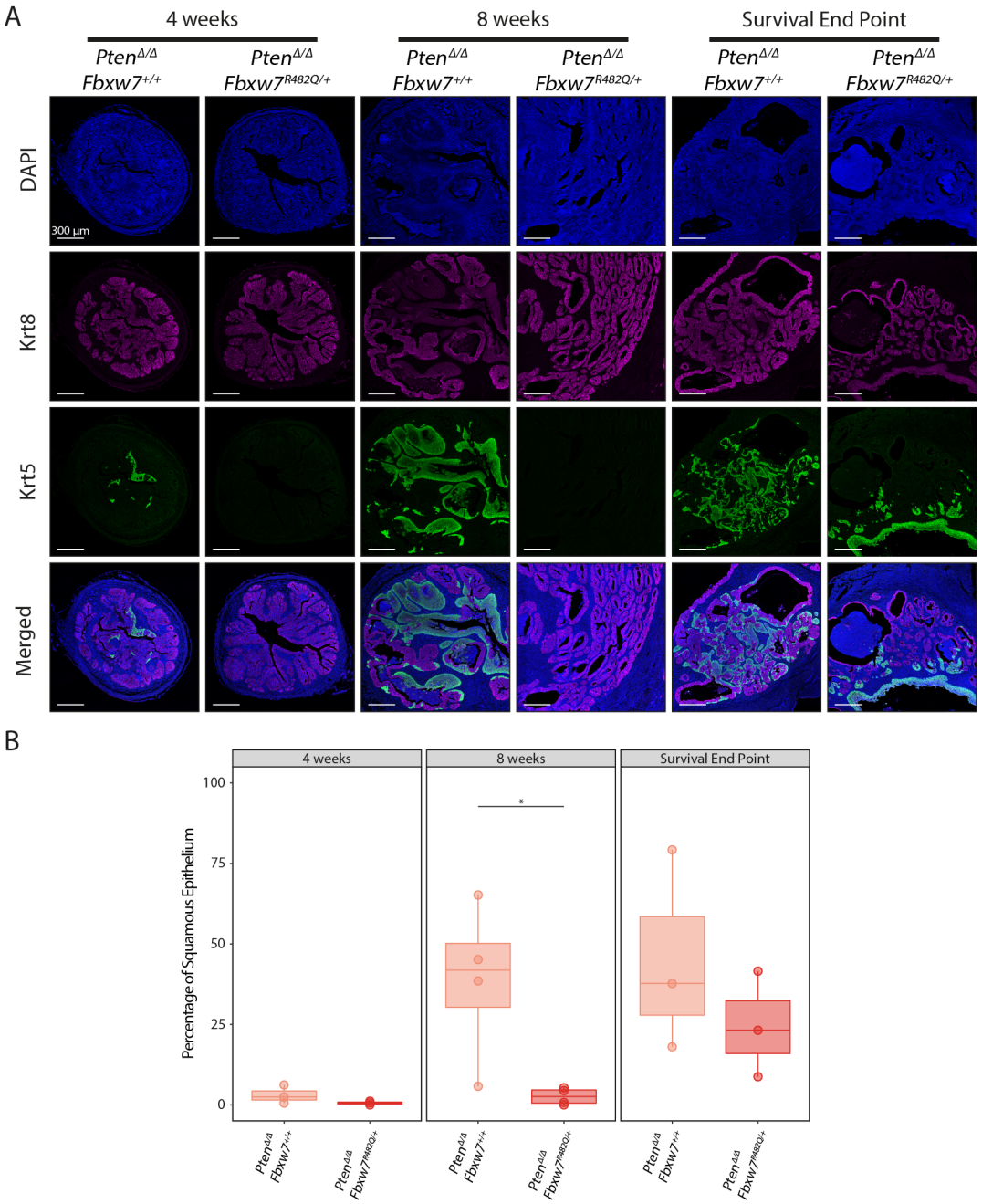

Figure 4.11: Analysis of the extent of squamous metaplasia in $Pten^{\Delta/\Delta}$ and $Pten^{\Delta/\Delta}$ $Fbxw7^{R482Q/+}$ mice at various time points. **A.** Co-immunofluorescent staining for DAPI (nuclear stain), Krt8 (columnar epithelium), and Krt5 (squamous epithelium) at all time points. **B.** Quantification of the proportion of epithelial cells that exhibits Krt5 staining for squamous identity relative to the total number of epithelial cells (squamous + columnar). Quantification was performed using 3 samples per genotype at 4 weeks and survival end point and 4 samples per genotype at 8 weeks.

expressed genes (DEGs) in the $Pten^{\Delta/\Delta}$ $Fbxw7^{R482Q/+}$ samples (Figure 4.12).

From this analysis numerous significantly DEGs were apparent, with 351 genes found to be upregulated and 177 genes downregulated ($Log_2(FC) \geq 1$ or $\leq$ -1; adjusted

$P \leq 0.05$). Among the most significantly upregulated genes, were those associated with extracellular matrix remodelling (*Mmp13*), TGF-β pathway (*Inhba*) and the inflammatory response (*Serpina3n*). Genes downregulated in $Pten^{\Delta/\Delta}$ $Fbxw7^{R482Q/+}$ uteri, included those associated with squamous epithelial cell identity (*Krt5*, *Krt15*, *Krt13*, and *Trp63*), consistent with the difference in squamous metaplasia between genotypes reported previously.

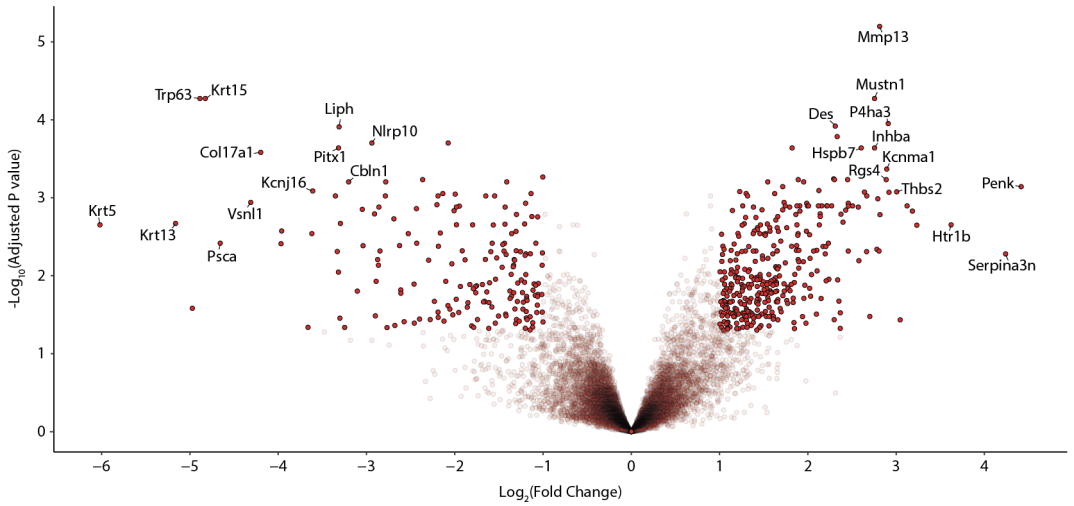

Figure 4.12: Transcriptomics changes induced by $Pten^{\Delta/\Delta}$ $Fbxw7^{R482Q/+}$ compared to $Pten^{\Delta/\Delta}$. The volcano plot represents the output of differential gene expression analysis performed on the intensity values determined from microarray analysis of fresh frozen uterine RNA.

GSEA was performed using gene sets defined by the Molecular Signatures Database. Analysis of the DEGs using the hallmark gene sets, which are designed to represent well-defined biological states or processes, highlighted several differentially enriched pathways (Figure 4.13A). The most significantly upregulated gene set was related to EMT, indicating greater activity in the $Pten^{\Delta/\Delta}$ $Fbxw7^{R482Q/+}$ samples (Figure 4.13B).

I also identified significantly enriched gene sets related to Fbxw7 targets. Interestingly, there was significant positive enrichment of genes related to Tgf-β signalling in the $Pten^{\Delta/\Delta}$ $Fbxw7^{R482Q/+}$ uteri (Figure 4.13C), which was unexpected as Fbxw7 targets the negative regulator of this pathway, Tgif1, for degradation. Similarly, two gene sets derived from target genes of Myc (Figure 4.13D) and one describing genes related to mTORC1 activity (Figure 4.13E) exhibited negative enrichment in the $Pten^{\Delta/\Delta}$ $Fbxw7^{R482Q/+}$ samples.

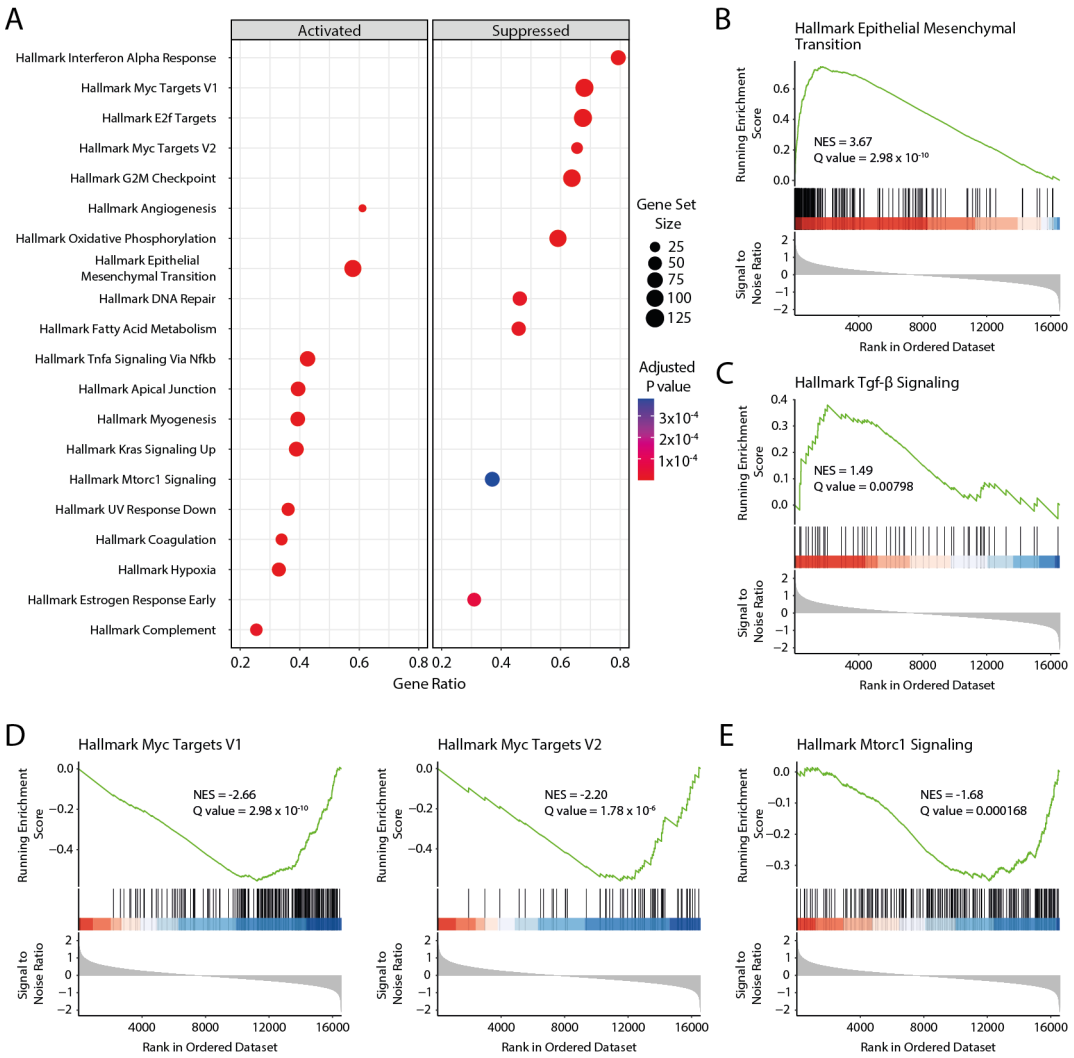

Figure 4.13: GSEA to examine for potential activation or suppression of cancer hallmark pathways in the transcriptomic data. **A.** Show the most activated and suppressed pathway present in the differential gene expression analysis of $Pten^{\Delta/\Delta}$ $Fbxw7^{R482Q/+}$ compared to $Pten^{\Delta/\Delta}$. **B-E.** GSEA plots highlighting pathways of particular interest due to their enrichment and statistical significance or their prior association with regulation by Fbxw7.

The Molecular Signatures database also provides gene sets derived from genetic or chemical perturbation of known oncogenic genes. Given the lack of obvious candidates to account for the $Fbxw7^{R482Q}$ phenotype, I performed GSEA using these gene sets to further examine the potential mechanistic drivers of the $Fbxw7^{R482Q}$ phenotype (Figure 4.14A). I first examined pathways related to known targets of Fbxw7 (Figure 4.14A). Genes that are positively regulated by Myc and Mtor were downregulated in $Pten^{\Delta/\Delta}$ $Fbxw7^{R482Q/+}$ uteri compared to $Pten^{\Delta/\Delta}$ $Fbxw7^{+/+}$ (MTOR UP.V1 UP, NES = -1.66, Q value = 0.0011; MYC UP.V1 UP, NES = -1.70, Q value = 0.00043). Similarly, genes that

are negatively regulated by Myc and Mtor were upregulated in *Pten*$^{\Delta/\Delta}$ *Fbxw7*$^{R482Q/+}$ uteri (MTOR UP.V1 DN, NES = 1.78, Q value = 0.000027; MYC UP.V1 DN, NES = 1.38, Q value = 0.020). Together these pathways suggest that both Myc and Mtor are not drivers of the carcinogenic phenotype exhibited by *Pten*$^{\Delta/\Delta}$ *Fbxw7*$^{R482Q/+}$ mice.

Two other pathways with known targets of Fbxw7 were highlighted by the analysis. Genes positively regulated by TGF-β (Figure 4.14B) and Notch were enriched in the genes upregulated in *Pten*$^{\Delta/\Delta}$ *Fbxw7*$^{R482Q/+}$ uteri (TGFB UP.V1 UP, NES = 1.77, Q value = 0.000041; NOTCH DN.V1 DN, NES = 1.31, Q value = 0.036). However, their reciprocal pathways representing negatively regulated genes were not significantly enriched in the genes downregulated in *Pten*$^{\Delta/\Delta}$ *Fbxw7*$^{R482Q/+}$ uteri (TGFB UP.V1 DN, NES = -1.08, Q value = 0.21; NOTCH DN.V1 UP, NES = 0.980, 0.32).

Interestingly, one of the most significantly, positively enriched pathways was related to genes that are positively regulated by the Wnt pathway effector and transcription factor, Lef1. In addition to this the reciprocal pathway for negatively regulated genes was also found to be significantly, negatively enriched in the *Pten*$^{\Delta/\Delta}$ *Fbxw7*$^{R482Q/+}$ uteri (Figure 4.14C). Together these two pathways suggest that there may be overexpression or increased activity of the Wnt pathway and, in particular, of Lef1 in the *Pten*$^{\Delta/\Delta}$ *Fbxw7*$^{R482Q/+}$ samples compared to the *Pten*$^{\Delta/\Delta}$ *Fbxw7*$^{+/+}$ samples. Increased Wnt activity is further supported by the enrichment of a pathway describing genes that are upregulated in a cell line expressing constitutively active CTNNB1 (BCAT 100 UP.V1 UP, NES = 1.61, Q value = 0.0193). Another notable pathway that was found to exhibit positive enrichment was related to the Yap/Taz pathway (Figure 4.14D).

To confirm the results of the GSEA, I identified known target genes of Lef1 and Yap1/Wwtr1 based on reports in prior literature and performed RT-qPCR for these target genes, on RNA from uteri collected at 4 and 8 weeks and survival endpoint to determine whether differential expression was maintained (Figure 4.15). For Lef1, the genes matrix metallopeptidase 13 (*Mmp13*) and cellular communication network factor 4 (*Ccn4*), also known as *Wisp1*, were examined [371, 372]. For the Yap/Taz pathway, the genes cellular communication network factor 1 (*Ccn1*), also known as *Cyr61*, and cellular communication network factor 2 (*Ccn2*), also known as *Ctgf*, were examined

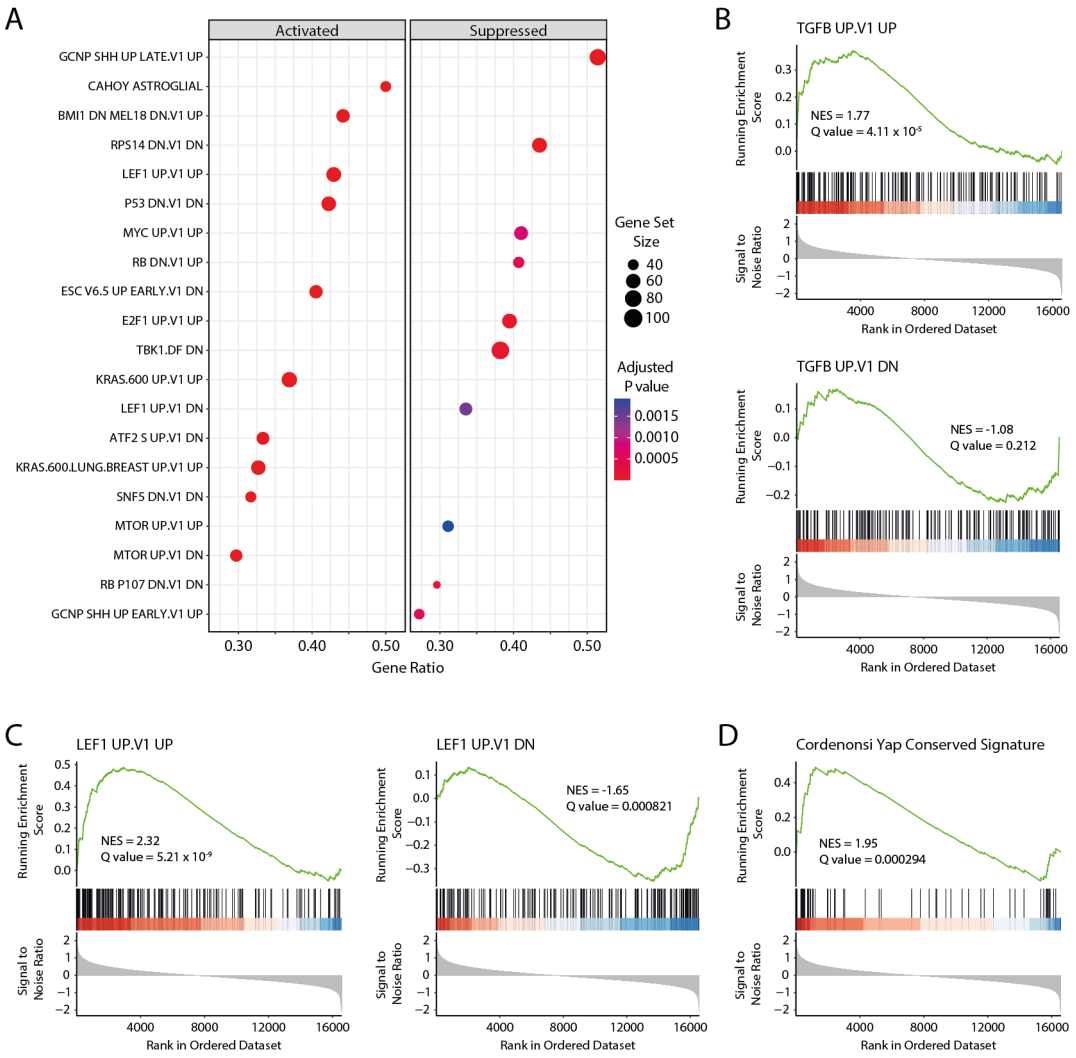

Figure 4.14: GSEA to examine for enrichment of pathways and gene sets with known links to cancer development. **A.** Shows the most significantly enriched pathways that exhibit activation or suppression in the differential gene expression analysis of $Pten^{\Delta/\Delta}$ $Fbxw7^{R482Q/+}$ compared to $Pten^{\Delta/\Delta}$. **B-D.** Individual GSEA plots highlighting pathways with historic relevance to Fbxw7 activity or that appear functionally relevant from the analysis.

[373].

For Lef1 target genes, at 4 weeks there was no significant difference in expression between $Pten^{\Delta/\Delta}$ $Fbxw7^{+/+}$ and $Pten^{\Delta/\Delta}$ $Fbxw7^{R482Q/+}$ (Figure 4.15A). At 8 weeks, differential upregulation of both *Mmp13* and *Wisp1* was found in $Pten^{\Delta/\Delta}$ $Fbxw7^{R482Q/+}$ uteri, validating the findings of the microarray (Figure 4.15C). Interestingly, *Mmp13* was significantly upregulated in $Pten^{\Delta/\Delta}$ $Fbxw7^{+/+}$ mice compared to wild-type, but *Wisp1* was not. Significant upregulation of both target genes in $Pten^{\Delta/\Delta}$ $Fbxw7^{R482Q/+}$ compared to $Pten^{\Delta/\Delta}$ $Fbxw7^{+/+}$ mice was maintained at survival end point (Figure 4.15E).

Ctgf was found to be significantly upregulated in $Pten^{\Delta/\Delta}$ $Fbxw7^{R482Q/+}$ uteri at 4 weeks, but *Cyr61* was not (Figure 4.15B). Although, *Cyr61* was significantly upregulated in both $Pten^{\Delta/\Delta}$ $Fbxw7^{+/+}$ and $Pten^{\Delta/\Delta}$ $Fbxw7^{R482Q/+}$ compared to wild-type mice. The findings of the microarray were validated for Yap1/Wwtr1, with both *Ctgf* and *Cyr61* found to be significantly upregulated in $Pten^{\Delta/\Delta}$ $Fbxw7^{R482Q/+}$ uteri compared to $Pten^{\Delta/\Delta}$ $Fbxw7^{+/+}$ (Figure 4.15D). At survival end point, significant upregulation was maintained in the $Pten^{\Delta/\Delta}$ $Fbxw7^{R482Q/+}$ uteri compared to $Pten^{\Delta/\Delta}$ $Fbxw7^{+/+}$ (Figure 4.15F).

4.3.8 Lef1 gene signature is not caused by immune infiltration

Lef1 is a vital component of the developmental signalling pathways that are required for maturation of thymocytes and maintenance of T cells [374, 375]. Therefore, a potential driving force of the signature highlighted by GSEA could be differential alterations to the immune environment of the uteri in both genotypes. To examine this possibility, gene sets related to T-cell mediated immune response were examined in the expression data for $Pten^{\Delta/\Delta}$ $Fbxw7^{+/+}$ and $Pten^{\Delta/\Delta}$ $Fbxw7^{R482Q/+}$ mice at 8 weeks (Figure 4.16A). Three different gene set associated with T-cell activity were examined, none of which exhibited any indication of significant upregulation or downregulation between $Pten^{\Delta/\Delta}$ $Fbxw7^{+/+}$ and $Pten^{\Delta/\Delta}$ $Fbxw7^{R482Q/+}$ uteri.

Further to this, expression of CD3 epsilon subunit of T-cell receptor complex (*Cd3e*) was examined by RT-qPCR in both 8 week (Figure 4.16B) and survival end point samples (Figure 4.16C). Cd3e forms a vital component of the T-cell receptor complex that is expressed on the surface of T-cells, expression in tissue such as the uterus is likely to reflect the extent of immune infiltration and, therefore, would indicate the likelihood of the Lef1 signature arising from an immune component. At both time points expression of Cd3e was not found to be significantly upregulated in the $Pten^{\Delta/\Delta}$ $Fbxw7^{R482Q/+}$ samples, instead a non-significant trend towards downregulation was observed, suggesting that an increased T-cell infiltrate is unlikely to be the cause of the Lef1 gene signature observed.

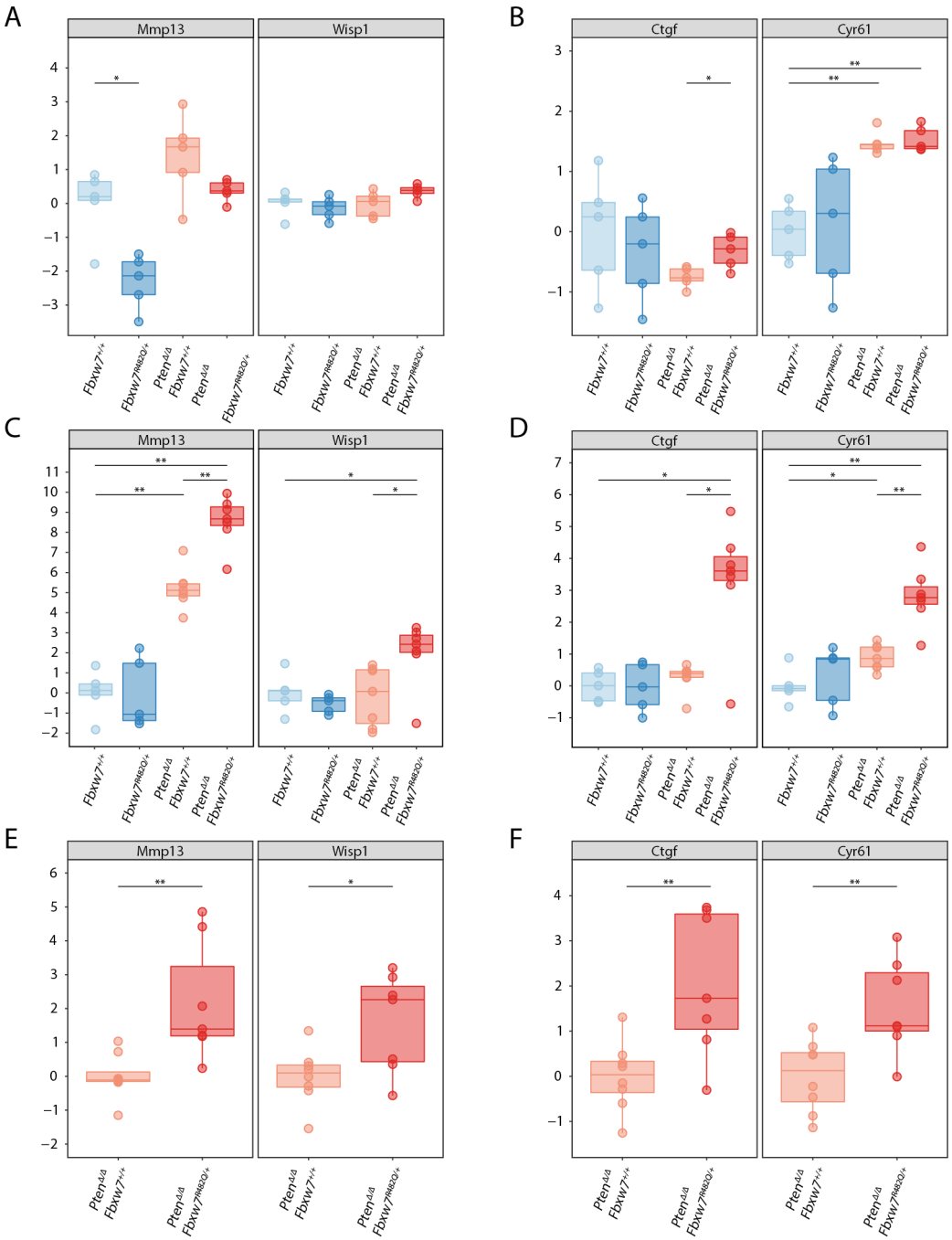

Figure 4.15: Examination of target genes of the pathways highlighted by GSEA in additional time points. Relative gene expression as determined by RT-qPCR of RNA extracted from fresh frozen bulk uterine tissue. **A, C, E.** Expression of *Mmp13* and *Wisp1*, Lef1 target genes, collected at 4 weeks - **A**, 8 - weeks - **C**, and survival end point - **E**. **B, D, F.** Expression of *Ctgf* and **Cyr61**, Yap1 target genes, collected at 4 weeks - **B**, 8 - weeks - **D**, and survival end point - **F**. Expression is normalised to the $Fbxw7^{+/+}$ genotype for samples at 4 and 8 weeks and to the $Pten^{\Delta/\Delta}$ $Fbxw7^{+/+}$ genotype at survival end point.

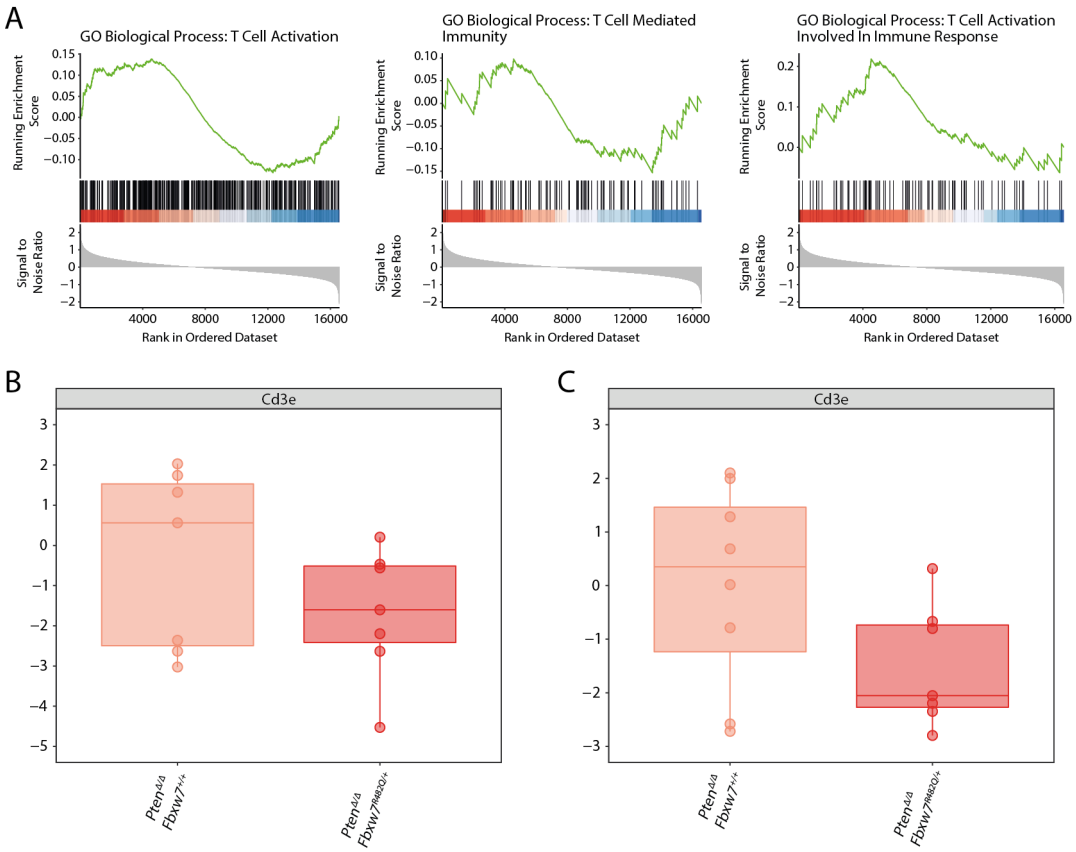

Figure 4.16: Examination of the gene sets associated with immune response and markers of T-cells in $Pten^{\Delta/\Delta}$ $Fbxw7^{+/+}$ and $Pten^{\Delta/\Delta}$ $Fbxw7^{R482Q/+}$ mice. **A.** Individual GSEA plots showing a lack of enrichment of genes associated with a T-cell response in the differentially expressed gene list derived from the microarray analysis. **B, C.** Expression of Cd3e, T-cell marker, as determined by RT-qPCR from fresh frozen, bulk uterine RNA collected at 8 weeks - **B** and survival end point - **C**. Expression is normalised to the $Pten^{\Delta/\Delta}$ $Fbxw7^{+/+}$ genotype.

4.3.9 Validation of Lef1 signature enrichment in alternative human models of *FBXW7* mutation

To validate the findings of the microarray, I wanted to examine for similar pathway dysregulation in alternative data sets based on *FBXW7* mutation. A recent publication by Thirimanne *et al.* generated colorectal cancer cell lines derived from HCT116, with homozygous deletion or heterozygous R505C mutation of *FBXW7* [346]. In the study, these cell lines were subjected to RNA sequencing analysis and DEGs were determined for both the $FBXW7^{\Delta/\Delta}$ and $FBXW7^{R505C/+}$ cells compared to $FBXW7^{+/+}$ cells [346].

In order to examine the DEGs from Thirimanne *et al.*'s study, I ranked genes based on fold change and statistical significance from their DEG analysis and performed GSEA using the oncogenic signature gene sets used to analyse the microarray data (Figure

4.17). Pathway analysis for the cells with *FBXW7* deletion revealed numerous similarities with the results from the $Pten^{\Delta/\Delta}$ $Fbxw7^{R482Q/+}$ mouse model (Figure 4.17A). Most significantly, both the LEF1 UP.V1 UP and LEF1 UP.V1 DN pathways were significantly positively and negatively enriched, respectively, matching the observations from the microarray analysis. In addition, pathways indicating downregulation of targets of MTOR were significantly enriched, suggesting a lack of MTOR activity.

The enriched pathways in the $FBXW7^{R505C/+}$ cell lines resembled the pathways found in the $FBXW7^{\Delta/\Delta}$ cells and the $Pten^{\Delta/\Delta}$ $Fbxw7^{R482Q/+}$ mice. The LEF1 UP.V1 UP pathway exhibited the highest level of positive enrichment in these cells and the LEF1 UP.V1 DN pathway was also significantly, negatively enriched. Interestingly, in this analysis pathways suggesting a reduction of MYC activity (negative enrichment of MYC UP.V1 UP), and a potential increase in YAP1 target genes were also present, equivalent to the observations from the mouse expression data. However, a matching pattern was not observed with MTOR, which in this data set exhibited potentially increased activity, contrasting with the mouse model results and the $FBXW7^{\Delta/\Delta}$ cell line.

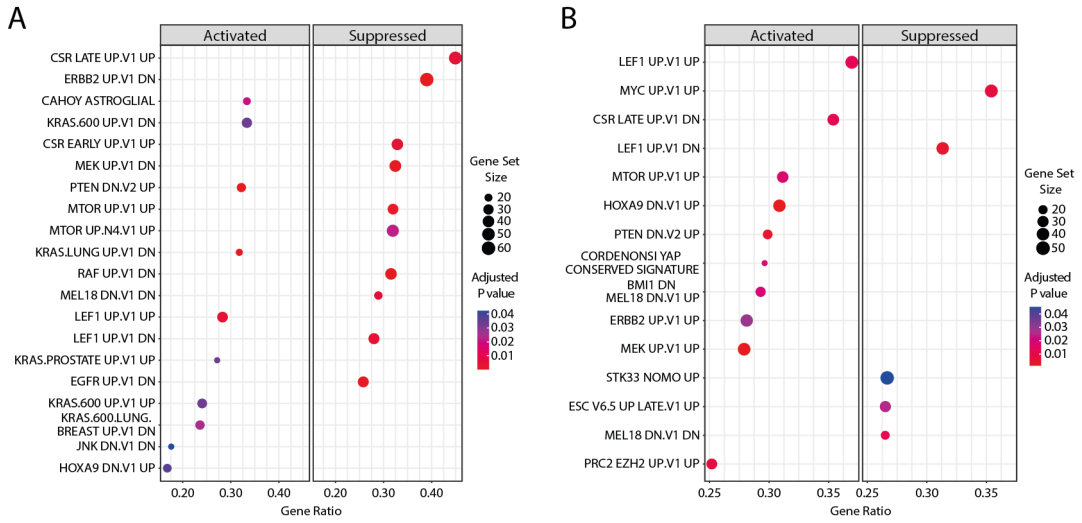

Figure 4.17: GSEA analysis of published differential gene expression data from FBXW7-mutant colorectal cancer cell line model. **A, B.** Show the most positively and negatively enriched oncogenic gene sets from GSEA of the differentially expressed genes provided by [346]. **A.** Represents the comparison of HCT116 cells exhibiting $FBXW7^{\Delta/\Delta}$ and $FBXW7^{+/+}$. **B.** Represents the comparison of HCT116 cells exhibiting $FBXW7^{R505C/+}$ and $FBXW7^{+/+}$.

4.3.10 *In silico* search for *FBXW7* target CPD highlights sites in LEF1 and other Wnt and Hippo pathway transcription factors

The observed differential gene expression signatures in two independent data sets suggests increased activity of the Wnt and/or Hippo pathways in the $Pten^{\Delta/\Delta}$ $Fbxw7^{R482Q/+}$ samples. It is likely that the increased activity is driven by the heterozygous mutation of *Fbxw7* leading to loss of, or reduced, proteasomal degradation of positive regulators of these pathways. In order to examine whether members of these pathways could in fact be ubiquitination targets of FBXW7, I performed a literature search to identify published reports of FBXW7 substrates, which performed experimental confirmation of the CPD sequence within the identified target. This led to identification of a total of 21 papers (Appendix C). From these papers, I extracted the amino acid sequences of the identified CPDs, 24 in total, and collated sequences +/- 4 amino acids either side of the "0" and "+4" positions, to generate a consensus sequence (Figure 4.18A). This sequence closely resembled the previously discussed consensus, however, it also highlighted significant variation at many of the positions, particularly those preceding the initial "0" position. From this literature search, I decided to use the core sequence of "T/S P X X T/S/E" to search the primary protein sequences available from the UniProt database to identify potential FBXW7 targets.

Interestingly, this agnostic search highlighted CPDs in the transcriptional cofactors of both the Wnt and Hippo pathways, including one in LEF1 and YAP1 (Figures 4.18B and 4.19). Examination of the CPDs showed that the same "T P L I T" sequence was found in 3 of the 4 Wnt transcription factors (LEF1, TCF7L1, and TCF7L2) with three additional CPDs in TCF7L1 and two in TCF7L2. As the "0", and usually the "+4", position of the CPD must be phosphorylated for interaction with FBXW7, I examined the PhosphoSite Plus database to confirm if there is published evidence of phosphorylation at these sites, indicated as a red highlight (Figures 4.18B and 4.19). The recurring "T P L I T" site present in the three Wnt transcription factors has evidence of phosphorylation of both T residues in LEF1, but only the first T residue in TCF7L1, and TCF7L2 indicating that this could be a candidate CPD. Finally, if these identified motifs do represent

FBXW7 CPDs they would be a vital aspect of protein control and therefore these regions would, likely, be evolutionarily conserved. Alignment of protein sequences from various vertebrates revealed the common "T P L I T" sequence exhibits high levels of conservation across all three Wnt transcription factors. Two of the additional sites in TCF7L2 and one in TCF7L1 also exhibit good conservation, particularly in the core of the motif.

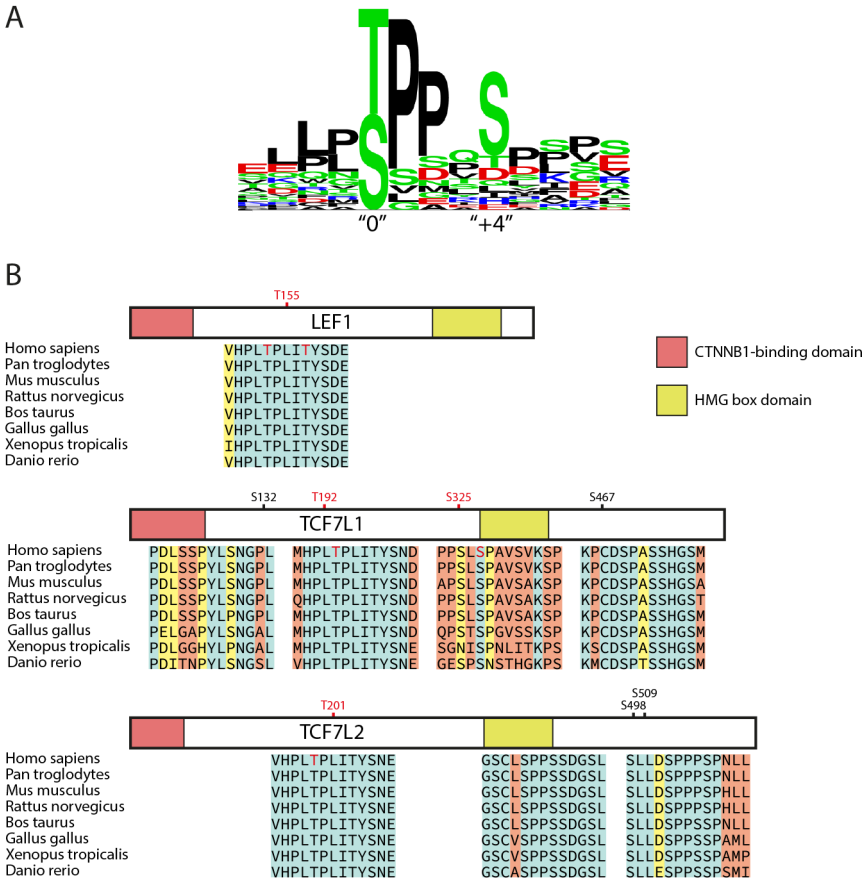

Figure 4.18: *In silico* evaluation of FBXW7 CPDs and their presence in Wnt transcription factors. **A.** The primary sequence motif of published CPDs that used SDM to disrupt the interaction between FBXW7 and the target (n = 20). **B.** Results of a regular expression search informed by the sequence motif in **A** to identify potential CPD sequences in the primary protein sequences of Wnt transcription factors. Also shown is the sequence conservation of the potential CPD sequences in a selection of vertebrates. Perfect conservation is highlighted in green, a single variant is highlighted in yellow, and more than one variant is highlighted in red. All sequence data was acquired from UniProt. Red text colour indicates a known phosphorylation event at that position recorded in the PhosphoSitePlus database.

The identified CPD, S367, in YAP1 exhibits poor conservation with core sequence having multiple variable AAs. Although not highlighted by the initial search, a secondary CPD was identified in YAP1 that matched closely with CPDs identified by the

literature search. Additionally, the same sequence was found in Wwtr1, and is found to be phosphorylated in both proteins along with being well conserved in both, matching the likely profile of an FBXW7 CPD.

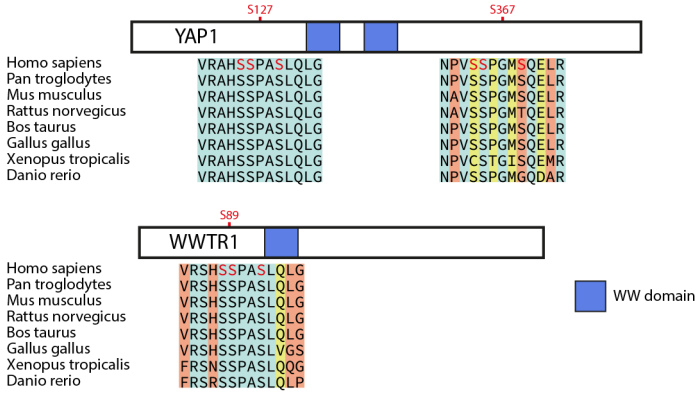

Figure 4.19: *In silico* evaluation of FBXW7 CPDs presence in Hippo transcription factors. Results of a regular expression search informed by the sequence motif in 4.18A to identify potential CPD sequences in the primary protein sequences of Hippo pathway transcription factors. Also shown is the sequence conservation of the potential CPD sequences in a selection of vertebrates. Perfect conservation is highlighted in green, a single variant is highlighted in yellow, and more than one variant is highlighted in red. All sequence data was acquired from UniProt. Red text colour indicates a known phosphorylation event at that position recorded in the PhosphoSitePlus database.

4.3.11 Wnt and Hippo pathway regulators do not exhibit increased expression in *Pten*$^{\Delta/\Delta}$ *Fbxw7*$^{R482Q/+}$ mice

The transcriptomic data suggested dysregulation of the Wnt or Hippo pathway concurrent with *Fbxw7*^{R482Q} mutation. Additionally, several transcription factors from both pathways contain potential CPDs that could allow interaction with Fbxw7. However, as the regulation by Fbxw7 occurs post-translationally, examination of the protein expression of these potential targets is vital to understand whether loss of regulation may be occurring. To examine protein expression, western blotting analysis for Lef1, Tcf7l2, Yap1, and Wwtr1 was performed using protein lysates from bulk fresh frozen uterine tissue at 8 weeks and survival end point (Figure 4.20). Unfortunately, at both time points staining for Lef1 was variable and weak, attempts at densitometric quantification proved unreliable precluding clear conclusions on expression of Lef1 in the *Pten*$^{\Delta/\Delta}$ *Fbxw7*$^{R482Q/+}$ mice. Detection of Tcf7l2 was more reliable, but densitometric analysis, at both time points, indicated no significant difference in expression. Similar results were

observed with Wwtr1, which exhibited good detection but no significant increase in expression at either time point. Finally, Yap1 was not found to be differentially expressed at 8 weeks, but was found to be significantly downregulated in the $Pten^{\Delta/\Delta}$ $Fbxw7^{R482Q/+}$ mice at survival end point (median $\log_2$(Relative Expression) -0.549, P=0.030 Wilcoxon Rank Sum test).

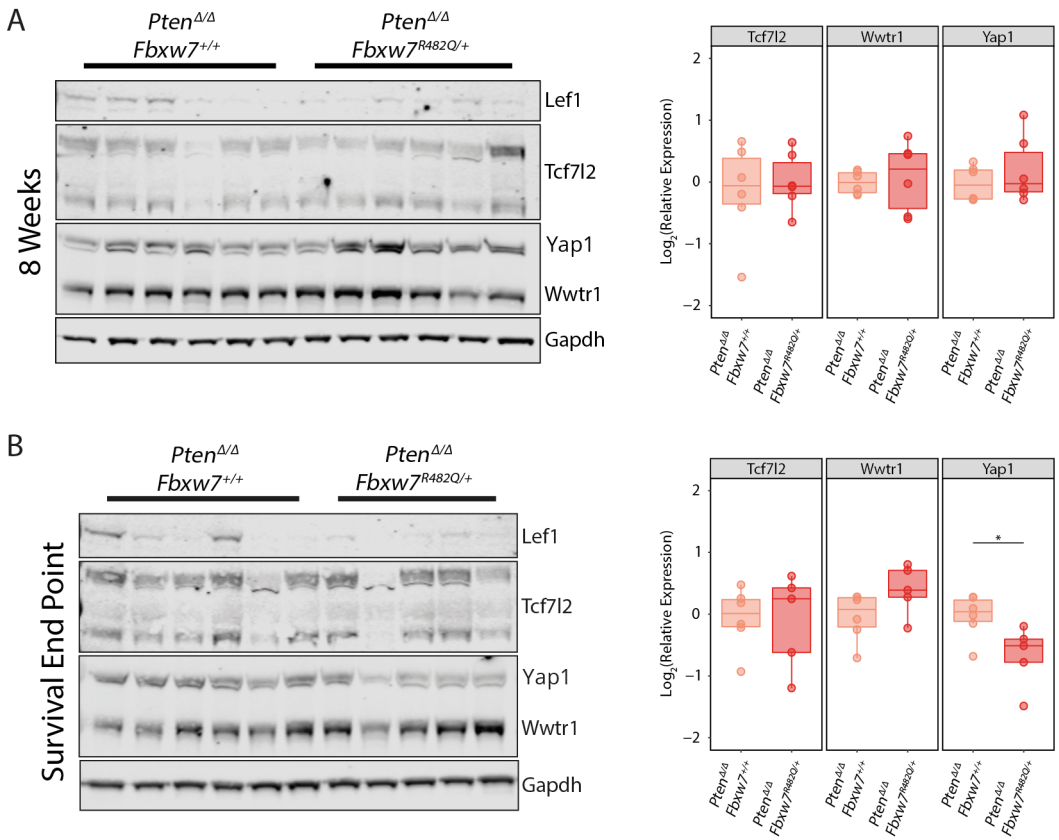

Figure 4.20: Western blotting analysis of potential targets highlighted by the transcriptomic profiling of $Pten^{\Delta/\Delta}$ and $Pten^{\Delta/\Delta}$ $Fbxw7^{R482Q/+}$ mice. **A, B.** Western blotting analysis of Lef1, Tcf7l2, Yap1 and Wwtr1 with concomitant densitometry quantification of the protein expression from the western blot, normalised to Gapdh expression. Analysis was performed on protein lysates generated from fresh frozen bulk uterus tissue collected from mice at 8 weeks - **A** and survival end point - **B**.

Due to the lack of differential expression observed and the lack of reliable detection of Lef1 by western blot, IHC was used to examine the contextual expression of these proteins (Figure 4.21). Tcf7l2 expression in normal mouse uterus was generally confined to the epithelium and was observed in both the glandular and luminal epithelium. However, the expression was more prominent in the glandular epithelium with heterogeneous positivity in the luminal epithelium. Expression patterns in both $Pten^{\Delta/\Delta}$ $Fbxw7^{+/+}$ and $Pten^{\Delta/\Delta}$ $Fbxw7^{R482Q/+}$ mice did not differ from that of the wild-

type samples. Nevertheless, there may have been stronger staining in the glands of *Pten*$^{\Delta/\Delta}$ *Fbxw7*$^{R482Q/+}$ mice compared to *Pten*$^{\Delta/\Delta}$ *Fbxw7*$^{+/+}$.

Lef1 expression in wild-type mice followed a similar pattern to Tcf7l2, with expression predominantly observed in the glandular epithelium, with faint luminal staining seen in a subset of samples. Interestingly, Lef1 staining was not uniform in the epithelium with glands and regions of glands in proximity to the stratum basalis exhibiting higher levels of expression (Figure 4.21). Additionally, Lef1 staining was more variable than Tcf7l2, with some samples exhibiting little to no expression and some exhibiting high epithelial expression with prominent stromal staining in the regions directly adjacent the epithelium, as can be seen in the *Fbxw7*$^{+/+}$ sample at survival end point (Figure 4.21). At 8 weeks, *Pten*$^{\Delta/\Delta}$ *Fbxw7*$^{+/+}$ mice exhibited low levels of Lef1 staining in the glandular epithelium proximal to the myometrium and epithelium adjacent stroma, however, there was no evidence of staining in the lumen. While Lef1 expression in *Pten*$^{\Delta/\Delta}$ *Fbxw7*$^{R482Q/+}$ samples was not widespread, the expression was not confined to just glandular epithelium or adjacent stroma as in the *Pten*$^{\Delta/\Delta}$ *Fbxw7*$^{+/+}$ mice, instead expression was found focally in glands throughout the tissue. At survival end point staining for Lef1 was less prominent in the epithelium of both *Pten*$^{\Delta/\Delta}$ *Fbxw7*$^{R482Q/+}$ and *Pten*$^{\Delta/\Delta}$ *Fbxw7*$^{+/+}$ mice and both genotypes exhibited some strong staining in epithelial-associated stroma. However, in general there appeared to be increased glandular positivity in the *Pten*$^{\Delta/\Delta}$ *Fbxw7*$^{R482Q/+}$ samples, compared to the *Pten*$^{\Delta/\Delta}$ *Fbxw7*$^{+/+}$ samples.

Alongside staining for Lef1 and Tcf7l2, Ctnnb1 staining was performed, as its dissociation from the plasma membrane and translocation to the nucleus forms a vital part of activation of the Wnt signalling pathway, making it a key indicator of pathway activation (Figure 4.21). As expected all genotypes showed intense staining for Ctnnb1 with the overwhelming majority of epithelial cells exhibiting strong membrane associated staining. Across all genotypes there was little evidence of strong nuclear staining, but a subset of glands did exhibit weaker membrane staining and more cytoplasmic staining. Interestingly, when correlated with Lef1 and Tcf7l2 staining, the glands that exhibited cytoplasmic Ctnnb1 tended to be positive for Lef1 expression, though no correlation in expression pattern was observed between Tcf7l2 and Ctnnb1. This pattern was ob-

served across all genotypes, but appeared more frequent in the $Pten^{\Delta/\Delta}$ $Fbxw7^{R482Q/+}$ samples, alongside the more frequent Lef1 staining.

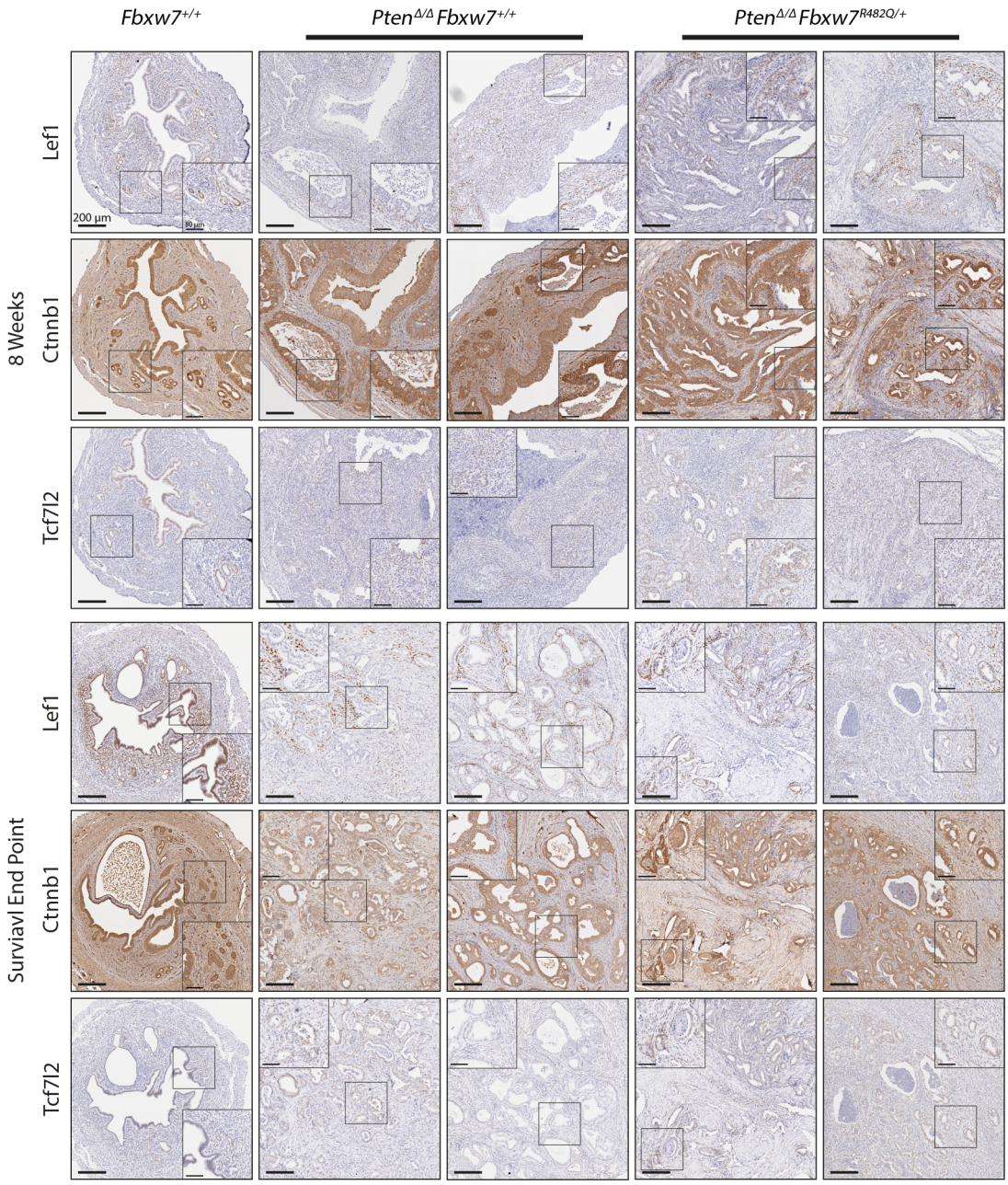

Figure 4.21: IHC staining for Wnt pathway proteins. Staining for Lef1, Ctnnb1, and Tcf7l2 in FFPE sections from $Pten^{\Delta/\Delta}$ and $Pten^{\Delta/\Delta}$ $Fbxw7^{R482Q/+}$ mouse uteri collected at 8 weeks and survival end point with $Fbxw7^{+/+}$ provided as reference for a wild-type mouse.

Expression of Hippo pathway targets, Yap1 and Wwtr1, was performed using a dual staining antibody, targeting both proteins (Figure 4.22). The staining in $Pten^{\Delta/\Delta}$ $Fbxw7^{+/+}$ mice was mainly confined to the epithelium, with the majority of cells exhibit-

ing cytoplasmic expression with apparent exclusion from the nucleus. However, a minority of cells did exhibit nuclear staining. In the 8 week samples, nuclear staining was generally found in the cells closest to the stratum basalis, similar to the staining pattern of Lef1. Whereas, at survival end point nuclear staining was found more sporadically in glands throughout the tissue. The pattern of staining in $Pten^{\Delta/\Delta}$ $Fbxw7^{R482Q/+}$ mice did not notably differ from that seen in $Pten^{\Delta/\Delta}$ $Fbxw7^{+/+}$ mice. Overall, there does appear to be minor changes in the pattern of staining for Lef1 and Ctnnb1 however, but obvious changes are not apparent in Tcf7l2, Yap1, and Wwtr1.

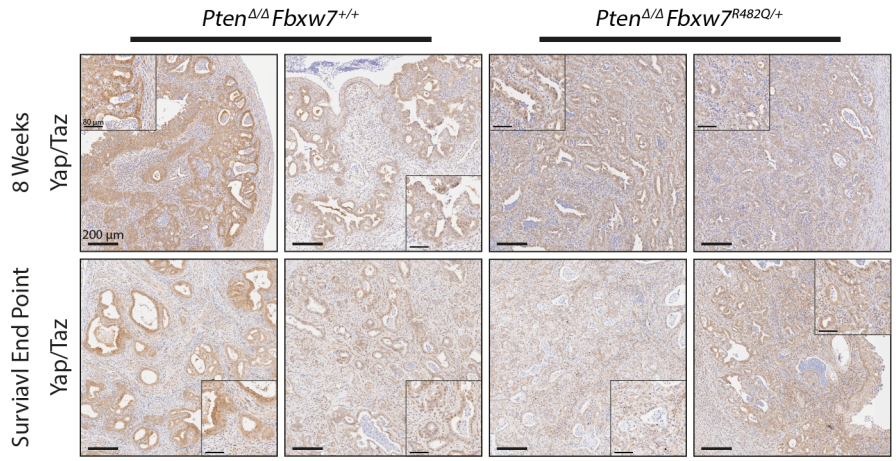

Figure 4.22: IHC staining for Wnt pathway proteins. Combined staining for Yap1 and Wwtr1 in FFPE sections from $Pten^{\Delta/\Delta}$ and $Pten^{\Delta/\Delta}$ $Fbxw7^{R482Q/+}$ mouse uteri collected at 8 weeks and survival end point.

4.3.12 Interaction between Fbxw7 and Wnt transcription factors is present and is disrupted by WD40 mutation

Given that the previous results suggested that the identified Wnt and Hippo pathway components could be targets of FBXW7, I performed co-immunoprecipitation analysis to examine this. Firstly, I generated plasmids to allow expression of epitope tagged wild-type versions of FBXW7, LEF1, YAP1, WWTR1, and CCNE1, as a positive control. Following this SDM was used, as described in Section 2.6.4, to mutate potential CPDs or the WD40 domain of FBXW7. A list of all plasmids used for this analysis can be found in Appendix A.

HEK293T cells were transfected with FLAG-HA-tagged FBXW7 and MYC-tagged

CDS of either LEF1, YAP1, WWTR1 or CCNE1. Lysates were collected and incubated with magnetic beads conjugated with an antibody specific for the FLAG epitope to allow precipitation of FBXW7 and its interacting partners, which were then assayed by western blot with a MYC-tag specific antibody (Figure 4.23A). When co-transfected with FBXW7, strong pull down of CCNE1 was observed, as expected. Additionally, when co-transfected with FBXW7 but not when transfected alone, pull down of both LEF1 and WWTR1 was detected, indicating they must interact with FBXW7. YAP1 did not appear to be pulled down when co-transfected with FBXW7 suggesting the two proteins do not interact.

As the *in silico* CPD prediction found a more classical motif in LEF1, I decided to attempt to disrupt the observed interaction of FBXW7 and LEF1 by introducing common mutations exhibited in the WD40 domain of FBXW7, R465C, R479Q, and R505C, or by changing the "0" position of the suspected CPD to an alanine residue, T155A (Figure 4.23B). Pull down of wild-type FBXW7 when expressed with wild-type LEF1 produced the expected detection of LEF1 by western blot, however, introduction of the T155A mutation did not abrogate the interaction. Similarly, mutations to the substrate binding domain of FBXW7 did not stop the interaction, although the amount of LEF1 pulled down appeared to be reduced in these conditions. One confounding factor for this analysis was large expression difference observed between wild-type FBXW7 and mutant FBXW7 despite equal material being transfected and similar transfection efficiencies observed. The reason for this difference is unclear.

Although these experiments were indicative of an interaction between FBXW7 with LEF1 and WWTR1, the determination of the CPD sequence in LEF1 could not easily be made. One potential confounding factor for this was the variability in the nature of the interaction that was observed in repetitions of the experiment and, in particular, variation in the expression of FBXW7 when mutated. In order to address these issues, I looked at methods that could be used to stabilise the interaction between the potential targets and FBXW7. As a positive interaction between FBXW7 and its targets should lead to degradation of the target and a reduction in the pool of protein available for interaction, the main method explored to stabilise the interaction was to block ubiqui-

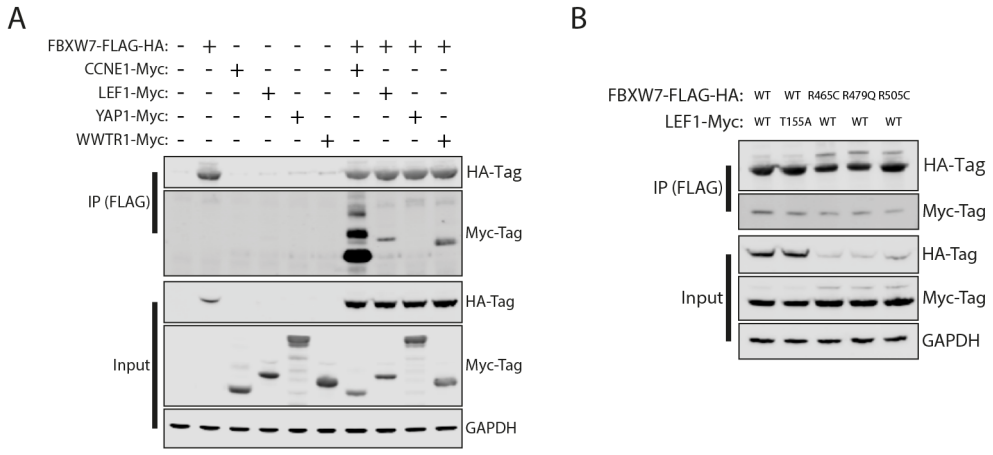

Figure 4.23: Co-immunoprecipitation analysis of the interaction between FBXW7 and potential novel targets. Co-immunoprecipitation by pull down of the FLAG-tag, associated with FBXW7, from lysates generated in HEK293T cells transiently transfected with the indicated plasmids. **A.** Shows the extent of interaction between wild-type FBXW7 and each of the potential targets. **B.** Shows the extent of interaction between wild-type FBXW7 or FBXW7 with introduction of common WD40 domain mutations with wild-type LEF1 or LEF1 exhibiting mutation of the "0" position T of the predicted CPD sequence.

tination. To achieve this, I used SDM to delete the Fbox domain from the FBXW7 CDS, which as previously discussed, is responsible for the interaction with the SKP1 allowing formation of the larger SCF^{FBXW7} complex required for ubiquitination. In addition, for examining if mutation could disrupt interaction, I also performed SDM to combine the three most common WD40 mutations, R465C, R479Q, and R505C, together in to the FBXW7 CDS which was then termed the WD40 variant.

Transfection of the ΔFbox and FBXW7-WD40 plasmids, alone and in combination with LEF1, in to HEK293T followed by co-immunoprecipitation did not result in stabilisation of the interaction between FBXW7 and LEF1 (Figure 4.24A). Formation of the SCF^{FBXW7} complex was successfully disrupted, as evidenced by the large decrease in SKP1 detected in the IP fraction of the samples transfected with ΔFbox versions of FBXW7. However, while the interaction between FBXW7 and LEF1 was evident in the wild-type condition and FBXW7-WD40 transfected conditions, there was no evidence of interaction in the ΔFbox condition. Interestingly, the ΔFbox and FBXW7-WD40 transfected conditions exhibited much higher expression of FBXW7 in the input fraction, suggesting self-ubiquitination may be occurring with functionally competent FBXW7.

As the interaction between FBXW7 and its targets is dependent on phosphorylation, thus adding an additional element of regulatory control to potential interactions. If the

kinase cascades that lead to phosphorylation of the target are not active in the cell examined, then interaction cannot be observed. This leads to a scenario where targets can be regulated differentially by FBXW7 in different cell types. To examine the possibility that heightened phosphorylation of LEF1 may be an endometrial cell specific event, I repeated the previous transfections in the NOU1 cell line, an endometrial cancer cell line exhibiting loss of PTEN (Figure 4.24B). While the interaction of FBXW7 with LEF1 can be observed in this cell line, the efficiency of the pull down was poor, as evidenced by the weak detection of SKP1. When compared to the analysis in HEK293T cells, there did not appear to be evidence of a stronger interaction in the endometrial cell line, potentially due to the low transfection efficiency in NOU1 compared to HEK293T. Interestingly, the introduction of ΔFbox mutants in to NOU1 appeared to have an opposite effect to that seen in the HEK293T cells, with a stronger interaction observed. However, there was still a lack of evidence of FBXW7-WD40 mutation disrupting the interaction with LEF1.

As the deletion of the Fbox domain did not stabilise the interaction, I looked at alternative methods to block the ubiquitination of the targets. Post-translational modification, through neddylation of CUL1, plays a vital role in activation of enzyme activity, thereby enabling ubiquitination of bound targets [376]. The addition of a small molecule inhibitor of neddylation, MLN4924, prior to collection of the protein lysates could provide disruption of ubiquitination without modification to the FBXW7 CDS. Therefore, MLN4924 was added to transfected cells for 24 hours before collection of protein lysates. Co-immunoprecipitation analysis of these lysates (Figure 4.24C) show reduced neddylation of CUL1 as the loss of the higher molecular weight (neddylated) form. While not a large difference, there was a notable increase in the amount of LEF1 detection in the IP fraction following treatment with MLN4924, indicating some stabilisation of the interaction. In addition, there was also an increase in the input expression of FBXW7 across the conditions, further suggesting that FBXW7 self-ubiquitination may be responsible for the variable expression observed.

Examination of protein interaction was repeated using MLN4924 treatment for 24 hours prior to the extraction of protein lysates. For this analysis a CDS for TCF7L2

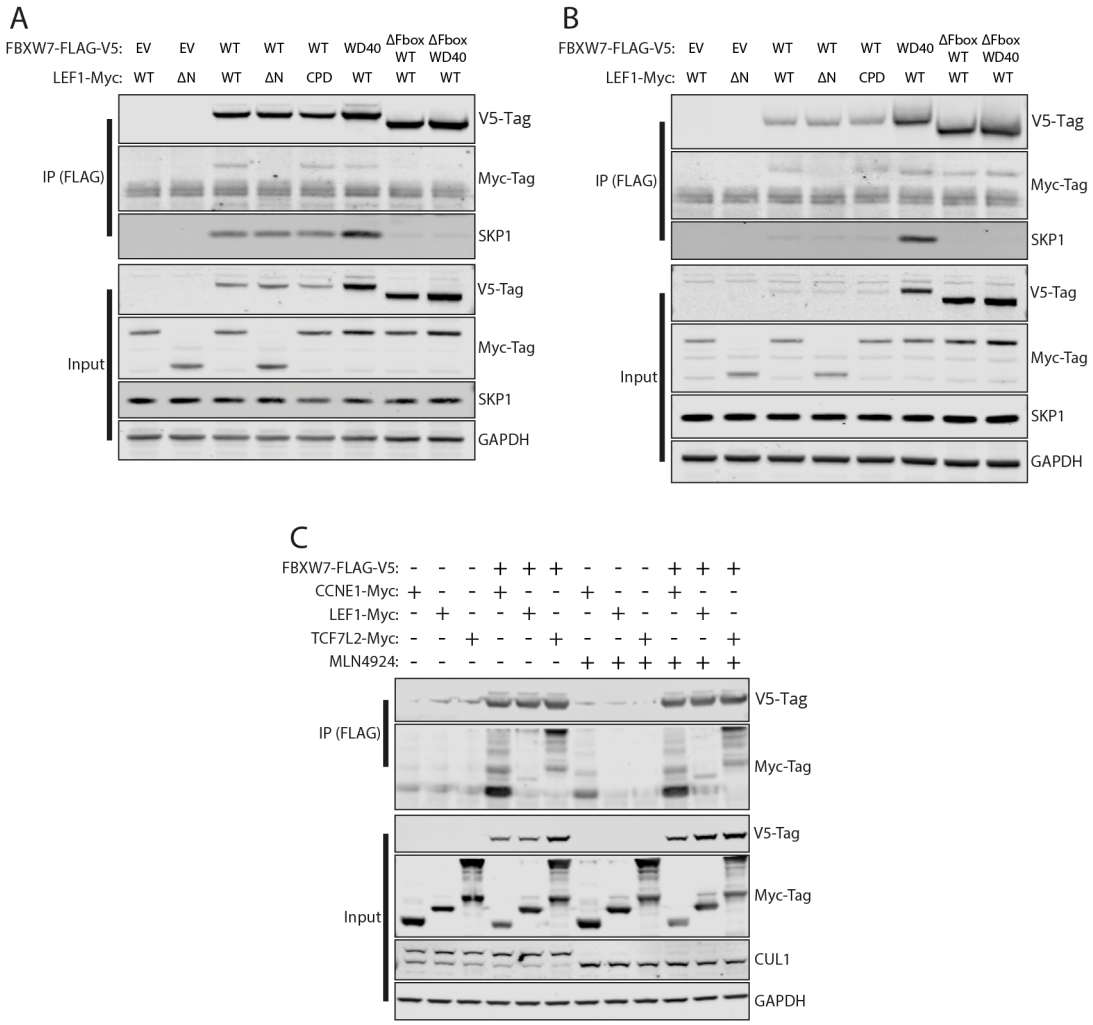

Figure 4.24: Extent of disruption of the interaction between FBXW7 and Wnt transcription factors by SDM. **A, B.** Co-immunoprecipitation performed on lysates from transiently transfected of HEK239T - **A** or NOU1 - **B** cells with FBXW7 and/or LEF1 plasmids with the following modifications: ΔN - deletion AAs 1-61 of the LEF1 CDS, CPD - substitution of T155 and T159 of LEF1 with alanine residues, WD40 - combined mutation of R465, R479 and R505 in the FBXW7 CDS, ΔFbox - deletion of the F-box domain from the FBXW7 CDS. **C.** Co-immunoprecipitation of protein lysates of HEK293T cells transiently transfected and treated with 300 nM MLN4924 for 24 hours prior to cell lysis, as indicated.

was acquired and included, and inversion of the molecular tags was performed to allow reciprocal pull down of FBXW7 by the target of interest (Figure 4.25). Pull down of FBXW7 co-transfected with LEF1 clearly indicated an interaction, due detection of LEF1 in the IP fraction, furthermore, the reciprocal experiment precipitating LEF1, using the FLAG-tag, also showed interaction with FBXW7 (Figure 4.25A). Similar results are observed with TCF7L2 with evidence of interaction observed with precipitation of FBXW7 and TCF7L2 (Figure 4.25B). Interestingly, the amount of TCF7L2 that precipitated with

FBXW7, and vice versa, appeared higher than that seen with LEF1.

Results for Hippo pathway proteins were less clear. For WWTR1, when FBXW7 was immunoprecipitated there was evidence of interaction with WWTR1 (Figure 4.25C). However, when WWTR1 was immunoprecipitated, pull down of FBXW7 was not apparent. Whereas for YAP1, the interaction appeared weak when FBXW7 was precipitated, but when YAP1 is pulled down a potential interaction with FBXW7 is more evident (Figure 4.25D).

The previous analysis demonstrated interaction of FBXW7 with the transcriptional effectors of the Wnt pathway, LEF1 and TCF7L2. However, Jiang *et al.* previously published that FBXW7 targets CTNNB1 for ubiquitination and degradation [377]. Although, this was not observed in an alternative study from Yang *et al.* [378]. If there is interaction between FBXW7 and CTNNB1, the observed pull down of LEF1 and TCF7L2 may be due to mutual interaction with CTNNB1 and not a direct interaction with FBXW7. To examine this, FBXW7 was transfected alone and in combination with LEF1 or TCF7L2 and immunoblotting for endogenous CTNNB1 was performed after immunoprecipitation of FBXW7 (Figure 4.26). A very small amount of CTNNB1 was pulled down when FBXW7 is transfected alone, and a similarly small amount pulled down when co-transfected with LEF1 (Figure 4.26A). Similar results were seen with TCF7L2, weak detection of CTNNB1 was observed in the IP fraction when FBXW7 was transfected alone (Figure 4.26B). However, when combined with TCF7L2, there appears to be a much stronger interaction between FBXW7 and CTNNB1, suggesting that the interaction between FBXW7 and CTNNB1 is facilitated by TCF7L2 (Figure 4.26B).

In order to further examine this, SDM was used to delete the first 61AA from the CDS of LEF1, which are required for CTNNB1-binding. This plasmid was transfected and pull down of LEF1 was performed. As expected, CTNNB1 was strongly detected in the IP fraction when transfected with the full length version of LEF1, whereas, no CTNNB1 was detected with the ΔN version (Figure 4.26C). However, the interaction between LEF1 and FBXW7 was evident when transfected with both the full length and ΔN versions of LEF1. This indicated that the interaction of FBXW7 and LEF1/TCF7L2 does not occur indirectly through CTNNB1 and additionally shows that CTNNB1 is not

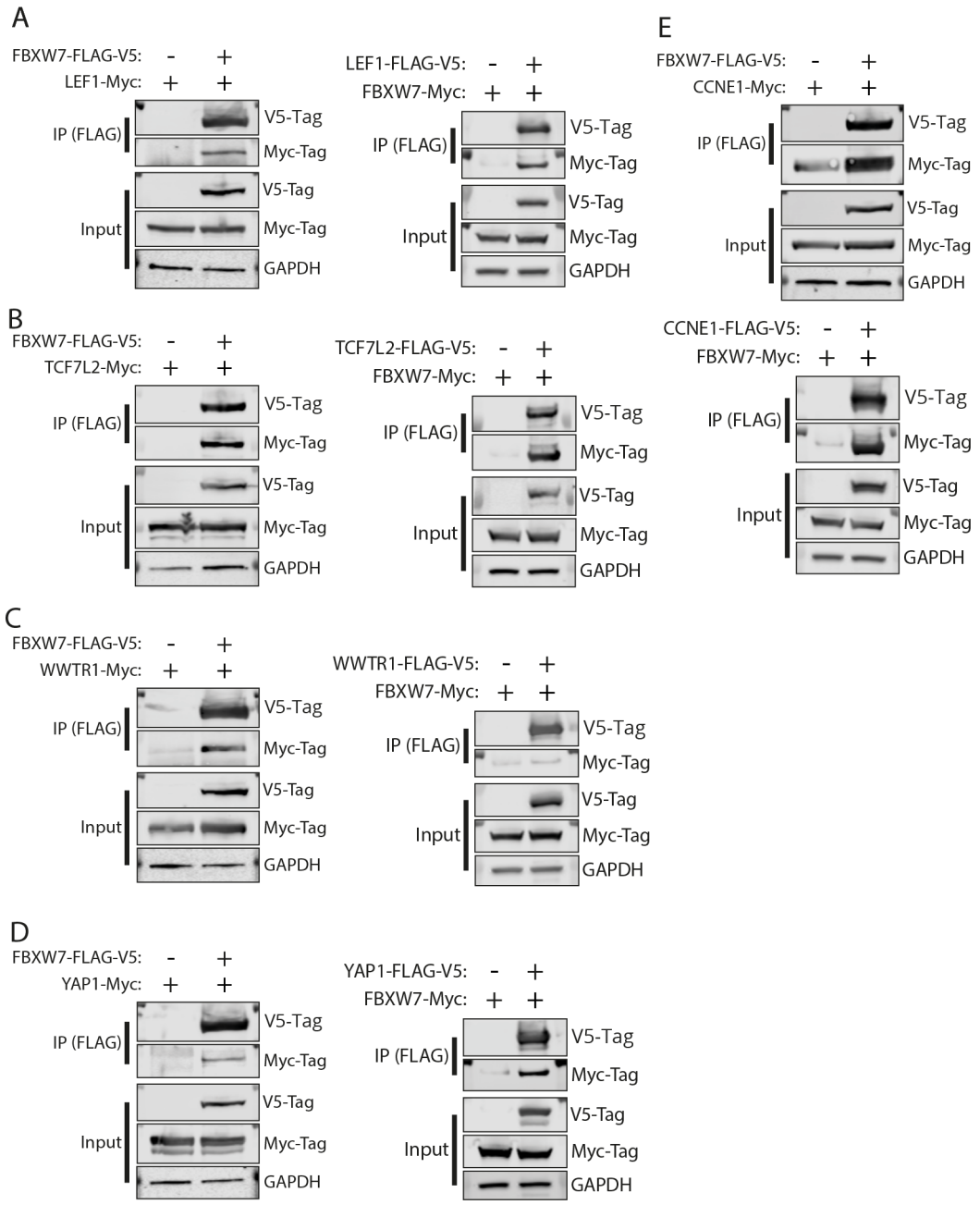

Figure 4.25: Individual co-immunoprecipitation analysis of interaction between FBXW7 and potential targets following treatment with MLN4924. **A, B, C, D, E.** Co-immunoprecipitation analysis by pull down of FLAG-tagged FBXW7 or target as indicated from protein lysates generated by transient transfection of HEK293T cells treated with 300 nM MLN4924 for 24 hours prior to lysis.

a direct target of FBXW7.

I then examined whether the now stabilised interaction with LEF1 and TCF7L2 was disrupted by FBXW7 mutation. Both FBXW7 wild-type and WD40 mutant plasmids were examined alongside a CPD mutant version of LEF1 in which the ″0″ and ″+4″

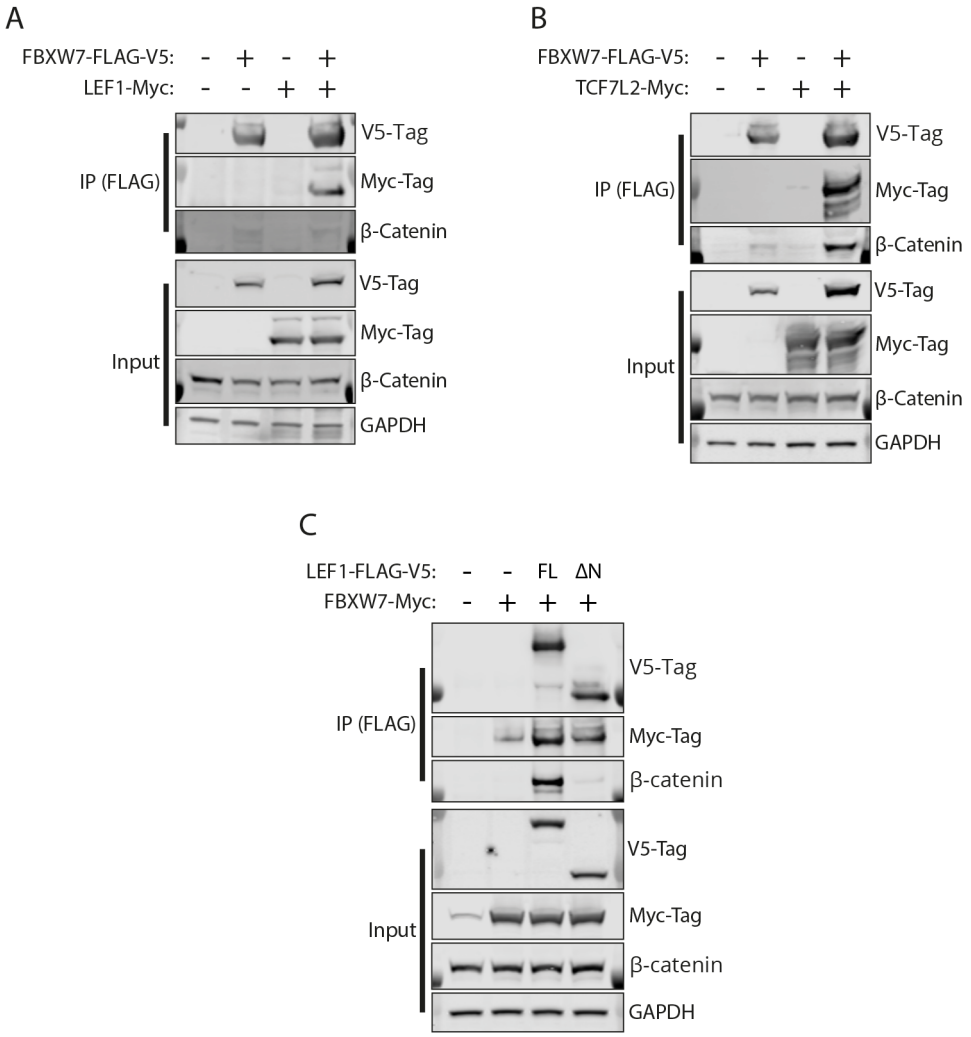

Figure 4.26: Evaluation of a published interaction between FBXW7 and CTNNB1. Co-immunoprecipitation of protein lysates from transiently transfected HEK293T cells treated with 300 nM MLN4924 for 24 hours prior to lysis. **A, B.** shows the extent of interaction between FBXW7 and endogenous Beta-catenin in the presence or absence of LEF1 - **A** or TCF7L2 - **B**. **C.** shows the pull down of either full length (FL) or a ΔN version of (lacking AAs 1-61 to disrupt Beta-Catenin binding) LEF1 through a FLAG-tag.

positions of the putative CPD had been mutated to alanine residues, T155A and T159A. CCNE1 was also included to see how the mutations affect a known target of FBXW7 (Figure 4.27A). When the FBXW7-WD40 mutant was pulled down there was evidence of a strong interaction with CCNE1, although the true extent of this was confounded by some non-specific pull down of CCNE1 in the control condition. However, with the reciprocal immunoprecipitation of CCNE1 a large decrease in the interaction was evident with the WD40 mutant, indicating that the interaction is disrupted, but not fully abrogated by mutations in the WD40 domain.

Corresponding immunoblots after co-transfection of LEF1 with FBXW7, showed that when FBXW7 is precipitated an interaction was still evident with the FBXW7-WD40 mutant (Figure 4.27B). Additionally, interaction was not completely disrupted by mutation of the suspected CPD in LEF1 or by the combination of this with FBXW7-WD40, but this was, again, confounded by substantially increased FBXW7 expression following mutation. The same results are observed with precipitation of LEF1, interaction of the FBXW7-WD40 with LEF1 and the CPD mutant LEF1 was still present.

When expressed alongside TCF7L2, pull down of FBXW7-WD40 exhibited a large decrease in amount of TCF7L2 that was detected in the IP fraction compared to pull down of wild-type FBXW7 (Figure 4.27C). A similar pattern was present with pull down of TCF7L2 when co-transfected with FBXW7-WD40, where despite its increased expression in the cells, less of the mutant protein was detected in the IP fraction, strongly indicating that introduction of FBXW7 mutations disrupts the interaction with TCF7L2.

It is apparent that there is an interaction between FBXW7 and TCF7L2 which can be effectively disrupted through mutation of the WD40 substrate binding domain of FBXW7. However, the evidence is less clear for LEF1 which is confounded by lower efficiency of pull down by FBXW7 and an expression differential between wild-type FBXW7 and FBXW7-WD40, with the WD40 mutant consistently expressed at higher levels. To try to account for this differential expression, densitometry analysis of amount of LEF1 precipitated by both wild-type FBXW7 and FBXW7-WD40 was performed and normalised to the amount of FBXW7 that was pulled down. This is based on the hypothesis that if an equivalent amount of LEF1 is pulled down by a larger quantify of FBXW7-WD40, this would indicate a weaker interaction compared to wild-type FBXW7. Quantification of the LEF1 mutants, ΔN and CPD, were also performed (Figure 4.28). In all conditions using a mutant version of either LEF1 or FBXW7, there appeared to be a decrease in the interaction of the two proteins, interestingly, this was least pronounced with the CPD mutant and was most pronounced with the WD40 mutant, which showed a median reduction of around 40% compared to wild-type.

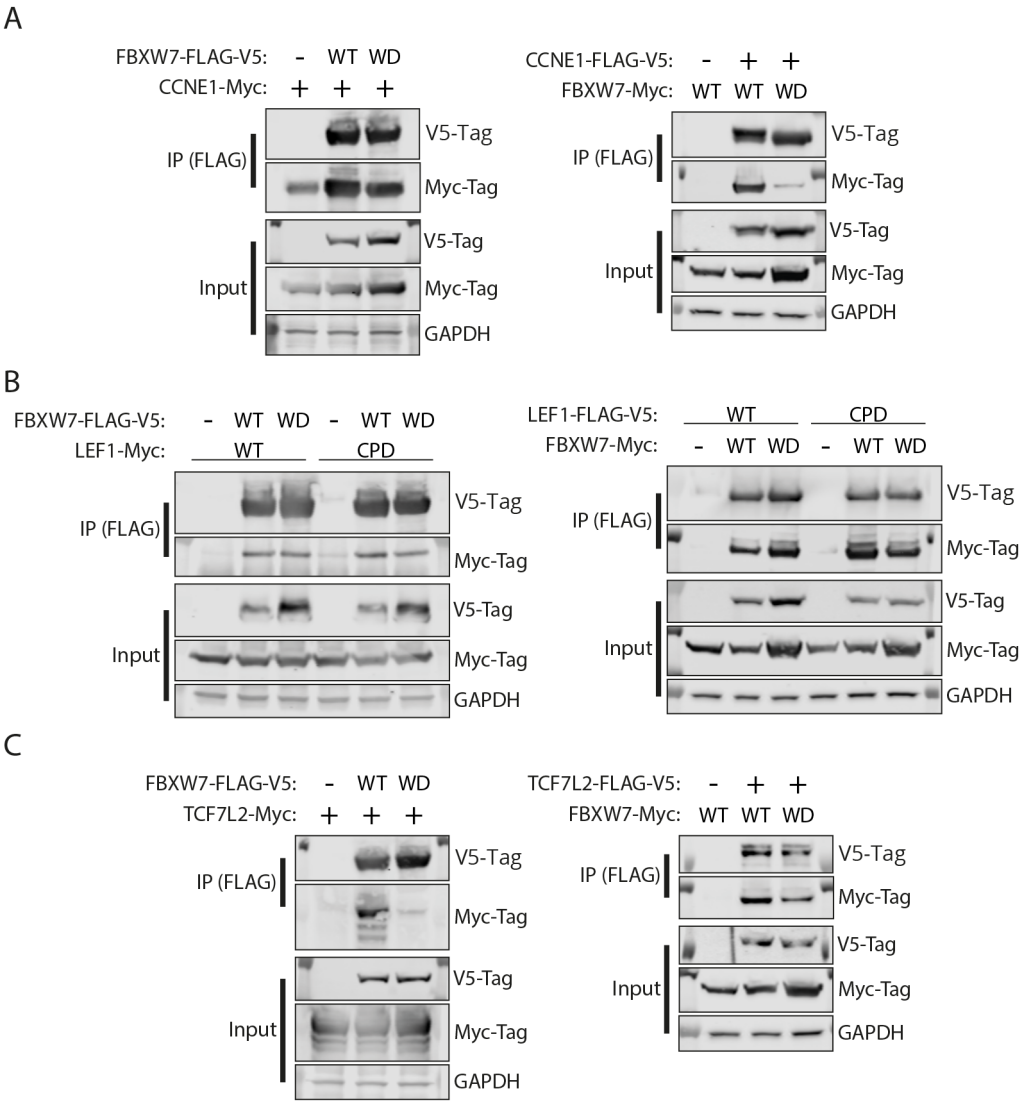

Figure 4.27: Extent of disruption of the interaction between FBXW7 and Wnt transcription factors by introduction of three combined WD40 domain mutations. **A, B, C.** Co-immunoprecipitation analysis using protein lysates from transiently transfected HEK293T cells treated with 300 nM MLN4924 for 24 hours prior to lysis.

4.4 Discussion

The findings of the previous chapter demonstrated that expression of *Fbxw7*^{R482Q} alone was insufficient to drive carcinogenesis in the murine uterus. However, its over representation in uterine cancer and the frequency with which it is observed in normal uterine glands suggest it may still be relevant for carcinogenesis, potentially by co-operating with and exacerbating the carcinogenic effects of other mutations. *PTEN* loss is one of the most frequent mutations in endometrial cancer and previous work highlighted that

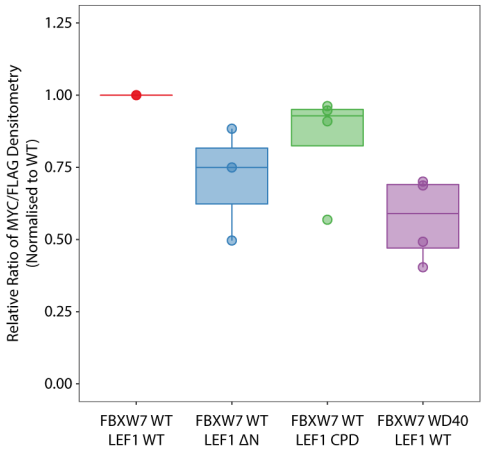

Figure 4.28: Relative amounts of LEF1 pulldown across co-immunoprecipitation experiments. Calculated using densitometry measures of the LEF1 band intensity in the immunoprecipitated fraction relative to the FBXW7 band intensity in the immunoprecipitated fraction.

its deletion from the uterus causes EC [126]. The work of this chapter demonstrates that *Pten* loss induced carcinogenesis is exacerbated by the addition of heterozygous $Fbxw7^{R482Q}$ mutation, leading to earlier onset of cancer and reduced survival of the $Pten^{\Delta/\Delta}$ $Fbxw7^{R482Q/+}$ mice.

In the subsequent investigation of the mechanism behind this phenotypic difference, a lack of dysregulation of known Fbxw7 targets, Ccne1, Notch1, Myc, and Jun was found from analysis of transcriptomic changes and protein expression. Nevertheless, transcriptomic analysis did highlight several potentially dysregulated pathways with Lef1/Wnt and Yap1/Hippo standing out. Interestingly, FBXW7 has been previously linked to proteomic regulation of YAP1 in the context of hepatocellular carcinoma, however, while an interaction was demonstrated using co-immunoprecipitation, no CPD was identified by the study [379]. To date the only published link between FBXW7 and regulation of the Wnt pathway is the previously discussed paper that suggested FBXW7 was responsible for ubiquitination of CTNNB1 [377]. However, I have shown that in the absence of co-transfection with either LEF1 or TCF7L2, only a small amount of CTNNB1 was precipitated with FBXW7, which could be due to pull down of endogenous Wnt transcription factors. Therefore, the results presented here indicate it is more likely that FBXW7 is interacting with Wnt transcription factors rather than CTNNB1 and that any interaction between the two is indirect.

Results from this chapter indicate that FBXW7 regulates the Wnt pathway, as evidenced by the interaction of FBXW7 with both LEF1 and TCF7L2. Additionally, the combined introduction of three common FBXW7 mutations, R465C, R479Q, and R505C was able to almost completely disrupt the interaction with TCF7L2 and to a lesser extent with LEF1, indicating a dependence on the substrate recognition domain of FBXW7 for interaction. However, I was unable to exhibit disruption of the interaction through identification and mutation of the CPD in either LEF1 or TCF7L2. This still leaves the possibility that the interaction with both proteins is not direct and could be through mutual interaction with a third protein. Further work to determine the CPD sequences of both LEF1 and TCF7L2 will be vital to defining them as true targets of FBXW7.

The Wnt pathway, and LEF1 in particular, plays a vital role in endometrial development and maintenance. Endometrial adenogenesis, the formation of endometrial glands in the days after parturition, has been shown to have a dependence on Wnt pathway activity. A study by Jeong *et al.* found that Pgr^{cre} driven activation of Ctnnb1, through exon 3 deletion, induced endometrial hyperplasia with deletion models displaying profound squamous metaplasia [380]. Lef1 is also linked to onset of adenogenesis with Lef1-deficient mice exhibiting a lack of endometrial gland formation despite normal lumen formation [381].

A recent study by Seishima *et al.* highlighted a population of Lgr5-positive cells in the uteri of postnatal mice that are responsible for gland development, with ablation of this cell population abrogating gland formation [131]. Furthermore, these cells were found to exhibit high levels of Wnt activity and readily formed organoids *in vitro*, thereby displaying self-renewing capability and leading to their identification as a Wnt-dependent stem cell population [131]. A similar population of Axin2 expressing cells was highlighted by Syed *et al.* as a stem cell population responsible for growth and repopulation of the uterus following injury or menstruation [130]. The Axin2-positive cell population formed *in vitro* organoids more readily than Axin2-negative cells and their ablation led to significantly reduced glandular epithelium *in vivo* [130]. They also demonstrated the involvement of these cells in oncogenic transformation; upon exposure to unopposed oestrogen in the form of tamoxifen, the Axin2-positive population

was found to have rapidly expanded generating hyperplastic lesions [130].

As well as glandular formation and replenishment, a further role for Wnt in epithelial identity has been uncovered. As previously mentioned, models of Ctnnb1-deletion in the uterus exhibit strong squamous metaplasia, which has also been observed with other Wnt pathway alterations [382]. It was subsequently noted that Wnt pathway activity plays a vital role in maintenance of the squamocolumnar junction in the cervix, where the columnar epithelium of the uterus transitions in to the squamous epithelium of the vagina. A junction denoted by high Wnt activity on the columnar side and an increasingly Wnt repressive environment towards the ectocervical, squamous side [383]. $Pten^{\Delta/\Delta}$ $Fbxw7^{+/+}$ mice, studied in this chapter, exhibited potent and highly penetrant squamous metaplasia present in most samples as early as 4 weeks of age. This corroborates previously published accounts of prevalent squamous metaplasia in the uteri of mice with Pgr^{cre} induced Pten-loss [126, 384, 385]. However, there was drastically less squamous metaplasia evident in the $Pten^{\Delta/\Delta}$ $Fbxw7^{R482Q/+}$ mice, with only a small number of samples exhibiting it at 8 weeks of age and even when more prominent, at survival end point, it is mainly exhibited in the luminal epithelium as opposed to the glandular epithelium. This difference of phenotype could therefore, be indicative of differential Wnt pathway activity between the $Pten^{\Delta/\Delta}$ $Fbxw7^{+/+}$ and $Pten^{\Delta/\Delta}$ $Fbxw7^{R482Q/+}$ mice.

Dysregulation of Wnt is well established in endometrial carcinogenesis with up to 40% of endometrial cancers found to exhibit alterations to Wnt pathway members, most frequently, mutations of *CTNNB1*, and further reports of aberrant CTNNB1 staining without identified mutation [386–388]. Interestingly, aberrant Lef1 and Ctnnb1 staining was observed in the $Pten^{\Delta/\Delta}$ $Fbxw7^{R482Q/+}$ mice and similarly aberrant CTNNB1 staining has been reported in FBXW7 mutant colorectal cancers [389]. Further suggesting FBXW7 may have a role in regulation of Wnt signalling, which could therefore be the link between FBXW7 and endometrial cancer.

Similarly to the combinatorial effect of Fbxw7 mutation with Pten loss reported in this chapter and in previous literature [316]. There have been reports of additive effects of Pten loss with Wnt pathway dysregulation. Combined loss of Pten and Apc

in the uterus exhibited accelerated tumourigenesis beyond that initiated by Pten-loss alone [384]. In the previously discussed Axin2-positive stem cell population, Syed *et al.* showed that mutation of *Pik3ca* and *Ctnnb1* together rapidly induced endometrial adenocarcinoma [130].

There is significant overlap between prevalent phenotypes observed in Wnt dysregulated EC and those of the $Pten^{\Delta/\Delta}$ $Fbxw7^{R482Q/+}$ mice modelled in this chapter. These overlapping phenotypes, coupled with the observed interaction of FBXW7 with LEF1 and TCF7L2, provides compelling evidence to suggest that FBXW7 could be a regulatory element of the Wnt pathway, driving proteasomal degradation of the transcription factors LEF1 and TCF7L2. However, identification of the CPD sequence in these proteins and further characterisation of the phenotype, such as examination of whether Lef1 loss in this model is capable of reversing the $Fbxw7^{R482Q}$ phenotype are still required to confidently confirm Wnt transcription factors as *bona fide* FBXW7 targets.

4.4.1 Future directions

The question remains of why the interaction between Fbxw7 and Lef1 is not disrupted to a larger extent by mutation of the WD40 domain or the suspected CPD of Lef1. In terms of the CPD, one obvious explanation is that this is not the actual or only CPD present in Lef1. This may be highlighted by the reduced pull down of Lef1 observed after removal of the Ctnnb1-binding domain, despite there not being a recognised CPD in this region. Alternatively this reduction of interaction may be due to conformational changes in the structure of Lef1 leading to occlusion of the true CPD.

The possibility of multiple CPDs has been apparent since identification of the first substrate, CCNE1, which is known to have two recognition motifs [245, 390]. However, several recent studies have begun to highlight the prevalence of multiple CPD sequences in FBXW7 targets, which are known co-operate to drive interaction and ubiquitination. Recent work by Welcker *et al.* identified a previously unappreciated CPD in the C-terminal portion of MYC and found that alteration of both sites is necessary to abrogate interaction [249].

Additionally, many studies base their searches for FBXW7 CPDs on those found in

the earlier identified substrates, as was done in this study. This methodology will have a tendency to positively select for CPDs that may not be wholly representative of the binding capability of FBXW7. It can be seen from the analysis of published CPDs that there is more variation than was used for my search in this chapter. The use of nuclear magnetic resonance (NMR) by Csizmok *et al.* in their report of FBXW7 interaction with JUN highlights this point [252]. They were able to show resonance changes suggesting interaction at five different serine or threonine residues in JUN with several not exhibiting the "canonical" pattern of an FBXW7 CPD [252]. Therefore, expanding the search to other similar sequences in the Wnt transcription factors, potentially focussing on known phosphorylated serines and threonines, would provide clarity on the potential interaction and allow identification of additional interaction sites.

The potential for additional CPDs does not explain the partial disruption of interaction between Lef1 and Fbxw7 by mutation of the WD40 domain, especially when compared to the almost total disruption seen with Tcf7l2. A potential hypothesis is that the interaction between Lef1 and Fbxw7 may be dependent on dimerisation of Fbxw7 monomers. It has been previously demonstrated that Fbxw7 dimerisation may be important for the differential regulation of targets, and a protein containing two "weak" or suboptimal CPDs can be targeted for degradation by Fbxw7 dimers, but not by monomers [251]. It may be the case that these targets have multiple CPDs and the interaction with Lef1 is more reliant on dimerisation. Interestingly, the efficiency of Lef1 pull down with wild-type Fbxw7 was lower than both Ccne1 and Tcf7l2, which could be explained by an increased reliance on dimerisation. As Fbxw7-WD40 was transfected in to cell lines with endogenous wild-type Fbxw7, it may be possible to that residual interaction observed is the result of dimerisation with this endogenous wild-type Fbxw7. Repeating the co-immunoprecipitation experiments with a dimerisation-deficient version of FBXW7 may help to determine if dimer formation is a confounding factor after the mutation of FBXW7.

One further confounding factor for identifying Fbxw7 targets is the dependence on phosphorylation to facilitate interaction. If the regulatory pathways that drive the phosphorylation event are not active it would not be possible to see an interaction. This is-

sue was considered during the work of this chapter and led to the use of NOU1 cells for generating protein lysates for co-immunoprecipitation, however this was hampered by the poor transfection efficiency in these cells. To clarify the potential interaction, it would be useful to better understand the dynamics of Wnt signalling throughout the oestrus cycle. It has been previously demonstrated that Lef1 expression peaks in concert with oestrogen production during the proliferative phase, with similar trends observed with overall Wnt activity, whereas, induction of progesterone production suppresses Wnt activity in the uterus [381, 391, 392]. It is therefore likely that the peak time for Lef1 degradation would be during the transition from high oestrogen to high progesterone. If a sex hormone responsive cell line model could be established using a normal endometrial cell line, such as that recently reported by Park *et al.* or through *in vitro* culture of mouse endometrial cells, then the dynamics of this transition could be examined to determine whether there is involvement of Fbxw7 or not [393].

Better characterisation of these interactions will help to determine whether Fbxw7 is a regulator of Wnt transcription factors. However, this would still not determine whether the loss of Wnt regulation is the driving force behind the worse survival of $Pten^{\Delta/\Delta}$ $Fbxw7^{R482Q/+}$ mice. Examining whether overexpression of Lef1 in combination with Pten-loss phenocopies the $Pten^{\Delta/\Delta}$ $Fbxw7^{R482Q/+}$ mice, or whether the observed phenotype in $Pten^{\Delta/\Delta}$ $Fbxw7^{R482Q/+}$ mice could be reverted by targeting the Wnt pathway, genetically or pharmaceutically, may help to answer these questions. If this could be established, alongside better characterisation of the FBXW7 interaction with Wnt transcription factors it would help to define the role of FBXW7 in EC.

Chapter 5

Functional characterisation of *Fbxw7*$^{R482Q/+}$ in combination with *Trp53*$^{\Delta/\Delta}$ or *Trp53*$^{R172H/\Delta}$ in the mouse uterus

5.1 Introduction

The previous chapters have shown that cancer-associated *Fbxw7* missense mutation alone does not induce cancer in the mouse uterus but does significantly accelerate endometrial cancer development caused by *Pten* loss. This co-operation with a common EC mutation raises the question of whether *FBXW7* mutation could co-operate with other common EC mutations.

5.1.1 *TP53* mutations are frequently found in endometrial cancer

In EC the importance of *TP53* mutation has been apparent since the earliest methods of classification, in which *TP53* mutations were found to typify one of the two proposed classes of EC [66]. Since then deeper molecular analysis has continued to highlight the frequency and importance of *TP53* mutations, with 91.7% of CN-high cancers in the

TCGA UCEC cohort and 91% of the UCS cohort containing *TP53* mutations [90, 91]. Interestingly, outside of carcinosarcoma or the CN-high subtype, the mutation rate of *TP53* is low, with only 12 patients out 172 (7%) from the combined POLE-mutant, MSI, and CN-low subtypes exhibiting *TP53* mutation [90].

Due to the association of *TP53* mutation with both CN-high and carcinosarcoma subtypes, it is perhaps unsurprising that p53 characterisation plays an important role in prognostication of EC [74, 95, 96]. Evidence of abnormal p53 staining by IHC has been increasingly used as a surrogate for p53 mutation status and CN-status due to the strong association of p53 mutation with CNAs [95, 96]. Through IHC characterisation and sequencing of human cancers, it has been well established that mutations or abnormal staining of *TP53* are associated with poor overall survival, increased FIGO stage, and aggressive nature (LVSI and myometrial invasion) [95, 98, 394, 395].

5.1.2 Normal endometrial tissue does not exhibit *TP53* mutations

A key indicator of the potential role of *TP53* in neoplastic transformation, is the lack of mutations in the gene found in histologically normal endometrial tissue [352–354, 360]. From the four major studies to have examined mutations in normal endometrium, mutations of *TP53* were only reported by two studies [353, 354]. Moore *et al.* showed that cancer-associated *TP53* mutations (R172H, R158H, G187D) were present in normal endometrium however, only heterozygous mutations were observed and even those were at a frequency significantly lower than exhibited by EC (<2% vs 28%) [353]. Similarly, Yamaguchi *et al.* reported around 1.2% of glands in normal endometrium exhibited *TP53* mutations with a mutant allele frequency of 0.5 suggesting the mutations were heterozygous [354]. Furthermore, examination of the mutational profiles of endometrial hyperplasia again finds a mutation rate for *TP53* that is below what is observed in EC (6% vs 28%) [359]. Together, these studies suggest that *TP53* mutation may play a significant role in malignant transformation during carcinogenesis.

5.1.3 Functional characterisation of *TP53* mutation in the endometrium

5.1.3.1 Modelling of *TP53* mutation using *in vitro* endometrial models

With the vital role that *TP53* plays in maintaining cellular homeostasis and restraining cancer development, an extensive array of studies have been performed to examine the effects of p53 loss or mutation in both cell line and murine models. Furthermore, the frequency of *TP53* mutation in EC has driven numerous studies in endometrial models. Endometrial cancer cell line models have been extensively used for examination of the effects of both *TP53* loss and the potential gain-of-function effects of point mutation. From these models, it has been shown that deficiency of p53 expression drives a phenotype of reduced cell cycle arrest and apoptosis [396].

Examination of common cancer-associated *TP53* point mutations (R172H, R248Q, and R273H) in cell models have demonstrated increased proliferation and decreased apoptosis, particularly through repression of classical p53 target genes, such as p21, Bax, Mdm2 [397–399]. However, these studies have also consistently identified activation of an EMT phenotype, with cells expressing these point mutations exhibiting increased migration and invasiveness [397–400]. This difference in the consequences of *TP53* point mutation and loss was further examined by Meng *et al.* who treated cells with anti-mitotic agents (paclitaxel or BI2536, an inhibitor of polo-like kinase 1 (PLK1)) and found that these agents were effective against cell lines deficient for p53 but those expressing point mutations were resistant [401].

5.1.3.2 Modelling of endometrial *TP53* mutation in mice

The earliest studies linking p53 deficiency with EC in murine models came from the work of two groups that used constitutive deletion or mutation of p53 with subsequent treatment with genotoxic agents to induce cancer development [123, 124]. Mitsumori *et al.* showed that $Trp53^{\Delta/+}$ mice treated with N-ethyl-N-nitrosourea developed uterine sarcomas with an incidence greater than $Trp53^{+/+}$ mice [123]. In a similar study Zhang *et al.* used transgenic $Trp53^{C135V/+}$ and $Trp53^{+/+}$ mice treated with 1,2-dimethylhydrazine and found similarly increased incidence of uterine sarcoma [124].

The first report of conditional deletion of *Trp53* from the mouse uterus came from Daikoku *et al.*, who used $Pgr^{Cre/+}$ to target the deletion [126]. With this model, they did not observe any alterations to uterine histology up to the age of 5 months and a limited effect on mouse survival through 250 days [126]. A further study from Wild *et al.* performed a similar analysis using conditional homozygous deletion of *Trp53*, however, they utilised a Ksp1.3-Cre transgene to drive recombination in the glandular and luminal epithelium with a mosaic pattern [402]. In their model female mice exhibited no evidence of a uterine phenotype through 52 weeks [402]. However, between 65 to 79 weeks mice began to exhibit uterine tumours with predominantly serous and clear cell histology with some carcinosarcomas also observed [402]. No studies have yet been performed to examine the impact of *Trp53* missense mutation in the mouse uterus.

Despite the known carcinogenic role of *TP53* mutation and its frequent co-occurrence with *FBXW7* mutation in human EC, to date no study has examined the combined effects of *Fbxw7* and *Trp53* mutation in endometrial tissue, in murine models. The closest to such a study comes from the previously discussed report from Cuevas *et al.* who examined the effects of combined *Pten* and *Fbxw7* deletion [316]. It was reported that subsequent spontaneous mutation of p53 was a vital factor in driving cancer development in their model [316]. Furthermore, *in vitro* models have implicated *FBXW7* and *TP53* as co-operative regulators of the cell cycle and genomic stability [403]. However, whether this co-operation is maintained *in vivo* or induced by *FBXW7* missense mutation has yet to be determined.

5.1.4 Motivation for studying loss or missense mutation of *Trp53* combined with mutation of *Fbxw7*

TP53 is commonly mutated in EC but not in normal endometrium or hyperplasia, and both *in vitro* and *in vivo* EC models have shown *TP53* is a key tumour suppressor. Furthermore, mutational profiling of EC has identified frequent overlap of *FBXW7* mutation and *TP53* mutation, particularly in CN-high and UCS subtypes [90, 91, 404]. The frequent co-occurrence of mutations in *FBXW7* and *TP53* suggest there may be some form of co-operative interaction between them that promotes EC and, in particular,

more aggressive subtypes of EC. While there have been some studies examining the effects of *Trp53* loss or missense mutation on development of EC in mouse model systems, there has not been any study published examining the combined effects of *Fbxw7* mutation with *Trp53* deletion or missense mutation in the murine uterus. *In vitro* studies performed in human cell lines provide some context and suggest that development of cancer could be expected, but whether these mutations together could initiate cancer and what pathways could be dysregulated, has yet to be determined and therefore warrants examination.

5.2 Materials and methods

5.2.1 Breeding of experimental animals

For analysis of the carcinogenic effects of $Trp53^{\Delta/\Delta}$ combined with $Fbxw7^{R482Q}$, the $Trp53^{tm1Brn}$ allele was used in combination with the previously discussed $Fbxw7^{tm1Itom}$ allele. $Trp53^{fl/fl}$ $Pgr^{cre/cre}$ mice were cross-bred with $Fbxw7^{fl(R482Q)/+}$ mice (Figure 5.1A). Breeding of these mice was performed by Dr David Church.

To generate mice with a *Trp53* missense mutant and LOH, the above alleles were used in combination with the $Trp53^{tm2Tyj}$ allele, described in Section 2.1.1. Mice were bred for heterozygosity of both *Trp53* alleles, $Trp53^{fl(R172H)/fl}$ and absence or heterozygosity for $Fbxw7^{fl(R482Q)}$ (Figure 5.1B).

5.3 Results

5.3.1 Generation of $Trp53^{\Delta/\Delta}$ mice with or without $Fbxw7^{R482Q/+}$ mutation

From the previous chapter it is apparent that $Fbxw7^{R482Q}$ mutation cause more aggressive cancer when combined with $Pten^{\Delta/\Delta}$ than $Pten^{\Delta/\Delta}$ does alone. As dysregulation of *TP53* is also a common feature of EC, I wanted to examine whether there was a similar combinatorial effect of $Trp53^{\Delta/\Delta}$ and $Fbxw7^{R482Q}$ mutations. To examine the effects of these mutations, mice were generated as outlined in Section 5.2.1. Genotyping of the mice was performed by PCR with confirmation of $Trp53^{fl/fl}$ allele apparent due to the

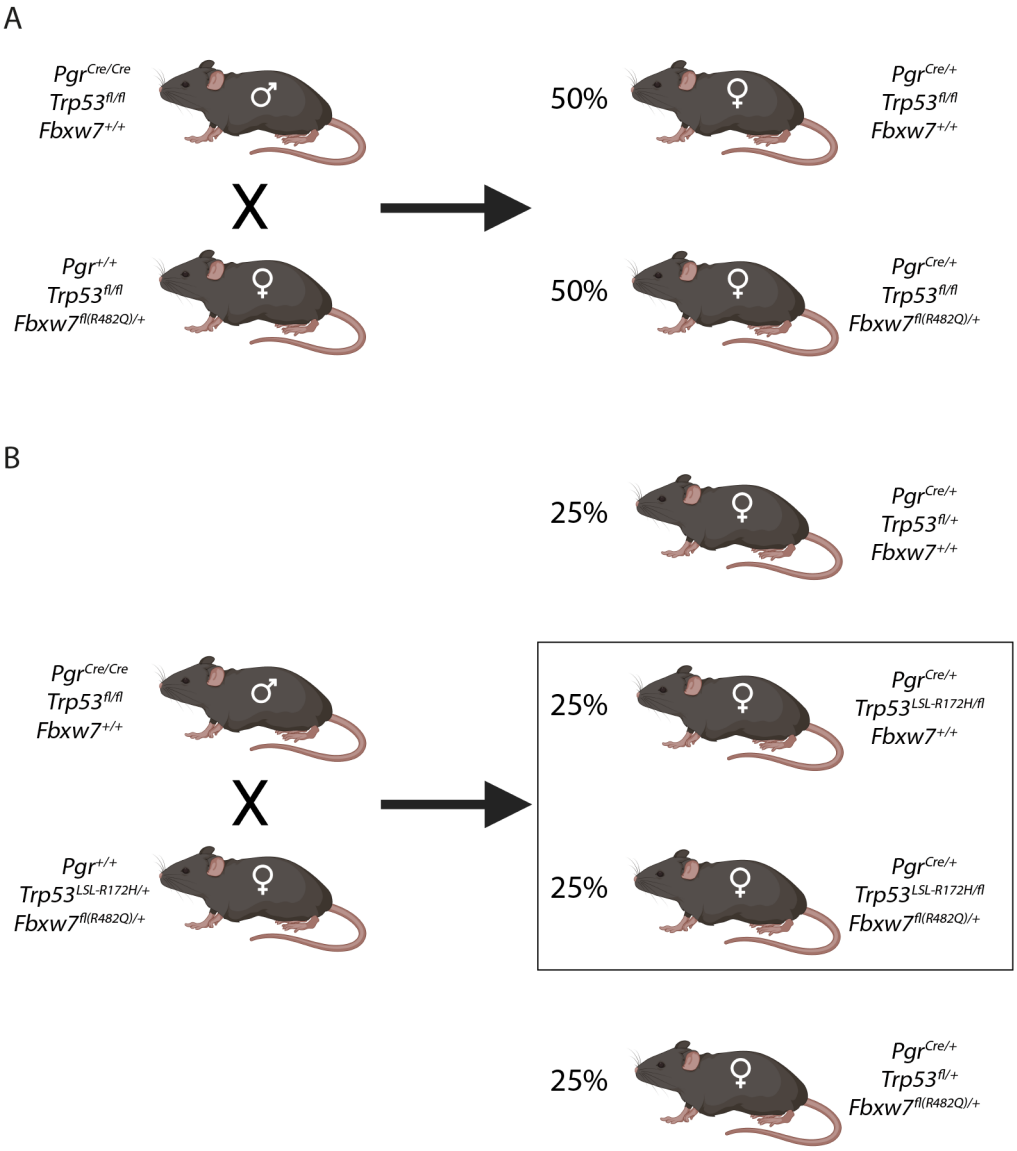

Figure 5.1: Breeding schematic for the mice used in this chapter, all percentages shown are representative of the female offspring and disregard the male offspring. **A.** Breeding combination used to generate *Trp53*$^{\Delta/\Delta}$ and *Trp53*$^{\Delta/\Delta}$ *Fbxw7*$^{R482Q/+}$. **B.** Breeding combination used to generate *Trp53*$^{R172H/\Delta}$ and *Trp53*$^{R172H/\Delta}$ *Fbxw7*$^{R482Q/+}$.

lack of a wild-type band (Figure 5.2A). Successful recombination in the uterus was also examined by PCR using DNA extracted from the mouse uterus and was observed in both *Trp53*$^{\Delta/\Delta}$ *Fbxw7*$^{+/+}$ and *Trp53*$^{\Delta/\Delta}$ *Fbxw7*$^{R482Q/+}$ mice.

To ensure that successful recombination coincided with downregulation of *Trp53* expression, RT-qPCR was performed using RNA extracted from fresh frozen uteri at 4 and 8 weeks of age (Figure 5.2B,C). At both time points there was profound downregulation of *Trp53* in both the *Trp53*$^{\Delta/\Delta}$ *Fbxw7*$^{+/+}$ (median $\log_2$(fold change) -2.80, P =

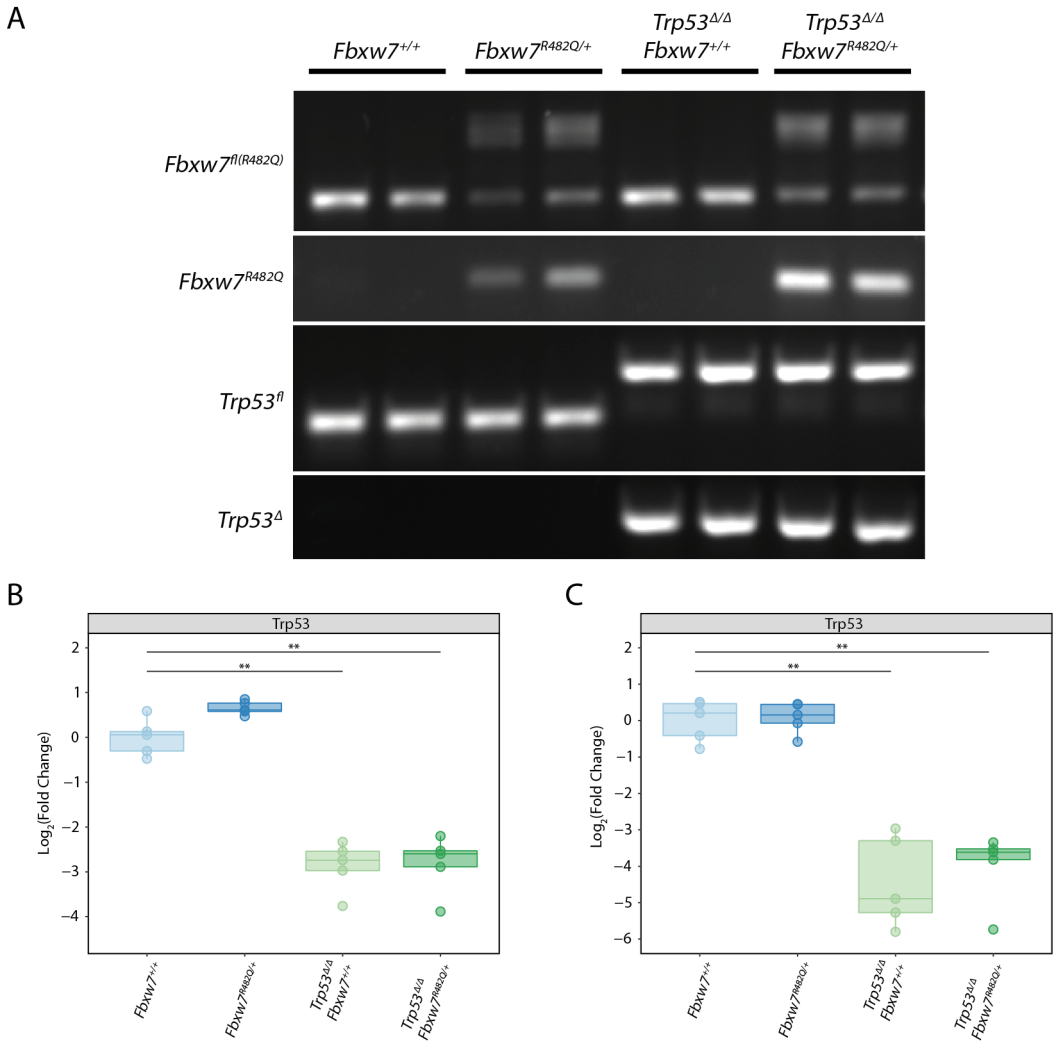

Figure 5.2: Confirmation of mouse genotypes and functionality of the *Trp53*$^{\Delta/\Delta}$ allele. **A.** Agarose gel of the PCR products from genotyping for the *Trp53*^{fl} allele. **B, C.** *Trp53* gene expression determine by RT-qPCR of bulk RNA extracted from uterine tissue collected at 4 weeks - **B** and 8 weeks - **C**.

0.0079 at 4 weeks; median $\log_2$(fold change) -5.10, P=0.00794 at 8 weeks) and *Trp53*$^{\Delta/\Delta}$ *Fbxw7*$^{R482Q/+}$ (median $\log_2$(fold change) -3.19, P=0.0079 at 4 weeks; median $\log_2$(fold change) -3.82, P=0.0079 at 8 weeks) mice compared to wild-type mice, with no significant difference evident between *Trp53*$^{\Delta/\Delta}$ *Fbxw7*$^{+/+}$ and *Trp53*$^{\Delta/\Delta}$ *Fbxw7*$^{R482Q/+}$ mice at either time point.

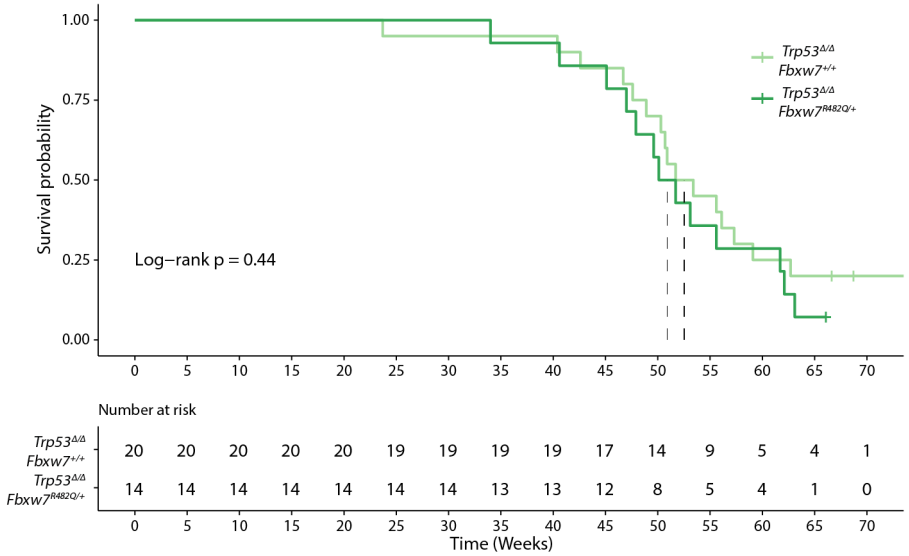

Figure 5.3: Pathological and survival analysis of $Trp53^{\Delta/\Delta}$ and $Trp53^{\Delta/\Delta}$ $Fbxw7^{R482Q/+}$ mice. **A.** Classification of uterine pathology exhibited by $Trp53^{\Delta/\Delta}$ and $Trp53^{\Delta/\Delta}$ $Fbxw7^{R482Q/+}$ mice at various time points, as determined by expert pathological review. **B.** Kaplan-Meier estimator analysis of the overall survival of $Trp53^{\Delta/\Delta}$ and $Trp53^{\Delta/\Delta}$ $Fbxw7^{R482Q/+}$ mice.

5.3.2 $Trp53^{\Delta/\Delta}$ reduces overall survival and is not made worse by $Fbxw7^{R482Q/+}$ mutation

Mice were aged until survival endpoint, onset of ill-health or abdominal distension. Interestingly, in this cohort most mice were sacrificed due to development of non-uterine phenotypes, predominantly extrauterine tumours. To examine the effect of $Trp53^{\Delta/\Delta}$ alone and in combination with $Fbxw7^{R482Q}$ on overall survial, Kaplan-Meier estimator analysis was performed (Figure 5.3). Both $Trp53^{\Delta/\Delta}$ $Fbxw7^{+/+}$ and $Trp53^{\Delta/\Delta}$ $Fbxw7^{R482Q/+}$ mice exhibited reduced survival compared to wild-type mice, with median survival of 52.5 weeks and 50.9 weeks, respectively. Wild-type mice had not reached median overall survival by 80 weeks. Interestingly, unlike the $Pten^{\Delta/\Delta}$ model, there was no significant difference in overall survival between the $Trp53^{\Delta/\Delta}$ $Fbxw7^{+/+}$ and the $Trp53^{\Delta/\Delta}$ $Fbxw7^{R482Q/+}$ mice (Log-rank Test P=0.44).

5.3.3 $Trp53^{\Delta/\Delta}$ causes infrequent endometrial cancer with long latency

The majority of mice were sacrificed due to non-uterine phenotypes and necropsy of these animals highlighted a lack of uterine enlargement. However, to examine whether loss of *Trp53* alone or when combined with $Fbxw7^{R482Q}$ altered normal uterine histol-

ogy, uteri from mice at three time points (4 weeks, 8 weeks, and survival end point) were examined by H&E staining and IHC staining for Krt8 to determine the gross histology (Figure 5.4). In addition, H&E sections were examined by expert pathologists (Dr Tjalling Bosse and Dr Alicia Leon-Castillo) to determine the presence of any uterine pathology (Figure 5.5). At 4 and 8 weeks of age, H&E and Krt8 staining indicate that both the $Pten^{\Delta/\Delta}$ $Fbxw7^{+/+}$ and the $Pten^{\Delta/\Delta}$ $Fbxw7^{R482Q/+}$ mice exhibit normal histology. This was confirmed by the pathological review, which found that 100% of $Trp53^{\Delta/\Delta}$ $Fbxw7^{+/+}$ and $Trp53^{\Delta/\Delta}$ $Fbxw7^{R482Q/+}$ mice at these time points exhibited no uterine pathology.

At survival end point samples from both genotypes were found to exhibit endometrial adenocarcinoma based on the expert pathological review, 5.6% for $Trp53^{\Delta/\Delta}$ $Fbxw7^{+/+}$ and 18.2% for $Trp53^{\Delta/\Delta}$ $Fbxw7^{R482Q/+}$ (Figure 5.5). Although the proportion of mice with endometrial adenocarcinoma was higher in $Trp53^{\Delta/\Delta}$ $Fbxw7^{R482Q/+}$ mice this was not statistically significant (P=0.54, Fisher Exact Test). Endometrial hyperplasia was observed in 16.7% of $Trp53^{\Delta/\Delta}$ $Fbxw7^{+/+}$ mice and in 9.10% of $Trp53^{\Delta/\Delta}$ $Fbxw7^{R482Q/+}$ mice. Interestingly, in both genotypes there was evidence of uterine sarcoma, 11.1% in $Trp53^{\Delta/\Delta}$ $Fbxw7^{+/+}$ mice and 9.10% in $Trp53^{\Delta/\Delta}$ $Fbxw7^{R482Q/+}$ mice. However, the majority of mice in both genotypes exhibited uterine histology that is within normal parameters, 66.7% in the case of $Trp53^{\Delta/\Delta}$ $Fbxw7^{+/+}$ and 63.6% of the $Trp53^{\Delta/\Delta}$ $Fbxw7^{R482Q/+}$ mice. The variability in uterine pathology is reflected in the histological appearance of the uterus, with most samples exhibiting normal uterine structure, but others exhibiting abnormal features associated with uterine pathology such as cystic glands (Figure 5.4).

5.3.4 *Trp53* loss drives frequent extrauterine tumour development that is reduced by $Fbxw7^{R482Q/+}$

As previously discussed, many of the mice in the survival endpoint cohort were sacrificed due to development of extrauterine tumours. Many of these tumours arose in mammary tissue, which is another site of recombination by Pgr^{cre}, therefore the tissue from these sites were collected and pathology determined by expert review (Figure 5.6). The vast majority of these extrauterine tumours were sarcomatous and oc-

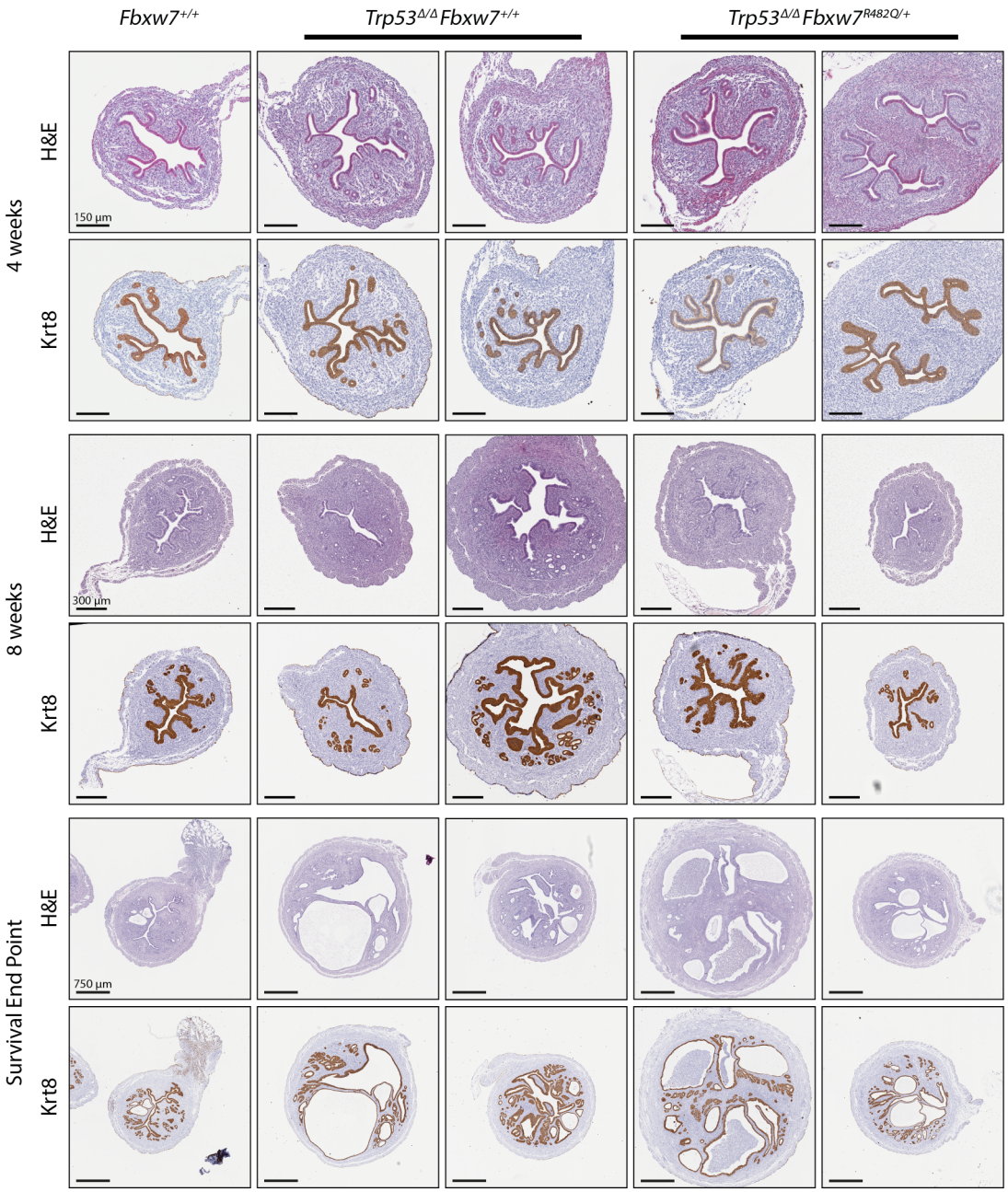

Figure 5.4: Examination of the histological changes that occur due to introduction of $Trp53^{\Delta/\Delta}$ and $Trp53^{\Delta/\Delta}$ $Fbxw7^{R482Q/+}$ mutations to the mouse uterus. H&E staining and IHC staining for Krt8 (epithelial marker) highlights any changes to normal uterine appearance at 4 weeks, 8 weeks, and survival end point.

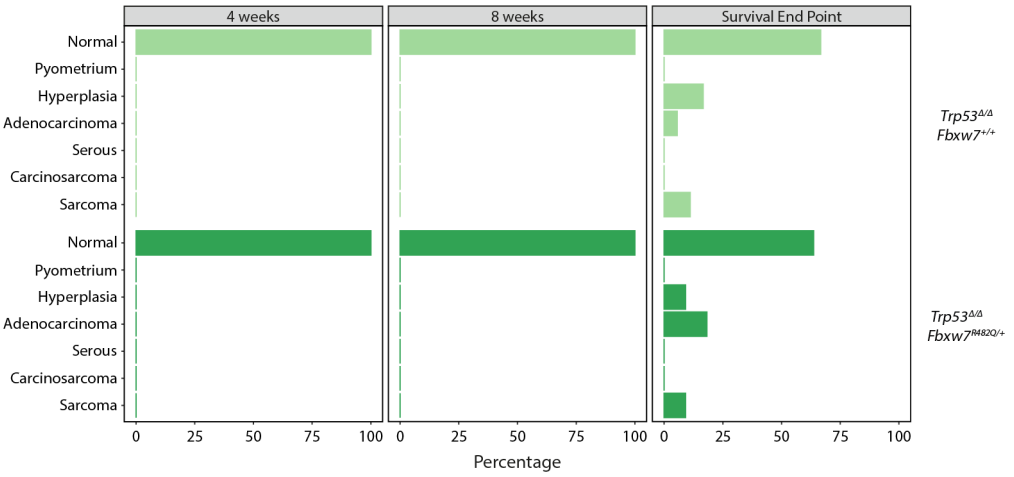

Figure 5.5: Classification of uterine pathology exhibited by *Trp53*$^{\Delta/\Delta}$ and *Trp53*$^{\Delta/\Delta}$ *Fbxw7*$^{R482Q/+}$ mice at various time points, as determined by expert pathological review. Number of mice analysed *Trp53*$^{\Delta/\Delta}$ *Fbxw7*$^{+/+}$: 4w = 4, 8w = 5, survival end point = 18; *Trp53*$^{\Delta/\Delta}$ *Fbxw7*$^{R482Q/+}$: 4w = 3, 8w = 5, survival end point = 11.

curred at a higher frequency in *Trp53*$^{\Delta/\Delta}$ *Fbxw7*$^{+/+}$ mice (68.4% vs 35.7% in *Trp53*$^{\Delta/\Delta}$ *Fbxw7*$^{R482Q/+}$), although not statistically significantly (P=0.085, Fisher Exact Test). Interestingly, the frequency of these extrauterine tumours was significantly lower in the *Trp53*$^{\Delta/\Delta}$ *Fbxw7*$^{R482Q/+}$ cohort, in which 64.3% did not exhibit an extrauterine tumour compared to just 26.3% in the *Trp53*$^{\Delta/\Delta}$ *Fbxw7*$^{+/+}$ mice (P=0.040, Fisher Exact Test). This potentially highlights a differential role for *Fbxw7* mutation in the induction of cancer arising from different tissue types.

5.3.5 Minimal transcription changes are induced after loss of *Trp53* and mutation of *Fbxw7*

To examine the effect of *Trp53*$^{\Delta/\Delta}$ alone and in combination with *Fbxw7*^{R482Q} on expression of the key genes under investigation, I performed RT-qPCR on RNA extracted from bulk, fresh frozen uterine tissue collected at 4 weeks and 8 weeks of age (Figure 5.7). At 4 weeks of age, expression of *Fbxw7* and *Pten* were not significantly altered between the *Trp53*$^{\Delta/\Delta}$ *Fbxw7*$^{+/+}$ or *Trp53*$^{\Delta/\Delta}$ *Fbxw7*$^{R482Q/+}$ mice or with either genotype compared to wild-type mice (Figure 5.7A). Similarly, at 8 weeks there was no evidence of statistically significant changes in transcription of either *Fbxw7* or *Pten*.

Previously, I showed that *Trp53* is significantly downregulated in the mice at 8

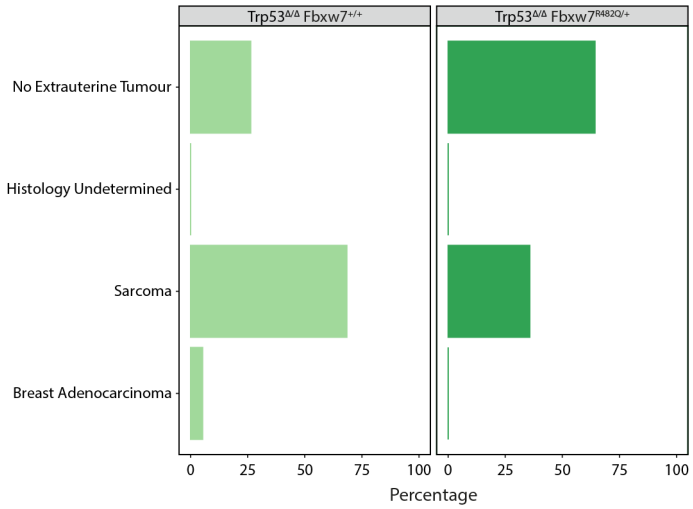

Figure 5.6: Pathological analysis of extrauterine tumours in *Trp53*$^{\Delta/\Delta}$ and *Trp53*$^{\Delta/\Delta}$ *Fbxw7*$^{R482Q/+}$ mice. Number of mice analysed *Trp53*$^{\Delta/\Delta}$ *Fbxw7*$^{+/+}$ = 19; *Trp53*$^{\Delta/\Delta}$ *Fbxw7*$^{R482Q/+}$ = 14.

weeks of age (Figure 5.2C). To examine whether this had any effect on the expression of *Trp53*-dependent target genes, the expression of *Bbc3* and *Cdkn1a* was examined. Despite the significant downregulation of *Trp53* in both *Trp53*$^{\Delta/\Delta}$ *Fbxw7*$^{+/+}$ and *Trp53*$^{\Delta/\Delta}$ *Fbxw7*$^{R482Q/+}$ mice, there is no evidence of decreased expression of its target genes.

5.3.6 No evidence of altered expression of key proteins after combined *Trp53*$^{\Delta/\Delta}$ and *Fbxw7*$^{R482Q/+}$ alterations

Examination of key protein expression was performed by IHC staining for Pten, p-Akt, Trp53 and Ccne1 using FFPE sections from mice at 8 weeks of age or at survival end point. Staining for Pten at 8 weeks showed strong staining in both the epithelial and stromal cells, with no obvious changes in the intensity or pattern of protein expression across the *Trp53*$^{\Delta/\Delta}$ *Fbxw7*$^{+/+}$ and *Trp53*$^{\Delta/\Delta}$ *Fbxw7*$^{R482Q/+}$ mice, and no difference when compared with *Fbxw7*$^{+/+}$ mice (Figure 5.8A). As expression of Pten was high, unsurprisingly no staining or weak staining for p-Akt was seen in *Trp53*$^{\Delta/\Delta}$ *Fbxw7*$^{+/+}$ and *Trp53*$^{\Delta/\Delta}$ *Fbxw7*$^{R482Q/+}$ mice. Both *Trp53*$^{\Delta/\Delta}$ *Fbxw7*$^{+/+}$ and *Trp53*$^{\Delta/\Delta}$ *Fbxw7*$^{R482Q/+}$ samples exhibited weaker p53 staining than the *Fbxw7*$^{+/+}$ mice, a further indication of the successful recombination of the *Trp53*$^{fl/fl}$ allele. Finally, examination Ccne1 expression showed no difference between the *Trp53*$^{\Delta/\Delta}$ *Fbxw7*$^{+/+}$ and *Trp53*$^{\Delta/\Delta}$ *Fbxw7*$^{R482Q/+}$ genotypes or with either genotype and wild-type mice.

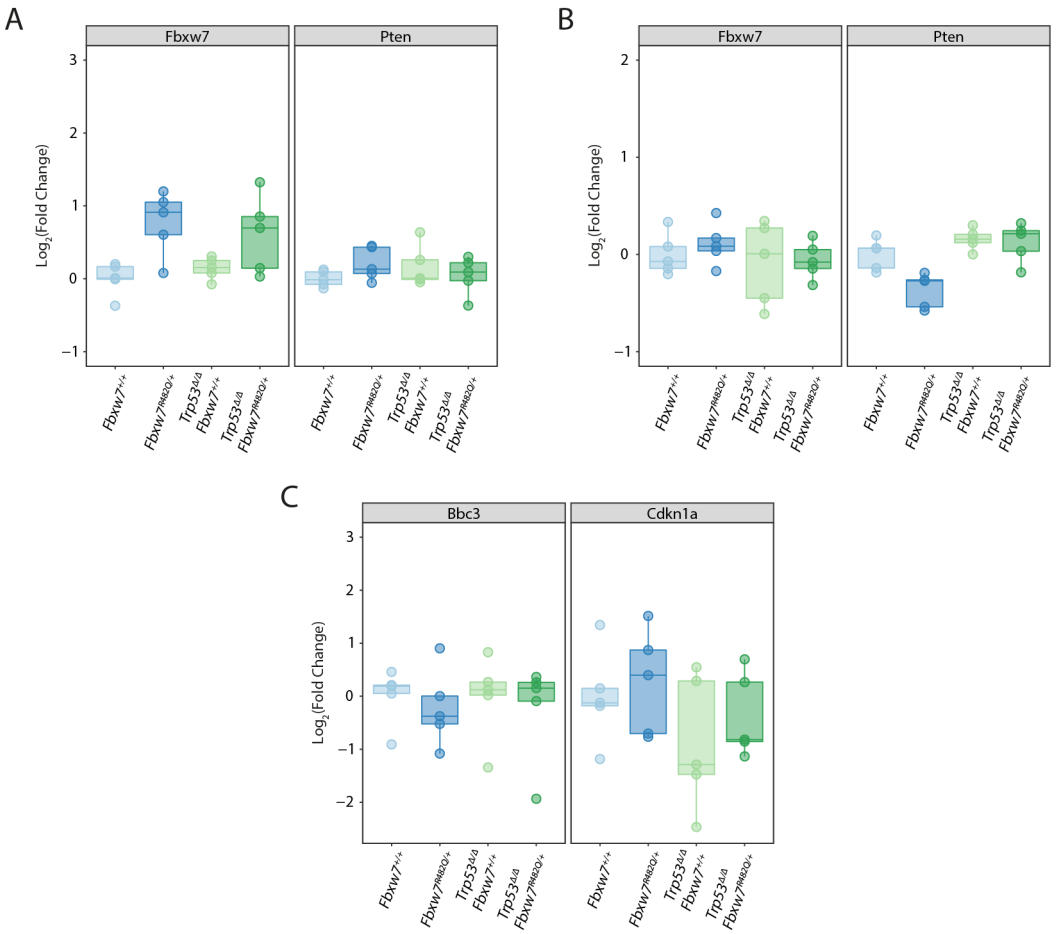

Figure 5.7: Targeted gene expression analysis by RT-qPCR from RNA extracted from fresh frozen uterine tissue collected from *Trp53*$^{\Delta/\Delta}$ and *Trp53*$^{\Delta/\Delta}$ *Fbxw7*$^{R482Q/+}$ mice. **A, B.** Relative expression of *Fbxw7* and *Pten* in uterine tissue collected at 4 weeks - **A** and 8 weeks - **B**. **C.** Relative expression of *Bbc3* and *Cdkn1a*, two p53-regulated genes examined in the uterine tissue of mice at 8 weeks.

To examine whether mutation of *Fbxw7* combined with $Trp53^{\Delta/\Delta}$ had an impact on expression of classical Fbxw7 targets, western blotting was performed on protein lysates from bulk-extracted, fresh-frozen uterine tissue collected from mice at 8 weeks (Figure 5.8B,C). Examination of Ccne1, Jun, Myc, and Notch1 showed no obvious differences between the $Trp53^{\Delta/\Delta}$ $Fbxw7^{+/+}$ and $Trp53^{\Delta/\Delta}$ $Fbxw7^{R482Q/+}$ mice. Quantification of the band intensity further showed the lack of significant difference in expression any of these targets between the two genotypes (Figure 5.8C).

Similar results were observed with IHC staining in sections from mice at survival end point (Figure 5.9). There was no difference in the expression of Pten, which remained highly expressed in both the epithelium and stroma of both $Trp53^{\Delta/\Delta}$ $Fbxw7^{+/+}$ and $Trp53^{\Delta/\Delta}$ $Fbxw7^{R482Q/+}$ mice. Concomitant with the high expression of Pten was low expression of p-Akt, which was mostly absent from both the epithelium and stroma except for some sporadic expression in the epithelial glands, which was similar to that observed in $Fbxw7^{+/+}$ mice (Figure 5.9). Trp53 expression was observed in the cytoplasm of epithelial cells of $Trp53^{\Delta/\Delta}$ $Fbxw7^{+/+}$ and $Trp53^{\Delta/\Delta}$ $Fbxw7^{R482Q/+}$ mice, however, this staining was less intense than in wild-type mice (Figure 5.9). Finally, Ccne1 expression did not appear to be altered in $Trp53^{\Delta/\Delta}$ $Fbxw7^{+/+}$ or $Trp53^{\Delta/\Delta}$ $Fbxw7^{R482Q/+}$ mice.

5.3.7 Generation of mice to examine whether *Trp53* missense mutation functions differently to *Trp53* loss

Considering the frequency of *TP53* mutations in EC and the known links between its dysregulation and cancer, it was surprising that the majority of mice exhibited no uterine phenotype. A high number of extrauterine tumours were observed in the $Trp53^{\Delta/\Delta}$ $Fbxw7^{+/+}$ mice but fewer in the $Trp53^{\Delta/\Delta}$ $Fbxw7^{R482Q/+}$ genotype. One potential explanation for the unexpected low frequency of cancer development is the difference in the functional consequences of *TP53* loss versus missense mutation. In EC missense mutations of *TP53* are much more common than truncating mutations (73.2% of all driver mutations are missense vs 19.3% being truncating), and it is known from previous literature that *TP53* missense mutation has additional oncogenic potential beyond that exhibited by loss alone, previously discussed in Section 1.4.2. Therefore, to examine whether

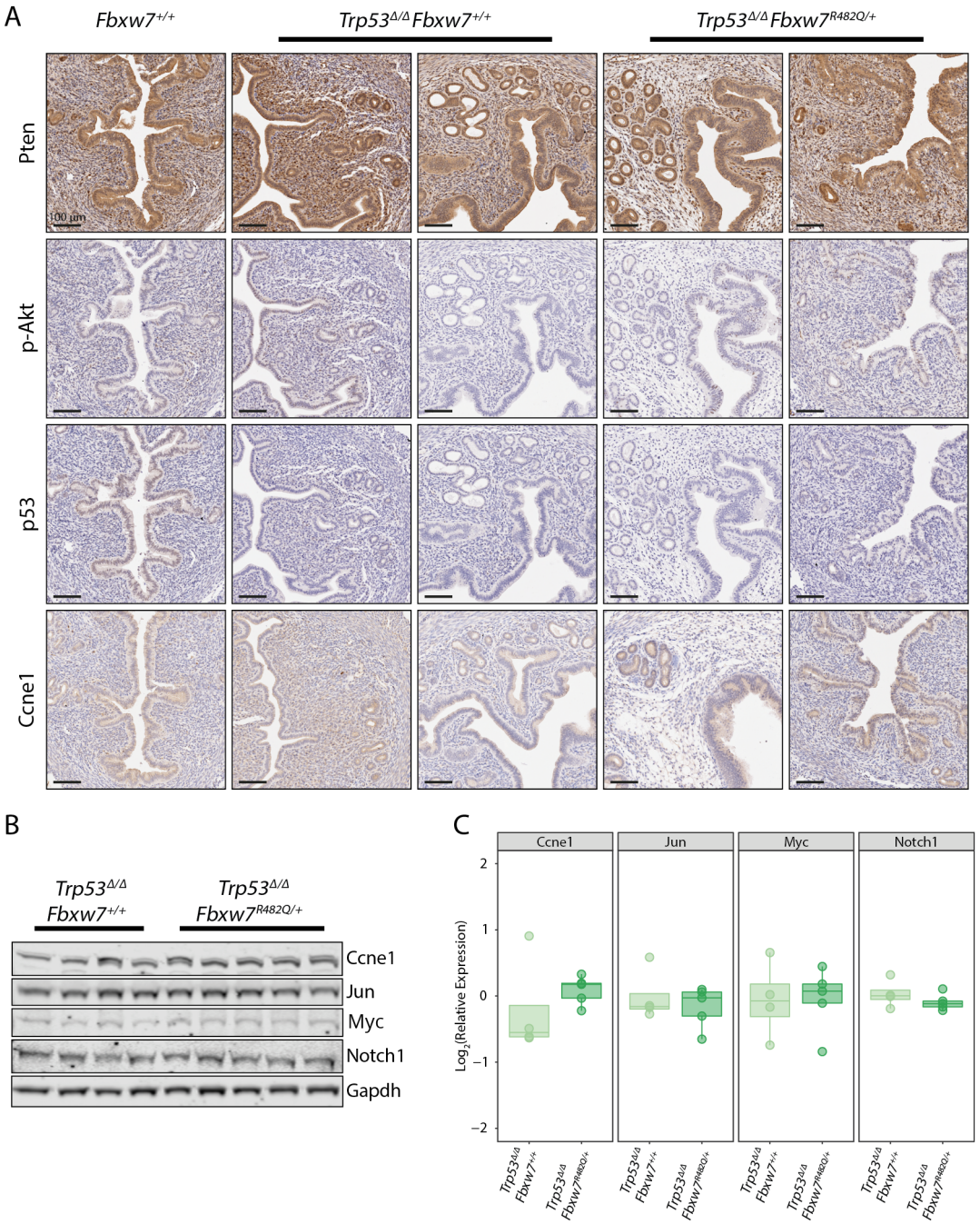

Figure 5.8: Protein expression changes examined in the uterus of $Trp53^{\Delta/\Delta}$ and $Trp53^{\Delta/\Delta}$ $Fbxw7^{R482Q/+}$ mice. **A.** IHC staining for Pten, p-Akt, Trp53, and Ccne1 in FFPE section of uterine tissue collected at 8 weeks of age. **B.** Western blotting analysis of known Fbxw7 targets in protein lysates extracted from bulk, fresh frozen uterine tissue collected at 8 weeks. **C.** Densitometry measures of the expression exhibited on the western blot with target expression normalised to Gapdh expression and shown relative to the expression level in $Trp53^{\Delta/\Delta}$ mice.

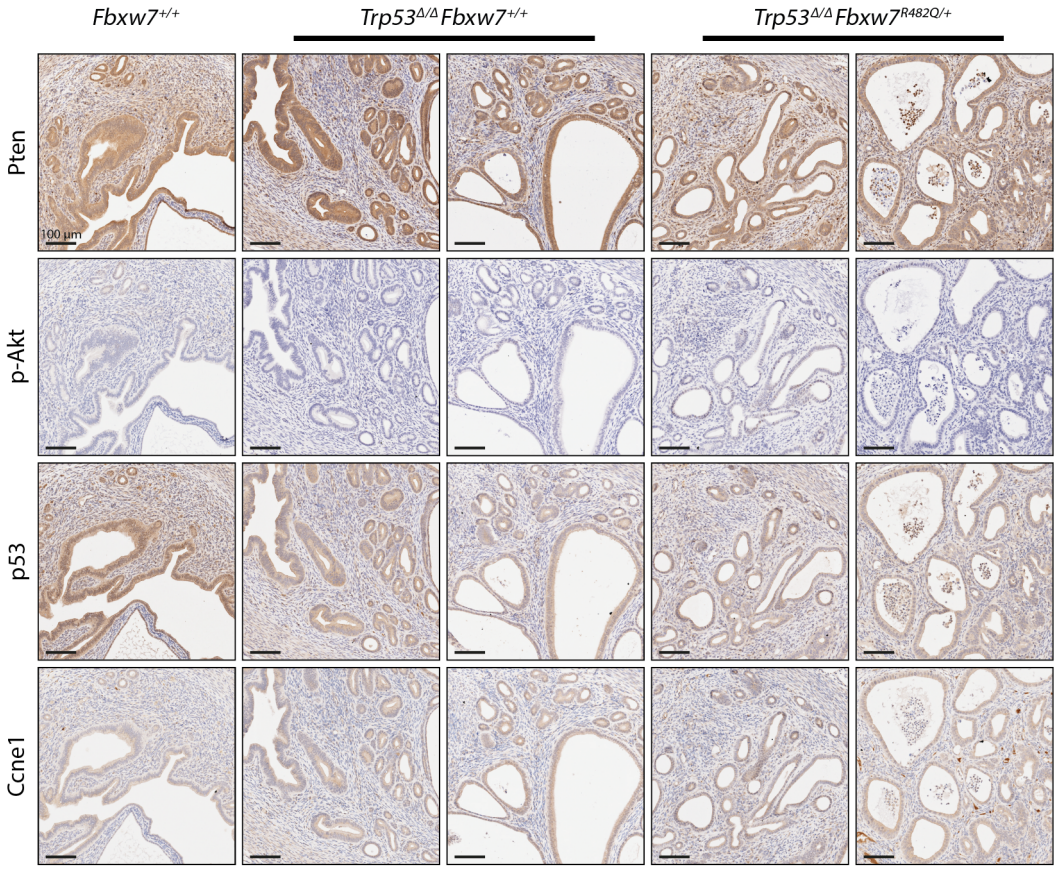

Figure 5.9: Protein expression changes examined in the uterus of $Trp53^{\Delta/\Delta}$ and $Trp53^{\Delta/\Delta}$ $Fbxw7^{R482Q/+}$ mice. IHC staining for Pten, p-Akt, Trp53, and Ccne1 in FFPE sections of uterine tissue collected at survival end point.

Trp53 missense mutation is capable of inducing EC and is potentiated by $Fbxw7^{R482Q}$, a mouse model of $Trp53^{R172H}$ mutation, equivalent to human R175H mutation, was generated.

To allow knock-in of the $Trp53^{R172H}$ mutation solely in tissues expressing *Pgr*, a Lox-Stop-Lox (LSL) allele was utilised. However, this type of allele functions as a deletion prior to recombination. Therefore, it was not possible to generate mice homozygous for the knock-in mutant allele, as they would express the mutation in the female reproductive tissues, but would be *Trp53*-deficient in all other tissues. Instead, a model of LOH was used in which the LSL knock-in mutant allele was combined with the conditional knock-out allele previously used, $Trp53^{LSL\text{-}R172H/fl}$ which would recombine to $Trp53^{R172H/\Delta}$. This allowed specific knock-in of the mutation in *Pgr*-expressing tissues with combined loss of the secondary allele, to mimic the frequent LOH observed with *TP53* mutation in human cancers, while maintaining wild-type p53 expression in remaining tissues.

Confirmation of mouse genotypes was performed by PCR (Figure 5.10A). Genotyping results for $Fbxw7^{+/+}$, $Trp53^{\Delta/\Delta}$ $Fbxw7^{+/+}$ and $Trp53^{\Delta/\Delta}$ $Fbxw7^{R482Q/+}$ are included for reference. It can be seen that the $Trp53^{R172H/\Delta}$ $Fbxw7^{+/+}$ and $Trp53^{R172H/\Delta}$ $Fbxw7^{R482Q/+}$ mice exhibit heterozygosity for the $Trp53^{fl}$ allele and the $Trp53^{LSL\text{-}R172H}$ allele. Recombination of the $Trp53^{fl}$ allele was confirmed, along with that of the $Fbxw7^{R482Q}$ allele in the $Trp53^{R172H/\Delta}$ $Fbxw7^{R482Q/+}$ mice. A PCR test for recombination of the $Trp53^{R172H}$ allele was not possible, therefore, to confirm correct expression of the mutation Sanger sequencing of cDNA derived from uterine RNA was performed (Figure 5.10B). From the electropherograms expression of the mutation was evident and the lack of a wild-type sequence trace shows that LOH had occurred.

5.3.8 $Trp53^{R172H/\Delta}$ induces endometrial cancer that is accelerated by $Fbxw7^{R482Q}$ mutation

To examine the impact of $Trp53^{R172H/\Delta}$ $Fbxw7^{+/+}$ and $Trp53^{R172H/\Delta}$ $Fbxw7^{R482Q/+}$ on overall survival, mice were aged until the onset of ill-health. Survival analysis performed on these animals indicated that $Trp53^{R172H/\Delta}$ $Fbxw7^{R482Q/+}$ mice exhibit significantly re-

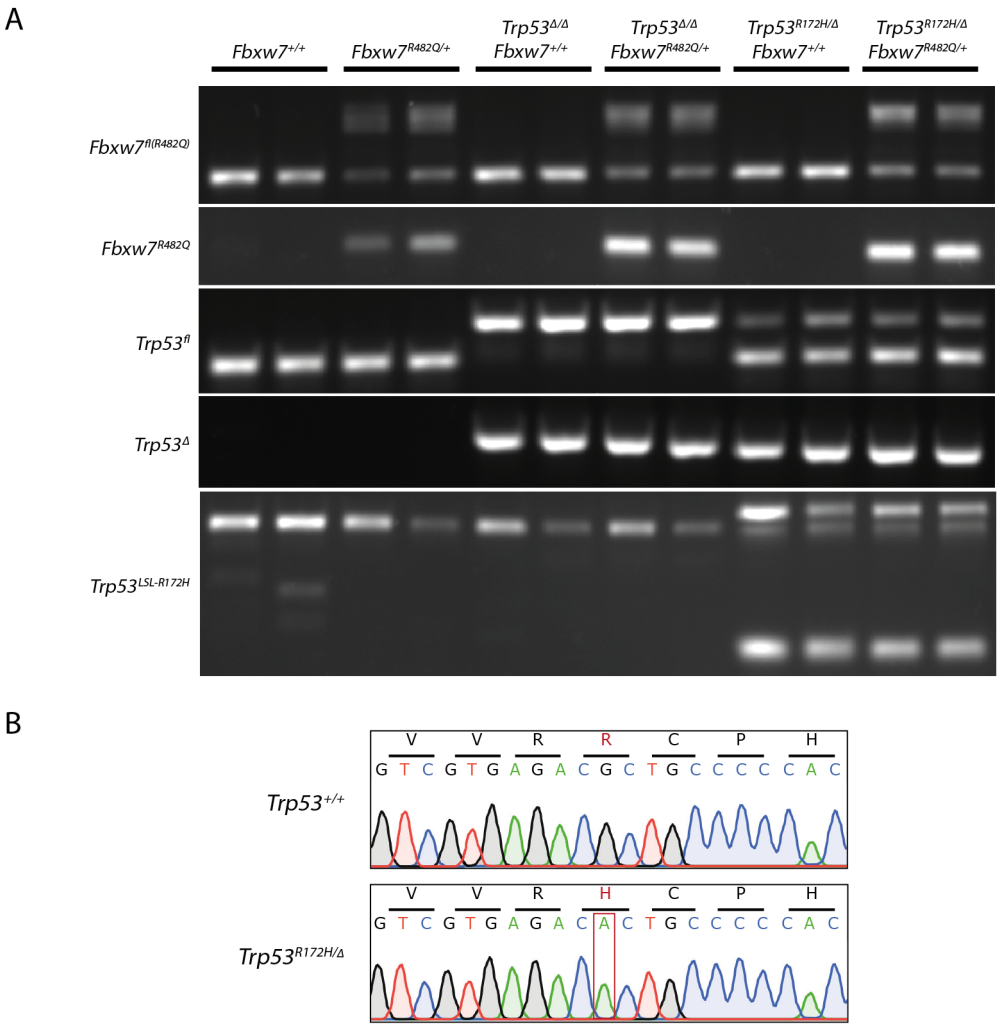

Figure 5.10: Confirmation of mouse genotypes and correct functionality of recombined alleles in the uterus. **A.** Agarose gel showing the PCR products of genotyping for the $Trp53^{fl}$, $Trp53^{LSL\text{-}R172H}$, and $Fbxw7^{fl(R482Q)}$ alleles. **B.** Electropherogram showing the sequence of the *Trp53* CDS in the uterus of $Trp53^{R172H/\Delta}$ and $Trp53^{+/+}$ mice.

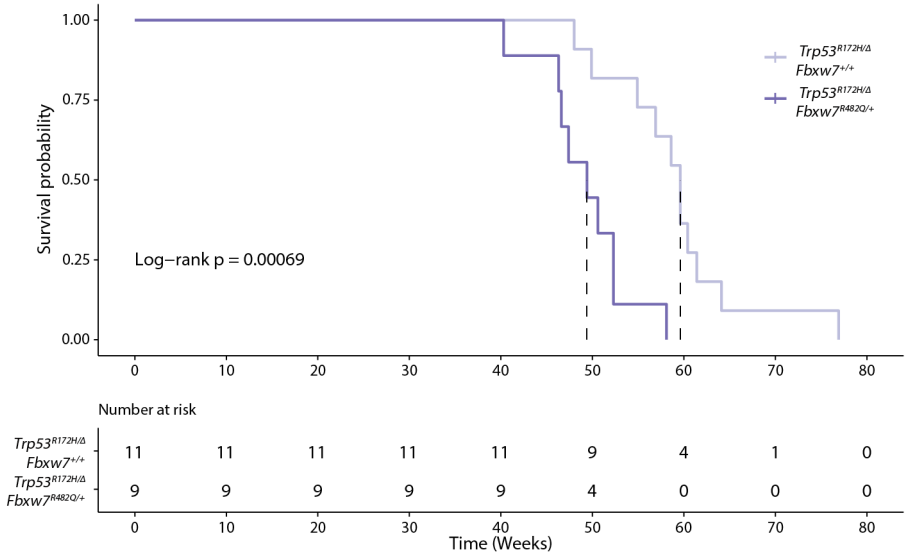

Figure 5.11: Survival analysis of *Trp53*$^{R172H/\Delta}$ and *Trp53*$^{R172H/\Delta}$ *Fbxw7*$^{R482Q/+}$ mice. Kaplan-Meier estimator analysis of the overall survival of *Trp53*$^{R172H/\Delta}$ and *Trp53*$^{R172H/\Delta}$ *Fbxw7*$^{R482Q/+}$ mice.

duced overall survival compared to *Trp53*$^{R172H/\Delta}$ *Fbxw7*$^{+/+}$ mice, with median survival reduced to 49.4 weeks from 59.6 weeks (P=0.00069). Unlike the *Trp53*$^{\Delta/\Delta}$ model, a uterine phenotype was more prominent in these mice, with frequent focal enlargement of one horn (or a region of one horn) of the uterus, although extrauterine tumours were still observed in both *Trp53*$^{R172H/\Delta}$ *Fbxw7*$^{+/+}$ and *Trp53*$^{R172H/\Delta}$ *Fbxw7*$^{R482Q/+}$ mice.

5.3.9 *Trp53*$^{R172H/\Delta}$ mutation induces endometrial cancer

Uterine histology was examined by H&E and IHC staining for Krt8 in FFPE tissue sections collected at 8 weeks and survival endpoint (Figure 5.12A). Pathological classification of the mice at both time points was determined by expert pathological review (Dr Tjalling Bosse and Dr Alicia Leon-Castillo) (Figure 5.12B). At 8 weeks, the uteri of both *Trp53*$^{R172H/\Delta}$ *Fbxw7*$^{+/+}$ and *Trp53*$^{R172H/\Delta}$ *Fbxw7*$^{R482Q/+}$ mice did not exhibit any variation from that of *Fbxw7*$^{+/+}$ mice, with no obvious changes to the structure or distribution of the glandular epithelium (Figure 5.12A). This was confirmed by expert pathological review, which found 100% of *Trp53*$^{R172H/\Delta}$ *Fbxw7*$^{+/+}$ and *Trp53*$^{R172H/\Delta}$ *Fbxw7*$^{R482Q/+}$ to exhibit normal uterine histology (Figure 5.12B).

However, at survival endpoint a drastic change in the uterine appearance was apparent with increased size and epithelial density in *Trp53*$^{R172H/\Delta}$ *Fbxw7*$^{+/+}$ and *Trp53*$^{R172H/\Delta}$

Fbxw7$^{R482Q/+}$ compared to wild-type (Figure 5.12A). Reflecting this histological change is the diagnosis of cancer in 81.8% of *Trp53*$^{R172H/\Delta}$ *Fbxw7*$^{+/+}$ and 100% of *Trp53*$^{R172H/\Delta}$ *Fbxw7*$^{R482Q/+}$ mice (Figure 5.12B). Hyperplasia and normal histology were both observed in 9.1% of *Trp53*$^{R172H/\Delta}$ *Fbxw7*$^{+/+}$ mice, but were not observed in *Trp53*$^{R172H/\Delta}$ *Fbxw7*$^{R482Q/+}$ mice (Figure 5.12B). The difference in frequency of cancer between *Trp53*$^{R172H/\Delta}$ *Fbxw7*$^{+/+}$ and *Trp53*$^{R172H/\Delta}$ *Fbxw7*$^{R482Q/+}$ mice was not statistically significant (P=0.48, Fisher Exact Test), although this is confounded by development of a phenotype being the end point for this cohort and the increased time to sacrifice in the *Trp53*$^{R172H/\Delta}$ *Fbxw7*$^{+/+}$ mice.

Unlike in the *Trp53*$^{\Delta/\Delta}$ *Fbxw7*$^{+/+}$ and *Trp53*$^{\Delta/\Delta}$ *Fbxw7*$^{R482Q/+}$ mice, which exhibited endometrial adenocarcinoma or sarcoma, the histological subtype of cancers arising in *Trp53*$^{R172H/\Delta}$ *Fbxw7*$^{+/+}$ and *Trp53*$^{R172H/\Delta}$ *Fbxw7*$^{R482Q/+}$ mice was more varied (Figure 5.12B). Carcinosarcoma was the most common histology in both *Trp53*$^{R172H/\Delta}$ *Fbxw7*$^{+/+}$ (36.4%) and *Trp53*$^{R172H/\Delta}$ *Fbxw7*$^{R482Q/+}$ (55.6%) genotypes, followed by endometrial adenocarcinoma (18.2% and 22.2%, respectively), serous carcinoma (18.2% and 11.1%, respectively), and sarcoma (9.09% and 11.1%, respectively). There were no significant differences in the frequency of each histological subtype between *Trp53*$^{R172H/\Delta}$ *Fbxw7*$^{+/+}$ and *Trp53*$^{R172H/\Delta}$ *Fbxw7*$^{R482Q/+}$ mice.

5.3.10 *Trp53*$^{R172H/\Delta}$ mutation also drives extrauterine tumour development

A more penetrant uterine cancer phenotype was observed in *Trp53*$^{R172H/\Delta}$ mice compared with *Trp53*$^{\Delta/\Delta}$ mice (90.0% in *Trp53*$^{R172H/\Delta}$ *Fbxw7*$^{+/+}$ and *Trp53*$^{R172H/\Delta}$ *Fbxw7*$^{R482Q/+}$ combined vs 20.7% in *Trp53*$^{\Delta/\Delta}$ *Fbxw7*$^{+/+}$ and *Trp53*$^{\Delta/\Delta}$ *Fbxw7*$^{R482Q/+}$ combined, P<0.00001, Fisher Exact Test). However, extrauterine tumours were still observed in both *Trp53*$^{R172H/\Delta}$ *Fbxw7*$^{+/+}$ and *Trp53*$^{R172H/\Delta}$ *Fbxw7*$^{R482Q/+}$ mice (Figure 5.13). Furthermore, the frequency of extrauterine tumours in *Trp53*$^{R172H/\Delta}$ mice was not significantly different than in *Trp53*$^{\Delta/\Delta}$ mice (69.6% in *Trp53*$^{R172H/\Delta}$ *Fbxw7*$^{+/+}$ and *Trp53*$^{R172H/\Delta}$ *Fbxw7*$^{R482Q/+}$ combined vs 57.6% in *Trp53*$^{\Delta/\Delta}$ *Fbxw7*$^{+/+}$ and *Trp53*$^{\Delta/\Delta}$ *Fbxw7*$^{R482Q/+}$ combined, P=0.41, Fisher Exact Test).

A lower frequency of extrauterine tumours were identified in *Trp53*$^{R172H/\Delta}$ *Fbxw7*$^{R482Q/+}$

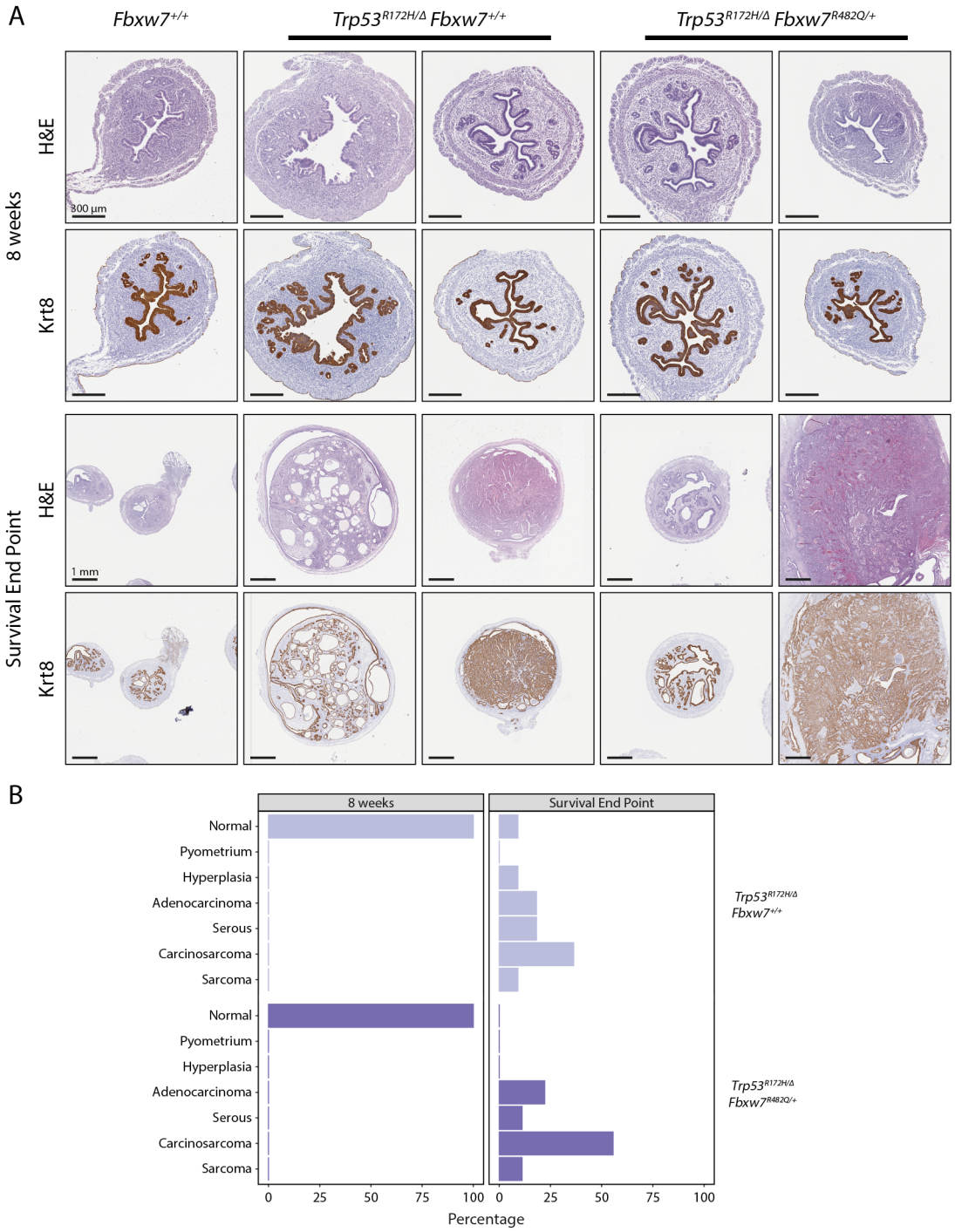

Figure 5.12: Histological examination and pathological classification of uterine tissue collected from $Trp53^{R172H/\Delta}$ and $Trp53^{R172H/\Delta}$ $Fbxw7^{R482Q/+}$ mice. **A.** H&E staining and IHC staining for Krt8 (epithelial marker) of FFPE tissue sections to examine the gross histological structure of the uterus. **B.** Classification of uterine pathology evident in mice at 8 weeks and survival end point as determined by expert pathological review. Number of mice analysed $Trp53^{R172H/\Delta}$ $Fbxw7^{+/+}$: 8w = 5, survival end point = 11; $Trp53^{R172H/\Delta}$ $Fbxw7^{R482Q/+}$: 8w = 5, survival end point = 9.

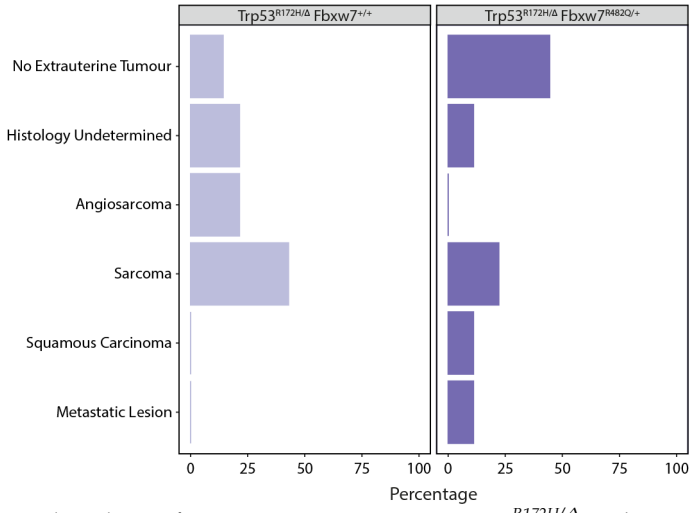

Figure 5.13: Pathological analysis of extrauterine tumours in *Trp53*$^{R172H/\Delta}$ and *Trp53*$^{R172H/\Delta}$ *Fbxw7*$^{R482Q/+}$ mice, as determined by expert pathological review. Number of mice analysed *Trp53*$^{R172H/\Delta}$ *Fbxw7*$^{+/+}$ = 14; *Trp53*$^{R172H/\Delta}$ *Fbxw7*$^{R482Q/+}$ = 9.

mice (44.4% did not exhibit an extrauterine tumour) compared to *Trp53*$^{R172H/\Delta}$ *Fbxw7*$^{+/+}$ mice (14.3% did not exhibit an extrauterine tumour), but the difference was not statistically significant (P=0.066, Fisher Exact Test; Figure 5.13). Across the two models of *Trp53* mutation, *Trp53*$^{\Delta/\Delta}$ and *Trp53*$^{R172H/\Delta}$, the presence of *Fbxw7*^{R482Q} mutation was associated with a lower frequency of extrauterine tumours (60.9% with no extrauterine tumour for *Trp53*$^{\Delta/\Delta}$ *Fbxw7*$^{R482Q/+}$ and *Trp53*$^{R172H/\Delta}$ *Fbxw7*$^{R482Q/+}$ combined vs 21.2% for *Trp53*$^{\Delta/\Delta}$ *Fbxw7*$^{+/+}$ and *Trp53*$^{R172H/\Delta}$ *Fbxw7*$^{+/+}$ combined, P=0.0046, Fisher Exact Test).

5.3.11 *Pten* and *Trp53* expression is altered following combined *Trp53*$^{R172H/\Delta}$ *Fbxw7*^{R482Q} mutation

Examination of the expression of key genes in RNA extracted from bulk, fresh-frozen tissue collected at 8 weeks of age, found no significant alterations in the expression of *Fbxw7* between *Trp53*$^{R172H/\Delta}$ *Fbxw7*$^{+/+}$ and *Trp53*$^{R172H/\Delta}$ *Fbxw7*$^{R482Q/+}$ mice (Figure 5.14A). In addition, no differences were observed between these two groups and *Fbxw7*$^{+/+}$ mice. However, statistically significant changes were observed in the expression of *Pten* between the *Trp53*$^{R172H/\Delta}$ *Fbxw7*$^{R482Q/+}$ and *Trp53*$^{R172H/\Delta}$ *Fbxw7*$^{+/+}$ mice (median $\log_2$(fold change) -0.306, P=0.016, Wilcoxon Rank Sum Test), suggesting downregulation of *Pten* with mutation of *Fbxw7* (Figure 5.14A). The *Trp53*$^{R172H/\Delta}$ *Fbxw7*$^{R482Q/+}$

mice also exhibited statistically significant downregulation of *Pten* when compared to *Fbxw7*$^{+/+}$ mice (median $\log_2$(fold change) -2.38, *P*=0.032, Wilcoxon Rank Sum Test).

Expression of *Trp53* in both *Trp53*$^{R172H/\Delta}$ *Fbxw7*$^{+/+}$ and *Trp53*$^{R172H/\Delta}$ *Fbxw7*$^{R482Q/+}$ uteri was significantly higher than in *Trp53*$^{\Delta/\Delta}$ *Fbxw7*$^{+/+}$ uteri (median $\log_2$(fold change) 3.34 *P*=0.0079; median 4.01 *P*=0.0079, respectively, Wilcoxon Rank Sum Test), and significantly lower than in *Fbxw7*$^{+/+}$ uteri (median $\log_2$(fold change) -1.76 *P*=0.0079; median $\log_2$(fold change) -1.09 *P*=0.0079 respectively, Wilcoxon Rank Sum Test) (Figure 5.14A). Expression of *Trp53* in *Trp53*$^{R172H/\Delta}$ *Fbxw7*$^{+/+}$ and *Trp53*$^{R172H/\Delta}$ *Fbxw7*$^{R482Q/+}$ uteri was, therefore, intermediate to that of *Fbxw7*$^{+/+}$ and *Trp53*$^{\Delta/\Delta}$ *Fbxw7*$^{+/+}$ uteri. Likely reflective of the heterozygous deletion that was used to induce the LOH of the missense mutation. Interestingly, *Trp53*$^{R172H/\Delta}$ *Fbxw7*$^{R482Q/+}$ mice exhibit significantly higher expression of *Trp53* compared to *Trp53*$^{R172H/\Delta}$ *Fbxw7*$^{+/+}$ (median $\log_2$(fold change) 0.672, *P*=0.016, Wilcoxon Rank Sum Test), suggesting there may be feedback caused by the missense mutation of *Fbxw7* driving increased expression of *Trp53*.

To examine whether these differences in *Trp53* expression correlated with target gene expression, expression of *Bbc3* and *Cdkn1a* was also examined (Figure 5.14B). Regulator of apoptosis, *Bbc3*, did not show any change in expression across all genotypes examined, despite the downregulation of *Trp53* seen in *Trp53*$^{R172H/\Delta}$ *Fbxw7*$^{+/+}$ and *Trp53*$^{R172H/\Delta}$ *Fbxw7*$^{R482Q/+}$ mice compared to wild-type. However, the cell cycle regulator *Cdkn1a* was found to be significantly downregulated in *Trp53*$^{R172H/\Delta}$ *Fbxw7*$^{R482Q/+}$ mice compared to *Trp53*$^{R172H/\Delta}$ *Fbxw7*$^{+/+}$ mice (median $\log_2$(fold change) 0.672, *P*=0.016, Wilcoxon Rank Sum Test), and was found to be borderline significantly downregulated in *Trp53*$^{R172H/\Delta}$ *Fbxw7*$^{R482Q/+}$ compared to wild-type mice (median $\log_2$(fold change) -1.57, *P*=0.056, Wilcoxon Rank Sum Test).

Unfortunately analysis of transcription changes at survival end point was not performed as, in most cases, the uterine enlargement observed in both *Trp53*$^{R172H/\Delta}$ *Fbxw7*$^{+/+}$ and *Trp53*$^{R172H/\Delta}$ *Fbxw7*$^{R482Q/+}$ mice was constrained to only one of the two uterine horns. The affected horn was retained for pathological examination by formalin fixation leaving insufficient tissue for molecular analysis. A second cohort of mice were aged until phenotype to allow collection of tissue for molecular analysis. From these mice,

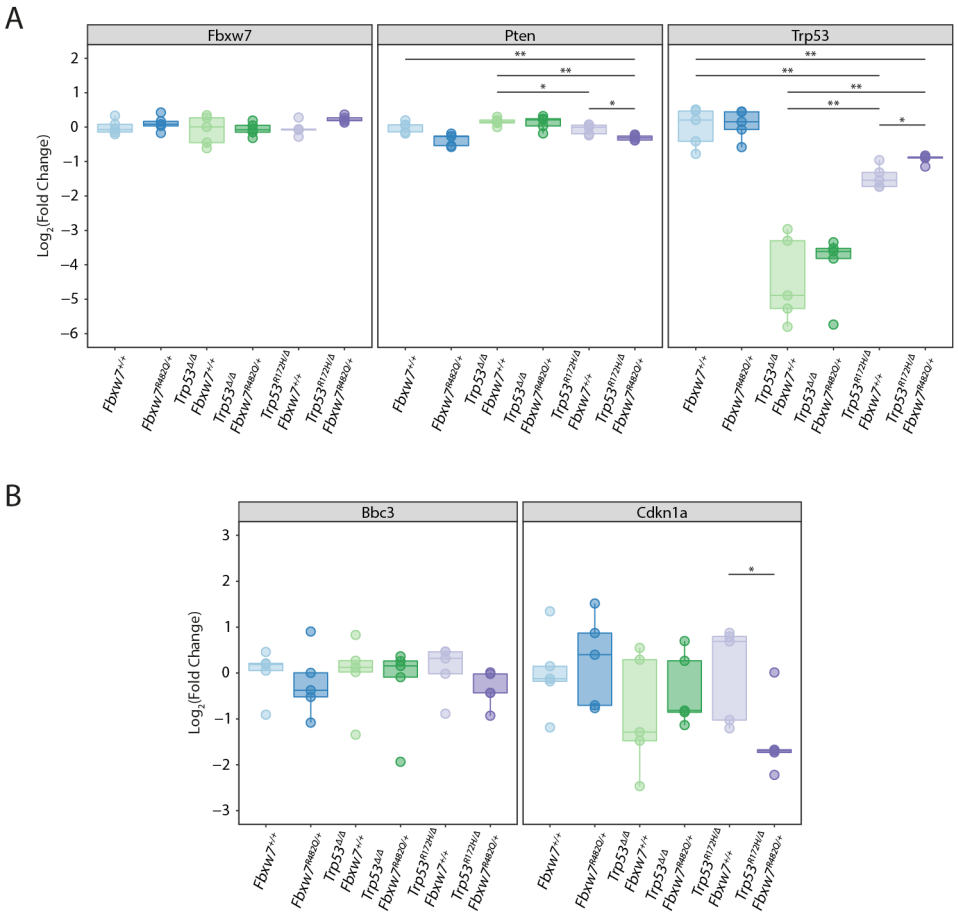

Figure 5.14: Targetted examination of gene expression changes by RT-qPCR analysis of RNA extracted from the uterus of $Trp53^{R172H/\Delta}$ and $Trp53^{R172H/\Delta}$ $Fbxw7^{R482Q/+}$ mice collected at 8 weeks. **A.** Relative gene expression for *Fbxw7*, *Pten*, and *Trp53* normalised to $Fbxw7^{+/+}$ mice. **B.** Relative gene expression for *Bbc3* and *Cdkn1a*, p53-regulated genes, normalised to $Fbxw7^{+/+}$ mice.

bulk DNA and RNA extraction was performed from sections of OCT-embedded uterine tumours. Expert pathological review of non-tumourous sections was performed (by Dr Lai Mun Wang) to identify regions of hyperplasia (usually from the second, non-tumourous horn), these regions were annotated and used to guide laser capture microdissection (LCM) of the tissue. From the LCM material, DNA and RNA was extracted, and alongside the bulk extracted nucleic acids, submitted for RNA and whole-exome DNA sequencing, but the results were not received in a time frame sufficient to allow their inclusion in this body of work.

5.3.12 p53 expression is significantly altered following *Trp53*$^{R172H/\Delta}$ mutation with simultaneous increases of *Fbxw7*-target expression

Following up on the transcription analysis, IHC was performed to stain for key proteins of interest (Figure 5.15A). Staining of FFPE uteri from mice at 8 weeks of age for Pten revealed similar expression to the transcription data with no obvious difference in intensity or localisation evident between the *Trp53*$^{R172H/\Delta}$ *Fbxw7*$^{+/+}$ and *Trp53*$^{R172H/\Delta}$ *Fbxw7*$^{R482Q/+}$ mice. As the with *Trp53*$^{\Delta/\Delta}$ models, there was no evidence of activation of the PI3K-pathway in either genotypes with samples negative for p-Akt staining, aside from sporadic positivity equivalent to that found in wild-type mice.

Interestingly, RNA expression data demonstrated significant downregulation of *Trp53* in *Trp53*$^{R172H/\Delta}$ *Fbxw7*$^{+/+}$ and *Trp53*$^{R172H/\Delta}$ *Fbxw7*$^{R482Q/+}$ uteri compared to wild-type uteri. However, IHC for p53 showed stronger staining in both the epithelium and stroma with increased frequency of nuclear staining in both compartments of *Trp53*$^{R172H/\Delta}$ *Fbxw7*$^{+/+}$ and *Trp53*$^{R172H/\Delta}$ *Fbxw7*$^{R482Q/+}$ uteri compared to wild-type (Figure 5.15A). This suggests that while the RNA expression is reduced, this is not mirrored at the protein level and raises the possibility that decreased proteasomal degradation of p53 may be occurring in these mice. Ccne1 expression exhibited some variation in staining between the *Trp53*$^{R172H/\Delta}$ *Fbxw7*$^{+/+}$ and *Trp53*$^{R172H/\Delta}$ *Fbxw7*$^{R482Q/+}$ genotypes. Ccne1 was mainly confined to the epithelium in the *Trp53*$^{R172H/\Delta}$ *Fbxw7*$^{+/+}$ mice, there was more frequent stromal staining apparent in the *Trp53*$^{R172H/\Delta}$ *Fbxw7*$^{R482Q/+}$ samples. However, the extent of expression in the epithelium did not differ. Based on the findings of the previous chapter, Lef1 expression was examined (Figure 5.15A). The extent of Lef1 expression was variable, with *Trp53*$^{R172H/\Delta}$ *Fbxw7*$^{+/+}$ and *Trp53*$^{R172H/\Delta}$ *Fbxw7*$^{R482Q/+}$ uteri ranging from no expression evident to focal expression in glandular epithelium to strong stromal expression, however, no difference between genotypes was found.

Despite the lack of histological change exhibited at 8 weeks of age, there was a slight difference in the distribution of Ccne1 staining in *Trp53*$^{R172H/\Delta}$ *Fbxw7*$^{R482Q/+}$ mice. To examine whether this is reflective of a change in Ccne1 expression, western blotting was performed on protein lysates from uteri at this age point, and further known Fbxw7 tar-

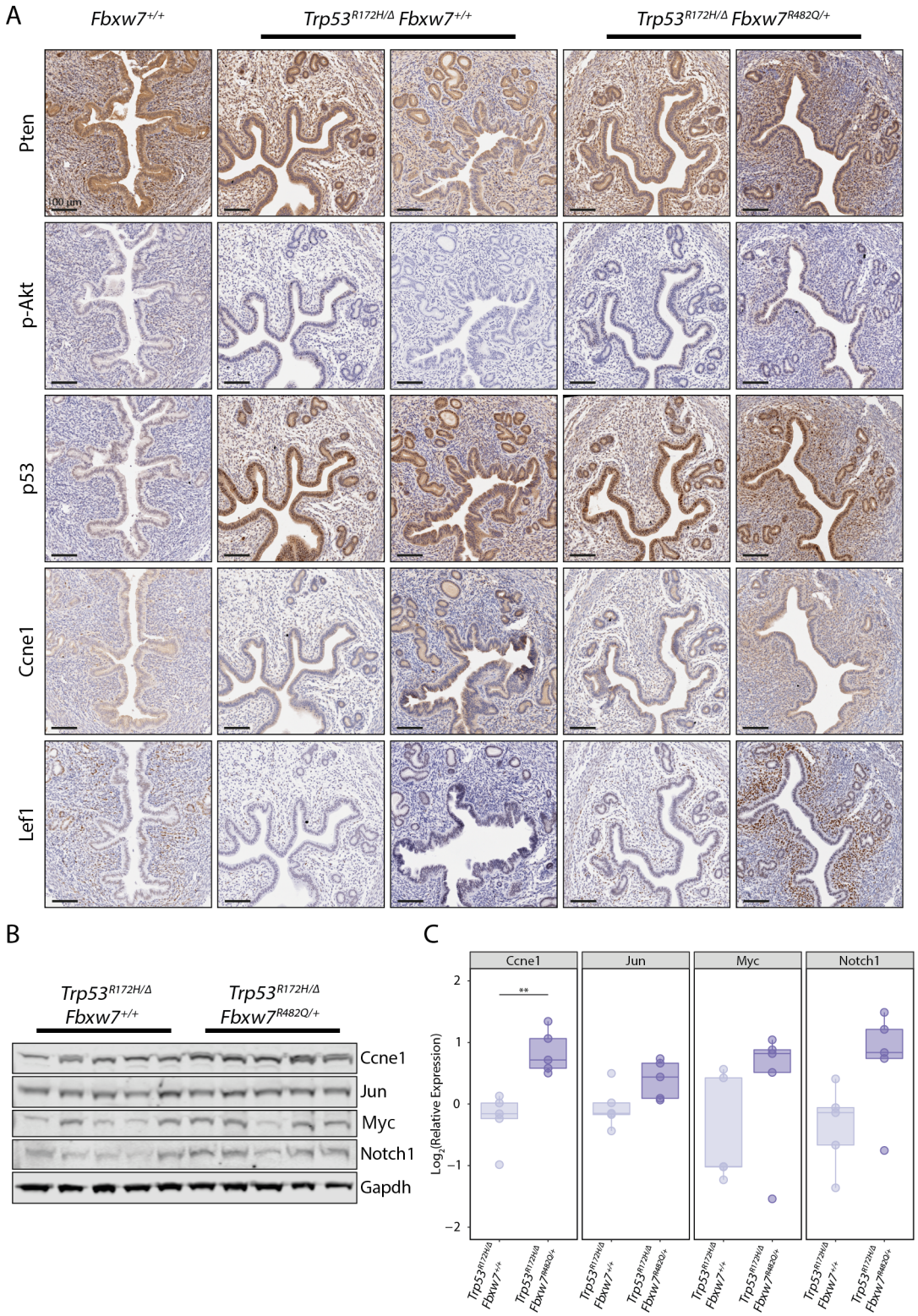

Figure 5.15: Examination of protein expression in the uterine tissue of *Trp53*$^{R172H/\Delta}$ and *Trp53*$^{R172H/\Delta}$ *Fbxw7*$^{R482Q/+}$ mice. **A.** IHC staining for Pten, p-Akt, Trp53, Ccne1 of uterine FFPE tissue sections collected from mice at 8 weeks. **B.** Western blotting analysis for known Fbxw7 substrates in protein lysates from bulk, fresh frozen uterine tissue collected at 8 weeks. **C.** Densitometry measures of the western blot band intensity for each protein examined normalised to Gapdh and expressed relative to *Trp53*$^{R172H/\Delta}$ mice.

gets were also examined (Figure 5.15B,C). Lef1 expression was not examined by western blot due to previous issues with antibody reliability. Perhaps surprisingly, there was a significant difference or borderline significant difference in expression of all targets examined. Ccne1 exhibited a statistically significant increase *Trp53*$^{R172H/\Delta}$ *Fbxw7*$^{R482Q/+}$ uteri (median $\log_2$(relative expression) 0.874, P=0.0079, Wilcoxon Rank Sum Test). Furthermore, while differences in Jun (median 0.590, P=0.056, Wilcoxon Rank Sum Test) and Notch1 (median 0.976, P=0.095, Wilcoxon Rank Sum Test) were not statistically significant, the data suggested there may be overexpression of these Fbxw7 targets. Together this suggests there is a loss of regulation of classical Fbxw7 targets in *Trp53*$^{R172H/\Delta}$ *Fbxw7*$^{R482Q/+}$ samples.

As previously noted, there was a significant change to uterine histology at survival end point, however, a lack of activation of the PI3K-pathway was apparent at this time point from IHC staining of uterine tissue (Figure 5.16). Pten expression remained high in both the epithelium and stroma of *Trp53*$^{R172H/\Delta}$ *Fbxw7*$^{+/+}$ and *Trp53*$^{R172H/\Delta}$ *Fbxw7*$^{R482Q/+}$ mice with concurrent negative staining for p-Akt. Ccne1 staining was uniform in the epithelium of both genotypes with no obvious increase in expression in the *Trp53*$^{R172H/\Delta}$ *Fbxw7*$^{R482Q/+}$ mice. Unfortunately, analysis by western blot was not possible for these samples, therefore, assessment of Ccne1 overexpression was not performed. Expression of Lef1 at survival end point was ubiquitous in both *Trp53*$^{R172H/\Delta}$ *Fbxw7*$^{+/+}$ and *Trp53*$^{R172H/\Delta}$ *Fbxw7*$^{R482Q/+}$ mice, with no obvious differences based on *Fbxw7*^{R482Q} status.

Expression of p53 was increased in *Trp53*$^{R172H/\Delta}$ *Fbxw7*$^{+/+}$ and *Trp53*$^{R172H/\Delta}$ *Fbxw7*$^{R482Q/+}$ mice compared to *Fbxw7*$^{+/+}$ at survival end point. However, at this time point the samples exhibited a prominent pattern of nuclear p53 staining in the epithelial cells, which was present in all samples evaluated and particularly those of the *Trp53*$^{R172H/\Delta}$ *Fbxw7*$^{R482Q/+}$ genotype (Figure 5.16). The expression in *Trp53*$^{R172H/\Delta}$ *Fbxw7*$^{+/+}$ was more variable with some samples exhibiting the same strong nuclear staining across the majority of the epithelium, but others exhibiting a total loss of nuclear p53 expression in large areas of the epithelium. As highlighted, this pattern of nuclear p53 loss was more prominent in the *Trp53*$^{R172H/\Delta}$ *Fbxw7*$^{+/+}$ mice, with 75% of samples examined exhibit-

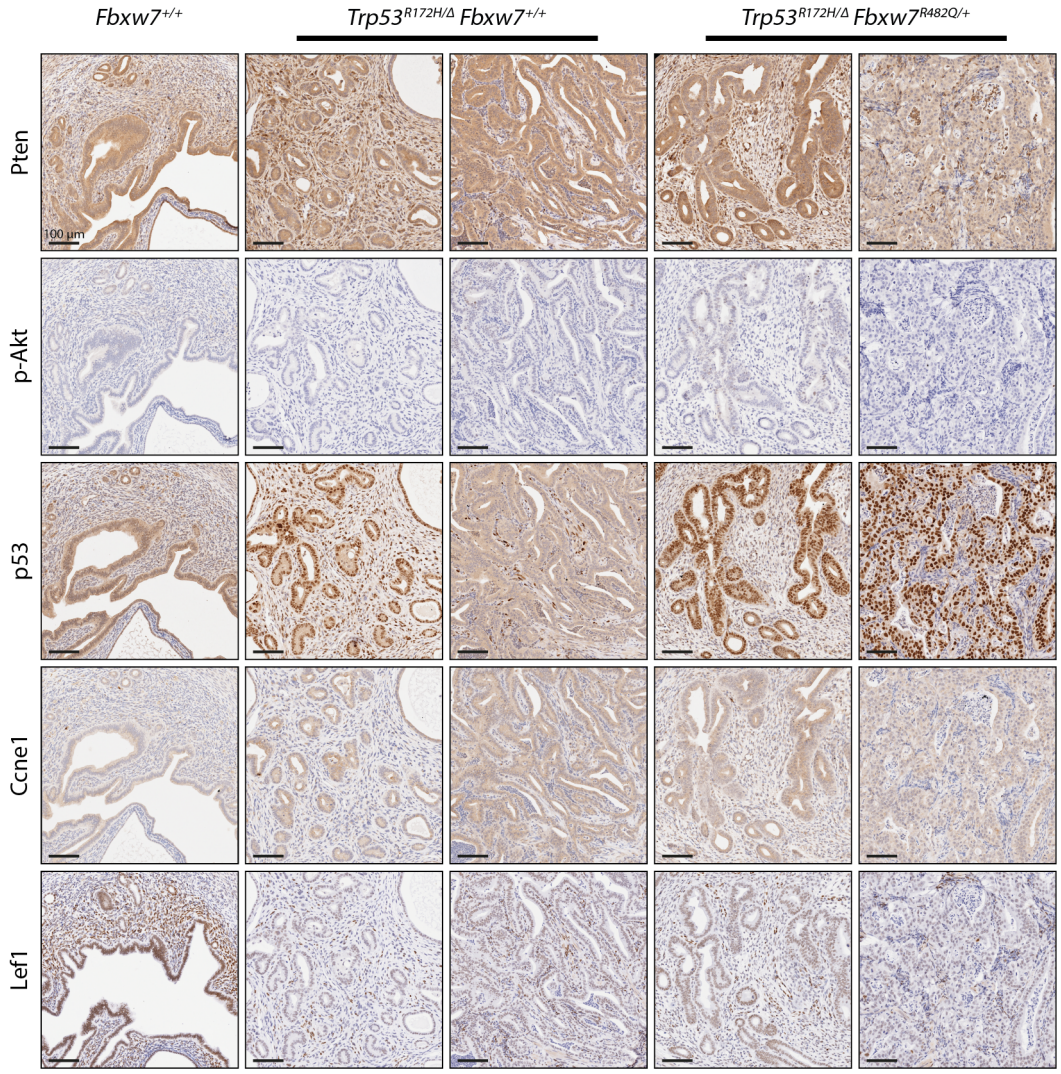

Figure 5.16: Examination of protein expression in the uterine tissue of *Trp53*$^{R172H/\Delta}$ and *Trp53*$^{R172H/\Delta}$ *Fbxw7*$^{R482Q/+}$ mice. IHC staining for Pten, p-Akt, Trp53, Ccne1 of uterine FFPE tissue sections collected from mice at survival end point.

ing loss in a large proportion of the epithelium. There was evidence of this loss in 50% of *Trp53*$^{R172H/\Delta}$ *Fbxw7*$^{R482Q/+}$ samples but in these, it was confined to a single or small group of glandular structures instead of being the predominant epithelial feature (Figure 5.16).

5.4 Discussion

In this chapter, I examined the effects of *Trp53* deletion and missense mutation in the mouse uterus. It was expected, due to the frequency of *TP53* mutation in human EC and

its status as an EC driver and tumour suppressor, that these mutations would potently induce cancer in these mice. This was not the case for $Trp53^{\Delta/\Delta}$ mice, while some mice did exhibit endometrial adenocarcinoma or uterine sarcoma, cancer was infrequent in both $Trp53^{\Delta/\Delta}$ $Fbxw7^{+/+}$ and $Trp53^{\Delta/\Delta}$ $Fbxw7^{R482Q/+}$ mice. However, the introduction of *Trp53* missense mutation greatly increased the frequency of EC with all but two animals from the $Trp53^{R172H/\Delta}$ survival cohort exhibiting EC and the majority determined to be carcinosarcomas. This further highlights the previous reports in the literature of a gain-of-function effect that is present following mutation of p53 and suggests that similar effects occur with *Trp53* missense mutation in the uterus [405].

Focussing on the potential role of *Fbxw7* mutation in combination with *Trp53* loss or missense mutation, it is evident from the $Trp53^{R172H/\Delta}$ cohort that combination with $Fbxw7^{R482Q}$ is associated with a worse survival outcome than $Trp53^{R172H/\Delta}$ alone, demonstrating that this mutation can co-operate with or promote the carcinogenic effects of *Trp53* missense mutation. It is, however, interesting that no evidence of worse survival was apparent from the $Trp53^{\Delta/\Delta}$ cohorts. One potential confounding factor for the $Trp53^{\Delta/\Delta}$ survival analysis was the presence of extrauterine tumours which will have obscured the uterine-related survival of both cohorts. In both the $Trp53^{\Delta/\Delta}$ and $Trp53^{R172H/\Delta}$ models, the majority of extrauterine tumours exhibited a sarcomatous histology, a cancer type that exhibits a very few *FBXW7* mutations in humans, with no missense mutations present in the TCGA sarcoma cohort [406]. The lack of missense mutation in human cancers combined with lower rate of extrauterine tumours observed with $Fbxw7^{R482Q}$, reinforces the concept that *FBXW7* mutations have differential effects in the tissues of the body and have a variable impact on carcinogenesis in various tissues.

The slightly higher rate of EC and lower rate of extrauterine tumours that was noted in the $Trp53^{\Delta/\Delta}$ $Fbxw7^{R482Q/+}$ mice points towards the possibility that an exacerbated uterine phenotype may still be present in these mice. However, this may be masked by the onset of the non-uterine phenotype which removes the ability to observe any potential uterine differences. Alternatively, it may be the case that *Fbxw7* mutation potentiates the dysregulation caused by the gain-of-function activities of mutant p53

which are lacking in the *Trp53*$^{\Delta/\Delta}$ mice. There have been many functions attributed as gain-of-function phenotypes associated with p53 mutation including metabolic reprogramming, enhanced survival under cellular stress, genomic instability and promotion of cell cycle activity [405, 407–409].

The dysregulation induced by *Fbxw7* mutation may complement many of these phenotypes based on known substrates for degradation. CCNE1 is perhaps the most well known target of FBXW7 and mutation has been previously linked with CCNE1 accumulation. Furthermore, Ccne1 expression was significantly increased in *Trp53*$^{R172H/\Delta}$ *Fbxw7*$^{R482Q/+}$ mice [227]. p53 is a well known regulator of the cell cycle, however, *TP53* mutations, including R175H (analogous to R172H in mice), lead to an inability to upregulate key cell cycle regulators, such as p21$^{\text{CIP1}}$ [410]. p21$^{\text{CIP1}}$ is a product of the *Cdkn1a* locus, and while reduced expression was not observed in *Trp53*$^{R172H/\Delta}$ *Fbxw7*$^{+/+}$ mice, there was significant downregulation of this gene in *Trp53*$^{R172H/\Delta}$ *Fbxw7*$^{R482Q/+}$ mice compared to *Trp53*$^{R172H/\Delta}$ *Fbxw7*$^{+/+}$ mice and borderline significantly reduced expression when compared to *Fbxw7*$^{+/+}$ mice. Therefore, in *Trp53*$^{R172H/\Delta}$ *Fbxw7*$^{R482Q/+}$ mice there appears to be reduction of negative regulation coinciding with increased expression of positive cell cycle regulators, suggesting that simultaneous mutation of *Trp53* and *Fbxw7* could be inducing rapid, uncontrolled cell proliferation.

Recent work examining pancreatic cancer genome evolution following p53 inactivation, highlights that this alone is not sufficient to drive carcinogenesis, and loss of regulation of ploidy and subsequent accumulation of CNAs is also required [411]. This lag phase of accumulation of CNAs would appear to contradict the noted lack of *TP53* mutation in early precancerous lesions in EC [352, 353, 359, 360]. However, it is possible that a short duration of this phase would render it difficult to capture a precancerous lesion containing p53 mutation. Furthermore, this requirement for accumulation of CNAs would also match the patterns of tumour formation observed in the *Trp53*$^{R172H/\Delta}$ mice. These mice exhibited focal lesions in the uterus, generally with only one of the two horns exhibiting enlargement and a cancerous phenotype. The second horn was, in most cases, unaffected and exhibited mostly normal histology, although evidence of hyperplasia was common. This suggests there may be a requirement for further ge-

netic alterations or accumulation of mutations that allow cancer formation, including those that reduce activity of anti-cancer pathways (TGF-β) or activate oncogenic pathways (MYC) [411]. This is opposed to pattern of tumour formation in the $Pten^{\Delta/\Delta}$ mice, which generally exhibited uniform enlargement of both horns of the uterus, suggesting that loss of *Pten* alone is sufficient to induce a cancerous phenotype.

From previous reports of the phenotypes induced by *Fbxw7* mutation a co-operative or accelerating effect on the accumulation of CNAs may also contribute to the reduced survival of $Trp53^{R172H/\Delta}$ $Fbxw7^{R482Q/+}$ mice. It has been previously reported that deletion of Fbxw7 initiates a process of Ccne1-driven genomic instability, although an alternative study has suggested Fbxw7 may not have a role in genomic instability [283, 412]. Independently of Fbxw7, cells expressing ubiquitination-resistant Ccne1 combined with p21 deletion were found to generate a growing population of aneuploid cells, which were not present in a population of cells with p21-deletion alone [413]. An expansion of this study using deletion of *Fbxw7* in place of *Ccne1* mutation found a similar genomic instability phenotype [403]. As previously mentioned, the $Trp53^{R172H/\Delta}$ $Fbxw7^{R482Q/+}$ mice in this study exhibited both increased expression of Ccne1, likely due to loss of proteasomal degradation by Fbxw7, and significantly reduced RNA expression of *Cdkn1a*, which encodes p21. Therefore, $Trp53^{R172H/\Delta}$ $Fbxw7^{R482Q/+}$ mutations could be recapitulating the conditions examined by Loeb *et al.*and Minella *et al.*, to drive genomic instability.

Aside from the potential CCNE1-driven genomic instability, more recently FBXW7 has been directly linked to DNA damage repair through the non-homologous end joining (NHEJ) pathway [287]. A loss of Fbxw7 functionality reduces polyubiquitination of XRCC4, which reduced activity of the NHEJ pathway leading to reduced efficiency of double strand break repairs [287]. The result of this defective NHEJ is genomic instability with potential for accumulation of chromosomal rearrangements [414].

While examination of CNAs in the $Trp53^{R172H/\Delta}$ $Fbxw7^{R482Q/+}$ mice was not possible due to time constraints, there is some evidence that they may have a role in cancer development in these mice. The prevailing histological subtype observed in both $Trp53^{R172H/\Delta}$ $Fbxw7^{+/+}$ and $Trp53^{R172H/\Delta}$ $Fbxw7^{R482Q/+}$ mice was carcinosarcoma with

several cases of serous carcinoma also noted. In human EC, these histological subtypes are frequently associated with large scale CNAs, with up to 90% of uterine carcinosarcomas having undergone at least one whole-genome doubling event and 100% of serous carcinomas in the TCGA analysis classified in the CN-high subtype [90, 91]. Whether these histological subtypes exhibit the same association with CNA in mice has yet to be determined. However, a recent publication implicating *Fbxw7* loss as a driver of uterine carcinosarcoma noted that spontaneous loss or mutation of p53 was a required factor for progression to carcinosarcoma [316]. As previously discussed, DNA samples from $Trp53^{R172H/\Delta}$ $Fbxw7^{+/+}$ and $Trp53^{R172H/\Delta}$ $Fbxw7^{R482Q/+}$ tumours and hyperplasia have been sent for whole-exome sequencing. The results of this analysis will allow deeper investigation of the extent of CNA in these mice and the potential accumulation of CNAs as a driving force behind progression from hyperplasia to malignancy.

As opposed to positively enforcing the dysregulated pathways initiated by mutant p53, it may be that mutation of *Fbxw7* directly promotes its activity. It has been shown that mutant p53 exhibits higher levels of protein stability in cancer, similar to the higher expression noted from the IHC staining of p53 in $Trp53^{R172H/\Delta}$ mice [409]. Two reported mechanisms by which this is achieved, are through the association of p53 with chaperones such as HSP90AA1, which are upregulated by HSF1 in response to cellular stress and leads to inhibition of association with MDM2 and subsequent protein stabilisation [409, 415]. The second method, as discussed in Section 1.4.1, involves phosphorylation and stabilisation following DNA damage by the ATM/ATR kinase cascade [409].

FBXW7 could be implicated in driving stabilisation of mutant p53 through both of these methods. HSF1, a master transcription factor of the stress response, is a known target of FBXW7 which may be dysregulated by mutation [280]. Furthermore, Fbxw7 has been implicated in acquisition of DNA damage, in particular, copy number alterations through the loss of CCNE1 regulation, which could trigger a DNA damage response [283, 403]. Finally, FBXW7 has been linked to direct regulation of p53 stability through interaction and ubiquitination [284, 285]. Therefore, it may be the case that through dysregulation of known targets such as Hsf1, induction of DNA-damage or loss of direct regulation of p53 itself, mutation of *Fbxw7* further stabilises p53 exacerbating its

oncogenic functions.

Interestingly, in the *Trp53*$^{R172H/\Delta}$ mouse models examined it is apparent from p53 staining at survival end point that expression of p53 was retained in a larger proportion of epithelial cells in *Trp53*$^{R172H/\Delta}$ *Fbxw7*$^{R482Q/+}$ mice compared to *Trp53*$^{R172H/\Delta}$ *Fbxw7*$^{+/+}$ mice. In addition, Ccne1 was found to be significantly overexpressed in tissue collected from *Trp53*$^{R172H/\Delta}$ *Fbxw7*$^{R482Q/+}$ mice. Therefore, co-operation through the above routes is possible, but determining whether the more aggressive cancer phenotype is driven by mutual pathway dysregulation or through p53 stabilisation, or both would require further examination.

5.4.1 Future directions

In this chapter, I have outlined several mechanisms by which *Fbxw7* mutation may be interacting with *Trp53* mutation in the generated mouse models to induce a more severe uterine phenotype. However, additional work would be required to determine which, if any, of these mechanisms may be active. It is apparent that both overexpression of Ccne1 and reduced expression of *Cdkn1a* are present in *Trp53*$^{R172H/\Delta}$ *Fbxw7*$^{R482Q/+}$ mice compared to *Trp53*$^{R172H/\Delta}$ *Fbxw7*$^{+/+}$. However, how these changes may contribute to carcinogenesis requires further analysis. Two of the major phenotypes associated with these alterations would be uncontrolled proliferation and/or enhanced genomic instability leading to accumulation of CNAs. If *Trp53*$^{R172H/\Delta}$ *Fbxw7*$^{R482Q/+}$ mice are exhibiting a higher level of proliferation from loss of cell cycle arrest then IHC staining for marker of proliferation Ki-67 (Ki67) could indicate the higher levels of proliferating cells. Alternatively, if an enhanced CNA phenotype is present it may be possible to observe higher rates of CNAs using a method such as low-pass whole genome sequencing.

As previously discussed, deeper analysis of the molecular dysregulation in these samples is in progress, but could not be completed due to time constraints. However, DNA and RNA samples were prepared from fresh-frozen OCT embedded tissue for both *Trp53*$^{R172H/\Delta}$ *Fbxw7*$^{+/+}$ and *Trp53*$^{R172H/\Delta}$ *Fbxw7*$^{R482Q/+}$ mice. This included extraction of bulk DNA and RNA from tumour samples and from LCM of hyperplastic epithelium. Performing low pass whole genome sequencing on these DNA samples would al-

low comparison of the extent of CNA in both genotypes and determination of whether an exacerbated phenotype is present in *Trp53*$^{R172H/\Delta}$ *Fbxw7*$^{R482Q/+}$ mice, as might be expected based on prior reports. In addition, it would be possible to examine the importance of CNA accumulation in progression to EC through comparison of CNAs in regions of hyperplasia and EC. This may also allow for determination of any genomic regions, which are commonly amplified or lost across the samples to which in turn may give an indication of other genes that could be promoting the transition from hyperplasia to cancer.

In addition to the DNA analysis, analysis of RNA sequencing data currently being generated would allow a comparison of the relative transcriptional environments of *Trp53*$^{R172H/\Delta}$ *Fbxw7*$^{R482Q/+}$ and *Trp53*$^{R172H/\Delta}$ *Fbxw7*$^{+/+}$ mice. Using a method such as GSEA, as in Chapter 4, to examine which pathways exhibit dysregulation or activation as a result of *Fbxw7* mutation and how this may interact with the effects of *Trp53*$^{R172H/\Delta}$. Furthermore, being able to examine both cancers and hyperplasia might give an indication of which pathways are driving the switch from precursory lesion to malignant neoplasia. This would also allow examination of the extent to which Wnt activation is present in this model, and whether this is altered by *Fbxw7*^{R482Q} mutation, as was found in the *Pten*$^{\Delta/\Delta}$ *Fbxw7*$^{R482Q/+}$ model. Limited examination of Wnt factors was possible in *Trp53*$^{R172H/\Delta}$ *Fbxw7*$^{R482Q/+}$ mice, due to time constraints, but examination of Lef1 by IHC indicated strong expression in both *Trp53*$^{R172H/\Delta}$ *Fbxw7*$^{+/+}$ and *Trp53*$^{R172H/\Delta}$ *Fbxw7*$^{R482Q/+}$ mice, suggesting a potential role for Lef1 in EC. It would therefore, be pertinent to examine further members of the Wnt pathway to determine if differential activity is present.

The difference between the phenotypes of *Trp53*$^{\Delta/\Delta}$ and *Trp53*$^{R172H/\Delta}$ mice also warrants further examination. It was apparent from the *Trp53*$^{\Delta/\Delta}$ mouse models that examination of any potential uterine phenotype is disrupted by the onset of extrauterine phenotypes. Therefore, it may be more worthwhile to examine this effect using *in vitro* cell line models. It would be possible to generate cell line models from the mouse strains used in this chapter by crossing with a tamoxifen-inducible CAG-Cre [416]. The use of this Cre would mean recombination would not occur until treatment with tamoxifen,

thus allowing collection of uteri from mice at an adult age, dissemination of the tissue, selection of epithelial cells and *in vitro* culture before induction of recombination by treatment with tamoxifen. Generating a model in this way would give a clean method of comparison for the effects of the individual mutations and their combinations in uterine epithelial cells, although it would have the consequence of losing the complexity of the mouse model system, such as interaction between epithelium and stroma.

Chapter 6

Conclusions and future Work

6.1 *FBXW7* mutations are important to the development of endometrial cancer

The work outlined in this thesis provides the first demonstration that heterozygous $Fbxw7^{R482Q}$ mutation alone is not sufficient to cause endometrial cancer or hyperplasia in the mouse uterus. However, when combined with either $Pten^{\Delta/\Delta}$ or $Trp53^{R172H/\Delta}$ mutation, it significantly accelerates endometrial cancer resulting in reduced survival. Investigation of pathway activation in the $Pten^{\Delta/\Delta}$ $Fbxw7^{R482Q/+}$ mice revealed Wnt transcription factors (Lef1 and Tcf7l2) as novel Fbxw7 targets and as potential factors contributing to reduced survival. However, further work involving disruption of the Wnt signalling pathway either genetically or pharmaceutically would be required to definitively determine the role that the interaction of Fbxw7 and Lef1 may play in these cancers.

Analysis of the $Trp53^{R172H/\Delta}$ $Fbxw7^{R482Q/+}$ mice shows they exhibit different histology to the $Pten^{\Delta/\Delta}$ model, with carcinosarcoma histology being most common, suggesting a different carcinogenic pathway may be driving cancer formation. While staining for Lef1 was evident in tumours of both $Trp53^{R172H/\Delta}$ $Fbxw7^{+/+}$ and $Trp53^{R172H/\Delta}$ $Fbxw7^{R482Q/+}$ mice, there was not an obvious difference in staining between the genotypes. This suggests that Lef1 expression may have a role in EC, but if so, its expression

is not driven by Fbxw7 mutation when combined with $Trp53^{R172H/\Delta}$ or that an alternative method of upregulation is active in the $Trp53^{R172H/\Delta}$ $Fbxw7^{+/+}$ mice. Nevertheless, $Trp53^{R172H/\Delta}$ $Fbxw7^{R482Q/+}$ mice exhibited increased expression of Ccne1 with concomitant reduced expression of *Cdkn1a*, a change which has previously been associated with both *Fbxw7* and *Trp53* mutation [403].

Despite a lack of differential Lef1 expression in the $Trp53^{R172H/\Delta}$ mice, Fbxw7 regulation of Lef1 in these tumours cannot be ruled out as a lack of change in the total protein expression does not necessarily equate with a lack difference in activity. It has been shown that the phosphorylation events that prime for ubiquitination can also be involved in protein activation [417, 418]. In particular, for Lef1 there have been reports that phosphorylation of T155 is associated with both activation of transcriptional activity and reduction of transcriptional activity, suggesting this site may have a role in providing a point of negative feedback, which could be linked to proteasomal degradation [419, 420]. Therefore, evaluation of activated transcriptional programs within these mice may be required to truly rule out Lef1 activation from cancer development.

6.2 Cellular context may determine role of *FBXW7* in endometrial cancer

One hypothesis for the role of *FBXW7* in endometrial cancer is that it can co-operate with multiple other cancer drivers through different mechanisms. Due to the varied role that it plays in cellular homeostasis and the wide range of reported targets, the function of *FBXW7* mutation in cancer may exhibit significant heterogeneity. If true, this plasticity could allow *FBXW7* mutation to promote carcinogenesis, but would also mean that current assumptions regarding prognosis or treatment of *FBXW7* mutant cancers would need to be re-evaluated to consider the mutational context of the tumour. Further study of the mechanisms of co-operation between *FBXW7* mutation and other drivers would be vital for determining whether different mechanisms are truly initiated by *FBXW7* mutation and whether mutations that target similar pathways have equivalent outcomes, such as loss of PTEN function and activation of PIK3CA.

Alternatively, if cancer driving mechanisms are retained in different mutational contexts and Fbxw7 does regulate Wnt transcription factor expression in the $Trp53^{R172H/\Delta}$ $Fbxw7^{R482Q/+}$ model, it provides an interesting hypothesis for the increased frequency of *FBXW7* mutations in type II endometrial cancer. These cancers are generally not dependent on high oestrogen environments for cancer development [66]. It has been highlighted in the literature that oestrogen exposure in the uterus leads to an increase in Wnt signalling, and in particular increased expression of both LEF1 and TCF7L2 [421]. However, if cells were able to acquire Wnt pathway activation independently of the need for oestrogen, such as through loss of proteasomal regulation of Wnt transcription factors, it may allow a carcinogenic transformation irrespective of oestrogen levels.

6.3 Does *FBXW7* provide a template for endometrial cancer formation?

As discussed in Section 3.4, *FBXW7* mutations have been frequently observed in both human cancers and in histologically normal endometrium [90, 91, 352–354]. Based on these reports, Gerstung *et al.*'s report of *FBXW7* mutations exhibiting clonality in human cancer, and the work from Chapter 1 showing a lack of neoplastic transformation with *Fbxw7* mutation alone, I hypothesised that *FBXW7* mutation may be an early event in endometrial carcinogenesis [356]. When considered with the findings of Chapters 4 and 5, that *Fbxw7* mutation contributes to a more aggressive cancer phenotype when combined with both $Pten^{\Delta/\Delta}$ and $Trp53^{R172H/\Delta}$, this suggests that areas of histologically normal endometrium that exhibit *FBXW7* mutations would be at higher risk of developing in to cancer, as a second hit in cells could initiate neoplastic transformation (Figure 6.1). Furthermore, if there are additional gene mutations, such as *PIK3CA*, that could also co-operate with *FBXW7* mutation, it would broaden the risk of cancer development from these endometrial glands.

While the work performed does suggest that accumulation of mutations in cells exhibiting *FBXW7* mutation could pose a risk of cancer development, due to the penetrant, cancer-initiating phenotype of the background models ($Pten^{\Delta/\Delta}$ or $Trp53^{R172H/\Delta}$), it was

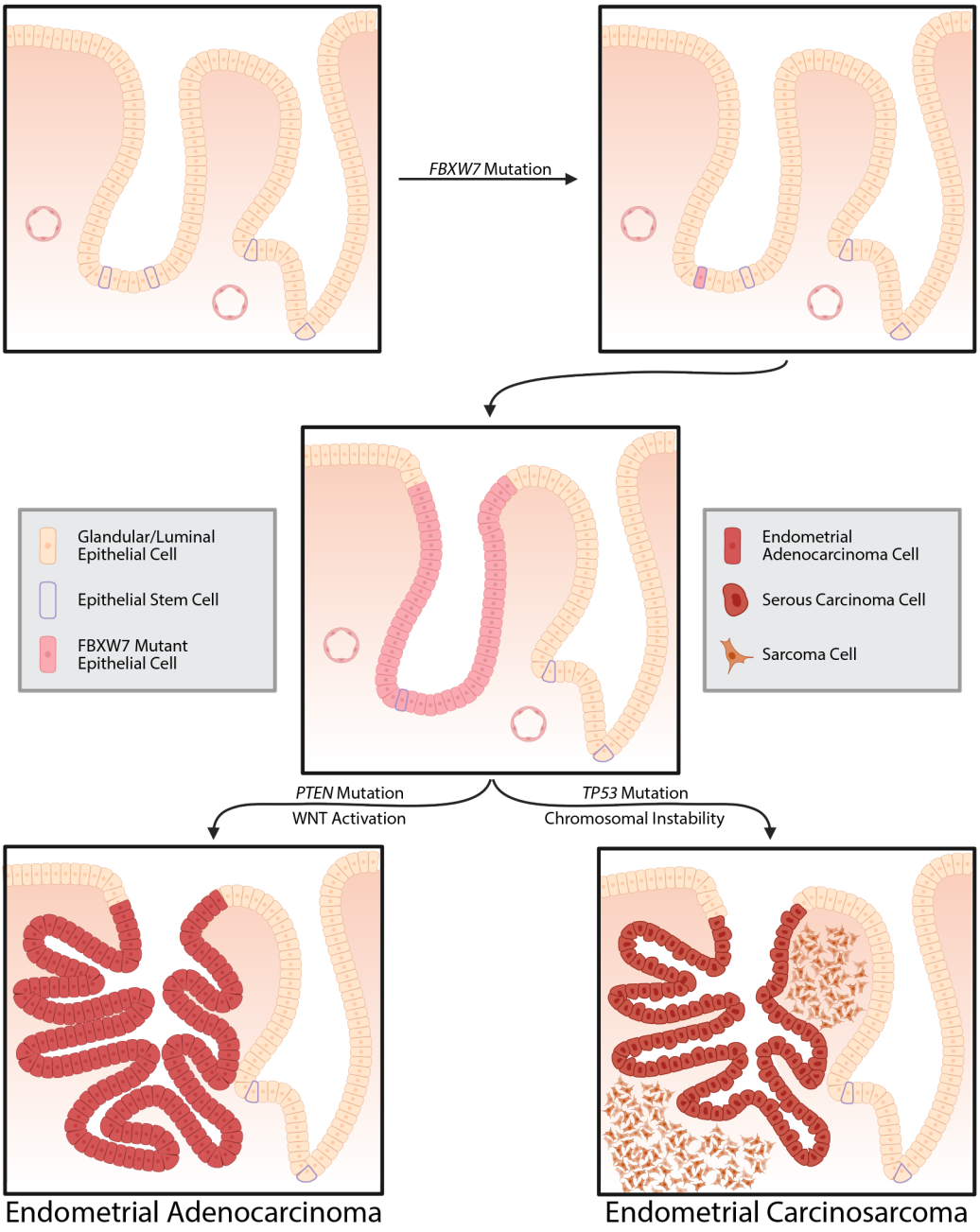

Figure 6.1: Schematic depicting the proposed role of *FBXW7* mutation in EC. Heterozygous *FBXW7* mutation occurring in an epithelial stem cell provides a growth advantage over neighbouring cells leading clonal expansion through the glandular structure. When a secondary hit in either *PTEN* or *TP53* occurs in these *FBXW7* mutant cells, the mutations co-operatively drive carcinogenesis and influence the histology of the resultant tumour. Figure panels were created using assets from BioRender.

not possible to establish whether heterozygous *Fbxw7* mutation is capable of driving transformation of a precursory lesion to a malignant neoplasm or whether it is solely capable of potentiating an already transformative phenotype. To address these issues, the role of *FBXW7* mutations as an early event in cancer formation warrants further investigation, particularly of the effects of *FBXW7* mutation on the characteristics of normal uterine cells. Assessment of whether there is any survival or growth advantage provided that could allow these cells to colonise a glandular structure or region of epithelium would be valuable to understanding the function of early *FBXW7* mutation. The use of *in vitro* models, described in Section 3.4 or lineage tracing models in the mouse uterus, would help to establish their ability to colonise the uterus. Furthermore, the use of a novel and more refined model of induction of the conditional alleles used in this work, would help to better define the ability to elevate a non-carcinogenic phenotype (discussed in more detail in Section 6.5).

6.4 Potential for different outcomes from specific *FBXW7* mutations

Throughout the extent of this thesis, I have investigated the effects of the R479Q (R482Q in mouse) mutation. This is one of the most frequently mutated *FBXW7* sites in all cancer types and along with R465C and R505C form the bulk of the research in to the effects of *FBXW7* missense mutation. It has been previously shown that there is a functional difference between *FBXW7* missense mutation and deletion [310, 346]. However, there has yet to be a thorough examination of the difference between individual point mutations. A preliminary study from Urick *et al.* introduced R465C, R479Q, and R505C mutations separately into two different serous endometrial cancer cell lines and determined the differentially expressed proteins and phosphorylated proteins by mass spectrometry [422]. While there was overlap in the differentially expressed proteins between 2- or 3-mutations, there were also many differentially expressed protein found in only one condition, suggesting there may be an element of mutation-specific loss of function [422].

Through examination of the available crystal structures of FBXW7 in complex with CPD-containing peptides, it is apparent that the predicted residues forming hydrogen bonds with the target CPD are variable (Figure 1.6D). Some residues are common amongst all targets evaluated (R465, R479), others present in several targets (S462, T463, R505, Y519), and some present in only one (S625, A626). Moreover, these structures represent only a small fraction of FBXW7 target proteins and likely underestimates the importance of many residues in facilitating the interaction between FBXW7 and its targets.

Comparisons of the mutation spectrums of *FBXW7* in different cancer types further questions whether specific mutations or groups of mutations may differentially affect substrate binding or FBXW7 function. Colorectal cancer and EC exhibit some of the highest rates of *FBXW7* mutation. Comparing the mutation spectrums in these cancers in data available from TCGA, highlights several cancer-type specific mutations present in both groups (Figure 6.2A). From the lollipop plot it can be seen that G423V and R479Q mutations are amongst the most frequent in EC, but do not occur or are infrequent in colorectal cancer. Similarly, S582L mutations are frequent in colorectal cancer, but do not occur in EC. Extending this to further studies, available through cBioPortal, that have examined *FBXW7* mutation status, a pocket of mutations can be seen in the 580-600 AA range that exhibit a collectively high frequency of mutation in colorectal cancer compared to endometrial cancer (32 vs 0 mutations) and segregate together in the 3D structure of FBXW7 (Figure 6.2B). Examination of whether these residues have a role in binding with a specific substrate (or substrates) that is important for colorectal carcinogenesis, but not for endometrial carcinogenesis, or whether there is a role for mutations, such as G423V, in EC, was outside the scope of this thesis, but warrants further investigation.

Interestingly, in EC there are even differences in the frequency of mutations across the different molecular subtypes (Figure 3.2C). Some mutations have differential distributions across the subtypes, such as G423, which is more commonly associated with the CN-high subtype, whereas R479 is more associated with UCS and CN-low subtypes. Whether these differences in occurrence are indicative of a functional difference in en-

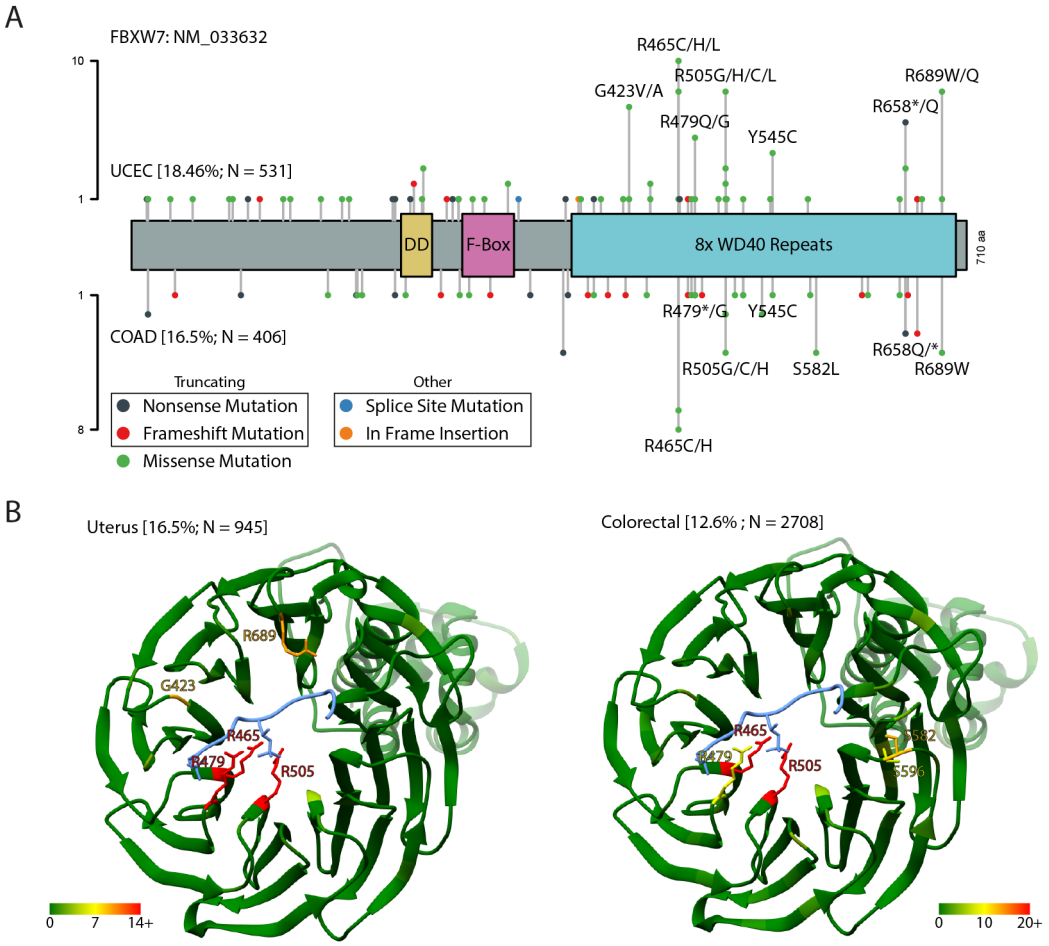

Figure 6.2: Comparison of the mutation spectrums of *FBXW7* in endometrial cancer and colorectal cancer. **A.** Lollipop plot of the frequency of mutations at each location of *FBXW7* in the TCGA UCEC and COAD cohorts. **B.** Crystal structure of *FBXW7* with a false colour gradient highlighting the frequency of mutations at particular locations for both uterine and colorectal cancers. The top 5 most frequently mutated amino acids in each cancer type are annotated with their amino acid side chains displayed. Data for this plot was obtained from all endometrial and colorectal cancer studies available in cBioPortal that performed sequencing of the entire *FBXW7* gene (Accessed April 2020).

dometrial cells or are purely stochastic has yet to be determined. However, if they do represent differences in substrate dysregulation caused by *FBXW7* it could have important implications for understanding of the drivers of different EC subtypes and for prognostication and treatment of patients.

6.5 Refining the uterine model

In recent years, more-targeted endometrial *Cre* models have been developed that allow recombination to be directed more specifically, one such model is *Ltf-Cre* [385]. *Ltf-Cre* is capable of driving recombination solely in the epithelium of the mouse uterus and not the stroma or myometrium, as is the case with *Pgr-Cre*. Utilisation of this Cre would allow examination of the effects of mutations more specifically in the cellular compartment that is associated with cancer development, the epithelium. Thus, allowing recapitulation of the cross-talk and interaction between the mutant epithelial cells and non-mutant stromal cells that occurs in human cancer. A further benefit of the *Ltf-Cre* system is that recombination occurs at sexual maturity (between 1-2 months of age), whereas *Pgr-Cre* drives recombination as early as 10 days [385]. This allows normal uterine development to occur without the impact of potentially disruptive, oncogenic mutations and would therefore more closely mimic the onset of sporadic mutation seen in humans.

A recent publication examining the effect of $Pten^{fl/fl}$ driven by *Ltf-Cre* has shown a less severe phenotype with mice developing complex atypical hyperplasia (CAH) at 6 months of age, but rarely developing EC [128]. This study highlights the importance of the cross-talk between stroma and epithelium, as it was determined that transformation of the mutant epithelial cells was restrained by TGF-β upregulation in the associated stroma [128]. Utilising a model such as this would help to answer the questions surrounding the potential role of *Fbxw7* as an early/initiating factor in carcinogenesis. Combination of heterozygous *Fbxw7* mutation with this model of a precursory endometrial lesion, would help to address whether *Fbxw7* mutation is capable of driving malignant transformation from a precursory lesion.

6.6 Final remarks

In this thesis, I have investigated the effect of *Fbxw7*^{R482Q} mutation on the development of EC alone and in combination with *Pten*$^{\Delta/\Delta}$, *Trp53*$^{\Delta/\Delta}$, and *Trp53*$^{R172H/\Delta}$. Expressed alone, *Fbxw7*^{R482Q} does not cause uterine pathology and only induced significant transcriptional changes at 4 weeks of age (upregulation of *Trp53*), but not at any other time point examined. In *Trp53*$^{\Delta/\Delta}$ mice, *Fbxw7*^{R482Q} mutation did not impact the frequency or latency of EC development, but did reduce frequency of extrauterine tumour development. However, when combined with *Pten*$^{\Delta/\Delta}$ and *Trp53*$^{R172H/\Delta}$, *Fbxw7*^{R482Q} accelerated the development of cancer and significantly reduced overall survival. Examination of the mechanisms behind acceleration, highlighted increased activity of Wnt transcription factor, Lef1, as a potential driver in *Pten*$^{\Delta/\Delta}$ *Fbxw7*$^{R482Q/+}$ mice. Further characterisation led to identification of LEF1 and TCF7L2 as novel FBXW7 substrates. In *Trp53*$^{R172H/\Delta}$ *Fbxw7*$^{R482Q/+}$ mice, overexpression of Ccne1 and significant downregulation of cell cycle regulator, *Cdkn1a*, implicated increased proliferative potential as a driver of decreased survival in *Trp53*$^{R172H/\Delta}$ *Fbxw7*$^{R482Q/+}$ mice. These findings highlight potentially varied contributions of *Fbxw7* mutation in EC, depending on the mutational context of tumour. Suggesting that treatment or prognostication of *FBXW7*-mutant cancer may not be one-size-fits-all.

Appendix A

Materials and methods

Table A.1: List of TaqMan probes used.

Target	Product Number
Fbxw7	Mm00504452_m1
Pten	Mm00477208_m1
Trp53	Mm01731290_g1
Mmp13	Mm00439491_m1
Wisp1	Mm01200484_m1
Ctgf	Mm01192933_g1
Cyr61	Mm00487498_m1
Cd3e	Mm01179194_m1
Gapdh	Mm99999915_g1
Vps4a	Mm00459928_m1

*All probes were purchased from ThermoFisher Scientific.

Table A.2: List of plasmids generated and used for transient transfections. Plasmid type key: GEC - Gateway Entry Clone, LEC - Lentiviral Expression Clone, GDV - Gateway Destination Vector, EV - Expression Vector

Plasmid Name	Plasmid Type	Uniprot ID	Mutations	Acquired From
LEF1-CDS	GEC	Q9UJU2	WT	Human ORFeome (#EU446873)
WWTR1-CDS	GEC	Q9GZV5	WT	Human ORFeome (#DQ893378)
FBXW7-WT	GEC	Q969H0	WT	Addgene (#81795)
R777-E359-Hs.YAP1	GEC	P46937	WT	Addgene (#70643)
TCF7L2 pLX307	LEC	A0A0D9SGH8	WT	Addgene (#98373)
pDONR221-TCF7L2	GEC	A0A0D9SGH8	WT	BP cloning
pMH-FLAG-HA	GDV	-	-	Addgene (#101766)
FBXW7-WT-FLAG-HA	EV	Q969H0	WT	LR cloning
FBXW7-R465C-FLAG-HA	EV	Q969H0	R465C	LR cloning
FBXW7-R479Q-FLAG-HA	EV	Q969H0	R479Q	LR cloning
FBXW7-R505C-FLAG-HA	EV	Q969H0	R505C	LR cloning
pMH-Myc	GDV	-	-	Addgene (#101765)
LEF1-Myc	EV	Q9UJU2	WT	LR cloning
CCNE1-Myc	EV	P24864	WT	LR cloning
WWTR1-Myc	EV	Q9GZV5	WT	LR cloning
YAP1-Myc	EV	P46937	WT	LR cloning
TCF7L2-Myc	EV	A0A0D9SGH8	WT	LR cloning
LEF1-T155A	GEC	Q9UJU2	T155A	SDM
LEF1-T155A-Myc	EV	Q9UJU2	T155A	LR cloning
LEF1-ΔN	GEC	Q9UJU2	Δ(1-62)	SDM
LEF1-ΔN-Myc	EV	Q9UJU2	Δ(1-62)	LR cloning
LEF1-CPD	GEC	Q9UJU2	T155A; T159A	SDM
LEF1-CPD-Myc	GEC	Q9UJU2	T155A; T159A	LR cloning
pcDNA3.1-3xFLAG-V5-ccdB	GDV	-	-	Addgene (#87064)
FBXW7-FLAG-V5	EV	Q969H0	WT	LR cloning
FBXW7-WD40	GEC	Q969H0	R465C; R479Q; R505C	SDM
FBXW7-WD40-FLAG-V5	EV	Q969H0	R465C; R479Q; R505C	LR cloning
FBXW7-ΔFbox-WT	GEC	Q969H0	Δ(282-325)	SDM

FBXW7-ΔFbox-WD40	GEC	Q969H0	Δ(282-325); R465C; R479Q; R505C	SDM
FBXW7-ΔFbox-WT-FLAG-V5	EV	Q969H0	Δ(282-325)	LR cloning
FBXW7-ΔFbox-WD40-FLAG-V5	EV	Q969H0	Δ(282-325); R465C; R479Q; R505C	LR cloning
FBXW7-Myc	EV	Q969H0	WT	LR cloning
LEF1-FLAG-V5	EV	Q9UJU2	WT	LR cloning
TCF7L2-FLAG-V5	EV	A0A0D9SGH8	WT	LR cloning
WWTR1-FLAG-V5	EV	Q9GZV5	WT	LR cloning
YAP1-FLAG-V5	EV	P46937	WT	LR cloning
CCNE1-FLAG-V5	EV	P24864	WT	LR cloning
LEF1-ΔN-FLAG-V5	EV	Q9UJU2	Δ(1-62)	LR cloning
FBXW7-WD40-Myc	GEC	Q969H0	R465C; R479Q; R505C	LR cloning
LEF1-CPD-FLAG-V5	EV	Q9UJU2	T155A; T159A	LR cloning

Table A.3: List of primary antibodies used, with the context and concentration in which they were used.

Target	Product Number	Manufacturer	Protocols and Concentration
Pten	ab53280	Abcam	IHC (1:250)
Phospho-Akt (Ser473)	4060	Cell Signaling Technology	IHC (1:50)
p53	CM5	Leica	IHC (1:250)
Krt8	ab53280	Abcam	IHC (1:250)
CCNE1	11554-1-AP	Proteintech	IHC (1:500), WB (1:1000)
Foxa2	ab108422	Abcam	IHC (1:750)
Lef1	ab137872	Abcam	IHC (1:100)
TCF7L2	2569	Cell Signaling Technology	IHC (1:100), WB (1:500)
YAP/TAZ	8418	Cell Signaling Technology	IHC (1:250), WB (1:500)
CTNNB1	610154	BD Biosciences	IHC (1:50), WB (1:500)
LEF1	2230	Cell Signaling Technology	WB (1:250)
JUN	9165	Cell Signaling Technology	WB (1:500)
MYC	9402	Cell Signaling Technology	WB (1:500)
Cleaved NOTCH1 (Val1744)	4147	Cell Signaling Technology	WB (1:500)
GAPDH	5174	Cell Signaling Technology	WB (1:2000)
HA-tag	ab9110	Abcam	WB (1:1000)
MYC-tag	2276	Cell Signaling Technology	WB (1:1000)
V5-tag	13202	Cell Signaling Technology	WB (1:1500)
SKP1	12248	Cell Signaling Technology	WB (1:500)
CUL1	4995	Cell Signaling Technology	WB (1:500)
Krt8/18	20R-CP004	Fitzgerald	IHC-F (1:200)
Krt5	905904	BioLegend	IHC-F (1:500)

*WB: Western blotting, IHC: Chromogenic immunohistochemistry, IHC-F: Fluorescent immunohistochemistry.

Table A.4: List of secondary antibodies or agents for antibody detection used.

Target	Product Number	Manufacturer	Protocols and Concentration
Goat Anti-Guinea Pig Alexa Fluor 568	A-11075	Invitrogen	IHC-F (1:1000)
Goat Anti-Chicken Alexa Fluor 647	A-21449	Invitrogen	IHC-F (1:1000)
IRDye 800CW Goat Anti-Rabbit IgG	926-32211	LI-COR	WB (1:20000)
IRDye 800CW Goat Anti-Mouse IgG	926-32210	LI-COR	WB (1:20000)
IRDye 680RD Goat Anti-Rabbit IgG	926-68070	LI-COR	WB (1:20000)
SignalStain Boost IHC Detection Reagent (HRP, Rabbit)	8114	Cell Signaling Technology	IHC
SignalStain Boost IHC Detection Reagent (HRP, Mouse)	31926	Cell Signaling Technology	IHC

*WB: Western blotting, IHC: Chromogenic immunohistochemistry, IHC-F: Fluorescent immunohistochemistry.

Appendix B

Functional characterisation of *Fbxw7*$^{R482Q/+}$ mutation in mouse uterus

Table B.1: Top 100 most significantly differentially expressed genes from analysis comparing *Fbxw7*$^{R482Q/+}$ against *Fbxw7*$^{+/+}$

Ensembl ID	Gene	LogFC	*P* value	Adjusted *P* value
ENSMUSG00000020297	Nsg2	-1.13	4.42e-05	0.732
ENSMUSG00000010057	Nprl2	-0.499	0.000685	1
ENSMUSG00000053219	Raet1e	1.04	0.000688	1
ENSMUSG00000034083	Ccdc174	-0.519	0.000905	1
ENSMUSG00000049811	Fam161a	-0.956	0.00153	1
ENSMUSG00000021685	Otp	0.683	0.00247	1
ENSMUSG00000028581	Laptm5	0.921	0.00257	1
ENSMUSG00000051056	Gja10	0.852	0.00273	1
ENSMUSG00000026398	Nr5a2	-0.893	0.00295	1
ENSMUSG00000031098	Syt8	1.29	0.00295	1
ENSMUSG00000054932	Afp	0.606	0.00303	1
ENSMUSG00000024653	Scgb1a1	0.627	0.00306	1
ENSMUSG00000053310	Nrgn	-0.607	0.00308	1
ENSMUSG00000047342	Zfp286	-0.737	0.0036	1
ENSMUSG00000086712	Mexis	0.913	0.00457	1
ENSMUSG00000025170	Rab40b	-0.553	0.00462	1

ENSMUSG00000042873	Lhfpl4	-0.751	0.00513	1
ENSMUSG00000060180	Myh13	-0.643	0.00554	1
ENSMUSG00000001366	Fbxo9	-0.455	0.00565	1
ENSMUSG00000020335	Zfp354b	-0.613	0.00592	1
ENSMUSG00000062496	4930431F12Rik	0.633	0.00664	1
ENSMUSG00000069584	Gm10272	0.516	0.0069	1
ENSMUSG00000024784	Gpha2	-0.581	0.00711	1
ENSMUSG00000043168	4930426D05Rik	-1.12	0.00712	1
ENSMUSG00000034071	Zfp551	-0.624	0.00721	1
ENSMUSG00000028332	Hemgn	-0.595	0.00726	1
ENSMUSG00000046561	Arsj	-1.02	0.00795	1
ENSMUSG00000030674	Qprt	0.629	0.00808	1
ENSMUSG00000005917	Otx1	0.543	0.00837	1
ENSMUSG00000037349	Nudt22	-0.707	0.00855	1
ENSMUSG00000038980	Rbbp8nl	-0.463	0.00872	1
ENSMUSG00000024064	Galnt14	-0.549	0.0088	1
ENSMUSG00000027643	Ghrh	0.658	0.0092	1
ENSMUSG00000071356	Reg3b	0.51	0.00939	1
ENSMUSG00000025243	Slc6a20b	0.394	0.00945	1
ENSMUSG00000048996	Olfr1366	-0.583	0.0103	1
ENSMUSG00000007610	Gtpbp3	-0.342	0.0105	1
ENSMUSG00000021263	Degs2	-1.09	0.0114	1
ENSMUSG00000021850	ccdc198	-1	0.0115	1
ENSMUSG00000000544	Gpa33	1.33	0.0116	1
ENSMUSG00000031384	Asb9	-0.525	0.0117	1
ENSMUSG00000027555	Car13	0.852	0.0117	1
ENSMUSG00000057149	Olfr1301	0.579	0.0119	1
ENSMUSG00000075040	Zfp408	-0.435	0.0119	1
ENSMUSG00000031840	Rab3a	-0.376	0.0121	1
ENSMUSG00000040724	Kcna2	-0.552	0.0129	1
ENSMUSG00000029605	Oas1b	0.513	0.0135	1
ENSMUSG00000053175	Bcl3	0.819	0.0135	1
ENSMUSG00000034488	Edil3	-1.02	0.0136	1
ENSMUSG00000024503	Spink1	-0.464	0.014	1
ENSMUSG00000020038	Cry1	-0.475	0.0142	1
ENSMUSG00000074595	Wfdc6a	-0.709	0.0142	1
ENSMUSG00000074847	Gm10775	-0.488	0.0144	1

ENSMUSG00000042694	Stn1	0.43	0.0145	1
ENSMUSG00000027944	Hax1	-0.378	0.0147	1
ENSMUSG00000032179	Bmp5	-0.95	0.0149	1
ENSMUSG00000054863	Tafa5	-0.908	0.015	1
ENSMUSG00000030004	Nat8	-0.571	0.0154	1
ENSMUSG00000022186	Oxct1	-0.486	0.0156	1
ENSMUSG00000026458	Ppfia4	-0.678	0.0156	1
ENSMUSG00000048108	Tmem72	-0.471	0.0156	1
ENSMUSG00000042632	Pla2g6	-0.583	0.0158	1
ENSMUSG00000031274	Col4a5	-0.644	0.0159	1
ENSMUSG00000018238	Gdf9	0.405	0.0159	1
ENSMUSG00000028441	1110017D15Rik	-0.754	0.0161	1
ENSMUSG00000068747	Sort1	-0.381	0.0163	1
ENSMUSG00000019464	Ptger1	-0.431	0.0165	1
ENSMUSG00000035208	Slfn8	0.724	0.0167	1
ENSMUSG00000046806	Cyren	-0.483	0.0167	1
ENSMUSG00000021342	Prl	-0.543	0.0167	1
ENSMUSG00000026166	Ccl20	1.35	0.0169	1
ENSMUSG00000056215	Lrguk	0.766	0.0174	1
ENSMUSG00000035201	Pramel17	0.508	0.0175	1
ENSMUSG00000004038	Gstm3	-0.496	0.018	1
ENSMUSG00000046008	Pnlip	0.558	0.0187	1
ENSMUSG00000026885	Ttll11	-0.669	0.0191	1
ENSMUSG00000007721	Ccdc124	-0.345	0.0196	1
ENSMUSG00000020993	Trappc6b	-0.343	0.0196	1
ENSMUSG00000029524	Sirt4	-0.416	0.0197	1
ENSMUSG00000054716	Zfp771	-0.44	0.0199	1
ENSMUSG00000026405	C4bp	-1.17	0.0202	1
ENSMUSG00000001750	Tcirg1	0.437	0.0203	1
ENSMUSG00000048534	Jaml	0.742	0.0205	1
ENSMUSG00000062542	Syt9	-0.741	0.0206	1
ENSMUSG00000046049	Rp1l1	-0.491	0.0209	1
ENSMUSG00000001467	Cyp51	0.897	0.0213	1
ENSMUSG00000041272	Tox	-0.778	0.022	1
ENSMUSG00000056061	Gata5os	-0.472	0.0221	1
ENSMUSG00000035112	Wnk4	-0.64	0.0221	1
ENSMUSG00000032131	Abcg4	0.418	0.0222	1

ENSMUSG00000045004	Spata21	0.647	0.0226	1
ENSMUSG00000009394	Syn2	-1.19	0.0233	1
ENSMUSG00000012777	Acp4	-0.464	0.0234	1
ENSMUSG00000001520	Nrip2	-0.695	0.0237	1
ENSMUSG00000021217	Tshz3	-0.861	0.0237	1
ENSMUSG00000038180	Spag4	-0.569	0.0237	1
ENSMUSG00000079364	Gm3558	-0.562	0.0239	1
ENSMUSG00000042042	Csgalnact2	-0.48	0.024	1
ENSMUSG00000028188	Spata1	-0.553	0.0243	1
ENSMUSG00000078912	Gm11011	-0.501	0.0243	1
ENSMUSG00000006389	Mpl	0.583	0.0244	1

Appendix C

Functional characterisation of *Fbxw7*$^{R482Q/+}$ in combination with *Pten* loss in the mouse uterus

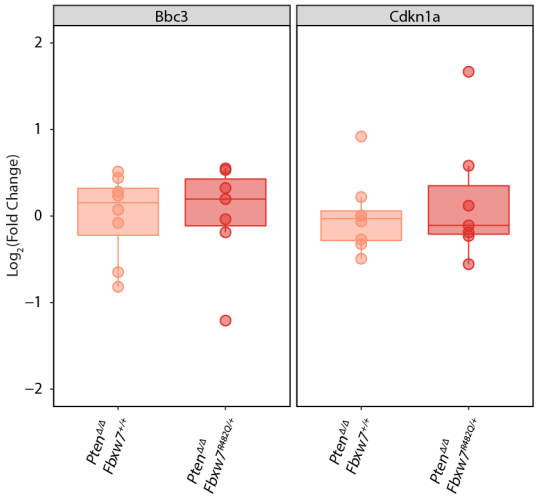

Figure C.1: Gene expression changes in p53 target genes at survival end point.

Table C.1: Top 100 most significantly differentially expressed genes from analysis comparing *Pten*$^{\Delta/\Delta}$ *Fbxw7*$^{R482Q/+}$ against *Pten*$^{\Delta/\Delta}$ *Fbxw7*$^{+/+}$

Ensembl ID	Gene	LogFC	*P* value	Adjusted *P* value
ENSMUSG00000050578	Mmp13	2.81	3.82e-10	6.33e-06
ENSMUSG00000042485	Mustn1	2.76	1.25e-08	5.32e-05
ENSMUSG00000022510	Trp63	-4.89	1.25e-08	5.32e-05
ENSMUSG00000054146	Krt15	-4.83	1.29e-08	5.32e-05
ENSMUSG00000051048	P4ha3	2.91	3.37e-08	0.000112
ENSMUSG00000026208	Des	2.31	4.36e-08	0.00012
ENSMUSG00000044626	Liph	-3.31	5.2e-08	0.000123
ENSMUSG00000026204	Ptprn	2.33	7.92e-08	0.000164
ENSMUSG00000049709	Nlrp10	-2.94	1.09e-07	0.000198
ENSMUSG00000026610	Esrrg	-2.07	1.2e-07	0.000198
ENSMUSG00000006221	Hspb7	2.6	1.64e-07	0.000229
ENSMUSG00000000555	Itga5	1.82	1.75e-07	0.000229
ENSMUSG00000041324	Inhba	2.76	1.83e-07	0.000229
ENSMUSG00000021506	Pitx1	-3.32	1.94e-07	0.000229
ENSMUSG00000025064	Col17a1	-4.2	2.37e-07	0.000261
ENSMUSG00000063142	Kcnma1	2.89	4.13e-07	0.000428
ENSMUSG00000023961	Enpp4	-1	5.55e-07	0.000541
ENSMUSG00000001131	Timp1	2.29	6.22e-07	0.000572
ENSMUSG00000024529	Lox	2.3	6.71e-07	0.000585
ENSMUSG00000001349	Cnn1	1.89	7.49e-07	0.000585
ENSMUSG00000055333	Fat2	-2.36	7.63e-07	0.000585
ENSMUSG00000031519	Asb5	2.45	8.1e-07	0.000585
ENSMUSG00000038530	Rgs4	2.89	8.11e-07	0.000585
ENSMUSG00000027500	Stmn2	1.95	9.26e-07	0.000625
ENSMUSG00000074156	Ces1h	-2.78	9.8e-07	0.000625
ENSMUSG00000031654	Cbln1	-3.2	1e-06	0.000625
ENSMUSG00000022816	Fstl1	1.55	1.03e-06	0.000625
ENSMUSG00000033857	Engase	-1.41	1.06e-06	0.000625
ENSMUSG00000033196	Myh2	1.72	1.26e-06	0.000719
ENSMUSG00000045573	Penk	4.42	1.3e-06	0.00072
ENSMUSG00000059430	Actg2	2.13	1.51e-06	0.000807
ENSMUSG00000051497	Kcnj16	-3.61	1.58e-06	0.000817
ENSMUSG00000035783	Acta2	1.23	1.66e-06	0.000833
ENSMUSG00000023885	Thbs2	3.01	1.72e-06	0.000838

ENSMUSG00000056427	Slit3	2.64	1.78e-06	0.000844
ENSMUSG00000032332	Col12a1	2.92	1.85e-06	0.000849
ENSMUSG00000029436	Mmp17	1.3	1.97e-06	0.000881
ENSMUSG00000057286	St6galnac2	-1.14	2.03e-06	0.000883
ENSMUSG00000031910	Has3	-2.14	2.09e-06	0.000883
ENSMUSG00000024713	Pcsk5	1.62	2.13e-06	0.000883
ENSMUSG00000030559	Rab38	-1.99	2.22e-06	0.000898
ENSMUSG00000038463	Olfml2b	2.67	2.57e-06	0.000945
ENSMUSG00000062098	Btbd3	0.897	2.57e-06	0.000945
ENSMUSG00000016386	Mpped2	-1.65	2.63e-06	0.000945
ENSMUSG00000078597	Cyp4a12b	-3.35	2.67e-06	0.000945
ENSMUSG00000032358	Fam83b	-2.19	2.67e-06	0.000945
ENSMUSG00000044986	Tst	-1.55	2.75e-06	0.000945
ENSMUSG00000087006	Gm13889	1.32	2.76e-06	0.000945
ENSMUSG00000037440	Vnn1	-2.79	2.8e-06	0.000945
ENSMUSG00000019997	Ccn2	2.79	3.11e-06	0.00103
ENSMUSG00000032085	Tagln	1.73	3.52e-06	0.00114
ENSMUSG00000054459	Vsnl1	-4.31	3.59e-06	0.00114
ENSMUSG00000050199	Lgr4	-1.2	3.81e-06	0.00118
ENSMUSG00000017817	Jph2	1.99	3.88e-06	0.00118
ENSMUSG00000027460	Angpt4	2.46	3.9e-06	0.00118
ENSMUSG00000062826	Ces2f	-2.2	4.14e-06	0.00123
ENSMUSG00000026228	Htr2b	1.99	4.39e-06	0.00127
ENSMUSG00000032060	Cryab	1.74	4.48e-06	0.00127
ENSMUSG00000031375	Bgn	2.16	4.52e-06	0.00127
ENSMUSG00000066705	Fxyd6	1.91	4.73e-06	0.00127
ENSMUSG00000039431	Mtmr7	0.897	4.86e-06	0.00127
ENSMUSG00000021388	Aspn	2.27	4.87e-06	0.00127
ENSMUSG00000029659	Medag	2.01	4.89e-06	0.00127
ENSMUSG00000028789	Azin2	1.26	4.91e-06	0.00127
ENSMUSG00000038729	Pakap	2.12	5.09e-06	0.00127
ENSMUSG00000031963	Bmper	2.51	5.18e-06	0.00127
ENSMUSG00000043366	Olfr78	1.88	5.19e-06	0.00127
ENSMUSG00000025610	Map3k7cl	3.12	5.28e-06	0.00127
ENSMUSG00000034997	Htr2a	2.21	5.31e-06	0.00127
ENSMUSG00000022122	Ednrb	2.22	5.36e-06	0.00127
ENSMUSG00000039092	Sptlc3	-1.95	5.48e-06	0.00128

ENSMUSG00000031380	Vegfd	2.46	5.55e-06	0.00128
ENSMUSG00000009588	St6galnac1	-2.86	5.87e-06	0.00131
ENSMUSG00000059898	Dsc3	-1.98	5.96e-06	0.00131
ENSMUSG00000017969	Ptgis	1.79	6e-06	0.00131
ENSMUSG00000029664	Tfpi2	2.57	6.14e-06	0.00131
ENSMUSG00000026638	Irf6	-1.43	6.18e-06	0.00131
ENSMUSG00000027335	Adra1d	1.38	6.19e-06	0.00131
ENSMUSG00000051431	Gpr87	-2.43	6.56e-06	0.00138
ENSMUSG00000022595	Lypd2	-3.05	6.79e-06	0.00141
ENSMUSG00000031841	Cdh13	1.48	6.97e-06	0.00143
ENSMUSG00000021913	Ogdhl	1.71	7.07e-06	0.00143
ENSMUSG00000027004	Frzb	2.43	7.21e-06	0.00144
ENSMUSG00000007783	Cpt1c	1.15	7.37e-06	0.00145
ENSMUSG00000026989	Dapl1	-2.01	7.51e-06	0.00146
ENSMUSG00000018339	Gpx3	1.91	7.73e-06	0.00148
ENSMUSG00000039323	Igfbp2	3.18	7.77e-06	0.00148
ENSMUSG00000025809	Itgb1	0.623	8.61e-06	0.00161
ENSMUSG00000021359	Tfap2a	-2.91	8.71e-06	0.00161
ENSMUSG00000064080	Fbln2	2.14	8.73e-06	0.00161
ENSMUSG00000044017	Adgrd1	2.38	8.92e-06	0.00162
ENSMUSG00000032788	Pdxk	-0.977	9.03e-06	0.00163
ENSMUSG00000039114	Nrn1	1.86	9.17e-06	0.00163
ENSMUSG00000025504	Eps8l2	-1.3	9.27e-06	0.00163
ENSMUSG00000021702	Thbs4	2.82	9.43e-06	0.00165
ENSMUSG00000023092	Fhl1	2.14	1.02e-05	0.00174
ENSMUSG00000057123	Gja5	1.66	1.03e-05	0.00174
ENSMUSG00000048251	Bcl11b	-1.13	1.03e-05	0.00174
ENSMUSG00000024975	Pdcd4	-1.06	1.05e-05	0.00176
ENSMUSG00000032387	Rbpms2	1.41	1.09e-05	0.00179
ENSMUSG00000035357	Pdzrn3	1.29	1.09e-05	0.00179

Table C.2: Results of literature search for publications identifying FBXW7 CPD sequences by SDM, used to generate the consensus sequence to allow agnostic search for potential FBXW7 CPDs. The AA indicated in red represents the ″0″ position and in orange represents the ″+4″ position.

Target Identified	CPD Sequence	Reference
PTPN11	ADQTSGDQSPLPP	[423]
PA2G4	VEASSSGVSVLSL	[424]
HSF1	EEPPSPPQSPRVE	[280]
MCL1	STDGSLPSTPPPA	[264]
MYC	ELLPTPPLSPSRR	[269, 270]
PLK1	TLCGTPNYIAPEV	[425]
NR1D1	PQQLTPPRSPSPE	[426]
FOXM1	EEWPSPAPSFKEE	[427]
XRCC4	TLRNSSPEDLFDE	[287]
SREBF1	EDTLTPPPSDAGS	[428]
SREBF2	VLLMSPPASDSGS	
KLF5 (CPD 1)	QLLNTPDLDMPSS	
KLF5 (CPD 2)	YFPPSPPSSEPGS	[429]
KLF5 (CPD 3)	LQNLTPPPSYAAT	
NFE2L1	FLLFSPEVESLPV	[430]
CCNE1	SGLLTPPQSGKKQ	[226]
MTOR	SRLLTPSIHLISG	[259]
SOX10	HGPPTPPTTPKTE	[431]
NFKB2	CPLPSPPTSDSDS	[432]
TP63	NKLPSVSQLINPQ	[433]
NDE1	EKPRTPMPSSVEA	[434]
BLM	KSFVTPPQSHFVR	[435]
RICTOR	AVLATPPKQPIVD	[436]
CRY2	AVLATPPKQPIVD	[437]

Bibliography

1. Kerr, D. J., Pezzella, F. & Tavassoli, M. *Oxford Textbook of Cancer Biology* (Oxford University Press, 2019).
2. Hanahan, D. & Weinberg, R. A. The hallmarks of cancer. *Cell* **100,** 57–70 (Jan. 2000).
3. Hanahan, D. & Weinberg, R. A. Hallmarks of cancer: The next generation. *Cell* **144,** 646–674 (Mar. 2011).
4. Hanahan, D. Hallmarks of cancer: New dimensions. *Cancer Discovery* **12,** 31–46 (Jan. 2022).
5. Sung, H. *et al.* Global cancer statistics 2020: Globocan estimates of incidence and mortality worldwide for 36 cancers in 185 countries. *CA: A Cancer Journal for Clinicians* **71,** 209–249 (Feb. 2021).
6. Ferlay, J. *et al.* Cancer incidence and mortality worldwide: Sources, methods and major patterns in Globocan 2012. *International Journal of Cancer* **136,** 359–386 (Sept. 2014).
7. Lin, L. *et al.* Global, regional, and national cancer incidence and death for 29 cancer groups in 2019 and Trends Analysis of the global cancer burden, 1990–2019. *Journal of Hematology & Oncology* **14** (Nov. 2021).
8. Van Leeuwen, M. *et al.* Understanding the quality of life (QOL) issues in survivors of cancer: Towards the development of an eortc qol cancer survivorship questionnaire. *Health and Quality of Life Outcomes* **16** (June 2018).
9. Kjaer, T. K. *et al.* Long-term somatic disease risk in adult Danish cancer survivors. *JAMA Oncology* **5,** 537–545 (Apr. 2019).
10. *Uterus* 2021. `https://emedicodiary.com/que/425/uterus`.
11. Konrad, L. *et al.* Composition of the stroma in the human endometrium and endometriosis. *Reproductive Sciences* **25,** 1106–1115 (July 2018).
12. Chavez-MacGregor, M. *et al.* Lifetime cumulative number of menstrual cycles and serum sex hormone levels in postmenopausal women. *Breast Cancer Research and Treatment* **108,** 101–112 (May 2007).
13. Owen, J. A. Physiology of the menstrual cycle. *The American Journal of Clinical Nutrition* **28,** 333–338 (Apr. 1975).
14. Reed, B. G. & Carr, B. R. *The Normal Menstrual Cycle and the Control of Ovulation* (MDText.com, Inc., South Dartmouth (MA), 2000).
15. Hawkins, S. M. & Matzuk, M. M. The Menstrual Cycle: Basic Biology. *Annals of the New York Academy of Sciences* **1135,** 10–18 (2008).

16. Makker, V. *et al.* Endometrial cancer. *Nature Reviews Disease Primers* **7** (Dec. 2021).
17. Salamonsen, L. A., Hutchison, J. C. & Gargett, C. E. Cyclical endometrial repair and Regeneration. *Development* **148** (Sept. 2021).
18. Masuda, K. *et al.* Carcinoma of the lower uterine segment (lus): Clinicopathological Characteristics and association with Lynch syndrome. *Current Genomics* **12,** 25–29 (Mar. 2011).
19. Roy, M., Musa, F., Taylor, S. E. & Huang, M. Uterine sarcomas: How to navigate an ever-growing list of subtypes. *American Society of Clinical Oncology Educational Book,* 910–919 (Apr. 2022).
20. Mahdy, H., Casey, M. J. & Crotzer, D. *Endometrial cancer* Feb. 2022. `https://www.ncbi.nlm.nih.gov/books/NBK525981/`.
21. *Uterine Cancer Incidence Statistics* Sept. 2021. `https://www.cancerresearchuk.org/health-professional/cancer-statistics/statistics-by-cancer-type/uterine-cancer/incidence`.
22. *Uterine Cancer Mortality Statistics* June 2022. `https://www.cancerresearchuk.org/health-professional/cancer-statistics/statistics-by-cancer-type/uterine-cancer/mortality`.
23. Henley, S. J. *et al.* Annual report to the nation on the status of cancer, part I: National cancer statistics. *Cancer* **126,** 2225–2249 (May 2020).
24. Smittenaar, C. R., Petersen, K. A., Stewart, K. & Moitt, N. Cancer incidence and mortality projections in the UK until 2035. *British Journal of Cancer* **115,** 1147–1155 (Oct. 2016).
25. Xu, W.-H. *et al.* Menstrual and reproductive factors and endometrial cancer risk: Results from a population-based case-control study in urban Shanghai. *International Journal of Cancer* **108,** 613–619 (Nov. 2003).
26. Wang, Z. *et al.* Joint effect of genotypic and phenotypic features of reproductive factors on endometrial cancer risk. *Scientific Reports* **5** (Oct. 2015).
27. Gong, T.-T., Wang, Y.-L. & Ma, X.-X. Age at menarche and endometrial cancer risk: A dose-response meta-analysis of prospective studies. *Scientific Reports* **5** (Sept. 2015).
28. Gavrilyuk, O., Braaten, T., Weiderpass, E., Licaj, I. & Lund, E. Lifetime number of years of menstruation as a risk index for postmenopausal endometrial cancer in the Norwegian women and cancer study. *Acta Obstetricia et Gynecologica Scandinavica* **97,** 1168–1177 (July 2018).
29. Yang, H. P. *et al.* Lifetime number of ovulatory cycles and risks of ovarian and endometrial cancer among postmenopausal women. *American Journal of Epidemiology* **183,** 800–814 (Apr. 2016).
30. Wu, Y., Sun, W., Liu, H. & Zhang, D. Age at Menopause and risk of developing endometrial cancer: A meta-analysis. *BioMed Research International* **2019,** 1–13 (May 2019).
31. Crosbie, E. J. *et al.* Endometrial cancer. *The Lancet* **399,** 1412–1428 (Apr. 2022).
32. Wu, Q.-J. *et al.* Parity and Endometrial Cancer Risk: A meta-analysis of epidemiological studies. *Scientific Reports* **5** (2015).

33. Ku, C. W. *et al.* Serum progesterone distribution in normal pregnancies compared to pregnancies complicated by threatened miscarriage from 5 to 13 weeks gestation: A prospective cohort study. *BMC Pregnancy and Childbirth* **18** (Sept. 2018).

34. Van Meurs, H. S. *et al.* The incidence of endometrial hyperplasia and cancer in 1031 patients with a granulosa cell tumor of the ovary. *International Journal of Gynecological Cancer* **23,** 1417–1422 (2013).

35. Barry, J. A., Azizia, M. M. & Hardiman, P. J. Risk of endometrial, ovarian and breast cancer in women with polycystic ovary syndrome: A systematic review and meta-analysis. *Human Reproduction Update* **20,** 748–758 (2014).

36. Collaborators, M. W. S. Endometrial cancer and hormone-replacement therapy in the Million Women Study. *The Lancet* **365,** 1543–1551 (Apr. 2005).

37. Feeley, K. M. & Wells, M. Hormone replacement therapy and the endometrium. *Journal of Clinical Pathology* **54,** 435–440 (June 2001).

38. Fleming, C. A. *et al.* Meta-analysis of the cumulative risk of endometrial malignancy and systematic review of endometrial surveillance in extended tamoxifen therapy. *British Journal of Surgery* **105,** 1098–1106 (July 2018).

39. Collaborative Group on Epidemiological Studies on Endometrial Cancer. Endometrial cancer and oral contraceptives: An individual participant meta-analysis of 27276 women with endometrial cancer from 36 epidemiological studies. *The Lancet Oncology* **16,** 1061–1070 (Sept. 2015).

40. Calle, E. E., Rodriguez, C., Walker-Thurmond, K. & Thun, M. J. Overweight, obesity, and mortality from cancer in a prospectively studied cohort of U.S. adults. *New England Journal of Medicine* **348,** 1625–1638 (Apr. 2003).

41. Renehan, A. G., Tyson, M., Egger, M., Heller, R. F. & Zwahlen, M. Body-mass index and incidence of cancer: A systematic review and meta-analysis of prospective observational studies. *The Lancet* **371,** 569–578 (Feb. 2008).

42. Lauby-Secretan, B. *et al.* Body fatness and cancer — viewpoint of the IARC Working Group. *New England Journal of Medicine* **375,** 794–798 (Aug. 2016).

43. Calle, E. E. & Kaaks, R. Overweight, obesity and cancer: Epidemiological evidence and proposed mechanisms. *Nature Reviews Cancer* **4,** 579–591 (Aug. 2004).

44. Renehan, A. G., Zwahlen, M. & Egger, M. Adiposity and cancer risk: New mechanistic insights from epidemiology. *Nature Reviews Cancer* **15,** 484–498 (July 2015).

45. Friberg, E., Orsini, N., Mantzoros, C. S. & Wolk, A. Diabetes mellitus and risk of endometrial cancer: A meta-analysis. *Diabetologia* **50,** 1365–1374 (May 2007).

46. Saed, L. *et al.* The effect of diabetes on the risk of endometrial cancer: An updated a systematic review and meta-analysis. *BMC Cancer* **19** (May 2019).

47. Parazzini, F., La Vecchia, C., Moroni, S., Chatenoud, L. & Ricci, E. Family history and the risk of endometrial cancer. *International Journal of Cancer* **59,** 460–462 (Nov. 1994).

48. Gruber, S. B. & Thompson, W. D. A population-based study of endometrial cancer and familial risk in younger women. Cancer and Steroid Hormone Study Group. *Cancer Epidemiology, Biomarkers & Prevention* **5,** 411–417. ISSN: 1055-9965 (June 1996).

49. Lucenteforte, E. *et al.* Family history of cancer and the risk of endometrial cancer. *European Journal of Cancer Prevention* **18,** 95–99 (Apr. 2009).

50. Win, A. K., Reece, J. C. & Ryan, S. Family history and risk of endometrial cancer. *Obstetrics & Gynecology* **125,** 89–98 (Jan. 2015).

51. Johnatty, S. E. *et al.* Family history of cancer predicts endometrial cancer risk independently of Lynch Syndrome: Implications for Genetic Counselling. *Gynecologic Oncology* **147,** 381–387 (Nov. 2017).

52. O'Mara, T. A. *et al.* Identification of nine new susceptibility loci for endometrial cancer. *Nature Communications* **9** (Aug. 2018).

53. Dörk, T., Hillemanns, P., Tempfer, C., Breu, J. & Fleisch, M. C. Genetic susceptibility to endometrial cancer: Risk factors and clinical management. *Cancers* **12,** 2407 (Aug. 2020).

54. Bafligil, C. *et al.* Association between genetic polymorphisms and endometrial cancer risk: A systematic review. *Journal of Medical Genetics* **57,** 591–600 (Feb. 2020).

55. Bafligil, C. *et al.* Development and evaluation of polygenic risk scores for prediction of endometrial cancer risk in European women. *Genetics in Medicine* (Sept. 2022).

56. Barrow, E. *et al.* Cumulative lifetime incidence of extracolonic cancers in Lynch Syndrome: A report of 121 families with proven mutations. *Clinical Genetics* **75,** 141–149 (Jan. 2009).

57. Møller, P. *et al.* Cancer risk and survival in path mmr carriers by gene and gender up to 75 years of age: A report from the prospective Lynch Syndrome Database. *Gut* **67,** 1306–1316 (July 2017).

58. Dominguez-Valentin, M. *et al.* Cancer risks by gene, age, and gender in 6350 carriers of pathogenic mismatch repair variants: Findings from the prospective Lynch Syndrome Database. *Genetics in Medicine* **22,** 15–25 (July 2019).

59. Riegert-Johnson, D. L. *et al.* Cancer and Lhermitte-Duclos disease are common in Cowden syndrome patients. *Hereditary Cancer in Clinical Practice* **8** (June 2010).

60. Tan, M.-H. *et al.* Lifetime cancer risks in individuals with germline PTEN mutations. *Clinical Cancer Research* **18,** 400–407 (Jan. 2012).

61. Barnetson, R. *et al.* Germline mutation prevalence in the base excision repair gene, MYH, in patients with endometrial cancer. *Clinical Genetics* **72,** 551–555 (Oct. 2007).

62. Church, D. N. *et al.* DNA polymerase ϵ and δ exonuclease domain mutations in endometrial cancer. *Human Molecular Genetics* **22,** 2820–2828 (Mar. 2013).

63. Briggs, S. & Tomlinson, I. Germline and somatic polymerase ϵ and δ mutations define a new class of hypermutated colorectal and endometrial cancers. *The Journal of Pathology* **230,** 148–153 (June 2013).

64. Win, A. K. *et al.* Risk of extracolonic cancers for people with biallelic and monoallelic mutations in MUTYH. *International Journal of Cancer* **139,** 1557–1563 (May 2016).

65. De Jonge, M. M. *et al.* Endometrial cancer risk in women with germline BRCA1 or BRCA2 mutations: Multicenter cohort study. *JNCI: Journal of the National Cancer Institute* **113,** 1203–1211 (Mar. 2021).

66. Bokhman, J. V. Two pathogenetic types of endometrial carcinoma. *Gynecologic Oncology* **15,** 10–17 (1983).

67. For Research on Cancer, I. A. *et al.* WHO classification of tumors of the female reproductive organs. *IARC, Lyon* (2014).

68. Board, T. *Female Genital Tumours* (IARC Lyon, Fance, 2020).

69. Morice, P., Leary, A., Creutzberg, C., Abu-Rustum, N. & Darai, E. Endometrial cancer. *The Lancet* **387,** 1094–1108 (Mar. 2016).

70. Johnson, A. L. *et al.* The role of histology on endometrial cancer survival disparities in diverse Florida. *PLOS ONE* **15** (July 2020).

71. Creutzberg, C. L. *et al.* Fifteen-year radiotherapy outcomes of the randomized PORTEC-1 trial for endometrial carcinoma. *International Journal of Radiation Oncology, Biology, Physics* **81** (Nov. 2011).

72. Voss, M. A. *et al.* Should grade 3 endometrioid endometrial carcinoma be considered a type 2 cancer—a clinical and pathological evaluation. *Gynecologic Oncology* **124,** 15–20 (Jan. 2012).

73. Hussein, Y. R., Broaddus, R., Weigelt, B., Levine, D. A. & Soslow, R. A. The genomic heterogeneity of Figo Grade 3 endometrioid carcinoma impacts diagnostic accuracy and reproducibility. *International Journal of Gynecological Pathology* **35,** 16–24 (Jan. 2016).

74. Bosse, T. *et al.* Molecular classification of Grade 3 endometrioid endometrial cancers identifies distinct prognostic subgroups. *American Journal of Surgical Pathology* **42,** 561–568 (May 2018).

75. Kato, M. K. *et al.* Unique prognostic features of Grade 3 endometrioid endometrial carcinoma: Findings from 101 consecutive cases at a japanese tertiary cancer center. *Taiwanese Journal of Obstetrics and Gynecology* **60,** 238–244 (Mar. 2021).

76. Soslow, R. A. *et al.* Clinicopathologic analysis of 187 high-grade endometrial carcinomas of different histologic subtypes: Similar outcomes belie distinctive biologic differences. *American Journal of Surgical Pathology* **31,** 979–987 (July 2007).

77. McCluggage, W. G. Malignant biphasic uterine tumours: Carcinosarcomas or metaplastic carcinomas? *Journal of Clinical Pathology* **55,** 321–325 (May 2002).

78. Thompson, L., Chang, B. & Barsky, S. H. Monoclonal origins of malignant mixed tumors (carcinosarcomas). *The American Journal of Surgical Pathology* **20,** 277–285 (Mar. 1996).

79. Gorai, I. *et al.* Uterine carcinosarcoma is derived from a single stem cell: Anin Vitro study. *International Journal of Cancer* **72,** 821–827 (Sept. 1997).

80. Abeln, E. C. *et al.* Molecular genetic evidence for the conversion hypothesis of the origin of malignant mixed Müllerian tumours. *The Journal of Pathology* **183,** 424–431 (Dec. 1997).

81. Kounelis, S. *et al.* Carcinosarcomas (malignant mixed mullerian tumors) of the female genital tract: Comparative molecular analysis of epithelial and mesenchymal components. *Human Pathology* **29,** 82–87 (Jan. 1998).

82. McConechy, M. K. *et al.* In depth molecular profiling of the biphasic components of uterine carcinosarcomas. *The Journal of Pathology: Clinical Research* **1,** 173–185 (Mar. 2015).

83. Felix, A. S. *et al.* Factors associated with type I and type II endometrial cancer. *Cancer Causes & Control* **21,** 1851–1856 (July 2010).

84. Evans, T. *et al.* Differential trends in the rising incidence of endometrial cancer by type: Data from a UK population-based registry from 1994 to 2006. *British Journal of Cancer* **104,** 1505–1510 (Apr. 2011).

85. Silverberg, S. G. Problems in the differential diagnosis of endometrial hyperplasia and carcinoma. *Modern Pathology* **13,** 309–327 (Mar. 2000).

86. Zaino, R. J. *et al.* Reproducibility of the diagnosis of atypical endometrial hyperplasia. *Cancer* **106,** 804–811 (Feb. 2006).

87. Reed, S. D. *et al.* Complex hyperplasia with and without atypia. *Obstetrics & Gynecology* **116,** 365–373 (Aug. 2010).

88. Emons, G., Beckmann, M., Schmidt, D. & Mallmann, P. New who classification of endometrial hyperplasias. *Geburtshilfe und Frauenheilkunde* **75,** 135–136 (2015).

89. Yen, T.-T., Wang, T.-L., Fader, A. N., Shih, I.-M. & Gaillard, S. Molecular classification and emerging targeted therapy in endometrial cancer. *International Journal of Gynecological Pathology* **39,** 26–35 (Jan. 2020).

90. Levine, D. A. & Network, T. C. G. A. R. Integrated genomic characterization of endometrial carcinoma. *Nature* **497,** 67–73 (May 2013).

91. Cherniack, A. D. *et al.* Integrated molecular characterization of uterine carcinosarcoma. *Cancer Cell* **31,** 411–423 (Mar. 2017).

92. DeLair, D. F. *et al.* The genetic landscape of endometrial clear cell carcinomas. *The Journal of Pathology* **243,** 230–241 (Sept. 2017).

93. Gotoh, O. *et al.* Clinically relevant molecular subtypes and genomic alteration-independent differentiation in gynecologic carcinosarcoma. *Nature Communications* **10** (Oct. 2019).

94. Thomas, S. *et al.* Interobserver variability in the diagnosis of uterine high-grade endometrioid carcinoma. *Archives of Pathology & Laboratory Medicine* **140,** 836–843 (May 2016).

95. Stelloo, E. *et al.* Refining prognosis and identifying targetable pathways for high-risk endometrial cancer; A Transportec initiative. *Modern Pathology* **28,** 836–844 (Feb. 2015).

96. Talhouk, A. *et al.* A clinically applicable molecular-based classification for endometrial cancers. *British Journal of Cancer* **113,** 299–310 (June 2015).

97. Talhouk, A. *et al.* Molecular classification of endometrial carcinoma on diagnostic specimens is highly concordant with final hysterectomy: Earlier prognostic information to guide treatment. *Gynecologic Oncology* **143,** 46–53 (July 2016).

98. Talhouk, A. *et al.* Confirmation of promise: A simple, genomics-based clinical classifier for endometrial cancer. *Cancer* **123,** 802–813 (Jan. 2017).

99. Stelloo, E. *et al.* Improved risk assessment by integrating molecular and clinicopathological factors in early-stage endometrial cancer—combined analysis of the Portec cohorts. *Clinical Cancer Research* **22,** 4215–4224 (Aug. 2016).

100. Concin, N. *et al.* ESGO/ESTRO/ESP guidelines for the management of patients with endometrial carcinoma. *International Journal of Gynecologic Cancer* **31,** 12–39 (Dec. 2020).

101. Galaal, K., Donkers, H., Bryant, A. & Lopes, A. D. Laparoscopy versus laparotomy for the management of early stage endometrial cancer. *Cochrane Database of Systematic Reviews* **2018** (Oct. 2018).

102. Janda, M. *et al.* Quality of life after total laparoscopic hysterectomy versus total abdominal hysterectomy for stage I endometrial cancer (LACE): A randomised trial. *The Lancet Oncology* **11,** 772–780 (Aug. 2010).

103. Creasman, W. T. *et al.* Surgical pathologic spread patterns of endometrial cancer: A Gynecologic Oncology Group Study. *Cancer* **60,** 2035–2041 (Oct. 1987).

104. Panici, P. B. *et al.* Systematic pelvic lymphadenectomy vs no lymphadenectomy in early-stage endometrial carcinoma: Randomized clinical trial. *JNCI Journal of the National Cancer Institute* **100,** 1707–1716 (Nov. 2008).

105. Volpi, L. *et al.* Long term complications following pelvic and para-aortic lymphadenectomy for endometrial cancer, incidence and potential risk factors: A single institution experience. *International Journal of Gynecologic Cancer* **29,** 312–319 (Jan. 2019).

106. Muallem, M. Z., Diab, Y., Jöns, T., Sehouli, J. & Muallem, J. Nerve-sparing systematic lymph node dissection in gynaecological oncology: An Innovative Neuroanatomical and surgical protocol for enhanced functional outcomes. *Cancers* **12,** 3473 (Nov. 2020).

107. Group, A. S. *et al.* Efficacy of systematic pelvic lymphadenectomy in endometrial cancer (MRC Astec Trial): A Randomised Study. *The Lancet* **373,** 125–136 (May 2009).

108. Lutman, C. V. *et al.* Pelvic lymph node count is an important prognostic variable for Figo Stage I and II endometrial carcinoma with high-risk histology. *Gynecologic Oncology* **102,** 92–97 (July 2006).

109. Barlin, J. N. *et al.* The importance of applying a sentinel lymph node mapping algorithm in endometrial cancer staging: Beyond removal of blue nodes. *Gynecologic Oncology* **125,** 531–535 (June 2012).

110. Rossi, E. C. *et al.* A comparison of sentinel lymph node biopsy to lymphadenectomy for endometrial cancer staging (Fires trial): A Multicentre, prospective, cohort study. *The Lancet Oncology* **18,** 384–392 (Feb. 2017).

111. Geppert, B., Lönnerfors, C., Bollino, M. & Persson, J. Sentinel lymph node biopsy in endometrial cancer—feasibility, safety and lymphatic complications. *Gynecologic Oncology* **148,** 491–498 (Mar. 2018).

112. De Boer, S. M. *et al.* Adjuvant chemoradiotherapy versus radiotherapy alone in women with high-risk endometrial cancer (PORTEC-3): Patterns of recurrence and post-hoc survival analysis of a randomised phase 3 trial. *The Lancet Oncology* **20,** 1273–1285 (Sept. 2019).

113. Brooks, R. A. *et al.* Current recommendations and recent progress in endometrial cancer. *CA: A Cancer Journal for Clinicians* (May 2019).

114. Ethier, J.-L., Desautels, D. N., Amir, E. & MacKay, H. Is hormonal therapy effective in advanced endometrial cancer? A systematic review and meta-analysis. *Gynecologic Oncology* **147,** 158–166 (Oct. 2017).

115. Soumerai, T. E. *et al.* Clinical utility of prospective molecular characterization in Advanced endometrial cancer. *Clinical Cancer Research* **24,** 5939–5947 (Aug. 2018).

116. Fader, A. N. *et al.* Randomized phase II trial of carboplatin–paclitaxel compared with carboplatin–paclitaxel–trastuzumab in advanced (stage III–IV) or recurrent uterine serous carcinomas that overexpress HER2/neu (NCT01367002): Updated overall survival analysis. *Clinical Cancer Research* **26,** 3928–3935 (Aug. 2020).

117. Marabelle, A. *et al.* Efficacy of pembrolizumab in patients with noncolorectal high microsatellite instability/mismatch repair–deficient cancer: Results from the phase II keynote-158 study. *Journal of Clinical Oncology* **38,** 1–10 (Jan. 2020).

118. Slomovitz, B. M. *et al.* Phase II study of Everolimus and letrozole in patients with recurrent endometrial carcinoma. *Journal of Clinical Oncology* **33,** 930–936 (Mar. 2015).

119. Mackay, H., Rimel, B. & Bender, D. NRG GY012: A randomized phase II study comparing single-agent olaparib, single agent cediranib, and the combination of cediranib/olaparib in women with recurrent, persistent or metastatic endometrial cancer. *Journal of Clinical Oncology* **37,** TPS5609–TPS5609 (2019).

120. Miller, K. D. *et al.* Cancer treatment and survivorship statistics, 2022. *CA: A Cancer Journal for Clinicians* (June 2022).

121. *Macmillan Cancer Support and National Cancer Registration and Analysis Service* June 2015. `http://www.ncin.org.uk/about_ncin/segmentation`.

122. Tanoguchi, K. *et al.* K-ras point mutations in spontaneously occurring endometrial adenocarcinomas in The donryu rat. *The Tohoku Journal of Experimental Medicine* **189,** 87–93 (Oct. 1999).

123. Mitsumori, K. Rapid induction of uterine tumors with p53 point mutations in heterozygous p53-deficient CBA mice given a single intraperitoneal administration of N-ethyl-n-nitrosourea. *Carcinogenesis* **21,** 1039–1042 (May 2000).

124. Zhang, Z. *et al.* p53 Transgenic Mice Are Highly Susceptible to 1, 2-Dimethylhydrazine-induced Uterine Sarcomas. *Cancer Research* **62,** 3024–3029 (June 2002).

125. Sauer, B. & Henderson, N. Site-specific DNA recombination in mammalian cells by the cre recombinase of bacteriophage P1. *Proceedings of the National Academy of Sciences* **85,** 5166–5170 (July 1988).

126. Daikoku, T. *et al.* Conditional loss of uterine pten unfailingly and rapidly induces endometrial cancer in mice. *Cancer Research* **68,** 5619–5627 (July 2008).

127. Daikoku, T. *et al.* Cell-specific conditional deletion of PTEN in the uterus results in differential phenotypes. *Gynecologic Oncology* **122,** 424–429 (Aug. 2011).

128. Liang, X. *et al.* The uterine epithelial loss of PTEN is inefficient to induce endometrial cancer with intact stromal PTEN. *PLOS Genetics* **14** (Aug. 2018).

129. Gargett, C. E., Schwab, K. E., Zillwood, R. M., Nguyen, H. P. & Wu, D. Isolation and culture of epithelial progenitors and mesenchymal stem cells from human endometrium1. *Biology of Reproduction* **80,** 1136–1145 (June 2009).

130. Syed, S. M. *et al.* Endometrial axin2+ cells drive epithelial homeostasis, regeneration, and cancer following oncogenic transformation. *Cell Stem Cell* **26** (Jan. 2020).

131. Seishima, R. *et al.* Neonatal wnt-dependent LGR5 positive stem cells are essential for uterine gland development. *Nature Communications* **10** (Nov. 2019).

132. Ghosh, A. *et al.* In vivo cell fate tracing provides no evidence for mesenchymal to epithelial transition in adult fallopian tube and uterus. *Cell Reports* **31,** 107631 (May 2020).

133. Nguyen, H. P., Sprung, C. N. & Gargett, C. E. Differential expression of Wnt signaling molecules between pre- and postmenopausal endometrial epithelial cells suggests a population of putative epithelial stem/progenitor cells reside in the basalis layer. *Endocrinology* **153,** 2870–2883 (Apr. 2012).

134. Finn, C. A. & Pope, M. Vascular and cellular changes in the decidualized endometrium of the ovariectomized mouse following cessation of hormone treatment: A possible model for menstruation. *Journal of Endocrinology* **100** (Mar. 1984).

135. Brasted, M. Mimicking the events of menstruation in the murine uterus. *Biology of Reproduction* **69,** 1273–1280 (May 2003).

136. Bellofiore, N., Rana, S., Dickinson, H., Temple-Smith, P. & Evans, J. Characterization of human-like menstruation in the spiny mouse: Comparative studies with the human and induced mouse model. *Human Reproduction* **33,** 1715–1726 (July 2018).

137. Burns, K. A. *et al.* Endometriosis in the mouse: Challenges and progress toward a best fit murine model. *Frontiers in Physiology* **12** (Jan. 2022).

138. Greaves, E. *et al.* A novel mouse model of endometriosis mimics human phenotype and reveals insights into the inflammatory contribution of shed endometrium. *The American Journal of Pathology* **184,** 1930–1939 (July 2014).

139. Jean, S. & Kiger, A. A. Classes of phosphoinositide 3-kinases at a glance. *Journal of Cell Science* **127,** 923–928 (Mar. 2014).

140. Hoxhaj, G. & Manning, B. D. The PI3K–Akt network at the interface of oncogenic signalling and cancer metabolism. *Nature Reviews Cancer* **20,** 74–88 (Feb. 2019).

141. Fruman, D. A. *et al.* The PI3K pathway in human disease. *Cell* **170,** 605–635 (Aug. 2017).

142. Lee, Y.-R., Chen, M. & Pandolfi, P. P. The functions and regulation of the PTEN tumour suppressor: New modes and prospects. *Nature Reviews Molecular Cell Biology* **19,** 547–562 (Sept. 2018).

143. Kuo, Y.-C. *et al.* Regulation of phosphorylation of THR-308 of Akt, cell proliferation, and survival by the B55A regulatory subunit targeting of the protein phosphatase 2A holoenzyme to Akt. *Journal of Biological Chemistry* **283,** 1882–1892 (Jan. 2008).

144. Nitulescu, G. *et al.* The AKT pathway in oncology therapy and beyond (review). *International Journal of Oncology* (Oct. 2018).

145. Manning, B. D. & Toker, A. AKT/PKB signaling: Navigating the Network. *Cell* **169,** 381–405 (Apr. 2017).

146. Sutherland, C. What are the bona fide GSK3 substrates? *International Journal of Alzheimer's Disease* **2011,** 1–23 (May 2011).

147. Brown, A. K. & Webb, A. E. Regulation of FOXO factors in mammalian cells. *Current Topics in Developmental Biology,* 165–192 (Nov. 2017).

148. Hornsveld, M., Dansen, T., Derksen, P. & Burgering, B. Re-evaluating the role of FOXOs in cancer. *Seminars in Cancer Biology* **50,** 90–100 (June 2018).

149. Takahara, T., Amemiya, Y., Sugiyama, R., Maki, M. & Shibata, H. Amino acid-dependent control of mtorc1 signaling: A variety of regulatory modes. *Journal of Biomedical Science* **27** (Aug. 2020).

150. Lawrence, M. S. *et al.* Discovery and saturation analysis of cancer genes across 21 tumour types. *Nature* **505,** 495–501 (Jan. 2014).

151. Chang, H. W. *et al.* Transformation of chicken cells by the gene encoding the catalytic subunit of pi 3-kinase. *Science* **276,** 1848–1850 (June 1997).

152. Samuels, Y. *et al.* High frequency of mutations of the PIK3CA gene in human cancers. *Science* **304,** 554–554 (Apr. 2004).

153. Mayer, I. A. & Arteaga, C. L. The PI3K/Akt pathway as a target for cancer treatment. *Annual Review of Medicine* **67,** 11–28 (Jan. 2016).

154. Fritsch, C. *et al.* Characterization of the novel and specific PIK3α inhibitor NVP-BYL719 and development of the patient stratification strategy for clinical trials. *Molecular Cancer Therapeutics* **13,** 1117–1129 (May 2014).

155. Stamatkin, C., Ratermann, K. L., Overley, C. W. & Black, E. P. Inhibition of class IA PI3K enzymes in non-small cell lung cancer cells uncovers functional compensation among isoforms. *Cancer Biology & Therapy* **16,** 1341–1352 (July 2015).

156. Lane, D. P. P53, guardian of the genome. *Nature* **358,** 15–16 (July 1992).

157. LANE, D. P. & CRAWFORD, L. V. T antigen is bound to a host protein in SY40-transformed cells. *Nature* **278,** 261–263 (Mar. 1979).

158. Linzer, D. I. & Levine, A. J. Characterization of a 54K dalton cellular SV40 tumor antigen present in SV40-transformed cells and uninfected embryonal carcinoma cells. *Cell* **17,** 43–52 (May 1979).

159. DeLeo, A. B. *et al.* Detection of a transformation-related antigen in chemically induced sarcomas and other transformed cells of the mouse. *Proceedings of the National Academy of Sciences* **76,** 2420–2424 (May 1979).

160. Rotter, V., Witte, O. N., Coffman, R. & Baltimore, D. Abelson murine leukemia virus-induced tumors elicit antibodies against a host cell protein, P50. *Journal of Virology* **36,** 547–555 (Nov. 1980).

161. Levine, A. J. & Oren, M. The first 30 years of p53: Growing ever more complex. *Nature Reviews Cancer* **9,** 749–758 (Oct. 2009).

162. Eliyahu, D., Raz, A., Gruss, P., Givol, D. & Oren, M. Participation of p53 cellular tumour antigen in transformation of normal embryonic cells. *Nature* **312,** 646–649 (Dec. 1984).

163. Jenkins, J. R., Rudge, K. & Currie, G. A. Cellular immortalization by a cDNA clone encoding the transformation-associated phosphoprotein p53. *Nature* **312,** 651–654 (Dec. 1984).

164. Parada, L. F., Land, H., Weinberg, R. A., Wolf, D. & Rotter, V. Cooperation between gene encoding p53 tumour antigen and Ras in cellular transformation. *Nature* **312,** 649–651 (Dec. 1984).

165. Finlay, C. A., Hinds, P. W. & Levine, A. J. The p53 proto-oncogene can act as a suppressor of transformation. *Cell* **57,** 1083–1093 (June 1989).

166. Laptenko, O. & Prives, C. Transcriptional regulation by p53: One protein, many possibilities. *Cell Death & Differentiation* **13,** 951–961 (Mar. 2006).

167. Kastenhuber, E. R. & Lowe, S. W. Putting p53 in context. *Cell* **170,** 1062–1078 (Sept. 2017).

168. Brady, C. A. *et al.* Distinct p53 transcriptional programs dictate acute DNA-damage responses and tumor suppression. *Cell* **145,** 571–583 (May 2011).

169. Hernández Borrero, L. J. & El-Deiry, W. S. Tumor suppressor p53: Biology, signaling pathways, and therapeutic targeting. *Biochimica et Biophysica Acta (BBA) - Reviews on Cancer* **1876,** 188556 (Aug. 2021).

170. Sakamuro, D., Sabbatini, P., White, E. & Prendergast, G. C. The polyproline region of p53 is required to activate apoptosis but not growth arrest. *Oncogene* **15,** 887–898 (Aug. 1997).

171. Baptiste, N., Friedlander, P., Chen, X. & Prives, C. The proline-rich domain of p53 is required for cooperation with anti-neoplastic agents to promote apoptosis of tumor cells. *Oncogene* **21,** 9–21 (Jan. 2002).

172. Chène, P. The role of tetramerization in p53 function. *Oncogene* **20,** 2611–2617 (May 2001).

173. Ho, W. C., Fitzgerald, M. X. & Marmorstein, R. Structure of the p53 core domain dimer bound to DNA. *Journal of Biological Chemistry* **281,** 20494–20502 (July 2006).

174. Kung, C.-P. & Weber, J. D. It's getting complicated—a fresh look at p53-MDM2-ARF triangle in tumorigenesis and cancer therapy. *Frontiers in Cell and Developmental Biology* **10** (Jan. 2022).

175. Zindy, F. *et al.* Myc signaling via the ARF tumor suppressor regulates p53-dependent apoptosis and immortalization. *Genes & Development* **12,** 2424–2433 (Aug. 1998).

176. Agrawal, A., Yang, J., Murphy, R. F. & Agrawal, D. K. Regulation of the p14arf-MDM2-P53 pathway: An overview in breast cancer. *Experimental and Molecular Pathology* **81,** 115–122 (Oct. 2006).

177. Appella, E. & Anderson, C. W. Post-translational modifications and activation of p53 by genotoxic stresses. *European Journal of Biochemistry* **268,** 2764–2772 (May 2001).

178. Kumari, R., Kohli, S. & Das, S. P53 regulation upon genotoxic stress: Intricacies and complexities. *Molecular & Cellular Oncology* **1** (Sept. 2014).

179. Meek, D. W. The p53 response to DNA damage. *DNA Repair* **3,** 1049–1056 (Aug. 2004).

180. Chen, X., Ko, L. J., Jayaraman, L. & Prives, C. P53 levels, functional domains, and DNA damage determine the extent of the apoptotic response of tumor cells. *Genes & Development* **10,** 2438–2451 (Oct. 1996).

181. Purvis, J. E. *et al.* P53 dynamics control cell fate. *Science* **336,** 1440–1444 (June 2012).

182. Kaeser, M. D. & Iggo, R. D. Chromatin immunoprecipitation analysis fails to support the latency model for regulation of p53 DNA binding activity in vivo. *Proceedings of the National Academy of Sciences* **99,** 95–100 (Dec. 2001).

183. Oda, K. *et al.* P53AIP1, a potential mediator of p53-dependent apoptosis, and its regulation by SER-46-phosphorylated p53. *Cell* **102,** 849–862 (Sept. 2000).

184. Waterman, M. J., Stavridi, E. S., Waterman, J. L. & Halazonetis, T. D. ATM-dependent activation of p53 involves dephosphorylation and association with 14-3-3 proteins. *Nature Genetics* **19,** 175–178 (June 1998).

185. Flores, E. R. *et al.* P63 and p73 are required for p53-dependent apoptosis in response to DNA damage. *Nature* **416,** 560–564 (Apr. 2002).

186. Hermeking, H. *et al.* Is a p53-regulated inhibitor of G2/M Progression. *Molecular Cell* **1,** 3–11 (Dec. 1997).

187. Jin, S. *et al.* GADD45-induced cell cycle G2-M arrest associates with altered subcellular distribution of cyclin B1 and is independent of p38 kinase activity. *Oncogene* **21,** 8696–8704 (Dec. 2002).

188. Olivier, M., Hollstein, M. & Hainaut, P. TP53 mutations in human cancers: Origins, consequences, and clinical use. *Cold Spring Harbor Perspectives in Biology* **2** (Nov. 2009).

189. Zhu, G. *et al.* Mutant p53 in cancer progression and targeted therapies. *Frontiers in Oncology* **10** (Nov. 2020).

190. Baker, S. J. *et al.* p53 Gene Mutations Occur in Combination with 17p Allelic Deletions as Late Events in Colorectal Tumorigenesis1. *Cancer Research* **50,** 7717–7722. ISSN: 0008-5472 (Dec. 1990).

191. Alexandrova, E. M. *et al.* P53 loss-of-heterozygosity is a necessary prerequisite for mutant p53 stabilization and gain-of-function in vivo. *Cell Death & Disease* **8** (Mar. 2017).

192. Ciriello, G. *et al.* Emerging landscape of oncogenic signatures across human cancers. *Nature Genetics* **45,** 1127–1133 (Sept. 2013).

193. Brosh, R. & Rotter, V. When mutants gain new powers: News from the mutant P53 field. *Nature Reviews Cancer* **9,** 701–713 (Aug. 2009).

194. Willis, A., Jung, E. J., Wakefield, T. & Chen, X. Mutant P53 exerts a dominant negative effect by preventing wild-type p53 from binding to the promoter of its target genes. *Oncogene* **23,** 2330–2338 (Jan. 2004).

195. Chan, W. M., Siu, W. Y., Lau, A. & Poon, R. Y. How many mutant p53 molecules are needed to inactivate a tetramer? *Molecular and Cellular Biology* **24,** 3536–3551 (Apr. 2004).

196. Olive, K. P. *et al.* Mutant p53 Gain of Function in Two Mouse Models of Li-Fraumeni Syndrome. *Cell* **119,** 847–860 (2004).

197. Xu, J. *et al.* Heterogeneity of li-fraumeni syndrome links to unequal gain-of-function effects of p53 mutations. *Scientific Reports* **4** (Feb. 2014).

198. Bush, J. A. & Li, G. Cancer chemoresistance: The relationship between p53 and multidrug transporters. *International Journal of Cancer* **98,** 323–330 (Mar. 2002).

199. Zhu, J. *et al.* Gain-of-function p53 mutants co-opt chromatin pathways to drive cancer growth. *Nature* **525,** 206–211 (Sept. 2015).

200. Pfister, N. T. *et al.* Mutant P53 cooperates with the SWI/SNF chromatin remodeling complex to regulate vegfr2 in breast cancer cells. *Genes & Development* **29,** 1298–1315 (June 2015).

201. Mercer, W. E. *et al.* Negative growth regulation in a glioblastoma tumor cell line that conditionally expresses human wild-type p53. *Proceedings of the National Academy of Sciences* **87,** 6166–6170 (Aug. 1990).

202. Isaacs, W. B., Carter, B. S. & Ewing, C. M. Wild-Type p53 Suppresses Growth of Human Prostate Cancer Cells Containing Mutant p53 Alleles1. *Cancer Research* **51,** 4716–4720. ISSN: 0008-5472 (Sept. 1991).

203. Sugrue, M. M., Shin, D. Y., Lee, S. W. & Aaronson, S. A. Wild-type p53 triggers a rapid senescence program in human tumor cells lacking functional p53. *Proceedings of the National Academy of Sciences* **94,** 9648–9653 (Sept. 1997).

204. Ventura, A. *et al.* Restoration of p53 function leads to tumour regression in vivo. *Nature* **445,** 661–665 (Jan. 2007).

205. Xue, W. *et al.* Senescence and tumour clearance is triggered by p53 restoration in murine liver carcinomas. *Nature* **445,** 656–660 (Jan. 2007).

206. Vassilev, L. T. *et al.* In vivo activation of the p53 pathway by small-molecule antagonists of MDM2. *Science* **303,** 844–848 (Feb. 2004).

207. Ray-Coquard, I. *et al.* Effect of the MDM2 antagonist RG7112 on the p53 pathway in patients with MDM2-amplified, well-differentiated or dedifferentiated liposarcoma: An exploratory proof-of-mechanism study. *The Lancet Oncology* **13,** 1133–1140 (Nov. 2012).

208. Andreeff, M. *et al.* Results of the phase I trial of RG7112, a small-molecule MDM2 antagonist in leukemia. *Clinical Cancer Research* **22,** 868–876 (Feb. 2016).

209. Friedler, A. *et al.* A peptide that binds and stabilizes p53 core domain: Chaperone strategy for rescue of oncogenic mutants. *Proceedings of the National Academy of Sciences* **99,** 937–942 (Jan. 2002).

210. Boeckler, F. M. *et al.* Targeted rescue of a destabilized mutant of p53 by an in silico screened drug. *Proceedings of the National Academy of Sciences* **105,** 10360–10365 (July 2008).

211. Yu, X., Vazquez, A., Levine, A. J. & Carpizo, D. R. Allele-specific p53 mutant reactivation. *Cancer Cell* **21,** 614–625 (May 2012).

212. Sallman, D. A. *et al.* EPRENETAPOPT (APR-246) and azacitidine in TP53-mutant myelodysplastic syndromes. *Journal of Clinical Oncology* **39,** 1584–1594 (May 2021).

213. Lu, Y., Lee, B.-h., King, R. W., Finley, D. & Kirschner, M. W. Substrate degradation by the proteasome: A single-molecule kinetic analysis. *Science* **348** (Apr. 2015).

214. Rock, K. L. *et al.* Inhibitors of the proteasome block the degradation of most cell proteins and the generation of peptides presented on MHC class I molecules. *Cell* **78,** 761–771 (Sept. 1994).

215. Craiu, A. *et al.* Lactacystin and Clasto-Lactacystin β-lactone modify multiple proteasome β-subunits and inhibit intracellular protein degradation and major histocompatibility complex class I antigen presentation. *Journal of Biological Chemistry* **272,** 13437–13445 (May 1997).

216. Morreale, F. E. & Walden, H. Types of Ubiquitin ligases. *Cell* **165** (Mar. 2016).

217. Hartwell, L. H. Genetic control of the cell division cycle in yeast. *Journal of Molecular Biology* **59,** 183–194 (July 1971).

218. Hartwell, L. H., Mortimer, R. K., Culotti, J. & Culotti, M. Genetic control of the cell division cycle in yeast: V. Genetic Analysis of *cdc* mutants. *Genetics* **74,** 267–286 (June 1973).

219. Schwob, E. The B-type cyclin kinase inhibitor P40SIC1 controls the G1 to S transition in S. cerevisiae. *Cell* **79,** 233–244 (Oct. 1994).

220. Verma, R. *et al.* Phosphorylation of sic1p by G1 Cdk required for its degradation and entry into S phase. *Science* **278,** 455–460 (Oct. 1997).

221. Verma, R., Feldman, R. M. & Deshaies, R. J. Sic1 is ubiquitinated in vitro by a pathway that requires cdc4, CDC34, and cyclin/CDK activities. *Molecular Biology of the Cell* **8,** 1427–1437 (Aug. 1997).

222. Skowyra, D., Craig, K. L., Tyers, M., Elledge, S. J. & Harper, J. F-box proteins are receptors that recruit phosphorylated substrates to the SCF ubiquitin-ligase complex. *Cell* **91,** 209–219 (Oct. 1997).

223. Feldman, R., Correll, C. C., Kaplan, K. B. & Deshaies, R. J. A complex of Cdc4p, skp1p, and Cdc53p/Cullin catalyzes ubiquitination of the phosphorylated CDK inhibitor sic1p. *Cell* **91,** 221–230 (Oct. 1997).

224. Sundaram, M. & Greenwald, I. Suppressors of a Lin-12 hypomorph define genes that interact with both LIN-12 and GLP-1 in caenorhabditis elegans. *Genetics* **135,** 765–783 (Nov. 1993).

225. Hubbard, E. J., Wu, G., Kitajewski, J. & Greenwald, I. sel-10, a negative regulator of lin-12 activity in Caenorhabditis elegans, encodes a member of the CDC4 family of proteins. *Genes & Development* **11,** 3182–3193 (Dec. 1997).

226. Koepp, D. M. *et al.* Phosphorylation-dependent ubiquitination of cyclin E by the SCFfbw7 Ubiquitin ligase. *Science* **294,** 173–177 (Aug. 2001).

227. Strohmaier, H. *et al.* Human F-box protein HCDC4 targets cyclin E for proteolysis and is mutated in a breast cancer cell line. *Nature* **413,** 316–322 (Sept. 2001).

228. Moberg, K. H., Bell, D. W., Wahrer, D. C., Haber, D. A. & Hariharan, I. K. Archipelago regulates cyclin E levels in drosophila and is mutated in human cancer cell lines. *Nature* **413,** 311–316 (Sept. 2001).

229. Öberg, C. *et al.* The notch intracellular domain is ubiquitinated and negatively regulated by the mammalian SEL-10 homolog. *Journal of Biological Chemistry* **276,** 35847–35853 (Sept. 2001).

230. Wu, G. *et al.* SEL-10 is an inhibitor of notch signaling that targets notch for ubiquitin-mediated protein degradation. *Molecular and Cellular Biology* **21,** 7403–7415 (Nov. 2001).

231. Welcker, M. & Clurman, B. E. FBW7 ubiquitin ligase: A tumour suppressor at the crossroads of cell division, growth and differentiation. *Nature Reviews Cancer* **8,** 83–93 (Feb. 2008).

232. Matsumoto, A., Onoyama, I. & Nakayama, K. I. Expression of mouse FBXW7 isoforms is regulated in a cell cycle- or p53-dependent manner. *Biochemical and Biophysical Research Communications* **350,** 114–119 (Nov. 2006).

233. Grim, J. E. *et al.* Isoform- and cell cycle–dependent substrate degradation by the FBW7 ubiquitin ligase. *Journal of Cell Biology* **181,** 913–920 (June 2008).

234. Sionov, R. V., Netzer, E. & Shaulian, E. Differential regulation of FBXW7 isoforms by various stress stimuli. *Cell Cycle* **12,** 3547–3554 (Sept. 2013).

235. Kimura, T., Gotoh, M., Nakamura, Y. & Arakawa, H. HCDC4B, a regulator of cyclin E, as a direct transcriptional target of p53. *Cancer Science* **94,** 431–436 (2003).

236. Mao, J.-H. *et al.* FBXW7/Cdc4 is a p53-dependent, haploinsufficient tumour suppressor gene. *Nature* **432,** 775–779 (Dec. 2004).

237. Balamurugan, K. *et al.* The tumour suppressor C/EBPδ inhibits FBXW7 expression and promotes mammary tumour metastasis. *The EMBO Journal* **29,** 4106–4117 (Dec. 2010).

238. Sancho, R. *et al.* FBW7 repression by HES5 creates a feedback loop that modulates notch-mediated intestinal and neural stem cell fate decisions. *PLoS Biology* **11** (June 2013).

239. Lerner, M. *et al.* Mirna-27A controls FBW7/HCDC4-dependent cyclin E degradation and cell cycle progression. *Cell Cycle* **10,** 2172–2183 (July 2011).

240. Xia, W. *et al.* MicroRNA-32 promotes cell proliferation, migration and suppresses apoptosis in breast cancer cells by targeting FBXW7. *Cancer Cell International* **17** (Jan. 2017).

241. Zhou, C. *et al.* Mir-92a is upregulated in cervical cancer and promotes cell proliferation and invasion by targeting FBXW7. *Biochemical and Biophysical Research Communications* **458,** 63–69 (Feb. 2015).

242. Gong, L., Ren, M., Lv, Z., Yang, Y. & Wang, Z. Mir-92B-3P promotes colorectal carcinoma cell proliferation, invasion, and migration by inhibiting fbxw7 in vitro and in vivo. *DNA and Cell Biology* **37,** 501–511 (May 2018).

243. Li, J. *et al.* MicroRNA-223 functions as an oncogene in human gastric cancer by targeting FBXW7/HCDC4. *Journal of Cancer Research and Clinical Oncology* **138,** 763–774 (Jan. 2012).

244. Welcker, M., Orian, A., Grim, J. A., Eisenman, R. N. & Clurman, B. E. A nucleolar isoform of the FBW7 ubiquitin ligase regulates c-myc and cell size. *Current Biology* **14,** 1852–1857 (Oct. 2004).

245. Nash, P. *et al.* Multisite phosphorylation of a CDK inhibitor sets a threshold for the onset of DNA replication. *Nature* **414,** 514–521 (Nov. 2001).

246. Welcker, M. *et al.* Multisite phosphorylation by Cdk2 and GSK3 controls cyclin E degradation. *Molecular Cell* **12,** 381–392 (Aug. 2003).

247. Hao, B., Oehlmann, S., Sowa, M. E., Harper, J. W. & Pavletich, N. P. Structure of a FBW7-SKP1-cyclin e complex: Multisite-phosphorylated substrate recognition by SCF ubiquitin ligases. *Molecular Cell* **26,** 131–143 (Apr. 2007).

248. Yalla, K. *et al.* FBXW7 regulates disc1 stability via the ubiquitin-proteosome system. *Molecular Psychiatry* **23,** 1278–1286 (July 2017).

249. Welcker, M. *et al.* Two diphosphorylated degrons control c-MYC degradation by the FBW7 tumor suppressor. *Science Advances* **8** (Jan. 2022).

250. Welcker, M. & Clurman, B. E. Fbw7/hCDC4 dimerization regulates its substrate interactions. *Cell Division* **2,** 7 (Feb. 2007).

251. Welcker, M. *et al.* FBW7 dimerization determines the specificity and robustness of substrate degradation. *Genes & Development* **27,** 2531–2536 (Dec. 2013).

252. Csizmok, V. *et al*. Multivalent interactions with FBW7 and pin1 facilitate recognition of c-jun by the SCFFBW7 ubiquitin ligase. *Structure* **26** (Jan. 2018).

253. Min, S.-H. *et al.* Negative regulation of the stability and tumor suppressor function of FBW7 by the pin1 prolyl isomerase. *Molecular Cell* **46,** 771–783 (June 2012).

254. Kanatsu-Shinohara, M., Onoyama, I., Nakayama, K. I. & Shinohara, T. SKP1-cullin-F-box (SCF)-type ubiquitin ligase FBXW7 negatively regulates spermatogonial stem cell self-renewal. *Proceedings of the National Academy of Sciences* **111,** 8826–8831 (May 2014).

255. Klotz, K. *et al.* SCFFBXW7/HCDC4 targets cyclin E2 for ubiquitin-dependent proteolysis. *Experimental Cell Research* **315,** 1832–1839 (July 2009).

256. Siu, K. T., Rosner, M. R. & Minella, A. C. An integrated view of Cyclin E function and regulation. *Cell Cycle* **11,** 57–64 (Jan. 2012).

257. The ICGC/TCGA Pan-Cancer Analysis of Whole Genomes Consortium. Pan-cancer analysis of whole genomes. *Nature* **578,** 82–93 (Feb. 2020).

258. Spruck, C. H., Won, K.-A. & Reed, S. I. Deregulated cyclin e induces chromosome instability. *Nature* **401,** 297–300 (Sept. 1999).

259. Mao, J.-H. *et al.* FBXW7 targets mtor for degradation and cooperates with PTEN in tumor suppression. *Science* **321,** 1499–1502 (Sept. 2008).

260. Kearns, C. A., Ravanelli, A. M., Cooper, K. & Appel, B. FBXW7 limits myelination by inhibiting mTOR signaling. *Journal of Neuroscience* **35,** 14861–14871 (Nov. 2015).

261. Saxton, R. A. & Sabatini, D. M. MTOR signaling in growth, metabolism, and disease. *Cell* **168,** 960–976 (Mar. 2017).

262. Zou, Z., Tao, T., Li, H. & Zhu, X. MTOR signaling pathway and mTOR inhibitors in cancer: Progress and challenges. *Cell & Bioscience* **10** (Mar. 2020).

263. Wang, H., Guo, M., Wei, H. & Chen, Y. Targeting MCL-1 in cancer: Current status and Perspectives. *Journal of Hematology & Oncology* **14** (Apr. 2021).

264. Inuzuka, H. *et al.* SCFFBW7 regulates cellular apoptosis by targeting MCL1 for ubiquitylation and destruction. *Nature* **471,** 104–109 (Mar. 2011).

265. Bray, S. J. Notch signalling: A simple pathway becomes complex. *Nature Reviews Molecular Cell Biology* **7,** 678–689 (Sept. 2006).

266. Ellisen, L. W. *et al.* Tan-1, the human homolog of the drosophila notch gene, is broken by chromosomal translocations in T lymphoblastic neoplasms. *Cell* **66,** 649–661 (Aug. 1991).

267. Aster, J. C., Pear, W. S. & Blacklow, S. C. The varied roles of notch in cancer. *Annual Review of Pathology: Mechanisms of Disease* **12,** 245–275 (Jan. 2017).

268. Weng, A. P. *et al.* Activating mutations of notch1 in human T cell acute lymphoblastic leukemia. *Science* **306,** 269–271 (Oct. 2004).

269. Welcker, M. *et al.* The FBW7 tumor suppressor regulates glycogen synthase kinase 3 phosphorylation-dependent c-myc protein degradation. *Proceedings of the National Academy of Sciences* **101,** 9085–9090 (May 2004).

270. Yada, M. *et al.* Phosphorylation-dependent degradation of c-myc is mediated by the F-box protein FBW7. *The EMBO Journal* **23,** 2116–2125 (Apr. 2004).

271. Madden, S. K., de Araujo, A. D., Gerhardt, M., Fairlie, D. P. & Mason, J. M. Taking the Myc out of cancer: Toward therapeutic strategies to directly inhibit C-Myc. *Molecular Cancer* **20** (Jan. 2021).

272. Dang, C. V. *et al.* The C-myc target gene network. *Seminars in Cancer Biology* **16,** 253–264 (Aug. 2006).

273. Dang, C. V. Myc on the path to cancer. *Cell* **149,** 22–35 (Mar. 2012).

274. Nateri, A. S., Lluís, R.-S., Costa, C. D. & Behrens, A. The ubiquitin ligase SCFfbw7 antagonizes apoptotic JNK signaling. *Science* **303,** 1374–1378 (Feb. 2004).

275. Wei, W., Jin, J., Schlisio, S., Harper, J. W. & Kaelin, W. G. The v-jun point mutation allows c-jun to escape GSK3-dependent recognition and destruction by the FBW7 ubiquitin ligase. *Cancer Cell* **8,** 25–33 (July 2005).

276. Meng, Q. & Xia, Y. C-jun, at the crossroad of the signaling network. *Protein & Cell* **2,** 889–898 (Nov. 2011).

277. Mariani, O. *et al.* Jun oncogene amplification and overexpression block adipocytic differentiation in highly aggressive sarcomas. *Cancer Cell* **11,** 361–374 (Apr. 2007).

278. Zhang, Y. *et al.* Critical role of c-jun overexpression in liver metastasis of human breast cancer xenograft model. *BMC Cancer* **7** (Aug. 2007).

279. He, H. *et al.* C-jun/AP-1 overexpression reprograms ERA signaling related to tamoxifen response in ERA-positive breast cancer. *Oncogene* **37,** 2586–2600 (May 2018).

280. Kourtis, N. *et al.* FBXW7 modulates cellular stress response and metastatic potential through HSF1 post-translational modification. *Nature Cell Biology* **17,** 322–332 (Feb. 2015).

281. Carpenter, R. L. & Gökmen-Polar, Y. HSF1 as a cancer biomarker and therapeutic target. *Current Cancer Drug Targets* **19,** 515–524 (Sept. 2019).

282. Hoang, A. T. *et al.* A novel association between the human heat shock transcription factor 1 (HSF1) and Prostate Adenocarcinoma. *The American Journal of Pathology* **156,** 857–864 (Mar. 2000).

283. Rajagopalan, H. *et al.* Inactivation of HCDC4 can cause chromosomal instability. *Nature* **428,** 77–81 (Mar. 2004).

284. Galindo-Moreno, M. *et al.* SCF(FBXW7)-mediated degradation of p53 promotes cell recovery after UV induced DNA damage. *The FASEB Journal* **33,** 11420–11430 (July 2019).

285. Cui, D. *et al.* FBXW7 confers radiation survival by targeting p53 for degradation. *Cell Reports* **30** (Jan. 2020).

286. Lan, H. & Sun, Y. Tumor suppressor FBXW7 and its regulation of DNA damage response and Repair. *Frontiers in Cell and Developmental Biology* **9** (Oct. 2021).

287. Zhang, Q. *et al.* FBXW7 facilitates nonhomologous end-joining via K63-linked polyubiquitylation of XRCC4. *Molecular Cell* **61,** 419–433 (Feb. 2016).

288. Zhang, Q. *et al.* The WD40 domain of FBXW7 is a poly(adp-ribose)-binding domain that mediates the early DNA damage response. *Nucleic Acids Research* **47,** 4039–4053 (May 2019).

289. Akhoondi, S. *et al.* FBXW7/hcdc4 is a general tumor suppressor in human cancer. *Cancer Research* **67,** 9006–9012 (Oct. 2007).

290. Kandoth, C. *et al.* Mutational landscape and significance across 12 major cancer types. *Nature* **502,** 333–339 (Oct. 2013).

291. Asnafi, V. *et al.* Notch1/FBXW7 mutation identifies a large subgroup with favorable outcome in adult T-cell acute lymphoblastic leukemia (T-all): A Group for research on Adult Acute Lymphoblastic Leukemia (GRAALL) study. *Blood* **113,** 3918–3924 (Apr. 2009).

292. The Cancer Genome Atlas Network. Comprehensive molecular characterization of human colon and rectal cancer. *Nature* **487,** 330–337 (July 2012).

293. The Cancer Genome Atlas Research Network. Integrated genomic and molecular characterization of cervical cancer. *Nature* **543,** 378–384 (Jan. 2017).

294. The Cancer Genome Atlas Research Network. Comprehensive genomic characterization of squamous cell lung cancers. *Nature* **489,** 519–525 (Sept. 2012).

295. The Cancer Genome Atlas Research Network. Comprehensive molecular characterization of gastric adenocarcinoma. *Nature* **513,** 202–209 (July 2014).

296. The Cancer Genome Atlas Research Network. Comprehensive molecular characterization of urothelial bladder carcinoma. *Nature* **507,** 315–322 (Jan. 2014).

297. Davis, H., Lewis, A., Behrens, A. & Tomlinson, I. Investigation of the atypical fbxw7 mutation spectrum in human tumours by conditional expression of a heterozygous propellor tip missense allele in the mouse intestines. *Gut* **63,** 792–799 (May 2013).

298. The Cancer Genome Atlas Research Network *et al.* The cancer genome Atlas Pan-Cancer Analysis Project. *Nature Genetics* **45,** 1113–1120 (Sept. 2013).

299. Davis, H. & Tomlinson, I. CDC4/FBXW7 and the 'just enough' model of tumourigenesis. *The Journal of Pathology* **227,** 131–135 (Apr. 2012).

300. Iwatsuki, M. *et al.* Loss of FBXW7, a cell cycle regulating gene, in colorectal cancer: Clinical significance. *International Journal of Cancer* **126,** 1828–1837 (Sept. 2009).

301. Sterian, A. *et al.* Mutational and Loh analyses of the chromosome 4q region in esophageal adenocarcinoma. *Oncology* **70,** 168–172 (July 2006).

302. Yokobori, T. *et al.* Copy number loss of FBXW7 is related to gene expression and poor prognosis in esophageal squamous cell carcinoma. *International Journal of Oncology* **41,** 253–259 (Apr. 2012).

303. Milne, A. N. *et al.* Loss of cdc4/fbxw7 in Gastric Carinoma. *Analytical Cellular Pathology* **32,** 347–359 (May 2010).

304. Yokobori, T. *et al.* p53-altered fbxw7 expression determines poor prognosis in gastric cancer cases. *Cancer Research* **69,** 3788–3794 (Apr. 2009).

305. Ibusuki, M., Yamamoto, Y., Shinriki, S., Ando, Y. & Iwase, H. Reduced expression of ubiquitin ligase FBXW7 mrna is associated with poor prognosis in breast cancer patients. *Cancer Science* **102,** 439–445 (Dec. 2010).

306. Ishii, N. *et al.* Reduced FBXW7 expression in pancreatic cancer correlates with poor prognosis and chemotherapeutic resistance via accumulation of MCL1. *Oncotarget* **8,** 112636–112646 (Nov. 2017).

307. Mun, G.-I., Choi, E., Lee, Y. & Lee, Y.-S. Decreased expression of FBXW7 by ERK1/2 activation in drug-resistant cancer cells confers transcriptional activation of MDR1 by suppression of ubiquitin degradation of HSF1. *Cell Death & Disease* **11** (May 2020).

308. Akhoondi, S. *et al.* Inactivation of FBXW7/HCDC4-β expression by promoter hypermethylation is associated with favorable prognosis in primary breast cancer. *Breast Cancer Research* **12** (Dec. 2010).

309. Soyal, S. M. *et al.* Cre-mediated recombination in cell lineages that express the progesterone receptor. *genesis* **41,** 58–66 (2005).

310. Davis, H. *et al.* FBXW7 mutations typically found in human cancers are distinct from null alleles and disrupt lung development. *The Journal of Pathology* **224,** 180–189 (2011).

311. Suzuki, A. *et al.* T cell-specific loss of Pten leads to defects in central and peripheral tolerance. *Immunity* **14,** 523–534 (2001).

312. Marino, S., Vooijs, M., van Der Gulden, H., Jonkers, J. & Berns, A. Induction of medulloblastomas in p53-null mutant mice by somatic inactivation of Rb in the external granular layer cells of the cerebellum. *Genes & development* **14,** 994–1004 (2000).

313. Truett, G. E. *et al.* Preparation of PCR-quality mouse genomic DNA with hot sodium hydroxide and tris (HotSHOT). *Biotechniques* **29,** 52–54 (2000).

314. Hellemans, J., Mortier, G., De Paepe, A., Speleman, F. & Vandesompele, J. qBase relative quantification framework and software for management and automated analysis of real-time quantitative PCR data. *Genome Biology* **8** (Feb. 2007).

315. Becker, J. R. *et al.* The ASCIZ-DYNLL1 axis promotes 53BP1-dependent non-homologous end joining and PARP inhibitor sensitivity. *Nature Communications* **9** (Dec. 2018).

316. Cuevas, I. C. *et al.* FBXW7 is a driver of uterine carcinosarcoma by promoting epithelial-mesenchymal transition. *Proceedings of the National Academy of Sciences* **116,** 25880–25890 (Nov. 2019).

317. Wang, Y. *et al.* Rapamycin inhibits FBXW7 loss-induced epithelial–mesenchymal transition and cancer stem cell-like characteristics in colorectal cancer cells. *Biochemical and Biophysical Research Communications* **434,** 352–356 (May 2013).

318. Yang, H. *et al.* FBXW7 suppresses epithelial-mesenchymal transition, stemness and metastatic potential of cholangiocarcinoma cells. *Oncotarget* **6,** 6310–6325 (Jan. 2015).

319. Li, N. *et al.* An FBXW7-Zeb2 axis links EMT and tumour microenvironment to promote colorectal cancer stem cells and chemoresistance. *Oncogenesis* **8** (Feb. 2019).

320. Wang, L.-L., Wan, X.-Y., Liu, C.-Q. & Zheng, F.-M. NDR1 increases NOTCH1 signaling activity by impairing FBW7 mediated NICD degradation to enhance breast cancer stem cell properties. *Molecular Medicine* **28** (May 2022).

321. Zhang, Y. *et al.* FBW7 loss promotes epithelial-to-mesenchymal transition in non-small cell lung cancer through the stabilization of snail protein. *Cancer Letters* **419,** 75–83 (Apr. 2018).

322. Xiao, G. *et al.* FBXW7 suppresses epithelial-mesenchymal transition and chemoresistance of non-small-cell lung cancer cells by targeting snai1 for Ubiquitin-dependent degradation. *Cell Proliferation* **51** (Aug. 2018).

323. Takeishi, S. & Nakayama, K. I. Role of FBXW7 in the maintenance of normal stem cells and cancer-initiating cells. *British Journal of Cancer* **111,** 1054–1059 (May 2014).

324. Hoeck, J. D. *et al.* FBW7 controls neural stem cell differentiation and progenitor apoptosis via notch and c-jun. *Nature Neuroscience* **13,** 1365–1372 (Oct. 2010).

325. Matsumoto, A. *et al.* FBXW7-dependent degradation of Notch is required for control of "stemness" and neuronal-glial differentiation in neural stem cells. *Journal of Biological Chemistry* **286,** 13754–13764 (Apr. 2011).

326. Sancho, R. *et al.* F-box and WD repeat domain-containing 7 regulates intestinal cell lineage commitment and is a haploinsufficient tumor suppressor. *Gastroenterology* **139,** 929–941 (Sept. 2010).

327. Matsuoka, S. *et al.* FBXW7 acts as a critical fail-safe against premature loss of hematopoietic stem cells and development of T-all. *Genes & Development* **22,** 986–991 (Mar. 2008).

328. Iriuchishima, H. *et al.* Ex vivo maintenance of hematopoietic stem cells by quiescence induction through fbxw7α overexpression. *Blood* **117,** 2373–2377 (Feb. 2011).

329. Naganawa, Y. *et al.* Decreased expression of FBXW7 is correlated with poor prognosis in patients with esophageal squamous cell carcinoma. *Experimental and Therapeutic Medicine* **1,** 841–846 (July 2010).

330. Cheng, Y., Chen, G., Martinka, M., Ho, V. & Li, G. Prognostic significance of FBW7 in human melanoma and its role in Cell Migration. *Journal of Investigative Dermatology* **133,** 1794–1802 (July 2013).

331. Li, M.-R. *et al.* FBXW7 expression is associated with prognosis and chemotherapeutic outcome in Chinese patients with gastric adenocarcinoma. *BMC Gastroenterology* **17** (May 2017).

332. Lui, H., Wang, K., Fu, H. & Song, J. Low expression of the ubiquitin ligase FBXW7 correlates with poor prognosis of patients with colorectal cancer. *International Journal of Clinical & Experimental Pathology* **11,** 413–419 (Jan. 2018).

333. Mouradov, D. *et al.* Survival in stage II/III colorectal cancer is independently predicted by chromosomal and microsatellite instability, but not by specific driver mutations. *American Journal of Gastroenterology* **108,** 1785–1793 (Nov. 2013).

334. Korphaisarn, K. *et al.* fbxw7 missense mutation: A novel negative prognostic factor in metastatic colorectal adenocarcinoma. *Oncotarget* **8,** 39268–39279 (Apr. 2017).

335. Shang, W. *et al.* Clinical significance of FBXW7 tumor suppressor gene mutations and expression in human colorectal cancer: A systemic review and meta-analysis. *BMC Cancer* **21** (July 2021).

336. Garcia-Dios, D. A. *et al.* High-throughput interrogation of Pik3ca, PTEN, KRAS, FBXW7 and TP53 mutations in primary endometrial carcinoma. *Gynecologic Oncology* **128,** 327–334 (Feb. 2013).

337. López-Reig, R. *et al.* Prognostic classification of endometrial cancer using a molecular approach based on a twelve-gene NGS panel. *Scientific Reports* **9** (Dec. 2019).

338. Watanabe, T. *et al.* Clinical relevance of oncogenic driver mutations identified in endometrial carcinoma. *Translational Oncology* **14,** 101010 (Mar. 2021).

339. Tetzlaff, M. T. *et al.* Defective cardiovascular development and elevated cyclin E and notch proteins in mice lacking the FBW7 F-box protein. *Proceedings of the National Academy of Sciences* **101,** 3338–3345 (Feb. 2004).

340. Tsunematsu, R. *et al.* Mouse FBW7/SEL-10/cdc4 is required for notch degradation during vascular development. *Journal of Biological Chemistry* **279,** 9417–9423 (Mar. 2004).

341. Thompson, B. J. *et al.* Control of hematopoietic stem cell quiescence by the E3 ubiquitin ligase FBW7. *Journal of Experimental Medicine* **205,** 1395–1408 (May 2008).

342. Onoyama, I. *et al.* FBXW7 regulates lipid metabolism and cell fate decisions in the Mouse Liver. *Journal of Clinical Investigation* **121,** 342–354 (Jan. 2011).

343. Babaei-Jadidi, R. *et al.* FBXW7 influences murine intestinal homeostasis and cancer, targeting notch, jun, and DEK for degradation. *Journal of Experimental Medicine* **208,** 295–312 (Jan. 2011).

344. King, B. *et al.* The ubiquitin ligase FBXW7 modulates leukemia-initiating cell activity by regulating myc stability. *Cell* **153,** 1552–1566 (June 2013).

345. Zhao, S. *et al.* Mutational landscape of uterine and ovarian carcinosarcomas implicates histone genes in epithelial–mesenchymal transition. *Proceedings of the National Academy of Sciences* **113,** 12238–12243 (Oct. 2016).

346. Thirimanne, H. N. *et al.* Global and context-specific transcriptional consequences of oncogenic FBW7 mutations. *eLife* **11** (Feb. 2022).

347. Ellrott, K. *et al.* Scalable open science approach for mutation calling of tumor exomes using multiple genomic pipelines. *Cell Systems* **6** (Mar. 2018).

348. Mayakonda, A., Lin, D.-C., Assenov, Y., Plass, C. & Koeffler, H. P. Maftools: Efficient and comprehensive analysis of somatic variants in cancer. *Genome Research* **28,** 1747–1756 (Oct. 2018).

349. Cerami, E. *et al.* The Cbio Cancer Genomics Portal: An open platform for exploring multidimensional cancer genomics data. *Cancer Discovery* **2,** 401–404 (May 2012).

350. Tate, J. G. *et al.* Cosmic: The catalogue of somatic mutations in cancer. *Nucleic Acids Research* **47** (Oct. 2018).

351. Martínez-Jiménez, F. *et al.* A compendium of mutational cancer driver genes. *Nature Reviews Cancer* **20,** 555–572 (Aug. 2020).

352. Suda, K. *et al.* Clonal expansion and diversification of cancer-associated mutations in endometriosis and normal endometrium. *Cell Reports* **24,** 1777–1789 (Aug. 2018).

353. Moore, L. *et al.* The mutational landscape of normal human endometrial epithelium. *Nature* **580,** 640–646 (2020).

354. Yamaguchi, M. *et al.* Spatiotemporal Dynamics of clonal selection and diversification in normal endometrial epithelium. *Nature Communications* **13** (2022).

355. Diaz Brinton, R. Minireview: Translational Animal Models of Human menopause: Challenges and emerging opportunities. *Endocrinology* **153,** 3571–3578 (July 2012).

356. Gerstung, M. *et al.* The evolutionary history of 2,658 cancers. *Nature* **578,** 122–128 (Feb. 2020).

357. Sun, H. *et al.* Mutational analysis of the pten gene in endometrial carcinoma and hyperplasia. *American Journal of Clinical Pathology* **115,** 32–38 (Jan. 2001).

358. Gbelcová, H. *et al.* pten sequence analysis in endometrial hyperplasia and endometrial carcinoma in Slovak women. *Analytical Cellular Pathology* **2015,** 1–7 (May 2015).

359. Russo, M. *et al.* Mutational profile of endometrial hyperplasia and risk of progression to endometrioid adenocarcinoma. *Cancer* **126,** 2775–2783 (Mar. 2020).

360. Lac, V. *et al.* Oncogenic mutations in histologically normal endometrium: The new normal? *The Journal of Pathology* **249,** 173–181 (July 2019).

361. Liu, J. *et al.* Wnt/β-catenin signalling: Function, biological mechanisms, and therapeutic opportunities. *Signal Transduction and Targeted Therapy* **7** (Jan. 2022).

362. Ma, S., Meng, Z., Chen, R. & Guan, K.-L. The hippo pathway: Biology and pathophysiology. *Annual Review of Biochemistry* **88,** 577–604 (June 2019).

363. Chang, H. J. *et al.* PIK3CA is required for mouse uterine gland development and pregnancy. *PLOS ONE* **13** (Jan. 2018).

364. Joshi, A., Miller, C., Baker, S. J. & Ellenson, L. H. Activated mutant P110A causes endometrial carcinoma in the setting of Biallelic Pten deletion. *The American Journal of Pathology* **185,** 1104–1113 (Apr. 2015).

365. Ruediger, R., Ruiz, J. & Walter, G. Human cancer-associated mutations in the AA subunit of protein phosphatase 2A increase lung cancer incidence in AA knock-in and knockout mice. *Molecular and Cellular Biology* **31,** 3832–3844 (Sept. 2011).

366. Taylor, S. E. *et al.* The highly recurrent PP2A AA-subunit mutation P179R alters protein structure and impairs PP2A enzyme function to promote endometrial tumorigenesis. *Cancer Research* **79,** 4242–4257 (Aug. 2019).

367. Kwon, Y.-W. *et al.* PTEN regulates Aurora-A and cooperates with FBXW7 in modulating radiation-induced tumor development. *Molecular Cancer Research* **10,** 834–844 (June 2012).

368. Giaccia, A. J. & Kastan, M. B. The complexity of p53 modulation: Emerging patterns from Divergent Signals. *Genes & Development* **12,** 2973–2983 (1998).

369. Andrade, D. A. *et al.* Squamous differentiation portends poor prognosis in low and intermediate-risk endometrioid endometrial cancer. *PLOS ONE* **14** (Oct. 2019).

370. Aslan, K. *et al.* The prognostic value of squamous differentiation in endometrioid type endometrial cancer: A matched analysis. *Journal of Obstetrics and Gynaecology* **42,** 494–500 (June 2021).

371. Yun, K. & Im, S.-H. Transcriptional regulation of MMP13 by LEF1 in chondrocytes. *Biochemical and Biophysical Research Communications* **364,** 1009–1014 (Dec. 2007).

372. Xu, L., Corcoran, R. B., Welsh, J. W., Pennica, D. & Levine, A. J. WISP-1 is a Wnt-1 and β-catenin-responsive oncogene. *Genes & Development* **14,** 585–595 (Mar. 2000).

373. Wang, Y. *et al.* Comprehensive molecular characterization of the Hippo Signaling Pathway in Cancer. *Cell Reports* **25** (Oct. 2018).

374. Xing, S. *et al.* TCF1 and LEF1 transcription factors establish CD8+ T cell identity through intrinsic HDAC activity. *Nature Immunology* **17,** 695–703 (Apr. 2016).

375. Shan, Q. *et al.* TCF1 and Lef1 provide constant supervision to mature CD8+ T cell identity and function by organizing genomic architecture. *Nature Communications* **12** (Oct. 2021).

376. Wu, J.-T., Lin, H.-C., Hu, Y.-C. & Chien, C.-T. Neddylation and deneddylation regulate CUL1 and CUL3 protein accumulation. *Nature Cell Biology* **7,** 1014–1020 (Aug. 2005).

377. Jiang, J.-x. *et al.* Tumor suppressor FBXW7 antagonizes Wnt signaling by targeting β-catenin for degradation in pancreatic cancer. *Tumor Biology* **37,** 13893–13902 (Aug. 2016).

378. Yang, F. *et al.* FBXW2 suppresses migration and invasion of lung cancer cells via promoting β-catenin ubiquitylation and degradation. *Nature Communications* **10** (Mar. 2019).

379. Tu, K. *et al.* FBXW7 is an independent prognostic marker and induces apoptosis and growth arrest by regulating yap abundance in hepatocellular carcinoma. *Molecular Cancer* **13** (May 2014).

380. Jeong, J.-W. *et al.* B-catenin mediates glandular formation and dysregulation of β-catenin induces hyperplasia formation in the murine uterus. *Oncogene* **28,** 31–40 (Sept. 2008).

381. Shelton, D. N. *et al.* The role of Lef1 in endometrial gland formation and carcinogenesis. *PLoS ONE* **7** (July 2012).

382. Shen, J. *et al.* Glucose-regulated protein 94 deficiency induces squamous cell metaplasia and suppresses PTEN-null driven endometrial epithelial tumor development. *Oncotarget* **7,** 14885–14897 (Feb. 2016).

383. Chumduri, C. *et al.* Opposing wnt signals regulate cervical squamocolumnar homeostasis and emergence of metaplasia. *Nature Cell Biology* **23,** 184–197 (Jan. 2021).

384. Van der Zee, M. *et al.* Alterations in Wnt-β-catenin and PTEN signalling play distinct roles in endometrial cancer initiation and progression. *The Journal of Pathology* **230,** 48–58 (Mar. 2013).

385. Daikoku, T. *et al.* Lactoferrin-ICRE: A new mouse line to study uterine epithelial gene function. *Endocrinology* **155,** 2718–2724 (July 2014).

386. Nei, H. *et al.* Nuclear localization of β-catenin in normal and carcinogenic endometrium. *Molecular Carcinogenesis* **25,** 207–218 (July 1999).

387. Kim, G. *et al.* Nuclear β-catenin localization and mutation of the CTNNB1 gene: A context-dependent association. *Modern Pathology* **31,** 1553–1559 (May 2018).

388. Fatima, I., Barman, S., Rai, R., Thiel, K. W. & Chandra, V. Targeting wnt signaling in endometrial cancer. *Cancers* **13,** 2351 (May 2021).

389. Escobar, D., Bushara, O., Sun, L., Liao, J. & Yang, G.-Y. Clinicopathologic characteristics of FBXW7-mutated colorectal adenocarcinoma and association with aberrant beta-catenin localization. *Human Pathology* **119,** 51–58 (Jan. 2022).

390. Orlicky, S., Tang, X., Willems, A., Tyers, M. & Sicheri, F. Structural basis for phosphodependent substrate selection and orientation by the SCFCDC4 ubiquitin ligase. *Cell* **112,** 243–256 (Jan. 2003).

391. Wang, Y., van der Zee, M., Fodde, R. & Blok, L. J. Wnt/B-catenin and sex hormone signaling in endometrial homeostasis and cancer. *Oncotarget* **1,** 674–684 (Oct. 2010).

392. McMellen, A., Woodruff, E. R., Corr, B. R., Bitler, B. G. & Moroney, M. R. Wnt signaling in gynecologic malignancies. *International Journal of Molecular Sciences* **21,** 4272 (June 2020).

393. Park, Y. *et al.* A novel human endometrial epithelial cell line for modeling gynecological diseases and for drug screening. *Laboratory Investigation* **101,** 1505–1512 (Aug. 2021).

394. Soong, R. *et al.* Overexpression of p53 protein is an independent prognostic indicator in human endometrial carcinoma. *British Journal of Cancer* **74,** 562–567 (Aug. 1996).

395. Sakuragi, N. *et al.* Functional Analysis of p53 gene and the prognostic impact of dominant negative p53 mutation in endometrial cancer. *International Journal of Cancer* **116,** 514–519 (Apr. 2005).

396. Albitar, L., Carter, M. B., Davies, S. & Leslie, K. K. Consequences of the loss of p53, RB1, and PTEN: Relationship to gefitinib resistance in endometrial cancer. *Gynecologic Oncology* **106,** 94–104 (July 2007).

397. Dong, P. *et al.* P53 dominant-negative mutant R273H promotes invasion and migration of human endometrial cancer HHUA cells. *Clinical & Experimental Metastasis* **24,** 471–483 (July 2007).

398. Dong, P., Xu, Z., Jia, N., Li, D. & Feng, Y. Elevated expression of p53 gain-of-function mutation r175h in endometrial cancer cells can increase the invasive phenotypes by activation of the EGFR/PI3K/akt pathway. *Molecular Cancer* **8,** 103 (Nov. 2009).

399. Wang, H. *et al.* Mutant p53 (p53-R248Q) functions as an oncogene in promoting endometrial cancer by up-regulating regγ. *Cancer Letters* **360,** 269–279 (May 2015).

400. Dong, P. *et al.* Mutant p53 gain-of-function induces epithelial–mesenchymal transition through modulation of the mir-130b–zeb1 axis. *Oncogene* **32,** 3286–3295 (July 2012).

401. Meng, X. *et al.* Induction of mitotic cell death by overriding G2/M checkpoint in endometrial cancer cells with non-functional p53. *Gynecologic Oncology* **128,** 461–469 (Mar. 2013).

402. Wild, P. J. *et al.* P53 suppresses type II endometrial carcinomas in mice and governs endometrial tumour aggressiveness in humans. *EMBO Molecular Medicine* **4,** 808–824 (June 2012).

403. Minella, A. C., Grim, J. E., Welcker, M. & Clurman, B. E. P53 and scffbw7 cooperatively restrain cyclin E-associated genome instability. *Oncogene* **26,** 6948–6953 (May 2007).

404. Schultheis, A. M. *et al.* TP53 mutational spectrum in endometrioid and serous endometrial cancers. *International Journal of Gynecological Pathology* **35,** 289–300 (July 2016).

405. Alvarado-Ortiz, E. *et al.* Mutant p53 gain-of-function: Role in cancer development, progression, and therapeutic approaches. *Frontiers in Cell and Developmental Biology* **8** (Feb. 2021).

406. Abeshouse, A. *et al.* Comprehensive and integrated genomic characterization of adult soft tissue sarcomas. *Cell* **171** (Nov. 2017).

407. Smith, M. L. & Fornace, A. J. Genomic instability and the role of p53 mutations in cancer cells. *Current Opinion in Oncology* **7,** 68–75 (Jan. 1995).

408. Di Agostino, S. *et al.* Gain of function of mutant p53: The mutant p53/NF-y protein complex reveals an aberrant transcriptional mechanism of cell cycle regulation. *Cancer Cell* **10,** 191–202 (Sept. 2006).

409. Mantovani, F., Collavin, L. & Del Sal, G. Mutant P53 as a guardian of the cancer cell. *Cell Death & Differentiation* **26,** 199–212 (Dec. 2018).

410. Redman-Rivera, L. N. *et al.* Acquisition of aneuploidy drives mutant p53-associated gain-of-function phenotypes. *Nature Communications* **12** (Aug. 2021).

411. Baslan, T. *et al.* Ordered and deterministic cancer genome evolution after p53 loss. *Nature* **608,** 795–802 (Aug. 2022).

412. Byrd, K. N. *et al.* FBXW7 and DNA copy number instability. *Breast Cancer Research and Treatment* **109,** 47–54 (June 2007).

413. Loeb, K. R. *et al.* A mouse model for cyclin E-dependent genetic instability and tumorigenesis. *Cancer Cell* **8,** 35–47 (July 2005).

414. Hastings, P. J., Lupski, J. R., Rosenberg, S. M. & Ira, G. Mechanisms of change in gene copy number. *Nature Reviews Genetics* **10,** 551–564 (Aug. 2009).

415. Li, D. *et al.* Functional inactivation of endogenous MDM2 and chip by hsp90 causes aberrant stabilization of mutant p53 in human cancer cells. *Molecular Cancer Research* **9,** 577–588 (May 2011).

416. Hayashi, S. & McMahon, A. P. Efficient recombination in diverse tissues by a tamoxifen-inducible form of CRE: A tool for temporally regulated gene activation/inactivation in the mouse. *Developmental Biology* **244,** 305–318 (Apr. 2002).

417. Hunter, T. The age of crosstalk: Phosphorylation, ubiquitination, and beyond. *Molecular Cell* **28,** 730–738 (Dec. 2007).

418. Gong, E.-Y. *et al.* Chk1 ka1 domain auto-phosphorylation stimulates biological activity and is linked to rapid proteasomal degradation. *Scientific Reports* **8** (Dec. 2018).

419. Ishitani, T., Ninomiya-Tsuji, J. & Matsumoto, K. Regulation of lymphoid enhancer factor 1/T-cell factor by mitogen-activated protein kinase-related nemo-like kinase-dependent phosphorylation in Wnt/β-catenin signaling. *Molecular and Cellular Biology* **23,** 1379–1389 (Feb. 2003).

420. Ota, S. *et al.* NLK positively regulates Wnt/β-catenin signalling by phosphorylating LEF1 in neural progenitor cells. *The EMBO Journal* **31,** 1904–1915 (Feb. 2012).

421. Ray, S., Xu, F., Wang, H. & Das, S. K. Cooperative control via lymphoid enhancer factor 1/T cell factor 3 and estrogen receptor-α for uterine gene regulation by estrogen. *Molecular Endocrinology* **22,** 1125–1140 (May 2008).

422. Urick, M. E. & Bell, D. W. Proteomic profiling of FBXW7 mutant serous endometrial cancer cells reveals upregulation of padi2, a potential therapeutic target. *Cancer Medicine* **9,** 3863–3874 (Apr. 2020).

423. Song, Y. *et al.* E3 ligase FBXW7 is critical for rig-I stabilization during antiviral responses. *Nature Communications* **8** (Mar. 2017).

424. Wang, Y. *et al.* Distinct interactions of EBP1 isoforms with FBXW7 elicits different functions in cancer. *Cancer Research* **77,** 1983–1996 (Apr. 2017).

425. Giráldez, S. *et al.* SCFFBXW7α modulates the intra-s-phase DNA-damage checkpoint by regulating polo like kinase-1 stability. *Oncotarget* **5,** 4370–4383 (May 2014).

426. Zhao, X. *et al.* Circadian amplitude regulation via FBXW7-targeted rev-erbα degradation. *Cell* **165,** 1644–1657 (June 2016).

427. Chen, Y. *et al.* Wnt induced deubiquitination FOXM1 ensures nucleus β catenin transactivation. *The EMBO Journal* **35,** 668–684 (Feb. 2016).

428. Sundqvist, A. *et al.* Control of lipid metabolism by phosphorylation-dependent degradation of the SREBP family of transcription factors by scffbw7. *Cell Metabolism* **1,** 379–391 (June 2005).

429. Liu, N. *et al.* The FBW7/human cdc4 tumor suppressor targets proproliferative factor klf5 for ubiquitination and degradation through multiple phosphodegron motifs. *Journal of Biological Chemistry* **285,** 18858–18867 (June 2010).

430. Biswas, M., Phan, D., Watanabe, M. & Chan, J. Y. The FBW7 tumor suppressor regulates nuclear factor E2-related factor 1 transcription factor turnover through proteasome-mediated proteolysis. *Journal of Biological Chemistry* **286,** 39282–39289 (Nov. 2011).

431. Lv, X.-B. *et al.* Regulation of sox10 stability via ubiquitination-mediated degradation by fbxw7α modulates melanoma cell migration. *Oncotarget* **6,** 36370–36382 (Oct. 2015).

432. Fukushima, H. *et al.* SCFFBW7 modulates the NFKB signaling pathway by targeting NFKB2 for ubiquitination and destruction. *Cell Reports* **1,** 434–443 (May 2012).

433. Galli, F. *et al.* MDM2 and FBW7 cooperate to induce P63 protein degradation following DNA damage and cell differentiation. *Journal of Cell Science* **123,** 2423–2433 (July 2010).

434. Maskey, D. *et al.* Cell cycle dependent ubiquitylation and destruction of NDE1 by CDK5 FBW7 regulates ciliary length. *The EMBO Journal* **34,** 2424–2440 (July 2015).

435. Kharat, S. S. *et al.* Mitotic phosphorylation of bloom helicase at THR182 is required for its proteasomal degradation and maintenance of chromosomal stability. *Oncogene* **35,** 1025–1038 (June 2015).

436. Koo, J., Wu, X., Mao, Z., Khuri, F. R. & Sun, S.-Y. Rictor undergoes glycogen synthase kinase 3 (gsk3)-dependent, FBXW7-mediated ubiquitination and proteasomal degradation. *Journal of Biological Chemistry* **290,** 14120–14129 (May 2015).

437. Fang, L. *et al.* Circadian clock gene CRY2 degradation is involved in chemoresistance of colorectal cancer. *Molecular Cancer Therapeutics* **14,** 1476–1487 (June 2015).